Paleoenvironmental Variability during the Middle Miocene Climatic Optimum Reconstructed using a Lake Sediment Record from the Otago Region, New Zealand

A thesis

submitted in partial fulfilment

of the requirements for the degree

of

Master of Science in Earth Science

at

The University of Waikato

by

FRANCIS DAVID ALAIN GARRITY

THE UNIVERSITY OF
WAIKATO
Te Whare Wānanga o Waikato

2017

i

ABSTRACT

Climate archives indicate that the varied interaction of several cycles across a range of timescales exerted a prevailing control on climate throughout the Holocene and Pleistocene. However, due to the scarcity of highly resolved lacustrine records, it has so far been difficult to recognize sub-Milankovitch scale cycles in earlier epochs. Climate variability during the Middle Miocene was particularly extensive, and included the Miocene Climatic Optimum, representing the maximum temperatures experienced during the Cenozoic. A high resolution account of Southern Hemisphere paleoenvironmental variability during the Miocene Climatic Optimum has never previously been produced and is thus of significant importance.

The Hindon Maar diatomite is a laminated lacustrine deposit dominated by *Aulacoseira spp.* diatoms. This lake formed due to a phreatomagmatic eruption as part of the Waipiata Volcanic Field, and accumulated during the Langhian Age (~15.2 Ma; Middle Miocene) in the Otago region of New Zealand. A high-resolution multi-proxy analysis was conducted on a 10.8-m-long core of this annually resolved lake sediment, which varve thicknesses suggest represents 7600 years of deposition. Gamma density, magnetic susceptibility, CIELAB L*a*b* colour, particle size, compositional data and petrographic images were collected. Compositional data included biogenic silica, total organic carbon and schist, determined using Fourier transform infrared spectroscopy.

Principal components analysis of these variables enabled the identification of underlying processes which I interpret to represent precipitation, wind speed and temperature. *Aulacoseira spp.* diatoms are highly sensitive to variations in wind speed, and thus most changes in lake productivity reflect wind strength changes relating to underlying cyclicity. In addition, electrofacies analysis is used to identify six reoccurring and persisting paleoenvironmental states. Based on electrofacies analysis of principal component factor scores, a high resolution reconstruction is proposed and related to the underlying cyclical factors.

It is suggested that wind strength on this time scale during the Middle Miocene may partially respond to the interaction of two solar cycles and one orbital cycle. These are the DeVries cycle (200 years), the Hallstatt cycle (2300 years) and precession (~26000 years). These cycles and others were identified using a combination of sum of sinusoidal signal analysis, Tukey-Hamming spectral analysis and wavelet transformations. Peaks in these cycles thus likely generated warm conditions, causing prevailing westerly winds to move northwards and intensify, whilst troughs correspond to a decline in oceanic temperatures and wind speeds. This investigation therefore demonstrates the influence of sub-Milankovitch scale cycles and solar forcing on conditions during the Miocene Climatic Optimum for the first time in the Southern Hemisphere.

ACKNOWLEDGEMENTS

TABLE OF CONTENTS

LIST OF FIGURES

CHAPTER ONE

Introduction

1.1 Background, motivation and structure

Climatic conditions during Middle Miocene (15.97 to 11.61 Ma) were highly variable, and include the 'Mid-Miocene Climatic Optimum' (MMCO), representing the maximum temperatures experienced during the Cenozoic (Flower and Kennett, 1993; Böhme 2003). Furthermore, distinct climatic fluctuations occurred within the MMCO. Shortly following this period, global temperature decreased rapidly and the volume of ice on East Antarctica expanded (Shackleton and Kennett, 1975; Verducci et al., 2007).

The Miocene thus provides a unique opportunity to understand global and Antarctic climate without the overprint of anthropogenic influence. New Zealand's small land mass and principally oceanic climate suggest that the climate in New Zealand would closely reflect global zonal conditions without the influence of large land areas and high relief. Despite the impetus to research the Mid-Miocene paleoclimatic history of New Zealand, there are few lacustrine or paleolimnological records and a lack of high-resolution chronologies available to further improve our understanding of climate change processes within New Zealand.

This thesis responds to this demand by producing a high-resolution paleoclimatic event stratigraphy for a maar crater lake (Hindon Maar Complex, Otago), at a critical location for evaluating Miocene paleoenvironmental change. I aim to identify the orbital and solar mechanisms that explain the cyclicity in paleoenvironmental signatures.

This introduction explores the geological and geographical history of the field area and surrounding region, and provides an overview of previous research at the Hindon Maar Complex (HMC). Previous Miocene climate research is discussed, and the fundamentals of paleolimnology are outlined. This includes backgrounds to compositional (biogenic silica, total organic carbon), and physical (magnetic-susceptibility, particle size distribution, colour) approaches.

Following this, the methods section describes the drilling approach used to retrieve core. An outline of the methods and intricacies associated with the acquisition of physical and compositional data is then provided. Finally, statistical methods used in this project are explained.

The results section first reports broad-scale, primary data such as appearance (particularly lamina thickness), particle size distributions and composition. Results from statistical methods including Pearson correlation, principal components analysis (PCA), and electrofacies analysis are presented, as are the results of Tukey-Hamming spectral analysis and sum of sinusoidal signals data.

The discussion section (Chapter 4) first outlines the inferred process by which laminae formed and provides an interpretation of the diatomite lamination styles observed in the deposit. A review of the conditions associated with observed diatom species is provided, and the accuracy of FTIR analysis is considered. I proceed to identify three processes which could account for the magnetic susceptibility variations identified in the core. Consideration is then given to the likely origin of organic carbon in the core, and this is followed by a discussion of trends seen in biogenic silica. A section is provided which aims to identify and explain unusual sections identified in the core based on physical or compositional data. Following this, the statistical results are interpreted including the Pearson correlation analysis,

the principal components analysis and the electrofacies analysis. I provide a hypothesis linking PCA, electrofacies, sum of sinusoidal signals and Tukey-Hamming spectral analysis to orbital and solar cycles, and then propose a reconstruction of paleoenvironmental conditions including relative temperature, wind speeds and precipitation. The remainder of the thesis, Chapter 5 and Section 6, include concluding remarks and an appendices of additional data.

1.2 Geographical Setting and field area

The Hindon field site from which the core for this study was retrieved is located within the Eastern Otago region, with the geographical coordinates: 45°43'58.9" South, 170°17'58.5" East (Figure 1.1). This maar complex is approximately 20 km NW of Dunedin City, among high-relief rolling hills underlain by the Otago Schist. Geophysical aeromagnetic surveys carried out by Glass Earth and the Otago Regional Council revealed the general extent of each of these features (Figure 1.2). Maar One has a diameter of 1100 m along its longest axis, whilst Maars Two and Three are both slightly smaller.
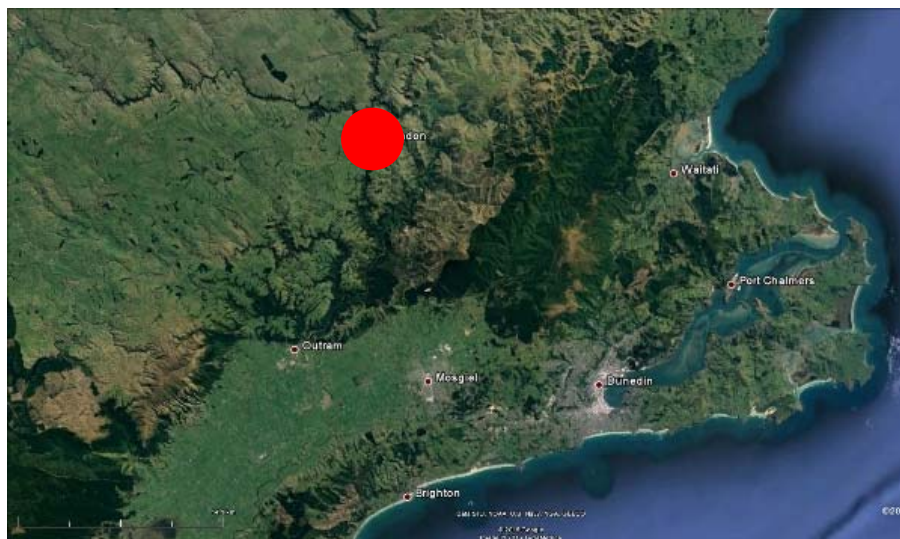
Figure 1.1 The Hindon Maar field site is located North-West of Dunedin (From Google Earth).
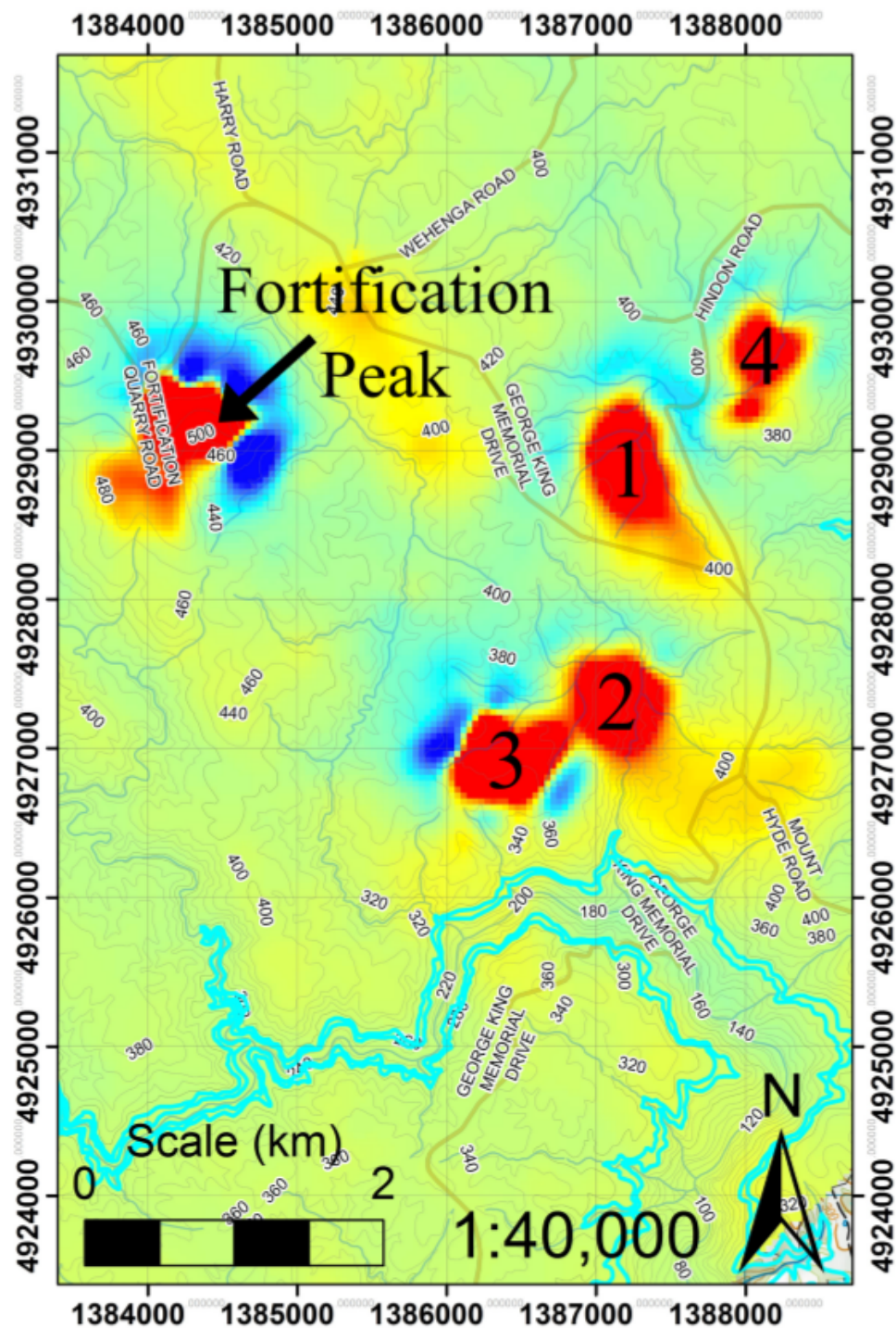
Figure 1.2: Glass Earth and Otago Regional Council aeromagnetic survey, 2007. This figure shows the location of Maars 1, 2, 3 and 4. Additionally, Fortification Peak denotes the location of a Mid-Miocene basaltic flow (From Bowie, 2015).

1.3 Geological Setting

1.3.1 Otago Schist

The Hindon Maar complex is hosted in the Otago Schist. The Otago Schist is considered to have developed due to the metamorphism of metagreywacke-dominated sedimentary sequences which were deposited more than 225 Ma (Adams & Graham, 1997). Formation of this unit began at approximately 200 Ma during the Rangitata Orogeny, when the Caples and Torlesse tectonostratigraphic terranes collided in a forearc setting, with the Caples terrane overthrust on the Torlesse terrane (Mortimer, 1993). Regional metamorphism occurred in the Early Jurassic, and the Otago Schist was gradually uplifted during the Cretaceous. Extensional faulting in the mid-Cretaceous (and further oblique compressional faulting in the Cenozoic) resulted in the Otago Schist becoming exposed and significantly deformed. The Late Cenozoic inception of a Pacific-Australian plate boundary through New Zealand has been linked to a major proportion of this deformation (Mortimer, 1993).

The Otago Schist is now exposed at a number of sites throughout Central Otago, and is thought be present at depth across a large area of the South Island of New Zealand, reaching a maximum length of 2000 km and a width of approximately 150 km. The centre of this metamorphic belt has been described as a greenschist facies with subhorizontal foliation. On either side of this greenschist facies, the structure is dominated by prehnite-pumpellyite units. This unit features bedding and foliation features characteristic of low-grade metamorphism (Mortimer, 1993).

It has been suggested that the orogenesis of the Otago Schist featured three cycles of compression-extension, leading to repeated uplift and collapse (Johnson, 1990).

While porphyroblast nonrotation may support this interpretation, such a model would predict more complex faulting relationships and foliation than can be observed within the Otago Schist (Mortimer, 1993). The central region of the Otago Schist exhibits relatively simple foliation overprinting congruous with a single compressional kinematic event and multiple transpositions (Mortimer, 1993).

The present-day topography of the Otago region was strongly defined by marine planation during the Cretaceous-Early Miocene, forming the Waipounamu Erosional Surface (Landis et al., 2008). This significant unconformity was the result of tectonic and epeirogenic movements, in combination with continuous eustatic change. For this reason the Waipounamu Erosion Surface is best described as diachronous, having formed due to multiple changes in sea level and erosional periods. Following this erosional event, the Otago Schist accretionary complex contributes to the total crustal thickness of <30 km in the Dunedin region. Widespread marine transgression in the Late Cretaceous generated significant marine clastic sedimentation in the region, and subsequent marine and non-marine sedimentation formed the pre-volcanic Cenozoic units. These units were deposited directly on the schist basement following Early Cretaceous uplift and erosion (LeMasurier and Landis, 1996, Landis et al., 2008).

1.3.2 Volcanism

The majority of Cenozoic volcanic activity in the South Island is related to the extensional tectonic regime operating during that era (Coombs et al., 2008). The Waiareka-Deborah volcanics represent the first expression of this period of volcanism which occurred from 40 to 32 Ma, with the eruption of both tholeiitic and alkali basaltic magmas near Oamaru. Between 32 and 23 Ma, a lamprophyric dike and diatreme swarm was emplaced near Lake Wanaka. This dike swarm was finally succeeded by the Waipiata Volcanics, which are believed to have formed the Hindon Maar Complex (Figure 1.2) (Coombs et al., 2008). A switch from the dominant extensional tectonic regime to the compressional regime associated with the Kaikoura Orogeny has been linked to a reduced supply of magma from the mantle, leading to the end of volcanism in this area at 9 Ma (Coombs et al., 2008).
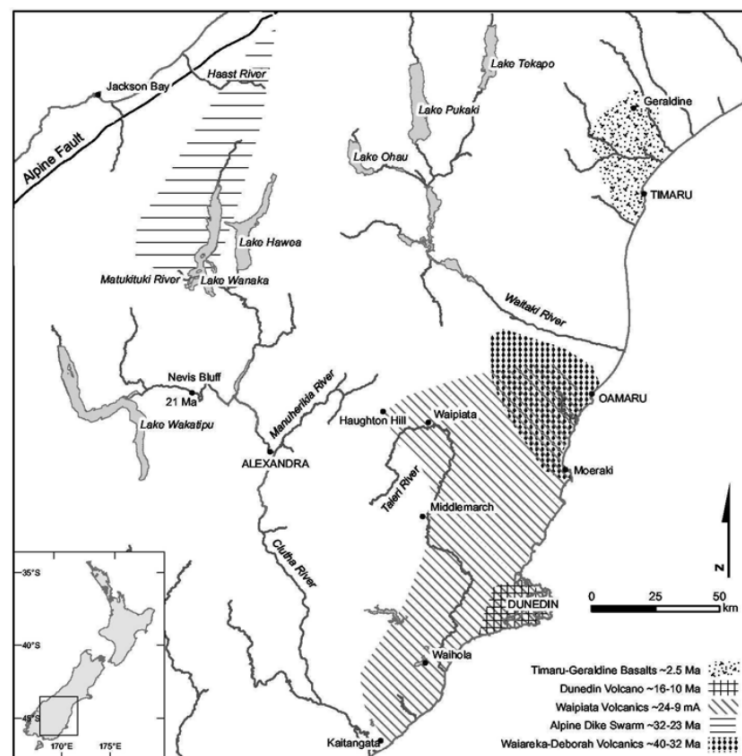
Figure 1.3. : Location of Cenozoic volcanic provinces in Otago (From Coombs et al., 2008).

1.3.3 Waipiata Volcanics

The Waipiata Volcanic Field is an eroded phreatomagmatic intracontinental volcanic field. It comprises more than 55 volcanoes distributed across an area of approximately 5000 km^2. Initial volcanism within this field was dominated by phreatomagmatic eruptions (Nemeth and White, 2003). This period of water-driven reactions eventually ceased and was followed by a series of Strombolian-style eruptions. Three vent types have been identified within the Waipiata Volcanic Field. The first vent type (Type One) present includes remnants of monogenetic volcanoes and their lava lakes, feeder dikes and lava flows. These vents may be completely filled with lava, or may contain pyroclastic deposits (Nemeth and White, 2003).

The second vent type (Type Two) commonly observed within the Waipiata Volcanic Field are located in close proximity to Type One vents, and have been derived from phreatomagmatic explosions (Nemeth and White, 2003). These vents commonly contain and are surrounded by base surge deposits. These are typically rich in non-volcanic lithic-rich massive tuff breccias and lapilli tuffs. Such deposits are commonly interbedded with unsorted, stratified tuff breccias, where any bedding is likely to dip towards the vent. Deposits of this nature often contain decimetre-scale blocks enclosed within the pyroclastic matrix, with these blocks most commonly being fragments of the Otago Schist (Nemeth and White, 2003). As a result of phreatomagmatic fragmentation, it is expected that lava expelled during these eruptions will contain a small proportion of tachylite, as well as sideromelane (Nemeth and White, 2003). The uppermost portion of Type Two vents commonly features lava spatter, indicating the cessation of phreatomagmatic fragmentation due to the exhaustion of the water supply (Nemeth and White, 2003).

The third volcanic feature commonly identified within the Waipiata volcanic field are complexes of overlapping maars, scoria cones and tuff rings, and these may be regarded as a combination of both Type One and Type Two vents. These complexes are typically accompanied by lava flows or lakes, and form when multiple, simultaneous eruptions occur from several vents (Nemeth and White, 2003).

The geochemical features of the Waipiata Volcanic Group have been analysed using electron microprobes. This analysis indicates that lava flows within the group are dominated by basanites, and that mantle-derived xenoliths including Iherzolite, mugearite and nepheline hawaiite are common (Coombs et al. 1986). Phreatomagmatic deposits are substantially more evolved than are the lava flows, and may include tephrite or phonotephrite, for example (Nemeth and White, 2003).

1.4.4 Hindon

The Hindon Maar Complex meets several of the criteria used to identify Type Three complexes: the vents are positioned within several hundred metres of one another, and lava flows likely to stem from multiple sources can be observed at the field site. Many of the volcanic landforms present within this field site exhibit features of the Type Two vents, and pyroclastic deposits at this site feature the non-volcanic lithics and stratified tuff breccias associated with phreatomagmatic eruptions of this type. This landform is surrounded by the Otago Schist, and outcrops derived from the Taratu Formation (late Cretaceous to late Eocene) have also been observed (Bowie, 2015).

1.4 Previous research conducted at the Hindon Maar site

Ar-Ar dating indicates that the HMC formed 15.2 Ma (Personal Communication, Daphne Lee), placing it within the Middle Miocene Climatic Optimum. Beyond this, relatively little research has previously been conducted at these maars, and the quality of this sediment as a paleoclimate record has not been established. These maar-diatremes have never been previously used for the purpose of climatic reconstruction. These landforms were first identified as potential maar deposits in 1993 (Youngson, 1993), when diatomaceous and carbonaceous laminites were identified overlying schistose siliciclastics. Interest in these features was renewed in 2007, after airborne geophysical surveys revealed significant magnetic and gravitational anomalies within the Hindon Maar Complex (Christie et al., 2012). A geophysical characterisation of the Hindon Maars was produced by Bowie (2015). This research revealed that Maars One, Two and Three have an elliptical shape with a diameter of 1100 m, 800 m and 800 m respectively. Maars Two and Three are presently separated by a 200 m wide body of rock, inferred to be the Otago Schist. While these maars formed during individual eruptions, the close proximity of these structures suggest that they likely share the same magma propagation vent, and subsequently split into two discrete vents.

While paleoclimate reconstruction has not yet been conducted using these maars, the deposits have formed the basis of a paleontological study detailing the discovery of a new cicada genus (Kaulfuss and Moulds, 2015). In support of this study a temporary excavation was conducted recently at Maar One. This project revealed that a 1 – 2 m thick overburden of Quaternary loess and alluvium is present at Maar One.

Two lacustrine facies were identified during the paleontological study of HM1 (Kaulfuss and Moulds, 2015). Both were noted to contain siliceous microfossils of a limnic origin, including chrysophycean cysts, pennate diatoms and spicules derived from freshwater sponges (Kaulfuss and Moulds, 2015).

The first lacustrine facies is similar to material earlier found in the Miocene Foulden Maar (Lindqvist and Lee, 2009). Foulden Maar is an Early-Miocene deposit located near the HMC, and like the HMC, formed due to the phreatomagmatic activity of the Waipiata Group and is annually laminated (Lindqvist and Lee, 2009). The Foulden Maar deposit is several million years older than the 15.2 Ma HMC, but nevertheless provides a valuable comparison. This facies is comprised predominantly of laminated fossiliferous diatomite, but also contains massive-graded diatomaceous mass-flow beds (Kaulfuss and Moulds, 2015). The second facies described is a dark-brown carbonaceous mudstone, with generally thick laminae interspersed with cm-scale beds of fine laminations. Thick laminations within the second facies have been found to contain fossilized pollen, spores, flowers, leaves, fruits, cones and seeds from various fern, conifer and angiosperm species. Coprolites have also been found, along with fossilized insects of various orders, including Hemiptera, Hymenoptera, Trichoptera and Coleoptera. Aquatic fauna, including galaxiid fish, were also preserved. The notable absence of bioturbation, and the preservation of soft leaf and animal tissues suggests that these fossils accumulated in an anoxic environment, and that this sediment may therefore record high quality climate and environmental information. The high quality of this sediment means it is likely to be suitable for answering my research questions. Because relatively little work has been done at this site, the methods followed throughout this research will be informed by work previously conducted at other

diatomaceous maar-lakes within the Waipiata volcanic field (particularly the nearby Foulden Maar), and at other lake sites world-wide (e.g. Poth and Negendank, 1993; Striewski et al., 2009; Sirocko et al., 2013).

1.5 Global scale Miocene climate research

The climate during the Miocene epoch was highly variable, and the Earth was frequently significantly warmer than it is presently (Billups & Schrag, 2002; Zachos et al., 2008; Gasson et al., 2016). Overall, this period is distinguished by long term cooling, which led to the establishment of modern terrestrial biomes and the Late Cenozoic icehouse mode (Kürschner et al., 2008). The factors which caused these developments are not well understood, and authors have previously considered the role of changes in carbon dioxide concentration; tectonism and associated ocean circulation (e.g. Heydt and Dijkstra 2006); solar variability, the periodic oscillations in Earth's eccentricity, obliquity and precession (which influence the amount and distribution of solar energy over timescales of 10^4-10^5 years) (Kern, et al., 2012); global albedo; and vegetation changes in driving the climate of the Miocene. Indeed, prior to the extensive study of marine CO_2 proxies including the $\delta^{13}C$ of marine phytoplankton (Pagani et al., 2005) and $\delta^{11}B$ of marine carbonate (Pearson and Palmer, 2000; Demicco et al., 2003), CO_2 variability was believed to be the dominant cause of variation in Miocene climate (Vincent and Berger, 1985; Raymo, 1991; Cerling et al., 1997). This idea was largely dismissed following the increased number of high quality sediment cores obtained by the Deep Sea Drilling Project and Ocean Drilling Project, which revealed that CO_2 concentrations within the Miocene were consistently low (200-280 ppm), similar to that of the glacial Pleistocene (Mikolajewicz and Crowley, 1997; You et al., 2009; Micheels et al., 2011). This discovery led to the conception that during the Miocene, climate and CO_2 were essentially decoupled (Zachos et al., 2001). In light of these records, the global impact of alterations in ocean gateways (such as the Panama seaway and

eastern Tethys region) and atmospheric composition have been analysed individually (Mikolajewicz and Crowley, 1997; Micheels et al., 2009; You et al., 2009) and as a coupled "Atmosphere-Ocean General Circulation Model" (AOGCM) configuration (Micheels et al., 2011; von der Heydt and Dijkstra, 2006, Knorr et al., 2014). Evaluating these factors individually is potentially misleading, as this approach ignores well-known interactions between the atmosphere and ocean. Several of the studies which used AOGCMs as coupled systems utilized relatively high CO_2 levels, inconsistent with marine carbon-cycle proxies (e.g. Micheels et al., 2011; von der Heydt and Dijkstra, 2006). Models constructed using carbon dioxide concentrations which were thought to be more appropriate indicate that changes in vegetation have a temperature-altering effect which is three times greater than the warming generated by tectonic change (Knorr et al., 2011). As a result, the warm climate of the Late Miocene was attributed equally to a reduction in planetary albedo and to an increased flux of water vapour to the atmosphere (Knorr et al., 2011). Despite the potentially effective approach utilized by Knorr et al. (2011), this study related primarily to the Late Miocene, and the Mid-Miocene remains poorly understood. Furthermore the actual concentration of atmospheric CO_2 remains contentious. Kürschner et al. (2008), for example, found that fossilized stomatal frequencies indicate that CO_2 fluctuated between 300 - 600 ppmv over the duration of the Miocene, with low CO_2 concentrations coinciding with glaciations (Knorr et al., 2011).

1.5.1 New Zealand/ Southern Hemisphere Miocene climate research

While an understanding of the general, global fluctuations in climate, and the factors which are believed to have influenced them during the Miocene is necessary in order to place this research into a global context, it is also necessary to identify gaps in the literature regarding paleoclimate on a local scale.

It is commonly recognized that, for various reasons, the availability and accuracy of the highly resolved proxies which have thus far offered a detailed account of climate during the Quaternary (including speleothems, tree rings and ice cores, and others) typically declines with age (e.g. Bozukov, et al., 2009). These archives are thus unavailable when considering the climate of the Mid-Miocene. Instead, analysis of this period is generally restricted to proxies with a comparatively low temporal resolution. For this reason, the current understanding of climate during the Early-to-Middle Miocene in New Zealand and the Southern Hemisphere is based primarily on marine sediment cores (e.g. Savin et al., 1985; Woodruff and Savin, 1991; Billups and Schrag, 2002; Shevenell and Kennett, 2004; Holbourn et al., 2005; Holbourn et al., 2007; Smart et al., 2007; Field et al., 2009; Johnson et al., 2010), and is further informed by a high quality Neogene plant fossil archive (e.g. Pole, 2003; Reichgelt, 2015). Plant fossils characterize the Early Miocene in New Zealand as wet and cool, but free from the occurrence of frosts (Pole, 2003). Towards the Middle Miocene, a transient dry period occurred, followed by a return to wet and cold conditions (Pole, 2003). The occurrence of dry periods has been attributed to an increase in the polar-equatorial temperature gradient, resulting in increased sub-tropical high pressure cells over New Zealand during the Miocene (Pole, 2003). The increased presence of these high pressure cells is believed to

cause 'blocking', whereby high pressure cells remain stationary for several days at high latitudes (Pole, 2003). Periods of increased blocking frequency are believed to have lasted for several thousand years, in order to have generated the observed floral shifts (Pole, 2003). Pole (2003) reinforces the importance of considering the effect of topography on climate. The limited topographic relief in New Zealand during the Miocene had a significant influence on temperature and precipitation (Pole, 2003).

Benthic foraminiferal $\delta^{18}O$ and Mg/Ca ratios have been widely used to identify the climatic warming and cooling trends during the Miocene (Savin et al., 1985; Woodruff and Savin, 1985; Billups and Schrag, 2002; Shevenell and Kennett, 2004; Holbourn et al., 2005; Holbourn et al., 2007 and Smart et al., 2007). On the basis of benthic foraminiferal $\delta^{18}O$ values, temperature changes appear to lag behind the global increase in ice volumes at the Oligocene to Miocene boundary (Billups and Schrag, 2002). Throughout the Miocene, brief glaciations typically have a cooling effect which is clearly recognizable in Mg/Ca ratios in benthic foraminiferal records (Billups and Schrag, 2002). Cooling periods are expected to be similarly identifiable (albeit at a much higher temporal resolution) using biogenic silica variability in lacustrine diatomaceous sediment.

Further models have also highlighted the importance of Antarctic ice sheet topography on the meridional thermal gradient, and the influence of this variable on climate (Singh et al., 2016). Declines in this thermal gradient (associated with reductions in Antarctic ice sheet topography) are thought to result in losses of atmospheric transient low level eddy heat flux and the eddy momentum flux, reducing heat transport from mid-latitudes to the pole (Singh et al., 2016). Thus, Antarctic ice volume is inversely correlated with equatorward heat transport, and

directly correlated with poleward heat transport (Justino et al., 2013). The use of model simulations such as the Speedy-Ocean (SPEEDO) coupled model (Severijns and Hazeleger, 2010) in conjunction with high resolution proxy data such as that from Hindon Maar may be valuable in further assessing this relationship.

The recent discovery of a uniquely highly resolved lake sediment deposit near Dunedin provided the first high-resolution terrestrial record of the Oligocene-Miocene from the mid-latitudes of the Southern Hemisphere (Fox et al., 2016). Investigations into these diatomaceous maar-lakes within the Waipiata Volcanic Field, Dunedin yielded valuable proxy data based on which paleoclimate studies have been conducted (e.g. Lindqvist and Lee, 2009; Fox, et al., 2015; Reichgelt, 2015; Fox et al., 2016). Prior to the present investigation, these studies were based exclusively on annually laminated sediment obtained from the Foulden Maar crater (45°31′41″S, 170°13′10″E). The Foulden Maar and the Hindon Maars are separated by a distance of 23 km, and these features share a number of characteristics. Both are believed to have formed during a volcanically active period in the Miocene (Fox, et al., 2015; Kaulfuss & Moulds, 2015), and were subsequently infilled by lake sediment. Thus, the work done at Foulden Maar will heavily inform the methods of this study. A 184 m core has been extracted from Foulden Maar, comprising ~70 m of basal mass flow deposits and ~113 m of laminated lacustrine diatomite. This core is thought to represent a period of approximately 100 k.y. of deposition dating from 23.033-22.931 Ma (Fox et al., 2016). Although the Hindon Maars are believed to have formed during a relatively similar period, it is considered unlikely that overlap will exist between these cores, and this record will likely be extended by sediment within the Hindon Maars. Fox et al. (2016) were able to identify the effect of obliquity on seasonality, and also recognized that

precession strongly influenced climate variability over the timescales recorded in this core. Ocean-atmosphere coupling was considered to be strong, as indicated by the importance of obliquity and precession cycles in this record, especially during the Mi-1 deglaciation, again highlighting the important effect of Antarctic ice cover on the polar-equatorial temperature gradient (Fox et al., 2015).

1.6 Physical properties overview

1.6.1 Magnetic susceptibility background

Magnetic susceptibility (MS) is the ability for sediments to become magnetised (Nowaczyk et al., 2001), and MS values (K) represent the relationship between an applied magnetic field (H) and the resulting magnetisation (M), according to the equation (Sandgren and Snowball, 2001):

$$M = K * H$$

MS values are particularly sensitive to the presence of ferromagnetic minerals such as magnetite or titanomagnetite (Sandgren and Snowball, 2001). Changes in grainsize and mineralogy can influence MS, as may changes in the influx of iron-bearing minerals and weathering rates (Sandgren and Snowball, 2001). MS may also act as a measure of pore-water pH, as alkaline water will cause the dissolution of ferromagnetic minerals, thus reducing magnetic susceptibility (Nowaczyk et al., 2007).

The acquisition and analysis of mineral magnetic data has several applications within the field of paleolimnology. Under appropriate sedimentary conditions, variations in the strength and direction of the Earth's geomagnetic field may be recorded in lake sediments (Sandgren and Snowball, 2001). A secondary benefit of this routine analytical technique is the observation that climatic and limnological factors can significantly influence the concentration and grain-size of magnetic minerals deposited within lacustrine environments (Sandgren and Snowball, 2001). Magnetic susceptibility data is thus valuable in enabling paleoenvironmental inferences to be drawn from sediment cores, and is a key component of this study (Sandgren and Snowball, 2002).

Like most fresh water lakes, the majority of maar lakes have well-defined catchments (Sandgren and Snowball, 2001), and a large proportion of magnetic minerals within lake deposits are derived from the erosion of soil and bedrock within the catchment (Sandgren and Snowball, 2001). In addition, in the case of volcanically derived lake structures, a significant proportion of magnetic minerals may be derived from sediment gravity flows, associated with the erosion of tuff rings into the crater (Sandgren and Snowball, 2001). The presence of macrophytes can also influence magnetic susceptibility (Kissoon et al., 2015). Further sources of magnetic minerals are likely to include volcano-derived aerosols and the aeolian deposition of dust during storm events (Sandgren and Snowball, 2002).

Materials may respond to magnetic fields in one of three principal ways, and this property can be exploited to provide insight into the ratio of differing materials within a deposit, and hence the relation with paleoenvironment (Morrish, 2001). Magnetic activity is produced at a sub-atomic level through the combined interaction of two vectors, these being the spin of electrons around their axis of rotation, and the motion of electrons as they spin around the nucleus (Morrish, 2001). Thus, the atomic composition and mineral structure of a sedimentary deposit exerts a fundamental control on magnetic susceptibility (Morrish, 2001).

Diamagnetic magnetism is a property of all matter, and is a weak force which occurs whenever an external field is applied. Lenz's law of electricity states that a current is induced when a magnetic flux enclosed by a current loop changes (Morrish, 2001). The direction of the magnetic field associated with this induced current opposes that of the original field. In this example, the atom's electronic motion behaves as the current loop, thus the application of an external field will induce a magnetic moment in a direction opposite to that field. Because electron orbits

provide no resistance, a diamagnetic moment induced in this manner will persist for the duration of the application of the external field. Temperature does not influence diamagnetism (Morrish, 2001).

Paramagnetic minerals include substances that obey one of two of Curie's laws. Normal paramagnets have a temperature-dependent and field-independent susceptibility given by:

$$x = \frac{C}{T}$$

where T is an absolute temperature, and C is Curie's constant. This behaviour is exhibited only by substances containing permanent magnetic dipoles. Another class of paramagnetic minerals follow the Curie-Weiss law:

$$x = \frac{C}{T - \theta}$$

where θ is a second constant. Atoms obeying the Curie or Curie-Weiss law are almost exclusively limited to the transition group elements. Any paramagnetic susceptibility must also be accompanied by diamagnetic susceptibility, so the total susceptibility is the sum of each of these components (Morrish, 2001). Of particular importance to paleoenvironmental studies is the observation that the strength of the paramagnetic field is multiple orders of magnitude larger than the diamagnetic signal, so it is likely that the diamagnetic contribution will be swamped in most circumstances (Morrish, 2001).

Ferromagnetic minerals are those with a spontaneous magnetization (i.e. a magnetic moment is present even in the absence of an external magnetic field). This effect is due to the parallel alignment of strongly coupled atomic dipole moments (Morrish, 2001).

1.6.2 Bulk Density background

Bulk density is a central parameter within marine and lake-based paleoenvironmental studies. An understanding of sediment density (an expression of the ratio of mass to volume, in kg/m^3) may allow the generation of porosity profiles and enables the characterization of core lithology (Gerland and Villinger 1995). Further, density measurements may also aid in the inference of depositional histories, and are a useful component in the calculation of accumulation rates. Prior to the development of gamma-ray attenuation based density measurements, wet bulk density was typically calculated using by examining a sample's weight and volume (Gerland and Villinger 1995). However, gamma-ray attenuation provides an automated alternative which is non-destructive, and can capture very small variations in density down core, at a high spatial resolution (Gerland and Villinger 1995). Because of the high proportion of light silicic and carbonaceous material within biogenic sediment, in comparison to the relatively heavier minerals likely to be found within terrigenous material, gamma density measurements are closely linked with composition in both marine and lake deposits (Gerland and Villinger 1995). Thus, variation in density can largely be attributed to changes in the relative concentration of terrigenous and organic material, which may be linked to factors influencing environmental conditions, potentially including orbital cycles, for example (Gerland and Villinger 1995).

It is valuable to examine correlations between density and other physical observations within a sediment core, including colour, reflectance, texture and magnetic susceptibility, as a multi-proxy approach is likely to yield more accurate facies to be identified, and enable them to be more effectively linked to paleoenvironmental conditions. For this reason, the use of electrofacies defined

using factor analysis and cluster analysis is valuable (Bucker et al., 2000) (see Section 2.6.2 for further discussion.

1.6.3 Grain size

Grain size analysis is used to provide information regarding changing weathering and erosion rates, the energy regime within the maar, and the source of inorganic material (Beierle et al., 2002).

Grain size is a physical property which is especially relevant to sedimentological examination, and alongside structure and composition is one of the most fundamentally informative aspects of any sedimentary deposit (Last, 2002). Textural descriptions seek to communicate the interrelationships between constituent grains within a facies, as well as the geometry of those particles. In this way, texture succinctly communicates the physical appearance of a geologically interesting deposit (Last, 2002).

Comprehensive textural descriptions are of value when researching paleolimnological deposits, not only because they enable explicit and quantitative classification of lacustrine sediment, but also because textural parameters can provide information regarding provenance and transport of sediment from the source (Last, 2002). Textural properties can also allow the inference of environmental conditions at the time of deposition from a physical, chemical and hydrological perspective, both within the basin and in the surrounding watershed (Last, 2002).

Table 1.1. Basic attributes of sediments (from Last, 2002).

Selected Physical Characteristics and Properties	**Internal**	**Texture** — Size	Average Size Range of Sizes Sorting
		Shape	Roundness (angularity) Sphericity Surface texture
		Arrangement (fabric)	Packing Orientation
		Sedimentary Structures	Bedding Interbedding Directional Features Post-depositional features
	External	External Form/Geometry	Size (thickness, width, length) Configuration/Shape Nature of boundaries
		Relation to Basin Framework	Position in Stratigraphic Sequence or Cycle Overall vertical trend Overall lateral trend
Selected Compositional Properties and Characteristics	**Mineralogy and Geochemistry**		Detrital Components Endogenic Components Authigenic Components Major & Minor Element Trace Element & Contaminant Isotopic Organic
		Biological	
Selected Derived Mass Properties	Porosity	Pore Size	Permeability
	Hardness	Acoustic Velocity	Strength
	Density	Colour	Magnetic properties

As shown in Table 1.1, texture is a combination of size, shape and fabric. Size analysis is complicated by the fact that similar sized particles may differ in shape, and as such size may be defined using a number of parameters including volume diameter, surface diameter or Stoke's diameter (Last, 2002). Size is most commonly quantified using the phi scale. The phi scale is defined by the equation:

$$\emptyset = -log_2 d_{mm},$$

where d_{mm} represents diameter in millimetres (Last, 2002).

Particle shape (a function of roundness, sphericity and surface texture) has a significant impact of size measurements, and can also independently provide sedimentological information (Last, 2002).

1.6.4 Particle size analysis techniques

Evaluating textural parameters can be complex, and a number of classical and modern techniques exist through which these parameters can be examined. Classical methods have seen relatively little modernisation. These techniques include settling of suspensions and sieving (Last, 2002). Modern techniques include particle counting, laser diffraction and photon correlation spectroscopy (Last, 2002). Point counting can be achieved traditionally using transmitted light microscopy, or at a finer scale using scanning electron microscopy (Last, 2002). In addition, image analysis and counting software is able to sense the boundaries of particles, identifying particle shape and size parameters through pixel counting and outline tracing (Last, 2002). Image analysis such as this is beneficial as it provides quantitative data, such as minimum and maximum grain diameter and circular area equivalent diameter (Last, 2002). Photon correlation spectroscopy is one of a small number of techniques that yield accurate data within the submicron range (Last, 2002). However, this method is unsuitable for larger particles (Last, 2002).

Laser diffraction particle size analysis is a rapid and accurate method of determining grain size, and is generally more practical than classical methods (Eshel et al., 2004). Despite the relative ease of laser particle size analysis, a number of considerations must be examined. For example, in order to limit textural analysis to terrigenous sediments and silicic microfossils, it is necessary to dissolve organic

carbon over a period of several weeks (Eshel et al., 2004). In addition, the grain shape is a critical consideration, with significant implications for both the accuracy and precision of measurements (for instance a cylindrical particle will appear larger if measured longitudinally, rather than in cross-section) (Eshel et al., 2004).

1.6.5 Laser diffraction spectroscopy

The primary principle behind laser diffraction analysis holds that particles of a given size diffract light through a specific angle (McCave et al., 1986). The size of the diffraction angle has an inverse relationship with grain size. By passing a beam of monochromatic light through a suspension, diffracted light is emitted which can be focused onto a multielement ring detector (McCave et al, 1986). The angular distribution of light scattered in this manner is detected by this component (McCave et al, 1986). Remaining undiffracted light is passed through a lens to a second detector and its effect is removed from the overall pattern, leaving a static diffraction pattern which is independent of particle movement (Figure 1.4) (McCave et al, 1986). The relationship between grain size and the light intensity produced by this system is given by:

$$I(\theta) = \frac{1}{\theta} \int\limits_{0}^{\infty} r^2 n(r) J_1^{\,2} \left(2\frac{\pi}{\lambda} r\theta\right) dr$$

Where $I(\theta)$ is light intensity, θ is the scattering angle, r is the particle radius and $n(r)$ is the size distribution function. J_1 is a Bessel function of the first kind, and λ represents the diffracted light's wavelength (McCave et al, 1986). By measuring light intensity, it is thus possible to use the above relationship to calculate a samples grain size distribution (McCave et al, 1986).
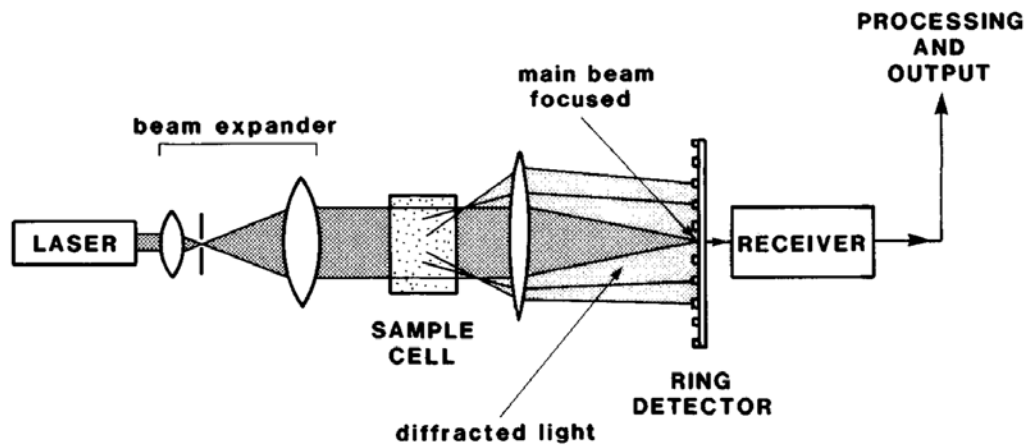
Figure 1.4 Schematic diagram of a laser particle size analyser. Primary components including the light source, sample, focusing lens, detector, and processing system are depicted (from McCave et al, 1986).

1.6.6 The effect of grain shape and density on size measurement

Irregularity in grain shape adds complexity to defining the size of a grain. This variation may also hinder the accuracy of analytical methods such as laser diffraction. In order to achieve a consistent metric, reported particle sizes are, by convention, related to an "equivalent" particle shape (usually a sphere) (Last, 2002). Reported grainsize values are therefore represented by an idealized variable. Unfortunately, many measurement techniques cannot accurately convert highly irregular grain shapes into equivalent spheres. This is because techniques can commonly only analyse size in two dimensions (Last, 2002). If a particle is exposed to the analyser along a non-representative axis, a crucial dimension may be lost, leading to an underestimate of grainsize (Last, 2002).

Particle density is typically not relevant when analysing grain size. An exception exists when using traditional settling methods, in which case polymodal densities within a single sediment sample will greatly reduce the accuracy of the grain size results (Last, 2002).

1.6.7 Colour

Colour measurement using reflectance spectroscopy is a rapid and non-destructive core scanning technique, with output that is commonly reported using the CIE L*a*b* convention. Colour parameters have previously been used to detect changes in North Atlantic ice-rafted debris (Helmke et al., 2002), and to track sediment changes resulting from monsoon conditions in Asia (Ji et al., 2005). As such, colour reflectance spectroscopy may provide insights into sedimentological dynamics and processes (Wei et al., 2014). The L*a*b* colour space is relatively intuitive. L* represents sediment lightness or luminescence, a* is a scale from green (-100) to red (100), and b* is a scale from blue (-100) to yellow (100).

1.7 Biological properties

1.7.1 Diatom genera (Aulacoseira spp.)

Diatom species are highly sensitive to environmental change and as such may reflect variation in nutrient status, salinity, temperature, wind speed and a number of other factors. Preliminary analysis of the deposit reveals an abundance of *Aulacoseira Spp* diatoms. For this reason, an outline of the morphological features that enable the recognition of this genus is provided.

Aulacoseira are the oldest non-marine diatoms, and samples have been found in sediment dating from the Late Cretaceous (Ambwani et al. 2003). *Aulacoseira* is regarded as one of the most successful and most widely distributed genera, and the abundance and diversity of these diatoms has relevance in paleoenvironmental reconstruction (Bozukov, et al., 2009). The first *Aulacoseira* species was identified in 1836 by Ehrenberg, and was given the name *Gallionella distans* (Krammer 1991). Subsequently, the genus was established by Thwaites in 1848 (Crawford

1981). In 1979, *Melosira* was recognized as a separate genus, and species were split into a separate genus by Simonsen (Crawford et al. 2003).

Because of their significant valve mantle depth, *Aulacoseira* frustules are cylindrical and are generally seen in girdle view, where frustules are often seen to form chains (Weckström et al., 1997). When examined in girdle view using light microscopy, simple round or rectangular areolae are clearly visible, and these areolae may be either dextrose or sinestrose (Takano 1981). Spines may also occur near the valve face and end-cells, and these spines may be defined as either linking or separation spines (the first of which are spatulate and connect sibling valves, whilst the latter taper) (Klee & Houk, 2007). A ringleist is usually visible at the intersection of the areolate section and the plain mantle edge, which takes the form of a thickened furrow. When considered from the valve view, the face may be plain or may feature puncta (Kelly et al. 2007).

Species within the *Aulacoseira* genus may be classified either on the basis of the orientation of pervalvar areolae rows, or using the ratio of mantle height to valve diameter (Takano 1981). Further species level classification can be achieved by considering variability in the separating spines (Siver & King 1997), or by ringleist structure, valve face morphology, linking spine shape, velum structure and rimoportulae position (Le Cohu 1991; Crawford & Likhoshway 1998, Likhoshway & Crawford 2001). Unfortunately, species level identification is generally considered impossible because characteristic features are not distinguishable using light microscopy (Houk 2003; Klee & Houk 2007), and SEM is required to confidently identify separate species within the genus. Furthermore, many taxa have not yet been examined under SEM, and thus the morphological characteristics of some species have not been fully examined.

Chapter Two

Methods

2.1 Sediment acquisition

Several cores were retrieved from the three of the maars which make up the Hindon Maar complex. Drilling locations explored during the November campaign are presented in Figure 2.14. Curiously, the greatest accumulation of lake sediment was observed between the inferred position of maars 3 and two, where the magnetic anomaly is significantly weaker than in the centre of either maar.
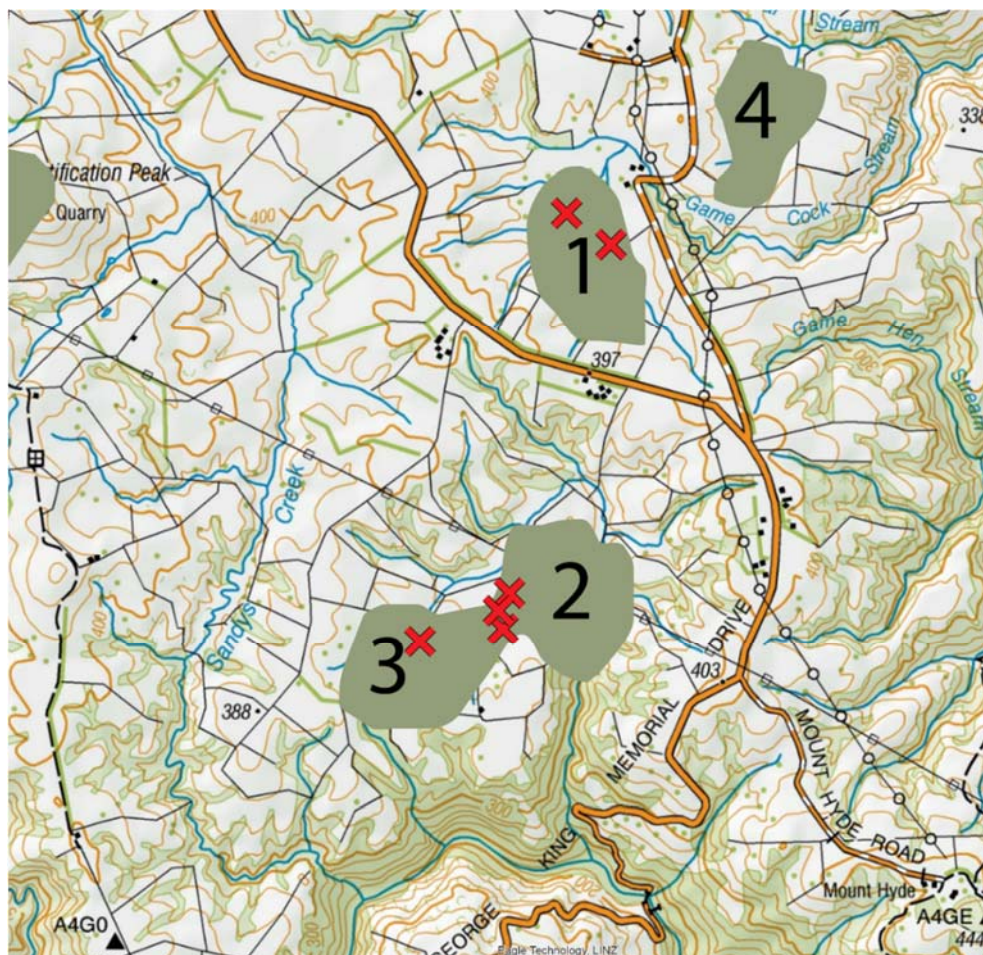
Figure 2.1 Topographic map of the field region, including the locations of each of the maar deposits. Xs represent sites where exploratory drilling was performed.

Coring was achieved using a combination of percussion sampling and rotary sampling methods using a heavily modified Geotechnical SPT rig (Figure 2.1). The primary goal during sediment coring was to recover an undisturbed sample whilst maintaining existing structures and without greatly altering water content and void ratio. It was also important that no major change to chemical composition occurred.

Open barrel samplers collect core as they are driven vertically into the sediment. Due to the consolidated nature of diatomaceous sediment, the mass of the device was insufficient to penetrate the substrate (as might be expected when sampling settled sediment in an active lake environment, for example). As a result, two alternate methods were trialled in order to drive the core barrel into the sediment with the aim of collecting undisturbed samples. The first of these was percussion sampling, performed following the method used while conducting standard penetration tests. The second method involved rotary sampling through the centre of a hollow-stem drill tube.
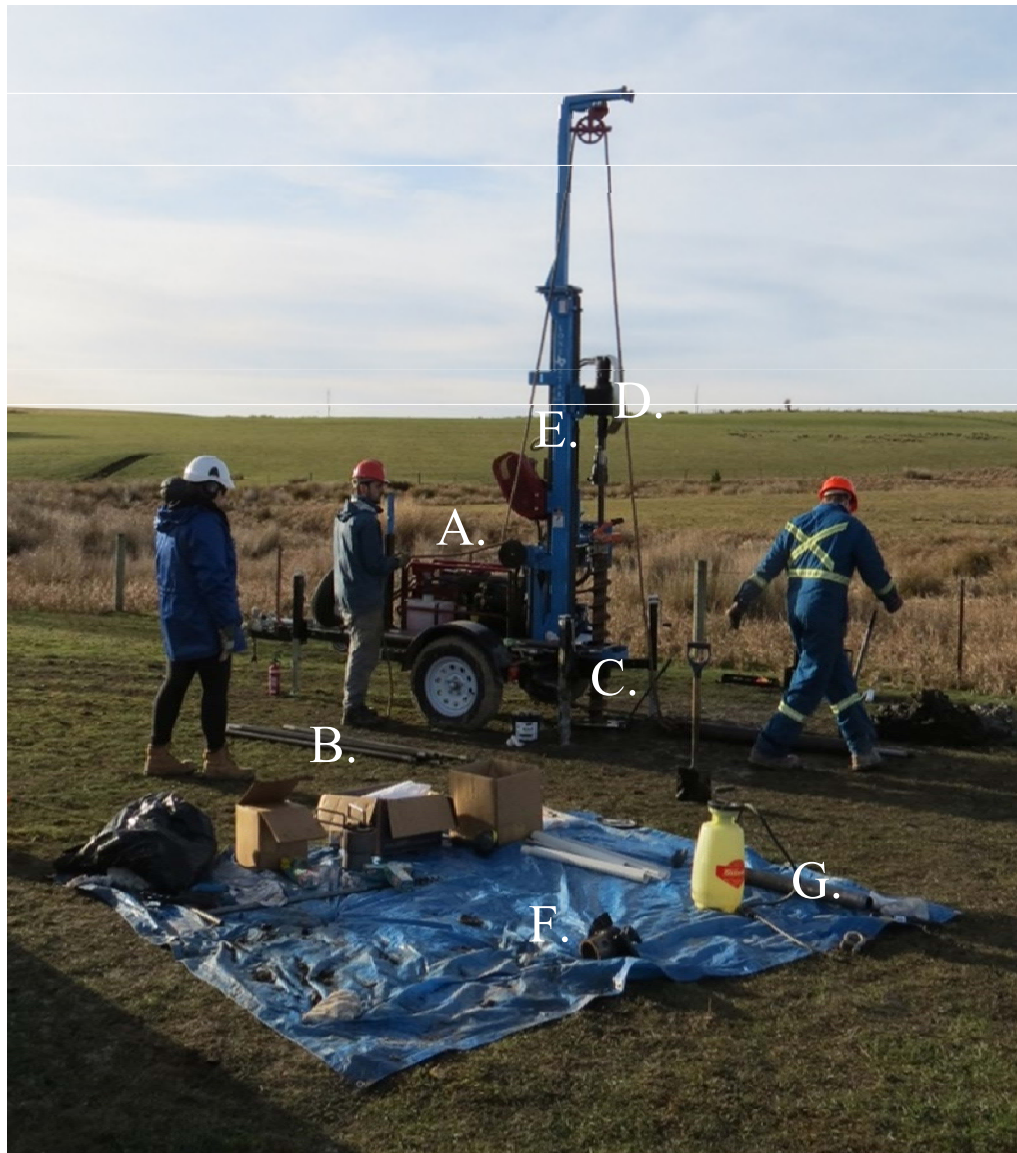
Figure 2.2 Photograph of the Lone Star/Little Beaver Geotechnical SPT rig at Hindon Maar One as it was configured during the July 2016 field work period. This system was designed to work with a percussion sampling method. Components include (a) the engine-powered cathead pulley and rope used to raise and lower the hammer, (b) spare centre rods and pilot drill bit, (c) the hollow-flight augers, (d) the drill-head, (e) the mast and drill chain, (f) a spare auger bit and (g) a spare sampling spoon. The hammer is not pictured.

2.1.1 Percussion Sampling – July 2016

Drilling conducted during the July 2016 sediment acquisition campaign was achieved through the use of an LSTG1 trailer-mounted geotechnical rig (Figure 2.1). This rig is designed for soil sampling, geotechnical testing and environmental well drilling. The LSTG1 is highly portable, and is capable of drilling and sampling at depths of up to 30 m. This rig has a lifting capacity of 2300 kgs, in order to remove auger sections using the drive head. Augers are rotated at up to 150 rpm using a 20 horsepower gas engine manufactured by Honda.

The LSTG1 geotechnical rig is intended to function through auger drilling. Auger drilling is typically used for the drilling of unconsolidated sediment and soft rocks, and many sediment types are unsuitable for this drilling method (Farrar, 1999). One potential limitation of auger drilling is the potential for subsurface water to enter a hollow-stem auger, contaminating samples from the base of the hole (Farrar, 1999). Despite this limitation, auger drilling can effectively and economically collect undisturbed samples from unconsolidated and shallow soils (Farrar, 1999). Continuous-flight augers may feature either a solid or hollow stem, depending on the desired application. Hollow stem augers were used during this project, and this method enables sampling to be achieved through the use of a centre-rod assembly (Farrar, 1999). Hollow-stem augers effectively allow the hole to be immediately "cased" preventing hole caving, collapse and contamination (Farrar, 1999). A visual comparison of the augers used in the July field work period and the flightless outer-tube system used in November can be seen in Figure 2.3.
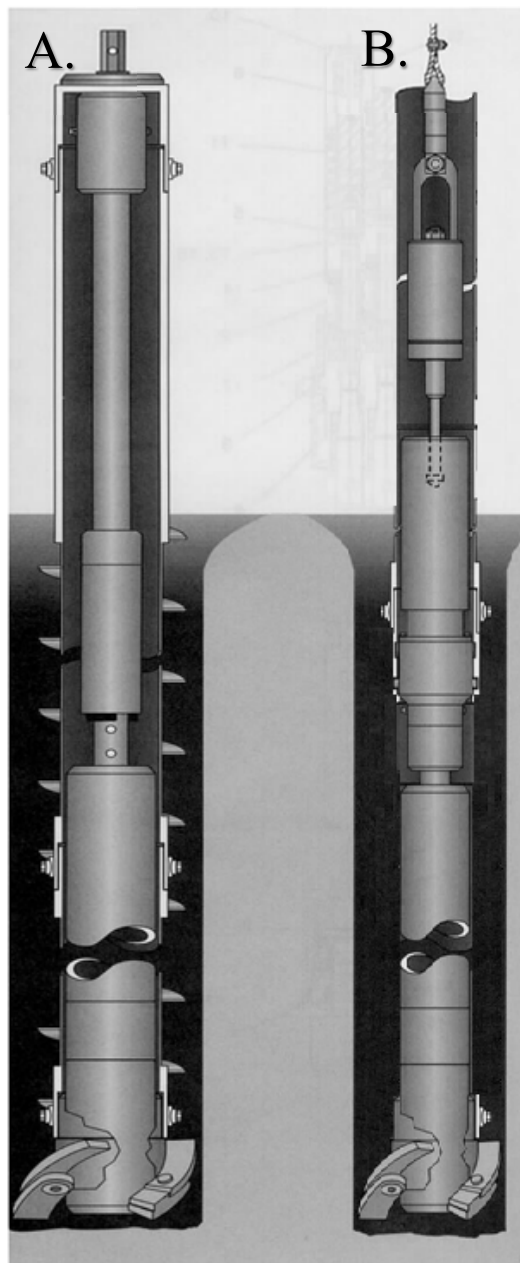
Figure 2.3 Schematic comparison of the drilling and core-retrieval systems used in July 2016 (A) and November 2016 (B). The system used in November is comparatively narrow as the outer tube component does not feature augur flights. In order to retrieve samples, a wireline is lowered which automatically attaches to the sampling spoon. This can then be hoisted from the outer tube using the cathead. This contrasts with the rod-based method, in which every rod in the drill stem is sequentially removed in order to extract the sampling spoon. (Modified from Farrar, 1999).

The centre-rod assembly consists of a rod-to-cap adaptor, centre rod, centre-assembly plug, and a pilot bit. In order to collect a sample, the centre-rod assembly used in drilling must be removed incrementally. The cathead and rope are attached to the centre rod drill stem, and these are drawn upwards. When a suitable height has been reached, a clamp is applied to prevent the drill stem from re-entering the hole. At this point, two pipe wrenches were used to separate a centre rod section, which is then lifted away from the drilling rig. Once the entire drill stem has been removed, the sampling spoon is attached to the leading drill rod, and the entire drill stem is reinserted into the earth. Reinsertion is also an incremental process, and similarly requires the use of a clamp to prevent equipment loss. A 70 kg hammer is connected to the final protruding centre rod, and the cathead is used to repeatedly raise and lower the hammer, striking the centre rods and forcing the sampling spoon into the soil. "Back-hammering" is a technique used to reverse this process and extract the filled sampling spoon from its position. The drill stem must again be removed to collect the filled sampling spoon, and must be reinserted to resume drilling (after replacing the sampling spoon with a pilot bit).

The sampling spoon barrel is designed to split longitudinally to enable sediment samples to be examined and retrieved. The sampler also features a driving shoe, designed to require a known amount of force to penetrate soil (Figure 2.4).

SPLIT BARREL PENETRATION RESISTANCE SAMPLER
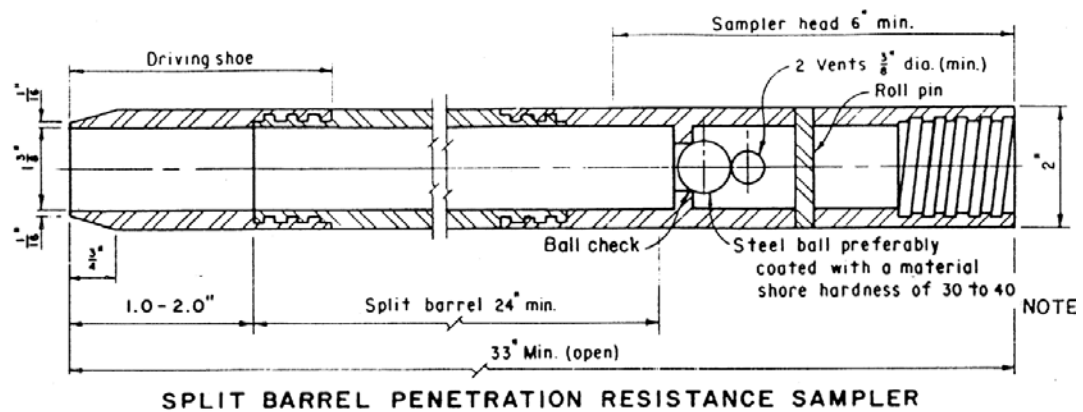
Figure 2.4 Schematic diagram of a split barrel penetration resistance sampler, showing the driving shoe, split barrel and sampler head (From Farrar, 1999).

A number of faults with the percussion sampling method meant that the effectiveness of this method was limited, and little useable core could be retrieved during the July field work period. These faults also necessitated extensive modifications to the drilling rig, resulting in its final conversion to a rotary sampling system. A primary limitation was imposed by the augering mechanism with which the rig was equipped. Combined with the sediment type encountered at the field site this system meant that the drill could only reach a maximal depth of eight metres below the soil surface. At depths greater than this, the lake sediment tended to liquefy and adhere to the auger flights (Figure 2.5). This adhesion of mud to the auger flights meant cuttings could not be removed from the hole.

In addition to the limited depth associated with the drill rig's design, the method of core retrieval also prevented samples from being extracted intact. The process of repeatedly dropping the hammer onto the rod assembly, and forcing sediment through the driving shoe was highly destructive, and usually resulted in the complete disaggregation of samples. Originally horizontal lake sediment laminations became blended and mixed due the percussion sampling method.

Figure 2.5 The percussion sampling method was unsuitable for core collection as it caused lake sediment to liquefy and adhere to the auger flights. This prevented the efficient removal of cuttings, and meant that drilling could not proceed past a depth of eight metres.

2.1.2 Rotary Sampling – November 2016

In order to continue sediment acquisition during the second field work period, it was necessary for extensive alterations to be made to the design of the drilling rig. To prevent sediment from adhering to the augur flights an outer rod configuration with a smooth cylindrical body was used in place of the auguring system, and water was continuously circulated during drilling. In addition it was necessary to remove the centre rod and percussion sampling systems. The process of removing the centre rods individually, replacing them with the sampling spoon, incrementally reconstructing the centre rod structure to sample, and then removing it after sampling was deemed too time consuming for deeper holes. Furthermore, the sampling method of hammering the sampling spoon into the lake sediment caused unacceptable damage to the sediment cores.

The centre-rod configuration was therefore replaced with a triple-tube wireline system (Farrar, 1999), enabling the split-tube sampling barrel to be lowered to the base of the hole using the cathead and rope, where it is locked into place (Figure 2.6). During rotary sampling, the barrel protrudes beyond the end of the outer tube, and rotates with the outer tube during drilling (Figure 2.6). The sample cut to a cylindrical shape and forced through the sampler drive shoe and core-catch by the downward force produced by the drive-head.
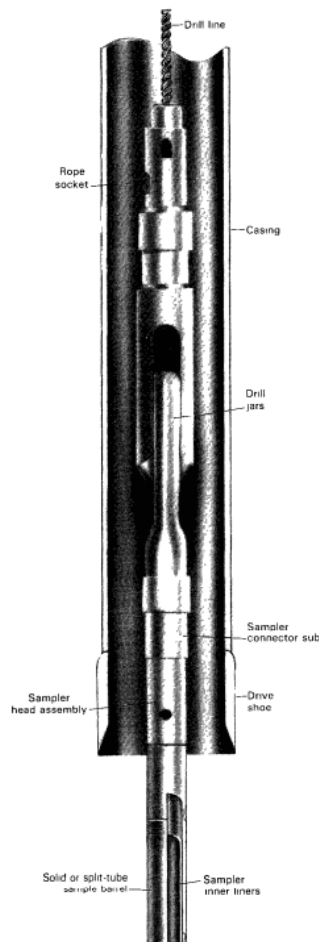
Figure 2.6 Cable-tool drive-sampling apparatus, as used in the November 2016 field work period (from Shuter & Teasdale, 1989).

Cuttings were continuously removed during drilling by pumping water into the hole. This fluid lifted excess material away from the drilling system, and cuttings were thereafter flushed through a ditch and distributed away from the site.

The sampling core consists of a single piece outer barrel. Two semi-cylindrical aluminium "splits" are lubricated with a polytetrafluoroethylene lubricant to prevent their adhesion to the lake sediment samples, and are inserted into the sampler. Water pressure is applied to the end of the assembly in order to extrude the splits after sampling (Shuter & Teasdale, 1989). The pump-out assembly consists of a hydraulic pump and hose, allowing the controlled extrusion of the sample.

2.2 Geotek analysis of the Hindon lake deposit

Magnetic susceptibility and gamma attenuation data were obtained at a low resolution (2 cm) using from whole-core samples using a Geotek Multi-Sensor Core Logger (MSCL), owned by the University of Otago. In addition, the Geotek MSCL apparatus was used to collect high-resolution magnetic susceptibility, gamma attenuation, spectrophotometer and digital colour image data from split core samples (Geotek Ltd, 2016).

2.2.1 Magnetic Susceptibility

The Geotek MSCL system used in this project was equipped with two magnetic sensors. High resolution (0.5 cm) magnetic susceptibility measurements were obtained using a MS2E magnetic susceptibility surface scanning system manufactured by Bartington Instruments ®. This instrument has a resolution of up to 2×10^{-6} SI, and a range of 0.1 SI (Geotek Ltd, 2016). It consists of an elliptical sensing coil housed within a ceramic tube. The MS2E automatically recalibrates after 20 measurements to account for temperature induced drift (Geotek Ltd, 2016). The point sensor is automatically lowered onto the core surface while taking each measurement. Point sensors are advantageous as they provide a high spatial resolution (Geotek Ltd, 2016). The point sensor design is also extremely sensitive to fluctuations in temperature, and as such it is useful to monitor and account for temperature variation during logging, and to endeavour to maintain a constant ambient temperature within the lab (Geotek Ltd, 2016).

Loop sensors were used to take low resolution magnetic susceptibility logs of the whole core, prior to splitting. This sensor model features the same electronic

components as are present in the point sensor (Geotek Ltd, 2016). Measurements obtained using the loop sensor can be compared with those obtained using the point sensor, to identify potential calibration errors (Geotek Ltd, 2016). Both sensor units function by emitting a low intensity alternating magnetic field with an approximate intensity of 80 A/m RMS. Magnetically susceptible substrates in close proximity to the sensor cause a change in the oscillator frequency, which can then be used to calculate magnetic susceptibility values (Geotek Ltd, 2016). The degree to which a material interacts with the magnetic field varies greatly depending upon its composition, with materials which strengthen the magnetic field being classified as either paramagnetic, ferromagnetic, antiferromagnetic or ferrimagnetic (Chen, 1977). Materials which weaken the magnetic field are described as diamagnetic (Chen, 1977). The magnetic susceptibility of several minerals commonly found in lake sediment deposits is presented in Table 2.1 (Geotek Ltd, 2016).

Table 2.1. The magnetic susceptibility of water and nine common minerals (from Geotek Ltd, 2016).

Material	Magnetic Susceptibility $(x10^{-6})$ SI
Water	9
Calcite	-7.5 to -39
Quartz, Feldspar	-13 to -17
Kaolinite	-50
Halite, Gypsum	-10 to -60
Illite, Montmorillonite	330 to 410
Biotite	1,500 to 2,900
Pyrite	5 to 3,500
Haematite	500 to 40,000
Magnetite	1,000,000 to 5,700,000

2.2.2 Data processing

It is not necessary to regularly calibrate the point and loop susceptibility sensors, as this is performed by the manufacturer. However, it is necessary to ensure ambient temperature remains constant during logging (Geotek Ltd, 2016). During processing, it is possible to obtain volume specific magnetic susceptibility or mass specific magnetic susceptibility. When determining volume specific magnetic susceptibility, the diameter of the loop sensor is used to correct the otherwise dimensionless raw measurements (Geotek Ltd, 2016).

Volume specific magnetic susceptibility measurements do not account for variation in the density of the target sample, and as a result, volume specific measurements of magnetic susceptibility may show variation that is unrelated to the proportion magnetically susceptible minerals (Geotek Ltd, 2016). In this case, the degree of compaction and related sample density will likely effect reported magnetic susceptibility variation. To account for this source of error, mass specific magnetic susceptibility can be calculated during data processing (Geotek Ltd, 2016). This calculation removes the effect of density, so that mineral composition is the only factor influencing reported magnetic susceptibility variation (Geotek Ltd, 2016).

2.2.3 Gamma-ray Density

Gamma-ray attenuation measurements are obtained by aligning a gamma ray source (10 milli-curie Caesium-137 capsule) with the centre of the sediment core (Siegbahn 1968). Gamma rays are emitted from the source as a narrow beam of photons, which travel through the core and are subsequently detected (Geotek Ltd, 2016). Attenuation of the gamma rays is caused by primarily by Compton scattering

(and partially by the photoelectric effect) (Mikhailik et al. 2015). Thus, attenuation correlates closely with core thickness and electron density, as these properties are related to the detectable number of electrons in the gamma ray beam (Mikhailik et al. 2015).

Gamma ray attenuation by Compton scattering is calculated using the following equation:

$$I = I_0 e^{-\mu p d}$$

Where I is the intensity of gamma rays after passing through a given material (in this case a whole or split sediment core). I_0 is the intensity of gamma rays in air, prior to any contact with the sediment core (Mikhailik et al. 2015). d refers to the thickness of the sample in cm, and μ is an absorption coefficient in (cm^2g^{-1}), which is specific to each material type. Finally, ρ represents density in g cm^{-3}. Once attenuation has been measured, the initial equation may be rearranged to calculate density, ρ, in g cm^{-3}:

$$\rho = \frac{1}{-\mu d} \ln \frac{I}{I_0}$$

While the majority of variables within these equations may be easily measured under laboratory conditions, it is not possible to measure the mass absorption coefficient, which is defined by the ratio of an element's atomic number to its mass number (Gerland and Villinger 1995). In most sediments, μ is approximately equal to 0.0774 cm^2g^{-1}. However, this variable is heavily dependent on water content in a saturated sample, and thus it is necessary to first calculate porosity and grain density before estimating the absorption coefficient (Gerland and Villinger 1995).

2.2.4 Gamma source and scintillator

The gamma ray source (A 10 milli-curie Caesium-137 capsule) has a half-life of 30.2 years, and gamma energy is emitted at 0.662 MeV. During operation, the MSCL is designed to include a rotating shutter system, which enables the beam to be collimated through one of who collimators (with a diameter of 5 or 2.5 mm (Figure 2.7). The source is contained within a lead-filled box, with stainless steel walls 3 mm thick. All density measurements were taken using the 5 mm diameter collimator (Geotek Ltd, 2016).

Position 1.	Source closed.	Approx. 50-200 CPS
Position 2.	2.5 mm collimator	Approx. 5000-10000 CPS
Position 3.	5.0 mm collimator	Approx. 25000-35000 CPS
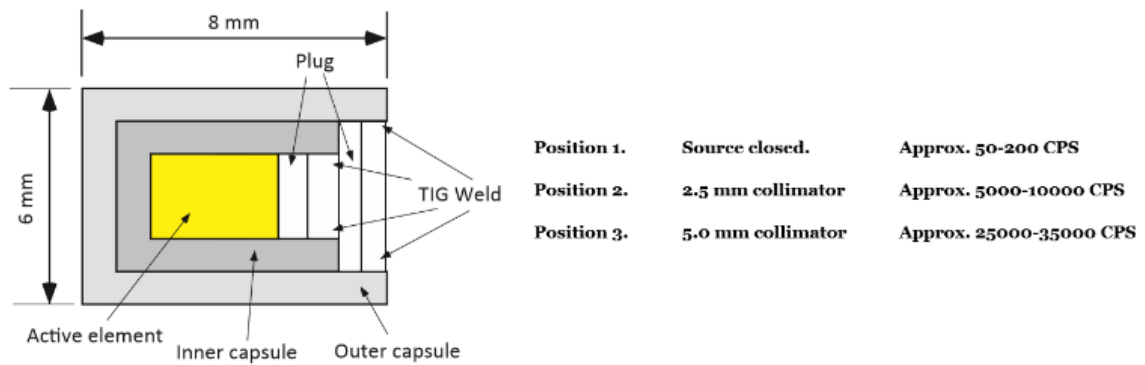
Figure 2.7 The caesium capsule is contained within a stainless steel, lead-filled housing. Adjustable collimators enable a beam of 2.5 or 5 mm to be emitted during operation (MSCL Manual).

2.2.5 Calibration

Prior to the measurement of core gamma density, it is necessary to account for experimental factors including beam spreading, the effect of pore water, and the attenuation that occurs as the beam passes through the liner wall. Through calibration, variation due to these factors can be mitigated. An empirical technique is used for calibration. This technique involves assembling a calibration sample (for example when assessing saturated sediment, a core liner containing a cylindrical piece of aluminium of varying thickness and filled with water is used) (Figure 2.8). 30 second gamma count averages are taken through the calibration sample at each thickness of aluminium, and these averages are plotted as a graph of $\rho d\ vs.\ln I$ (Figure 2.9) (Geotek Ltd, 2016).

$\rho_{water} =$ density of water
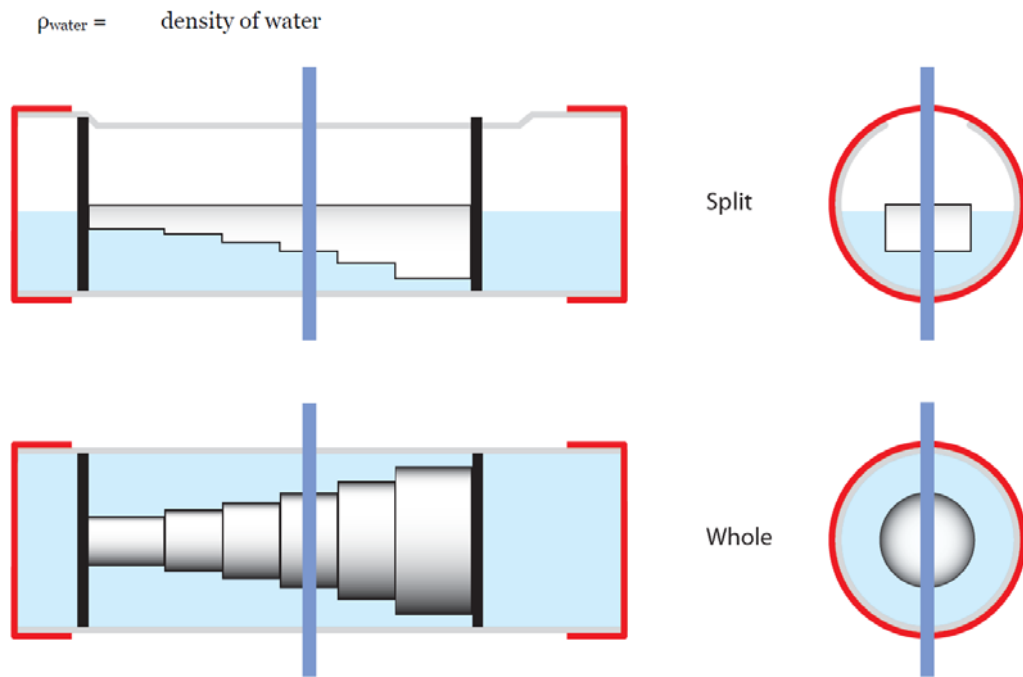
Figure 2.8 Diagram of aluminium and water gamma calibration tool (MSCL Manual).

$$y = -0.0011x^2 - 0.0436x + 9.8451$$
$$R^2 = 1$$

A= X^2 coefficient
B= X coefficient
C= Y intercept
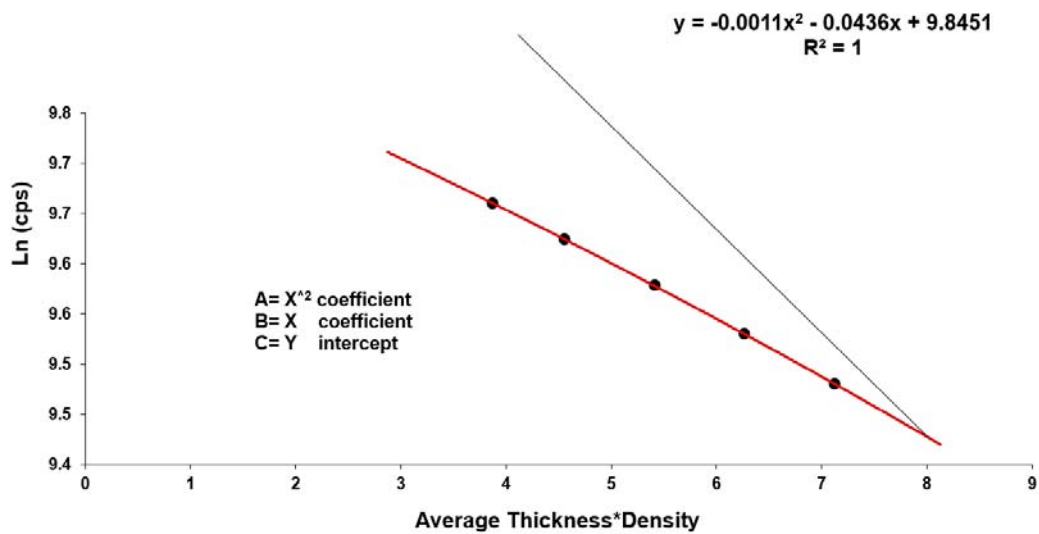
Figure 2.9 Example calibration plot for saturated cores. Each component of the given equation (A, B, and C) is used during data processing to correct for variation in experimental factors.

2.2.6 Colour Spectrophotometry

The measurement of sediment colour through the use of spectrophotometry is a suitable method of identifying potential changes in sediment composition (e.g. Wei, et al., 2014). This method is especially appropriate when analysing organic matter concentrations, because luminescence values (L*) are typically inversely correlated with the concentration of carbon present within the sediment (Wei, et al., 2014). A* (redness) values have also been successfully used as a proxy for terrigenous and organic matter concentration, as well as wet conditions (Wei, et al., 2014). The development of spectrophotometers has eliminated the previously qualitative analysis of sediment colour (which until recently relied on visual comparisons with Munsell colour charts).

Spectrophotometers are advantageous as they allow colour to be rapidly and precisely quantified in a manner that is consistent within the core and with other sediment sources. Colour data is reported using the CIE L*a*b* colourspace. This system divides the visible spectrum into three parameters. L* (luminescence) is a grayscale measurement of the total brightness of a sample (where 0 is equal black, and 100 represents white), a* represents a spectrum of red to green chromicity values (-60 is green, 60 is red), and b* measures yellow-blue chromicity values (-60 is blue, 60 is yellow) (Figure 2.10) (Cavanaugh, 2008).

These values have been widely used as proxies for sediment composition in both lacustrine and oceanic settings. For example, changes in North Atlantic ice rafted debris were identified by Helmke et al. (2002), and Ji et al. (2005) quantified variation in Asian monsoon conditions using sediment colour. Luminescence values (L*) have acted as a suitable proxy for carbonate content in Atlantic basin

sediments (Giosan et al. 2002), and blue-yellow chromicity values have provided an estimate of diatom concentrations in fjord sediments (Debret et al. 2006). The Konica Minolta colour spectrophotometer used in this project also reports spectral reflectance data.
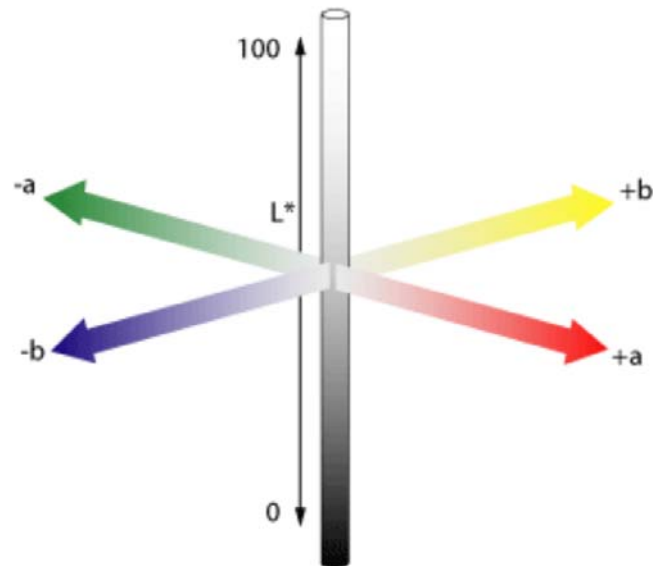
Figure 2.10 Conceptual diagram of the CIE L*a*b* colorspace. L*, a* and b* indicate luminescence, green-red chromicity and blue-yellow chromicity, respectively (from Cavanaugh, 2008).

2.2.7 Core Thickness

Measurement of core thickness variation is achieved using two laser distance transducers which are attached to each of the active faces on two opposing P-wave transducers. As the P-wave transducer is repositioned to rest on the core face, the distance between the laser distance transducers are decreases and variation in core thickness can therefore be recorded. Because both gamma density and magnetic susceptibility are influenced by core thickness, it is critical that thickness is accurately recorded. A plastic cylinder of a known thickness is used calibrate this instrument (Geotek Ltd, 2016).

2.2.8 GeoScan Digital Imaging

The GEOTEK MSCL is also equipped with a linescan camera with a horizontal resolution of 2048 pixels to produce digital images. The GeoScan colour line-scan camera uses three, 2048 pixel CCD arrays which are receptive to light in the 400-900 nm waveband. Each of these arrays processes light from the object using a red, green and blue receptor. Combining these three channels produces a final colour image. Because CCD detectors are more sensitive to longer wavelengths within the visible spectrum, it is necessary to amplify the blue channel to accurately capture and represent colour (Geotek Ltd, 2016).

Diachroic colour interference filters are used to eliminate any overlap between the wavebands associated with the three (red, green and blue) channels. Light travelling from the splitter is thus filtered before arriving at the filter. This process enables rigorous colour analysis to be performed. Conventional systems such as those using overlapping dye filters do not achieve true colour separation, and involve significant overlap between each of the channels (Geotek Ltd, 2016). Figure 2.11 shows that these diachroic interference filters allow colour to be effectively separated into these channels.
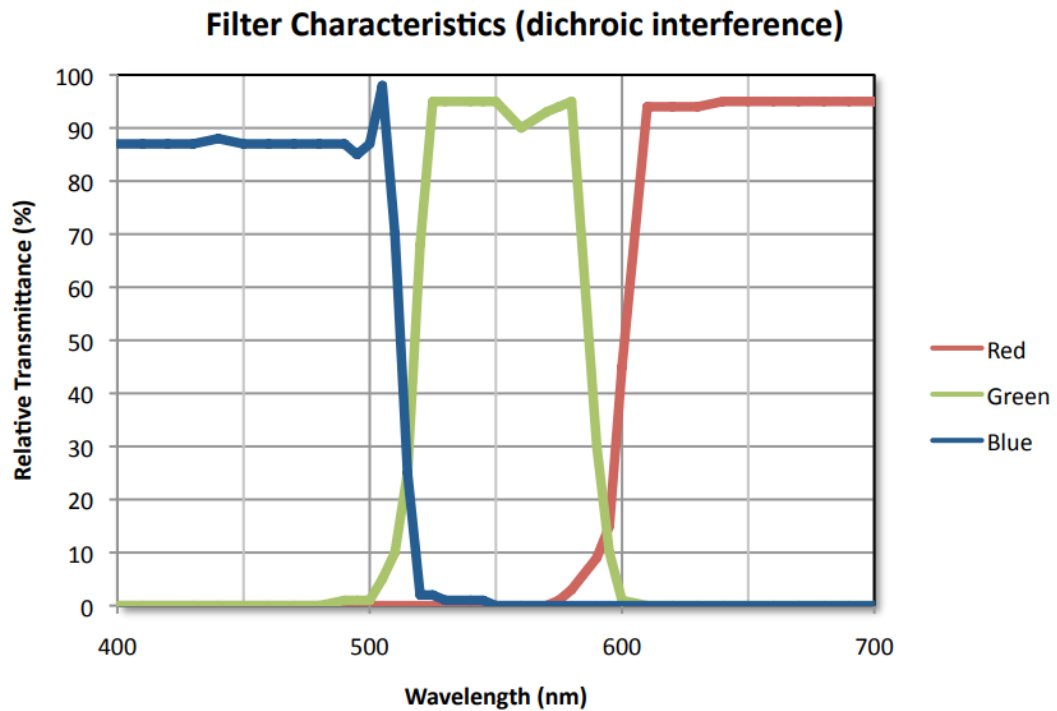
Figure 2.11 Diachroic interference filters are used to effectively divide colour data reaching the detector into one of three channels (Geotek Ltd, 2016).

It is important that synchronisation between the track and camera is maintained throughout the photo acquisition period. This is achieved through the use of stepper motor pulses, which trigger the camera to activate. Each motor pulse relates to a known amount of core movement, thus camera images are obtained at precise spatial intervals across the length of the core (Geotek Ltd, 2016).

Intense, consistent lighting is provided to the core during photo capture by a series of white LEDs, minimising the occurrence of shadows due to microtopography. Prior to acquiring imagery data, each element in the CCD must be calibrated to achieve correct colour balance. Low calibrations are collected with the lense cap on, and high calibrations are set using a white ceramic tile (Geotek Ltd, 2016).

2.3 Textural analysis of the Hindon lake deposit

2.3.1 Particle size analysis

Grain size measurements were obtained using a Malvern Mastersizer 3000. When analysing the range of grain sizes present within a sand-size or finer sample using this instrument, accurate grain size measurements can be obtained using a sample weighing as little as 0.001 g. In order to prevent organic matter from being included in the analysis, and to ensure that clay is completely dispersed, 10% hydrogen peroxide solution is added to the sample (Barth, 1984). As samples of the Hindon lake sediment contain a large quantity of organic matter, this step is needed prior to preforming grain size analysis. Hydrogen peroxide is progressively added while stirring the sample until the dark organic matter has been removed over the course of several weeks (Poppe et al., 2008). The process of digestion using hydrogen peroxide took up to 15 days, and the reaction was considered to be complete once effervescence had completely ceased. Washing the sample with a NaOAc buffer and with methanol removes remaining cations (Jackson, 1956). Following the use of hydrogen peroxide and hydrochloric acid, the samples are weighed again to determine the weight of the removed matter (Poppe et al., 2008).

Following the period of digestion, calgon was added to the samples to prevent the flocculation of clay particles. Prior to grainsize analysis, an ultrasonic bath was used to further disperse particle agglomerates, and to ensure all sediment was suspended (Poppe, et al., 2008).

The Mastersizer 3000 is an optical measurement unit and is equipped with a hydro dispersion unit designed to allow the particle sizing of aqueous samples. The sample is added to the hydro dispersion tank (600 ml), and the tank is then filled with an aqueous dispersant. Dispersion is achieved through the use of a pump within the tank, which continuously circulates the dispersant towards the optical unit via the 'to cell' port. During this process, the suspended sample is able to return to the tank via the 'from cell port' (Figure 2.12). A stirrer and ultrasonic transducer are also present within the tank, preventing the sample from settling (Malvern Ltd., 2011).
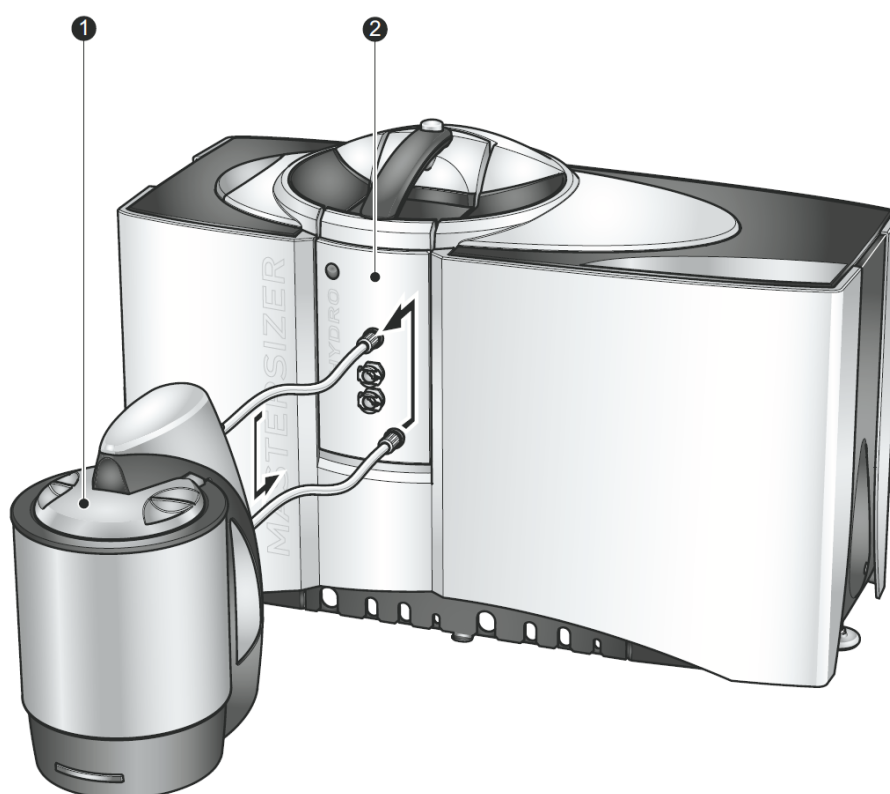
Figure 2.12 Diagram of the Malvern Mastersizer 3000, showing the hydro dispersion tank (1) and the optical unit (2). Sediment is able to circulate between these two units via two ports (*Malvern Ltd., 2011*).

2.4 Biogenic silica concentration and Fourier transform infrared spectroscopy

Biogenic silica is an amorphous form of SiO_2 and is formed as a result of precipitation by siliceous organisms including diatoms, sponges and radiolarians. As a direct measurement of past diatom, sponge spicule and chrysophyte abundance, BSi is a useful indicator of lacustrine primary productivity (e.g. Williams et al., 1997; Colman et al., 1999; Rosén et al., 2010). BSi is highly variable on short timescales and has previously been used as a proxy for summer temperatures (Blass et al., 2007; McKay et al., 2008). Total biogenic silica is a direct measurement of diatom, sponge spicule and chrystophyte abundance; and within limnic ecosystems, these are typically the dominant photoautotrophs present. Thus, total biogenic silica is an effective proxy for lake productivity (Szczuciński et al., 2012). BSi has important implications for paleoenvironmental research, and has been used to reconstruct air temperature over a decadal scale (Blass, Bigler, Grosjean, & Sturm, 2007) and other climate-related changes in lake productivity over both orbital and millennial timescales. Furthermore, the concentration of biogenic silica within a sample may also relate to the eutrophication and acidification of surface waters (McKay, Kaufman, & Michelutti, 2008).

Methods through which biogenic silica can be reliably estimated may be divided into five general categories, including the use of x-ray diffraction, infrared analysis, wet-alkaline digestion techniques, point counting of diatoms and estimation by difference from mineral silicates using a normative calculation (Conley and Schelske, 2006). The most common method is to perform a wet chemical digestion using a weak, moderate or strong base (1% NaCO, 2 M $NaCO_3$ or 0.5-1 M NaOH,

respectively). The time required for digestion is inversely correlated with the strength of the base (Conley and Schelske, 2006). X-ray diffraction techniques significantly overestimate BSi when compared to techniques which rely on wet chemical digestion (Conley and Schelske, 2006).

FTIR spectroscopy is the method of quantifying biogenic silica which is used in this research. Early attempts to employ FTIR spectroscopy to determine biogenic silica concentration met with limited success. Chester and Elderfield (1968) first calculated Bsi values using FTIR spectroscopy using the intensity of a single absorption band. The accuracy of this method was limited, however, as non-siliceous components with similar IR absorption features were found to overlap with the inferred position of Bsi, preventing an effective an Bsi calculation. In 1998, FTIR spectroscopy was used to estimate Bsi in lacustrine sediments through the use of linear mixing models (Bertaux et al, 1998). Recently, partial least squares regression has produced significantly more accurate estimates of biogenic silica concentration in lake sediments (Vogel et al. 2008, 2010, 2013; Hahn et al. 2012; Brigham-Grette et al. 2013; Cunningham et al. 2013a, Meyer-Jacob et al. 2014). Partial least squares regression can be conceptualised as a combination of principal component analysis and multiple regression, bearing features of both of these statistical techniques. PLSR functions by first extracting a set of latent factors that explain covariance between the independent and dependent variables (Meyer-Jacob et al. 2014). A regression step is then used to predict values of the dependent variable through the decomposition of the independent variables (Meyer-Jacob et al. 2014). Because PLRS is able to effectively analyse highly collinear and noisy datasets with multiple X-variables, the technique is well suited to processing infrared spectra (Meyer-Jacob et al. 2014). By modelling the relationship between

FTIR spectral information within a sediment sample and the associated Bsi concentration within that sample, it is possible to make predictions relating to sediment composition using a single matrix (Meyer-Jacob et al. 2014).

In 2014, Meyer-Jacob et al. constructed a global model of the relationship between biogenic silica concentration and IR spectra silica using Fourier transform infrared spectroscopy in conjunction with partial least squares regression. This model enables conventional, time consuming and error-prone wet-chemistry techniques to be avoided entirely. Instead, the relationship was established using six diatom-free synthetic sediment samples, each comprised of a combination of quartz and calcite, and other lake sediment samples. Pure diatom extracts were added in 2% increments to each of the synthetic sediment samples, creating a set of 306 sediment mixture series' comprising a complete gradient from 0 – 100 % diatom concentration in 2 % steps using various mineral compositions. Sediment was mixed with oven-dried spectroscopic grade potassium bromide. Linear baseline correction was used to normalize the FTIR spectra, whilst numeric analysis was completed through PLSR (Meyer-Jacob et al. 2014).

2.4.1 Components

 All FTIR spectrometers feature fundamental components, including a source, interferometer, sample, detector, amplifier, analog-to-digital converter and computer (Stuart, 1996). Radiation is emitted from the source and passes through the interferometer and sample (Stuart, 1996). Following this, radiation is detected and amplified, before being converted to a digital signal (Stuart, 1996). The computer then performs the Fourier transformation (Stuart, 1996). Most interferometers used in spectroscopy are known as Michelson interferometers. These components are made up of two perpendicular plane mirrors. The planes of

these two mirrors are bisected by a germanium or iron oxide beamsplitter, coated in potassium bromide (Figure 2.13). As the beam of radiation passes into the beamsplitter, half of the radiation is reflected to each of the opposing mirrors. The reflection of radiation from these mirrors then generates the interferogram, when radiation recombines at the beamsplitter (Stuart, 1996). Radiation travelling at 90 degrees to the beamsplitter is detected by the spectrometer, and is referred to as the transmitted beam.
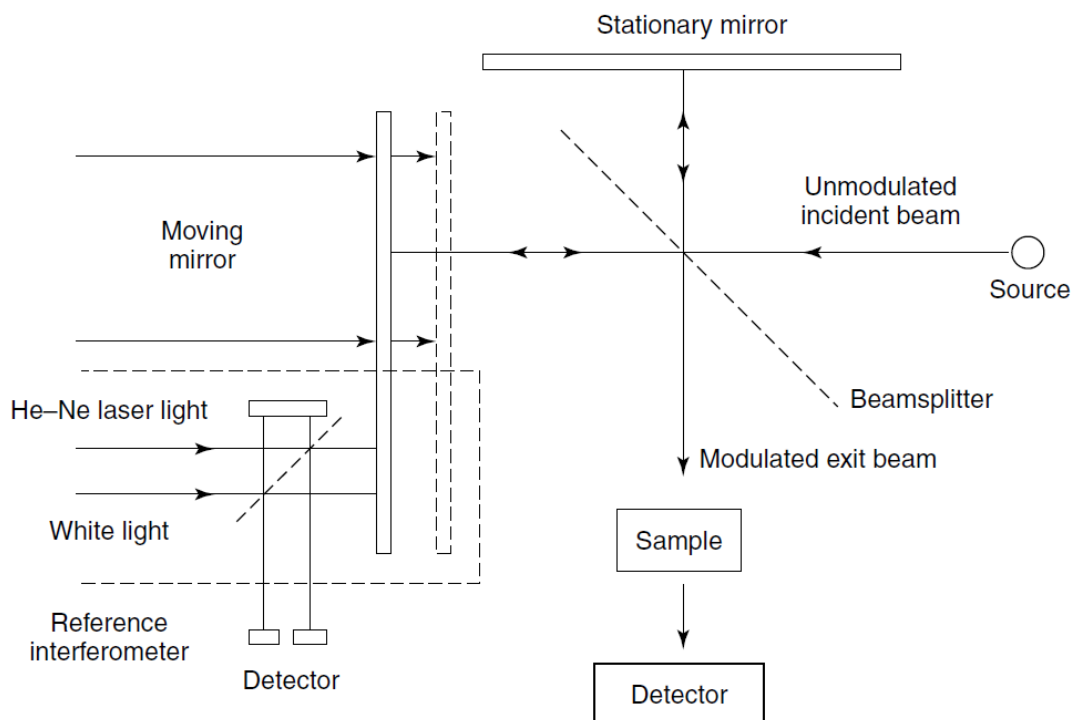
Figure 2.13 Schematic diagram of the structure of a Michelson interferometer (From Stuart, 1996)

For near-infrared spectroscopy, FTIR spectrometers use a tungsten-halogen lamp as a source, and a pyroelectric device comprised of deuterium trygliycine sulfate in an alkali halide window (Stuart, 1996).

The function of the computer is to control the instrument by setting scanning speed and limits, and to initialise the scan. Spectra obtained during a scan are digitized and stored in memory, and may be adjusted at this point. Finally, the computer is needed to plot spectra (Stuart, 1996).

2.4.2 Fourier transformation

Fourier transform infrared (FTIR) spectroscopy relies on the concept that the interference of radiation between two beams produces an interferogram (Coates, 2006). An interferogram pattern is a product of the variation in pathlength between the two beams. By applying the mathematical method known as a Fourier-transformation, distance and frequency become interconvertible (Coates, 2006).

The Fourier-transform pair is a set of two interconvertible equations used to relate the intensity of radiation falling on the detector to the spectral power density at a given wavelength.

The equation:

$$I(\delta) \ = \int_{0}^{+\infty} B(v)\cos\,(2\pi v\delta)dv$$

Reflects the variation in power density due to changes in path length which occur as a result of interference. Similarly, the equation:

$$B(v) \ = \int_{-\infty}^{+\infty} I(\delta)\cos\,(2\pi v\delta)d\delta$$

Represents changes in intensity in relation to wavenumber. In each of these equations, $I(\delta)$ represents the intensity of radiation falling on the detector, while $B(v)$ is the spectral power density at a particular wavenumber (Coates, 2006).

FTIR spectroscopy has several advantages when used for quantitative analysis, when compared to alternative spectroscopic techniques. Because the number of resolution elements measured simultaneously is very large, the signal:noise ratio is also increased (Coates, 2006). In addition, FTIR spectroscopy does not require the

use of a restricting device or slit, the source output passed through the sample is not limited, increasing the quantity of energy reaching the receptor (Coates, 2006). These advantages are termed the Fellgett and Jacquinot advantages, respectively (Coates, 2006). Finally, the speed advantage means it is possible to obtain spectra at a small timescale (milliseconds) (Coates, 2006). This is because the moving mirror used in infrared spectrometers is able to move very rapidly, and its exact position is known due to the presence of a helium-neon laser (Coates, 2006).

Due to instrument specific difference between the spectrometer used by Meyer-Jacob et al. (2014), it was not possible to apply their independent model to spectra acquired from sediment within the Hindon Maar Complex. Spectra obtained using the Perkin Elmer model spectrometer (available at the University of Waikato) display differing baseline slope and baseline offset values, when compared to those obtained through the use of a Bruker model spectrometer. One source of this error may be the fact that the Bruker spectrometer requires powdered samples, rather than pellets used for spectroscopy in the Perkin Elmer spectrometer.

In order to obtain estimates of biogenic silica concentration using spectroscopy, it was therefore necessary to construct a separate partial least squares regression model. This method required a set of synthetic lake sediment samples to be produced, each of which contained a unique concentration of biogenic silica.

Based on the composition of the lake sediment (measured using a portable X-ray fluorescence spectrometer at five locations down the core), a synthetic sediment was produced comprising a combination of analytical-grade powdered activated carbon (selected to minimise the inclusion of epiphytic diatoms), and powdered schist. Pure diatomaceous earth was purchased from PERMAGUARD ltd. This diatomaceous earth is minded in Nevada and is marketed as "food-grade".

Microscope analysis of the PERMAGUARD diatomaceous earth revealed that this product is ~100% pure diatoms, containing no other visible minerals. The purity of diatom samples used in defining the calibration dataset is therefore not considered a source of error.

51 synthetic sediment samples containing diatomaceous earth and activated carbon alone were produced. These ranged from 0 to 100% diatoms, and diatom concentrations were increased in 2% increments with each sample. The remaining proportion of each sample was made up by activated carbon. A further 15 samples were produced using ground samples of the Otago Schist. It is thought these samples will provide an accurate proxy for any increase in the rate of terrigenous material input into the lakes. From these samples, a partial least squares regression was produced to quantify the relationship between the spectra resulting from FTIR analysis, and the absolute concentration of components within each sample.

2.5 Petrography

Thin sections were constructed using the technique described by Brauer et al. (1999), and photomicrographs collected using a polarization microscope at 25-400x magnification. Several thin sections were produced in order to characterise "typical" lake sediment, whilst others are intended to capture and examine geophysical anomalies identified through GEOTEK MSCL analysis. To this end, a sampling plan (Figure 2.14) was produced. In addition to these thin sections, samples treated with hydrogen peroxide were used to examine diatom frustules and terrigenous components, without the presence of organic carbon.
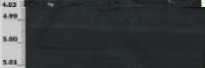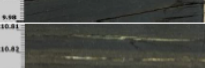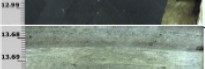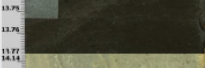
Slide No.	Hindon Core Depth (m)	Core Section	Image	Core Notes	Thin section Notes	Density (g/cc)	MS (x 10^{-8} (m^3/kg))
1	2.68	HMN163_3_262		Top of lake sediment, fractured core. Yellow particle at core centre.		1.12	-0.7
2	3.68	HMN163_3_357		Black lake sediment, some muscovite.		0.93	-0.8
3	4	HMN163_3_357		White cracks visible. High density and high Mag Sus.		1.19	0.7-1.3
4	4.99	HMN163_3_412		"Typical" lake sediment		0.93	-0.2
5	5.47	HMN163_3_508		Muscovite rich section		1.007	0--0.8
6	6.49	HMN163_3_589		Very high reflectance section. High diatom concentration		0.8	-0.73
7	7.9	HMN163_3_712		"Typical" lake sediment		0.69	-0.71
8	8.84	HMN163_3_809		Brighter lake sediment section.		0.79	-0.91
9	9.02	HMN163_3_902		Blue-grey layer. Higher density, higher mag sus.		0.93	0.337
10	9.4	HMN163_3_8.95		Brown sand lens, high density, high mag sus		0.95	0.34
11	9.53	HMN163_3_8.95		Bright diatomaceous layers		0.847	-1.826
12	9.75	HMN163_3_8.95		Brown sand lens		0.7595	" 0.7 to 1.448"
13	9.96	HMN163_3_9.92		High density section		1.09	"-2.4 to 0.97"
14	10.81	HMN163_3_9.92		Diatomaceous, low density		0.76	-1.27
15	10.86(?)	HMN163_3_10.79		Brighter lake sediment section.		0.87	-0.49
16	11.05	HMN163_3_10.79		Muscovite rich section		0.91	0.9
17	11.13	HMN163_3_10.79		Very high reflectance section. High diatom concentration		1.03	-0.114
18	11:36	HMN163_3_10.79		Dark lake sediment, increased magnetic susceptibility		0.97	4.57
19	12.49	HMN163_3_11.82		"Typical" lake sediment		0.62	0.61
20	12.92	HMN163_3_12.73		Muscovite rich section		0.9	13.42
21	12.97	HMN163_3_12.73		Very high mag sus section. Fresh surface is yellow-grey?		0.877	87.6
22	13.68	HMN163_3_12.73		Pale-grey section.		1.66-1.9	8.9-21
23	13.73	HMN163_3_13.72		Black -brown lake sediment		1.94	104.8
24	14.14	HMN163_3_13.72		High reflectance, yellow-white section		1.39	5.1
25	15.66	HMN163_3_15.49		High reflectance, yellow-white section		1.59	9.29

Figure 2.14 Sampling plan used to produce petrographic thin sections.

2.6 Statistical analysis

2.6.1. Factor analysis

In order to again consider the contribution of each variable and reduce computational dimensionality, multivariate data was combined into a reduced number of variables using principal components analysis. In order to prevent additional weighting on certain variables, all variables were normalised by subtracting the mean and dividing by the standard deviation.

Three PCAs were completed using different aspects of the core, and factor scores derived from two of these were subsequently used in electrofacies analysis. Both of these include all available variables (excluding organic carbon and RGB variables, as these are heavily correlated with other variables). The first represents lake sediment only, whilst the second incorporates all parts of the core.

2.6.2. Electrofacies analysis

The combination physical properties obtained using the GEOTEK MSCL system and compositional variability assessed with FTIR spectroscopy analysis can be used to define electrofacies which may assist the identification of actual lithofacies within the core. Electrofacies classification is based on the unique characteristics of core measurements, and is likely to reflect compositional variability that may not easily be recognised through other means (Jeong, 2011). It is thus not necessary to artificially subdivide the data population, as electrofacies are identified quantitatively based on the available data (Jeong, 2011). The method used to achieve an electrofacies classification is based on a combination of principal components analysis and model-based cluster analysis, and aims to identify clusters of responses which possess similar characteristics.

The objective of factor score clustering is to identify data groups within the population, thus enabling a clear representation of the system's behaviour to be produced (Trivedi, Dey, and Kumar 2017). Two-Step clustering is a data clustering technique which can form clusters using either categorical or continuous data. The clustering algorithm is based on the assumption that each variable is independent, with a normal distribution (Trivedi, Dey, and Kumar 2017). As such, it is suitable for the analysis of factor scores produced through principal components analysis (Trivedi, Dey, and Kumar 2017).

The two steps used in this analysis include preclustering, in which the algorithm reduces the size of the matrix by reading through the dataset and determining (based on a distance measure) whether new cases should be added to existing preclusters, or whether a new precluster should be created (Trivedi, Dey, and Kumar 2017). The second step in this analysis is to use a hierarchical clustering algorithm on the preclusters to evaluate the importance of each precluster, and to determine how many preclusters should be included (Trivedi, Dey, and Kumar 2017).

Cluster validation is used to determine the optimal number of clusters to include in the model. This is determined using the Schwarz Bayesian Criterion (Trivedi, Dey, and Kumar 2017). The Schwarz Bayesian Criterion prevents model overfitting by introducing a penalty for the number of additional parameters added to the model. An optimal number of clusters can be identified at the point where the Schwarz Bayesian Criterion becomes small, and the change in Schwarz Bayesian Criterion between adjacent clusters is also small (Trivedi, Dey, and Kumar 2017). Cluster analysis was completed in SPSS (IBM).

2.6.4. Spectral analysis using peridograms

Tukey-Hamming analysis is used to detect the presence of harmonic signals in a time series. Alternatively it can also be used to obtain phase relations between harmonic signal components being present in two different time series (cross-spectral analysis) (Schulz & Stattegger, 1997). This method is widely used in paleoclimatology and relies on the standard Fourier transform of a truncated and tapered autocovariance function (Schulz & Stattegger, 1997). I apply this approach to several of the high resolution variables to identify potential cycles in the data. Periodograms were prepared in SPSS (IBM).

2.6.3. Wavelet transformations

Wavelet transforms are beneficial as they allow cyclical elements to be analysed along many frequencies throughout the the time-series (Lau and Weng 1995). This analysis involves the calculation of a finite wave with a known wavelength, amplitude and phase (Lau and Weng 1995). These variables can then be altered to show all cyclical elements in a time series (Lau and Weng 1995). This analysis is commonly used in paleoclimatology studies (e.g. Wanner et al. 2001). A Morelet wavelet function is used in this analysis in order to analyse high resolution physical properties data, and an α value of 0.95 to calculate the red noise background. Wavelet figures were prepared in PAST (Paleontological Statistics).

2.6.4. Sum of sinusoidal signals

Because cycles in paleoclimate data may sometimes take the form of sinusoidal waves which may be overlain with varying phases and amplitudes, these relationships may be modelled using several added sinusoids (Trapero et al., 2008). Multiple solutions may produce a high R^2 value in this analysis, so it may be more

appropriate to use sinusoidal signals to model signals first identified through wavelet or via periodograms. This approach was applied to all the variables and principal components produced, and common cycles are highlighted in a table. This analysis was conducted using PAST (Paleontological Statistics).

CHAPTER 3
Results

3.1 Lake Sediment Appearance and Structure

The sediment record from the Hindon Maar 3 lake over the Mid-Miocene consists broadly of two major units: A low density, laminated, diatom-rich carbonaceous unit (upper 11 m), defined as Unit A (Figure 3.1) and a dense, minerogenic volcanic breccia (bottom 4 m), defined as Unit B (Figure 3.2).

Figure 3.1 Characteristic core image of sediment unit A from Hindon Maar 3. Unit A consists of low-density, laminated, diatomaceous, organic-rich lake sediment with a low magnetic susceptibility.
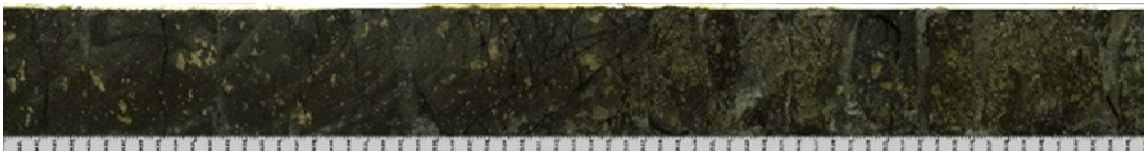
Figure 3.2 Characteristic core image of Unit B from Hindon Maar 3. Unit B consists of high density, minerogenic volcanic breccia with a high magnetic susceptibility

3.1.1 Lamina thickness and accumulation rate

Accumulation rates within the lake sediment unit (yr/cm) are calculated using the average thickness of laminae, as determined using brightfield microscopy and the image-J software (See section 4). These accumulation rates are calculated under the assumption that lamina were laid down annually, and that each represents an accumulation of diatoms, organic carbon and terrigenous sediment which built up over that period. This assumption is based on the observation that each lamina contains an accumulation of diatoms, likely to represent an algal bloom during productive seasons.

Photomicrograph analysis and analysis of core photographs using ImageJ indicates that lamina have an average thickness of 1.42±0.53 mm. As 10.8 m of useable lake sediment was obtained from this maar, it is estimated that the entire length of the core represents a period of approximately 7605±2067 years. Because thicker laminae are easier to distinguish during petrographic analysis, it is likely that larger laminae were preferentially measured over more abundant, thinner laminations. Thus it is probable that the true length of time encompassed by this sediment core is somewhat longer than the estimate provided here. This estimate indicates that a single metre of sediment corresponds to approximately 704 years.

The rate at which sediment accumulated during the existence of this lake is likely to be highly variable, however. For example, within the sections of the core that have the thickest laminae (between 8.95 and 9.92 m depth), laminae exhibit a thickness of 1.945±0.337 mm, suggesting that material at this point accumulated at a rate of 514±75 yr m^{-1}, or 0.514 yr mm^{-1}.

3.2 Texture

A total of 135 grain size measurements were performed on the Hindon Maar 3 sediment core, and each measurement was taken at a 10 cm intervals. The lake sediment core is composed predominantly of medium silt-sized grains (6.3-20 μm) (47.25 ± 14 %). The quantity of particles categorised as medium silt generally increases with depth (Figure 3.3), and a marked increase in grain size occurs at 9.92 m. The median grainsize present across all measurements in the sediment core is 17.15 ± 7.5 μm. The clay (<2 μm) size fraction contributes on average 6.67 ± 4.78% to sediment grain size distributions, whilst coarse and fine silt makes up 20.62 ± 10.59 % and 11.627 ± 4.57 %, respectively. The remaining sediment within the core (on average <15%) is made up predominantly of fine sand (9.3 ± 9.5 %), with a small contribution from medium to coarse sand sized particles.

Within the first 7.2 m of the core, the proportion of sediment comprised of fine, medium or coarse silt is relatively stable (Figure 3.3). After this point, the concentration of coarse silt declines sharply, whilst the concentration of medium silt is reduced and then gradually increases to a maximum of 86.4% volume at 10.52 m. The overall size of grains increases at this point (the tenth percentile of particle size increases from 3.2 μm to 5.1 μm, the 50th percentile increases from 15.82 μm to 19.1 μm, and the 90th percentile increases from 77.2 μm to 150.4 μm). Figure 3.4 confirms that the proportion of sediment within the fine sand category also increases at this point.
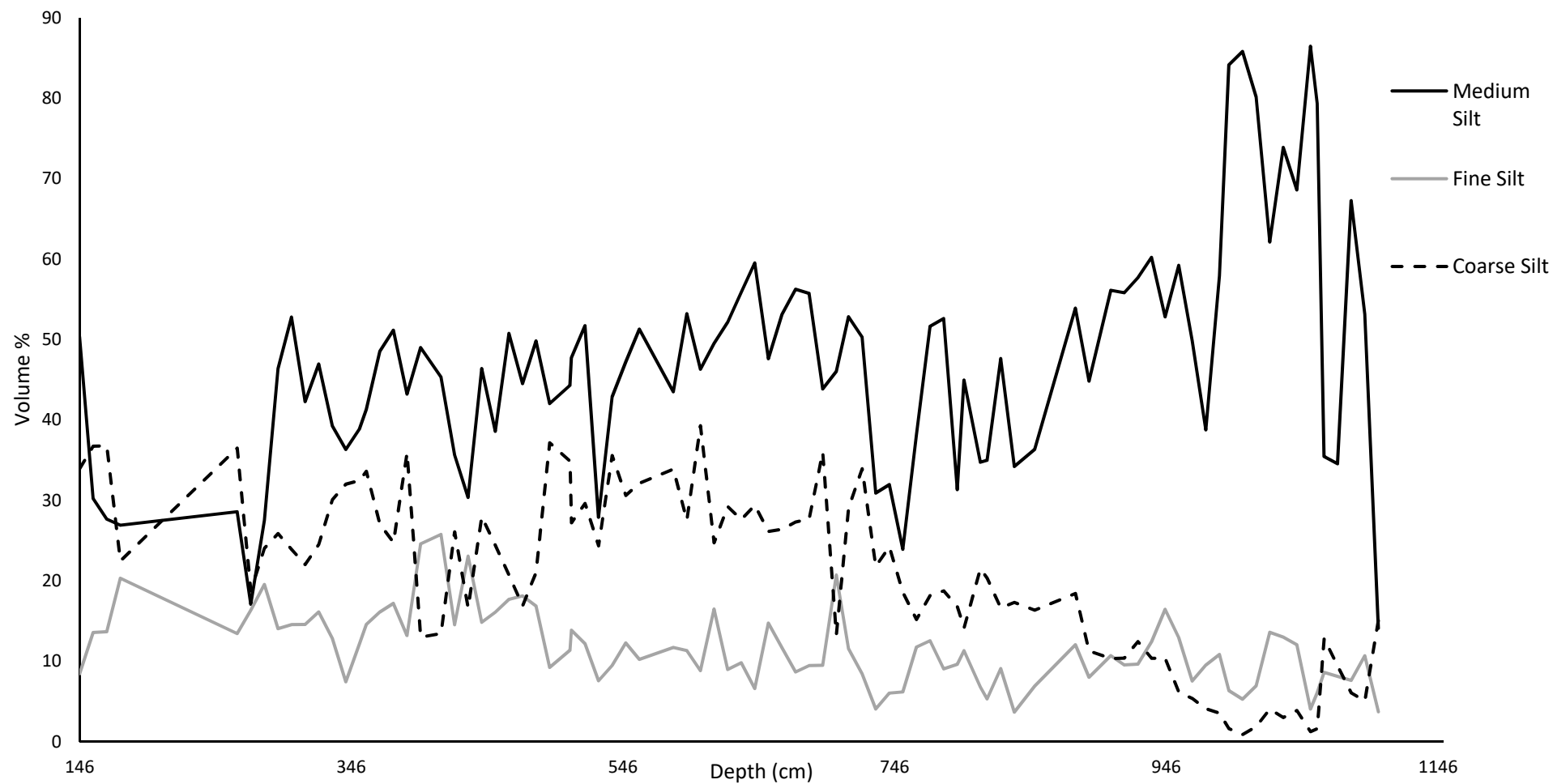
Figure 3.3 The proportion of sediment falling under the "Medium Silt" generally increases with depth, whilst the quantity of fine and coarse silt particles gradually declines after 7.46 m. This increase in medium silt sized particles coincides with an increase in biogenic silica (Figure 3.7).
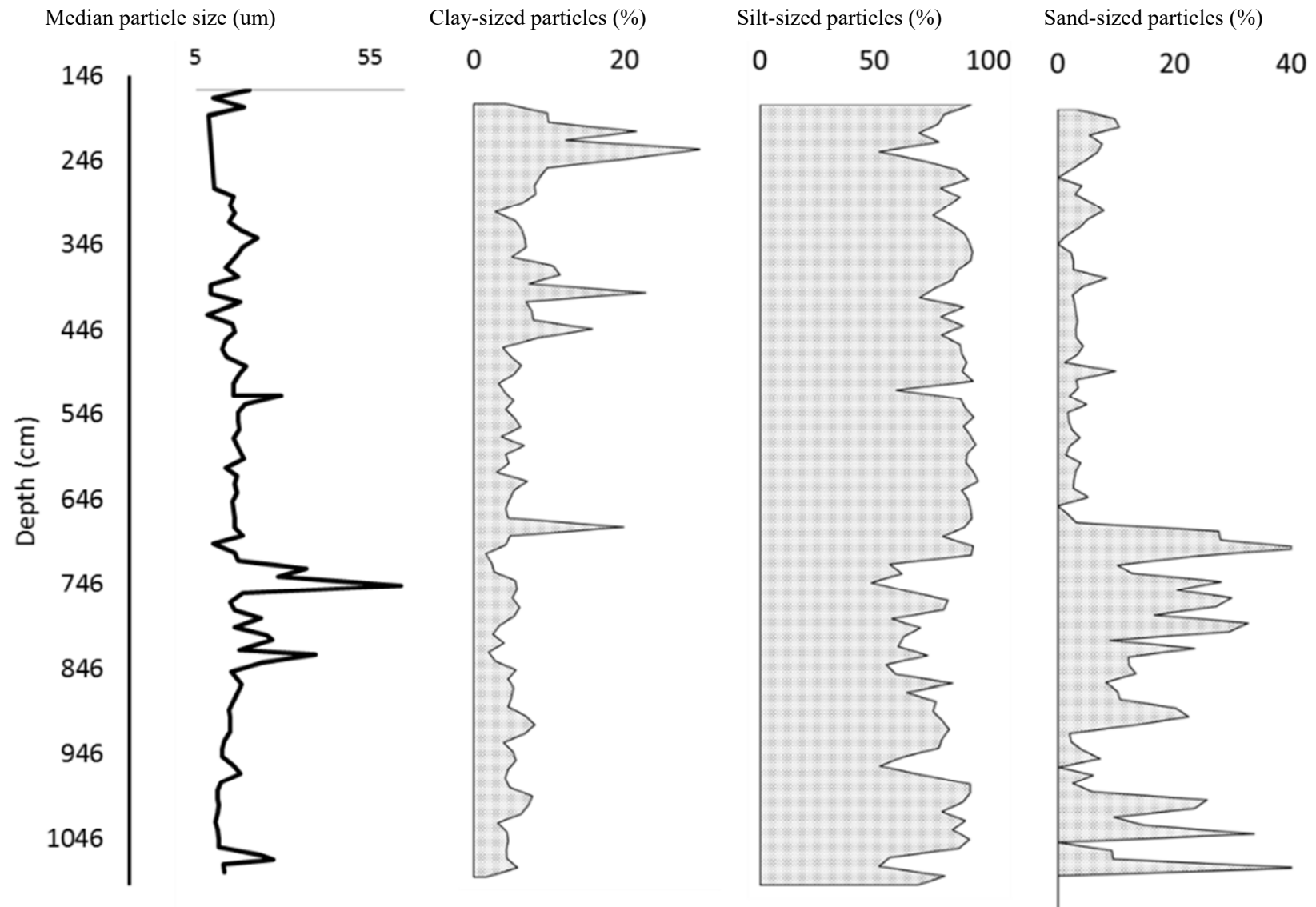
Figure 3.4 Volume-weighted median particle size (μm), and proportions of clay, silt and sand-sized particles (%). The majority of sediment is categorised as silt. Sand makes up a small proportion of sediment within the core above a depth of 7.32 m, whereupon the concentration of fine sand increases sharply. This is associated with an overall increase in particle side from this point onwards.

Petrographic analysis of the digested sediment indicates that diatom frustules are the dominant form of sediment present in these samples, and that the observed variability in grain size is likely predominantly due to changes within the diatom community over time. Despite this, changes due to terrigenous sediment input are also likely to have altered the particle size distribution. ImageJ software was used to evaluate the average size of diatom frustules at several depths. Because the laser particle sizer used in this analysis measures grains in a number of different orientations, it was necessary to measure diatom frustule size across multiple axes. Diatom frustules were found to have an average grainsize of 18.08 ± 6.96 μm. This value is similar to the median grain size calculated within the core (17.15 ± 7.5 μm), indicating that diatoms are the modal grain size. Diatom frustule size has low variability in this core (Figure 3.5), so particle variability may represent changes in the quantity of non-diatomaceous particles, not variations in taxa.

The distribution of volume density values across each grain size measurement is shown in Figure 3.6. This figure shows that almost all measurements are dominated by medium-silt sized material, reflecting the presence of the dominant species of diatom (*Aulacoseira* S*pp*).
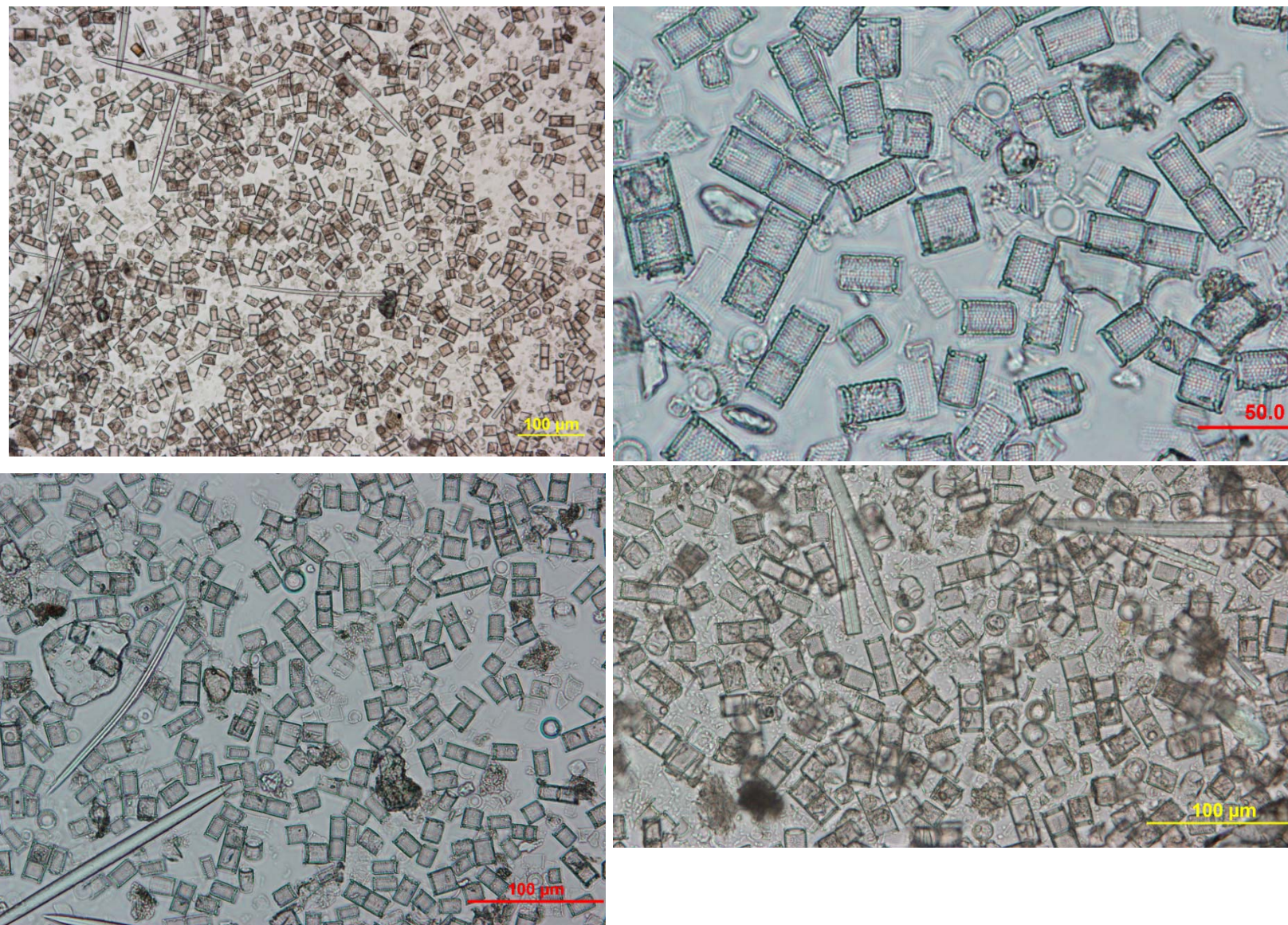
Figure 3.5 The size of diatom frustules was evaluated using microscopy and the ImageJ software at various depths within the core. Frustules were measured at multiple orientations, and have an average size of 18.08 ± 6.96 μm. The images were acquired at different magnification levels, and confirm that hydrogen peroxide digestion has removed the majority of organic carbon from the sediment.

73

The distribution of particle sizes across all measurements is presented in Figure 3.6. A clear volume density peak is identifiable in the medium-silt grain size class (6.3-20 μm), reflecting the average size of the diatom frustules which make up the majority of non-carbonaceous organic sediment in the core.
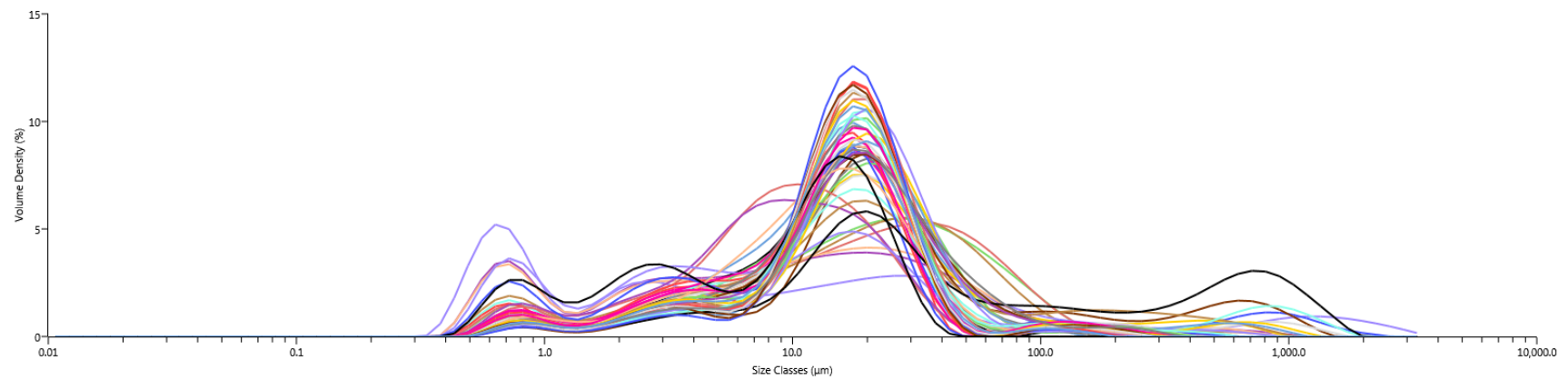
Figure 3.6 Volume density of particles across different size classes. The majority of sediment is made up of medium-silt sized particles.

3.3 Composition

3.3.1 FTIR spectroscopy calibration

In order to use FTIR spectroscopy analysis to determine sediment composition, it was first necessary to develop a calibration dataset using pure diatoms, activated carbon and schist. Plotting predicted compositional values and residuals against actual values indicates that the calibration process was effective, and residuals appear to be distributed randomly (Figure 3.7).
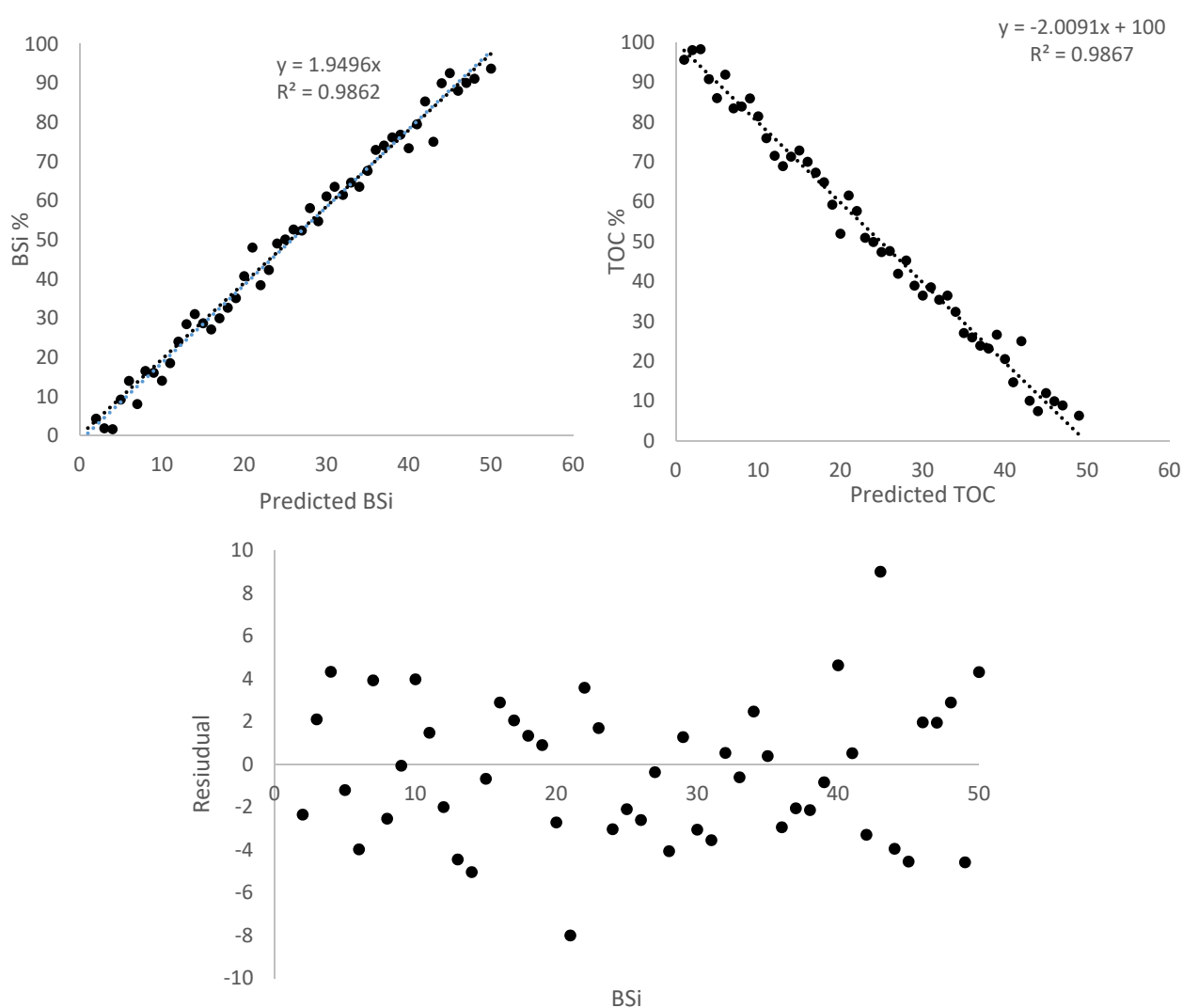
Figure 3.7 FTIR spectroscopy calibration was relatively accurate and predicted values were typically within 4% of actual measurements.

3.3.2 Biogenic silica, organic carbon and schist

Calculated biogenic silica values for the Hindon Maar 3 lake record are presented in Figure 3.8. BSi values are somewhat variable throughout the record, and the composition of the core varies from a minimum of 20.4% BSi, to a maximum of 96.6% BSi. The average weight percent of BSi within the Hindon Maar 3 lake record is 52.95%. The lowest value was recorded at a depth of 4.22 m, and the maximum recorded value occurred at a depth of 10.22 m. Material below 11.5 m is considered to be associated with turbidites (see Section 4.8.3) and BSi values from below this depth have therefore not been reported here.
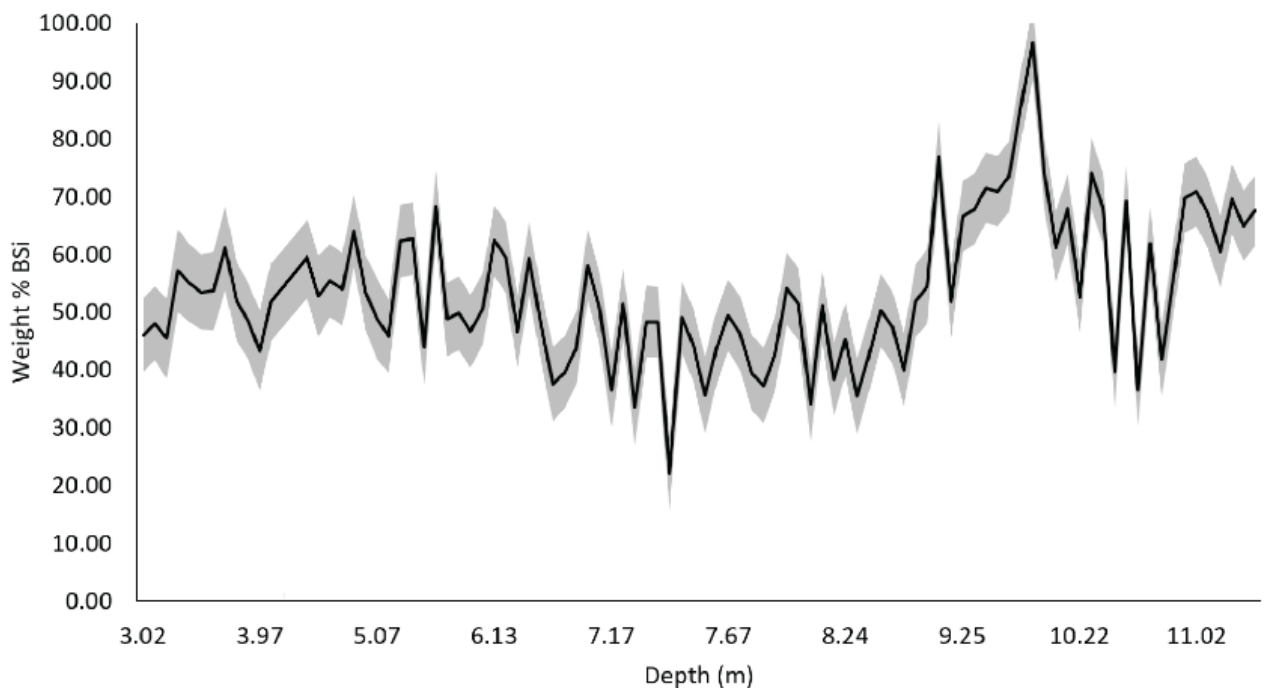
Figure 3.8 Biogenic silica is somewhat variable throughout the lake sediment within this core. Grey shaded areas represent the error associated with the partial least squares regression model.

Organic carbon and terrigenous sediment input were also estimated using FTIR spectroscopy (Figure 3.9). As BSi and organic carbon are the primary components within this core, their concentrations are inversely correlated. Calculated values of schist are high within the top several metres of the core, but decrease to less than 1% at greater depths.

Biogenic silica and organic carbon weight percent estimates were verified at several locations using bright field microscopy (Figure 3.10). This method confirmed that BSi values are highly variable within the core, and that the values obtained through FTIR spectroscopy are reasonable. Due to variability in slide thickness and the difficulty associated with producing effective thin sections using friable lake sediment, this method was not suitable for verifying BSi values across the length of the core.
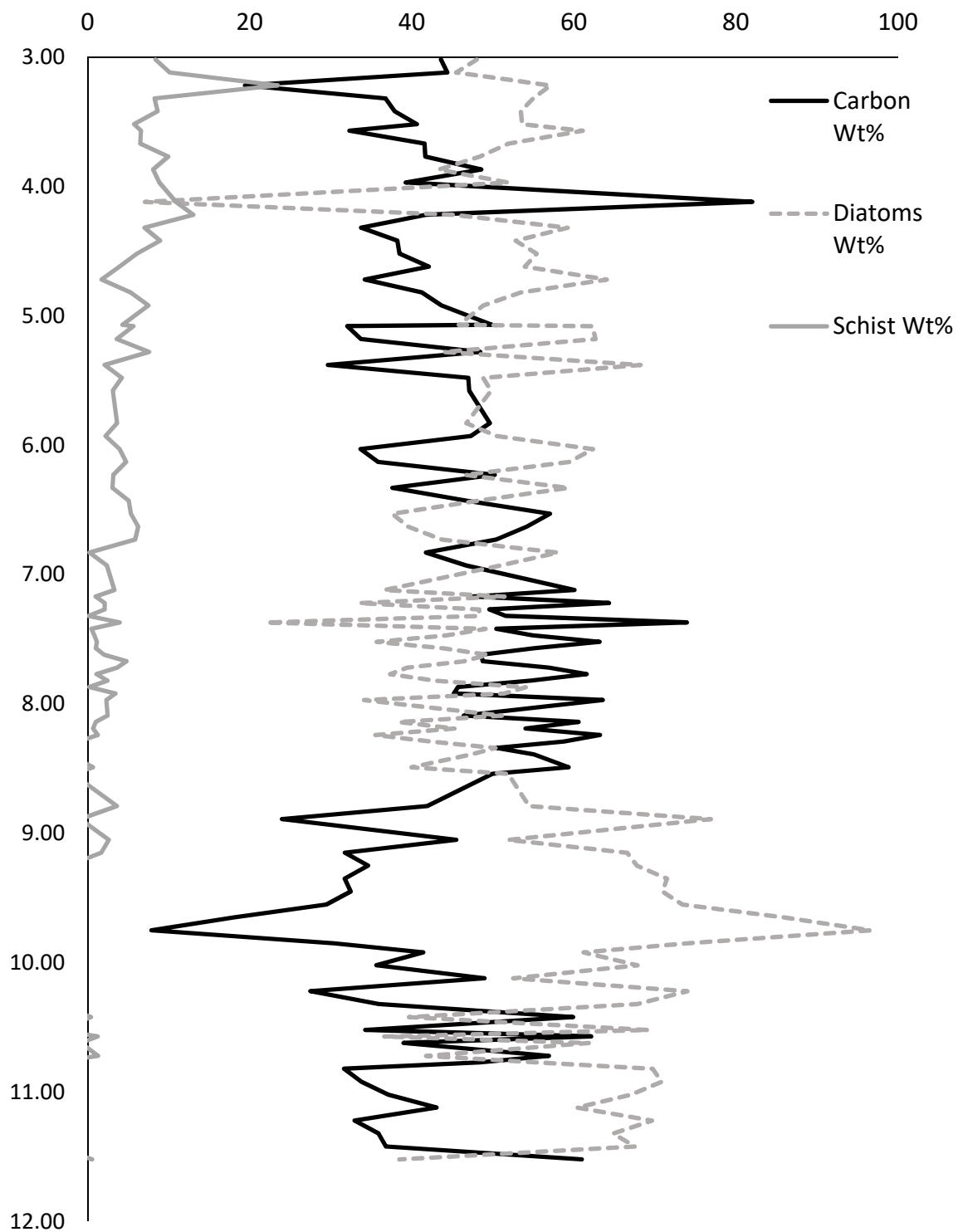
Figure 3.9 Biogenic silica is strongly inversely correlated with organic carbon as these two components make up the bulk of the sediment within the Hindon Maar complex. Terrigenous material derived predominantly from weathered schist appears to decline with depth.
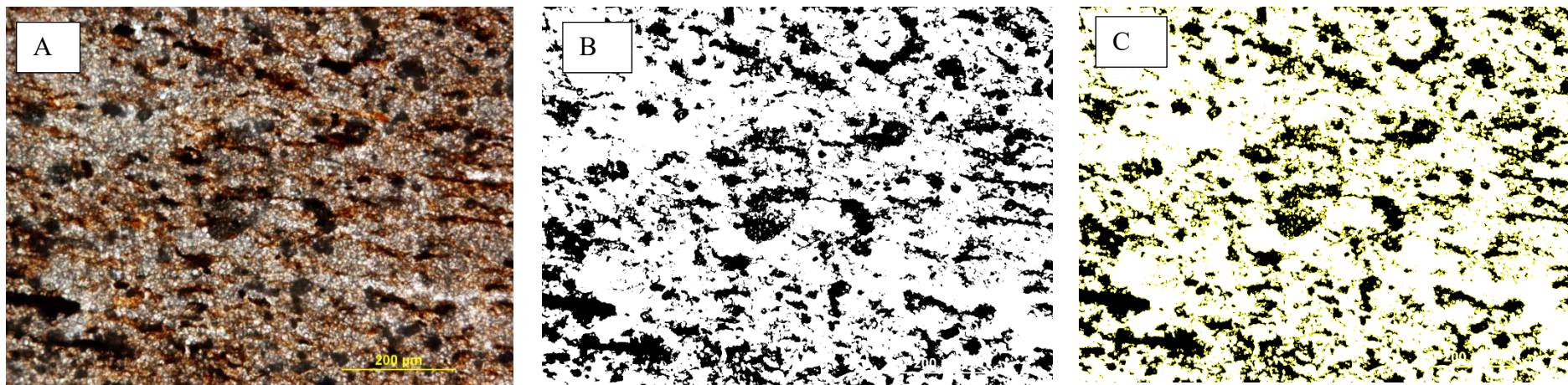
Figure 3.10 Biogenic silica was estimated using ImageJ software. Image A is a photomicrograph showing organic carbon and diatoms within a section of the core (taken at a depth of 9.45 m). The image B was produced using imageJ's "threshold" function. Areas inferred to be carbonaceous were then selected and measured (image C). This method indicates that biogenic silica accounts for 73% of the sediment in this thin section, and is in good agreement with FTIR spectroscopy estimates (Figure 3.9).

3.3.4 Diatom species

Point counting and grain size analysis indicate that the core is dominated by diatoms of the genus *Aulacoseira.* The diatom species assemblage is homogeneous throughout the core, and very little variation in diatom species was observed with depth (e.g. Figure 3.11). Sponge spicules also make up a portion of the BSi seen in this deposit.
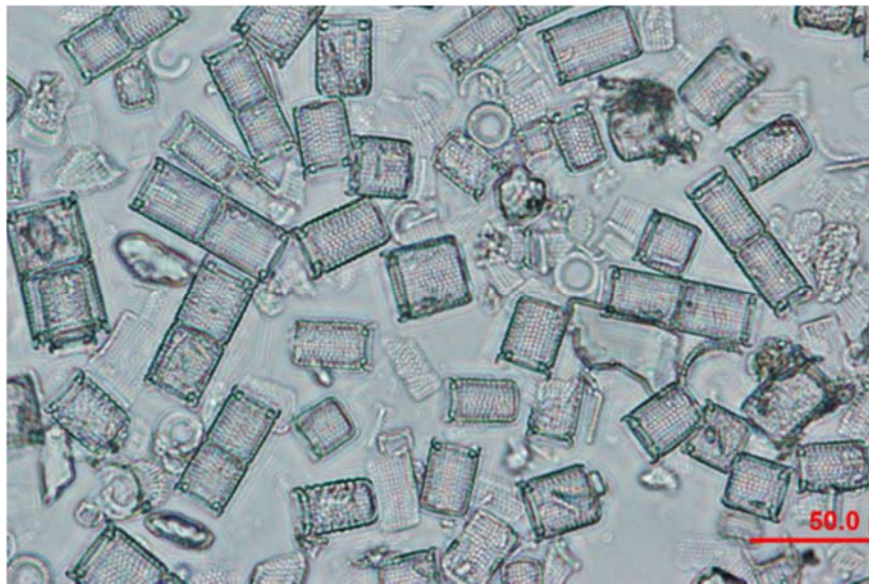
Figure 3.11. The Hindon Maar core was dominated by diatoms identified as Auilacoseira ambigua.

Species level identification was possible because *A. ambigua* is the only *Aulacoseira* species with a hollow ringleist, and is thus easily recognizable under light microscopy. *A. ambigua* typically has 4–15 μm in diameter and 3.5–15.0 μm high (Houk 2003), and valves are generally longer than they are wide. The mantle height is also greater than the valve diameter, so this species can be said to possess a high mantle. Areolae are dextrorse on the valve mantle and form pervalvar rows that propagate in a spiral pattern (Takano 1981; Houk 2003). Areolae are simple and generally round or square, but may be elongated. This species possesses small,

spatulate or flared linking spines which have been labelled as 'triangular,' 'bifurcate' or 'bicuspidate' (Potapova et al. 2008), and these spines are located at the end of each pervalvar mantle costa (Houk 2003). Valve faces generally have a random arrangement of pori, and the valves have two rimoportulae present at the ringleist. Many of these features could not be identified without the aid of electron microscopy, and this identification is based primarily on the hollow ringleist. Figure 3.12 is a comparison of light microscope images of *Aulacoseira ambigua* samples from the Hindon Maar 3 core (bottom row), to example images from (Buczko et al., 2010). This figure confirms that this identification is correct.
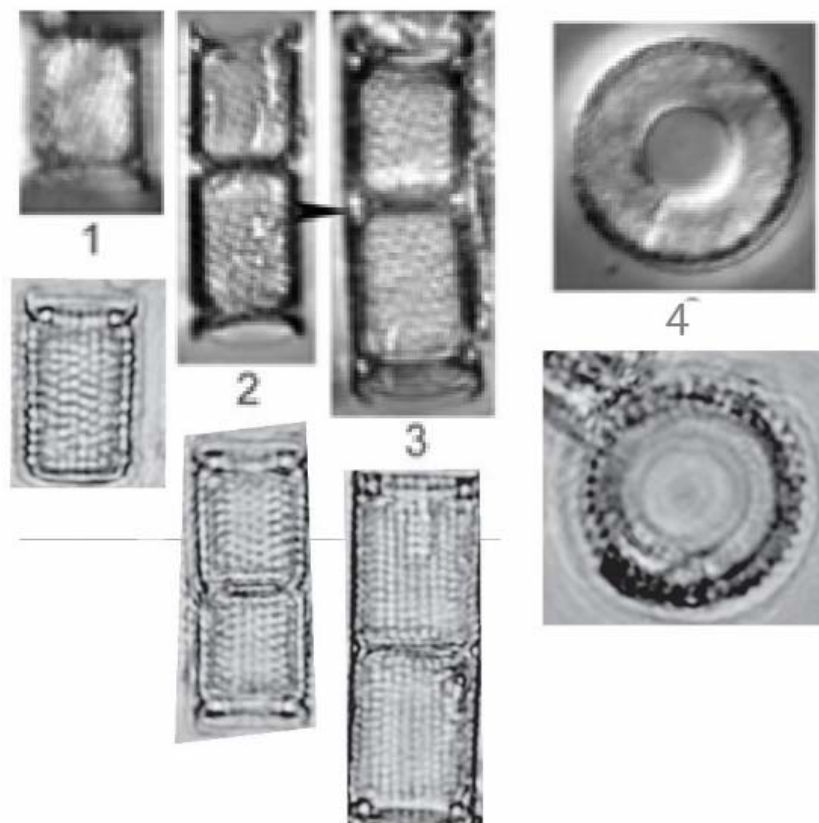
Figure 3.12 Aulacoseira *samples from Hindon Maar 3 (bottom row) closely match descriptions and images of A. ambigua (top row, from Buczko et al., 2010). The primary diagnostic feature of this species is the hollow ringleist (image 4).*

3.4 Physical properties

3.4.1 Magnetic susceptibility

Major changes in magnetic susceptibility begin to occur at depth of 11.5 m, where MS values are orders of magnitude greater than that observed elsewhere in the lake sediment. Visual inspection of the core and consideration of L*a*b* values at this point suggest a slight increase in luminescence and colour may be associated with this change in magnetic susceptibility. The magnetic susceptibility of Unit B is orders of magnitude higher than the majority of Unit A (Figure 3.13), except at the bottom of Unit A.
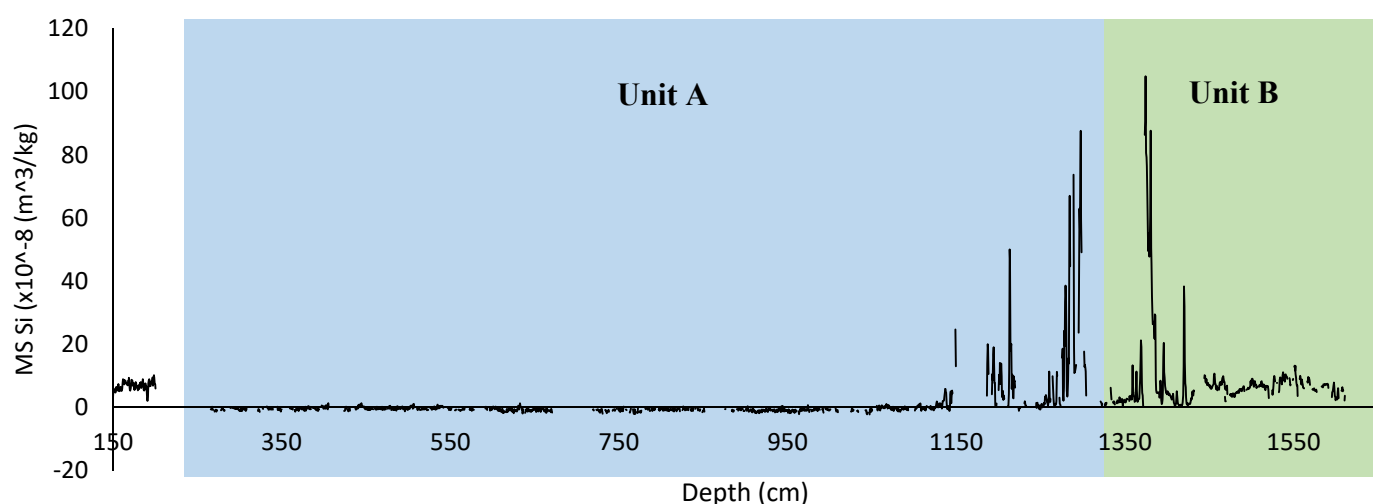
Figure 3.13 Magnetic susceptibility values from the Hindon Maar 3 core. Material highlighted in blue represents lake sediment whilst green represents the volcaniclastic breccia.

3.4.2 Density

The upper 11 m of this core have a relatively consistent density which is very distinct from the high values which begin to occur at a depth of 13.5 m, and are associated with a transition to Unit B (the volcaniclastic breccia) (Figure 3.14).
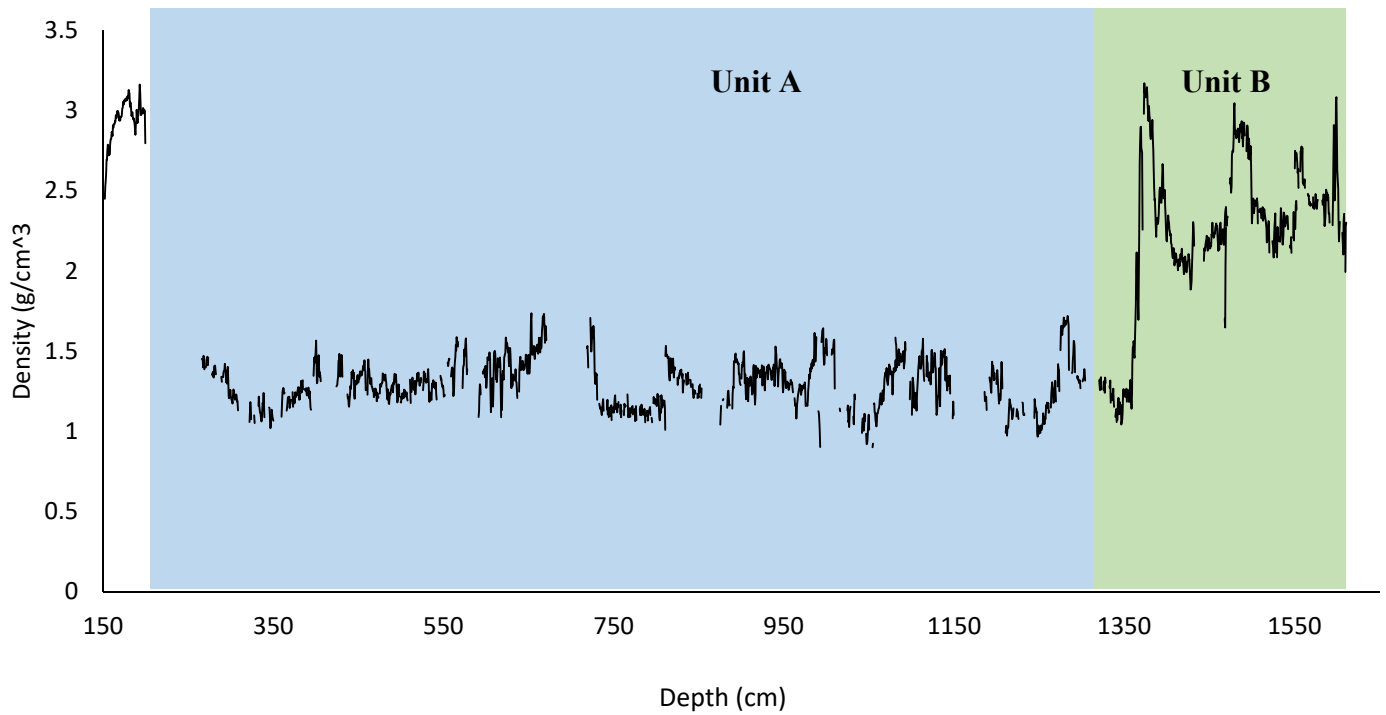
Figure 3.14 Density values from the Hindon Maar 3 core. Material highlighted in blue represents lake sediment, whilst green represents the volcaniclastic breccia.

3.4.3 L*a*b*

L*a*b* colour data is presented in Figure 3.15. The lake sediment has a low luminescence in comparison to the volcaniclastic breccia at the base of the core. Both colour components are also low reflecting the greyish colour present through most of the lake sediment. A slight peak in b* is noted at a depth of 9.35 m. The core possesses a weak yellow-red colour throughout the lake sediment, but the volcanic breccia has a green-yellow colour.
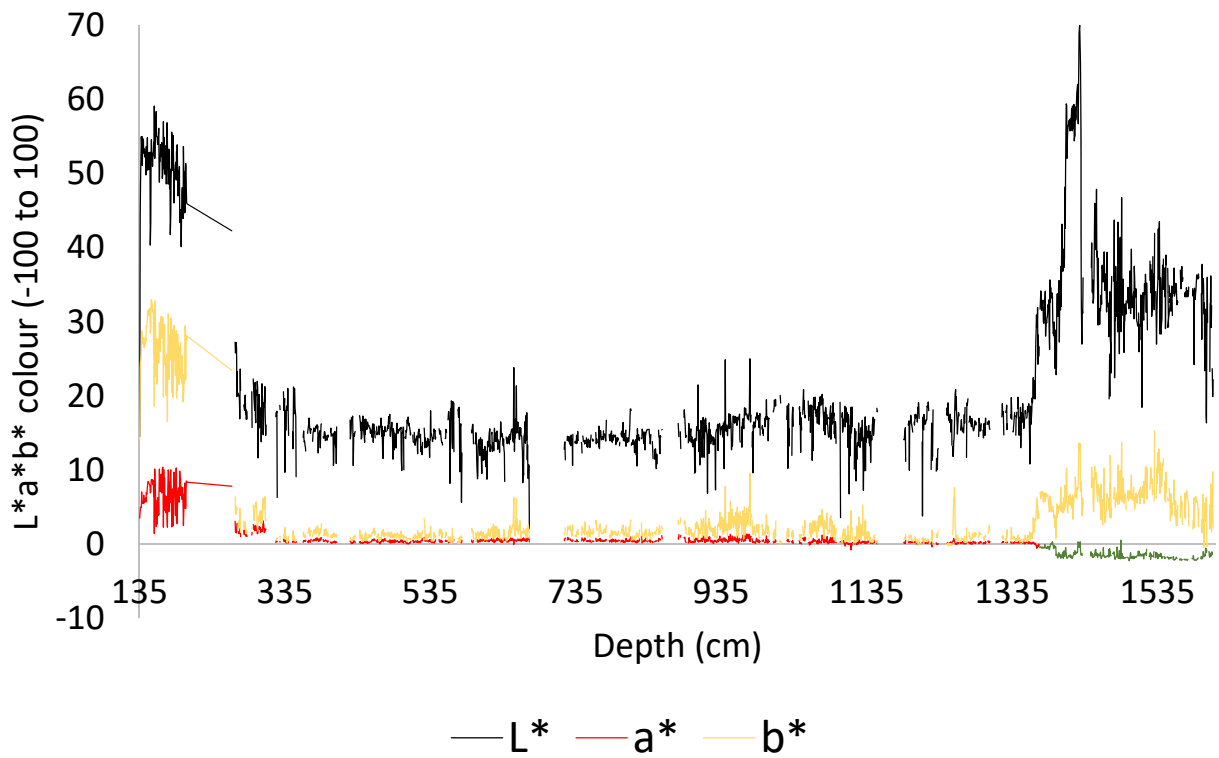
Figure 3.15. L*a*b* colour data from Hindon Maar 3. All components are low within the lake sediment. a* and b* components range from -100 to 100, with negative values representing green and blue colours, respectively.

3.5 Correlation Matrix

Table 3.1. presents the Pearson correlation coefficients and 2-tailed significance values for each of the variables assessed in this study. The biogenic silica and organic carbon values show a strong, significant inverse correlation ($r = -0.938$, $P < 0.05$), but neither of these variables bear any correlation with the GEOTEK or grainsize properties which is significant at the 0.05 alpha level. The concentration of biogenic silica is also inversely correlated with the concentration of schist within the deposit ($r = -0.433$, $p < 0.05$). A significant inverse correlation is present between the terrigenous sediment variable and the smallest 10% of grain particles ($r = -0.354$, $p = 0.002$). Terrigenous sediment is also inversely correlated with b* values, indicating that higher concentrations of schist may provide a blue appearance to the sediment core ($r = -0.239$, $p = 0.021$). The smallest 10% of particles as determined using laser grain size analysis bears a significant positive or negative relationship with each of the other variables in the dataset, with the exception of organic carbon and biogenic silica. Notably, the size of particles within this grainsize category is inversely correlated with density, such that larger particles are associated with a lower density of the overall core ($r = -0.341$, $p = 0.002$). Similarly, Dx10 is also inversely correlated with magnetic susceptibility ($r = -0.176$, $p = 0.004$). Sections of the core containing large particles within the 10th percentile are likely to possess a lighter appearance, with a yellow-red hue.

Table 3.1. Pearson Correlation matrix showing the relationships between key variables, and the significance of those correlations.

Correlations

		BSi	Schist	Dx10	Dx50	DX90	Density	MS	L*	A*	B*	R	G	B
Organic Carbon	Pearson Correlation	-.938**	.096	-.071	.200	.178	-.073	.094	-.139	-.015	-.052	-.184	-.156	-.135
	Sig. (2-tailed)	.000	.350	.544	.086	.126	.361	.301	.185	.890	.621	.077	.135	.198
BSi	Pearson Correlation		-.503**	.181	-.186	-.130	.097	-.122	.151	-.011	.134	.208*	.164	.121
	Sig. (2-tailed)		.000	.119	.111	.267	.334	.457	.148	.918	.201	.045	.117	.249
Schist	Pearson Correlation			-.354**	.001	-.096	-.073	.065	-.073	.079	-.239*	-.114	-.064	.001
	Sig. (2-tailed)			.002	.990	.413	.425	.530	.488	.451	.021	.275	.544	.991
Dx10	Pearson Correlation				.618**	.340**	-.341**	-.176**	-.085**	-.367**	-.329**	-.345**	-.342**	-.352**
	Sig. (2-tailed)				.000	.002	.002	.004	.002	.001	.003	.002	.002	.001
Dx50	Pearson Correlation					.445**	-.114	-.123	-.198	-.098	-.093	-.107	-.111	-.146
	Sig. (2-tailed)					.000	.316	.669	.230	.387	.412	.345	.328	.197
DX90	Pearson Correlation						-.070	-122	.046	-.012	.009	-.004	-.005	-.008
	Sig. (2-tailed)						.542	.896	.954	.917	.940	.969	.962	.945
Density	Pearson Correlation							.022**	-.136**	-.011**	.064**	.035**	.112**	.056**
	Sig. (2-tailed)							.415	.000	.000	.000	.000	.000	.000
MS	Pearson Correlation								.140**	-.238**	-.178**	.134**	.162**	.172**
	Sig. (2-tailed)								.000	.000	.000	.000	.000	.000
L*	Pearson Correlation									.924**	.935**	.972**	.974**	.989**
	Sig. (2-tailed)									.000	.000	.000	.000	.000
A*	Pearson Correlation										.975**	.960**	.944**	.889**
	Sig. (2-tailed)										.000	.000	.000	.000
B*	Pearson Correlation											.983**	.973**	.906**
	Sig. (2-tailed)											.000	.000	.000
R	Pearson Correlation												.998**	.963**
	Sig. (2-tailed)												.000	.000
G	Pearson Correlation													.971**
	Sig. (2-tailed)													.000

3.6 Principal components analysis

The Pearson correlation matrix produced above (Table 3.1) is relevant to principal components analysis. Highly correlated variables are likely to be measuring the same thing and will thus unduly influence the factor analysis. For this reason, the organic carbon variable was excluded from the analysis (this variable possesses a strong inverse correlation with biogenic silica). The RGB values were also excluded from this analysis as they represent colour variation and are thus closely related to the L*a*b* colour space. Similarly, variables with extremely low correlations may load onto only one principal component, thus failing to reduce the number of variables present in the dataset.

Variables were normalised prior to conducting the principal components analysis. In order to do so, the mean of each variable was subtracted from values within the dataset, and the resulting scores were divided by the standard deviation of the original dataset, converting each variable into a Z-score with a mean value of zero and a standard deviation of one.

A series of tables and figures were produced through this analysis. To provide a comprehensive examination of all aspects of the dataset, it was necessary to repeat the analysis multiple times while considering different variables and sections of the core. The results of the first PCA analysis presented here includes all variables deemed important based on the correlation matrix but considers only the diatomaceous lake sediment facies, excluding all the material associated with non-lacustrine deposition.

The second PCA uses only the GEOTEK MSCL variables and is limited to the diatomaceous lake sediment facies, as these values are available at a much greater resolution than are composition and particle size variables.

The tables associated with the second and third PCA are presented in the appendices (Sections 6.1.2 and 6.1.3) as these are not used in the discussion.

The final PCA conducted includes the all available variables, but incorporates all parts of the core, including the schist-rich overburden and the volcanic breccia located at the base of the lake sediment.

3.6.1 PCA limited to lake sediment and using all moderately correlated, normalised variables:

Table 3.2. is a correlation matrix featuring only the normalised variables included in the PCA analysis.

Table 3.2. Correlation matrix reporting the relationships between normalised Z-scores for the variables included in the principal components analysis within the lake sediment facies.

	MS	L	a	b	BSi	Schist	Dx10	Dx50	Dx90
Density.020	-.136	-.009	.065	.077	-.053	.023	-.048	-.123
MS		.138	-.237	-.176	-.015	-.037	-.020	-.009	-.006
L			-.015	.119	.147	-.072	-.067	-.139	.042
a*				.611	-.037	.079	-.016	-.029	.015
b*					.180	-.173	.037	-.087	.109
BSi						-.505	.124	-.271	-.129
Schist							-.324	.026	-.072
Dx10								.586	.358
DX50									.438

Table 3.3 presents the results of a Kaiser-Meyer-Olkin Measure of Sampling Adequacy, as well as those associated with the Bartlett's Test of Sphericity. The KMO index is designed to determine whether the original variables can be efficiently factorized (Kaiser, 1974). The KMO index defines an ideal solution as one that is unifactorial, where each row of the pattern matrix has only a single non-zero loading. This index thus measures the tendency of a standardised dataset towards unifactoriality for each row, and for the whole pattern matrix (Kaiser, 1974). A KMO index ranges from zero to one, with values greater than 0.5 being considered acceptable. The KMO value reported through this analysis (0.551, Table 3.3) is at the borderline of acceptability, and indicates that the variables are partially noncollinear and that factor analysis should be treated with caution in this instance (Kaiser, 1974).

The Bartlett Test of Sphericity is an inferential procedure which tests the null hypothesis that population variances are equal. A significant result in this test indicates that the original correlation r-matrix is not an identity matrix, and that relationships exist between the data included in the analysis. As the Bartlett's test is highly significant ($p < 0.001$), factor analysis is considered appropriate (Kaiser, 1974).

Table 3.3. Kaiser-Meyer-Olkin measure of sampling adequacy and Bartlett's Test of Sphericity

KMO and Bartlett's Test		
Kaiser-Meyer-Olkin Measure of Sampling Adequacy.		.551
Bartlett's Test of Sphericity	Approx. Chi-Square	2146.931
	df	45
	Sig.	.000

Table 3.4 reports the table of communalities before and after extraction. Because principal components analysis relies on the assumption that all initial variance is common, the communalities before extraction equal one. Values within the "extraction" column reflect the common variance in the data structure. For example, this table indicates that 73.9% of the variance in the biogenic silica variable is shared with other variables and is thus explained by an underlying factor. The greatest communalities are present in the b* and Dx50 variables (where 78.2% and 78.6 % of their variance is explained by underlying factors). Magnetic susceptibility is largely unrelated to other variables, and only 35.2% of variance for this variable is explained by an underlying factor.

Table 3.4. Table of communalities before and after extraction.

	Initial	Extraction
Density	1.000	.472
MS	1.000	.352
L*	1.000	.658
a*	1.000	.777
b*	1.000	.782
BSi	1.000	.739
Schist	1.000	.734
Dx10	1.000	.769
Dx50	1.000	.786
Dx90	1.000	.602

Ten linear components were identified using principal components analysis, with the first five components representing 76.157 % of variation within the dataset. Components 6 and beyond each account for less than 8 % of variability and are unlikely to be statistically important (Table 3.5).

Table 3.5. Variance explained by each of the ten components identified through principal components analysis using a subset of the available physical, textural and compositional data. The majority of variation is explained by the first four components, whilst subsequent eigenvectors have a limited influence on variability in the dataset.

Total Variance Explained

Component	Initial Eigenvalues			Extraction Sums of Squared Loadings		
	Total	% of Variance	Cumulative %	Total	% of Variance	Cumulative %
1	1.995	19.945	19.945	1.995	19.945	19.945
2	1.849	18.485	38.430	1.849	18.485	38.430
3	1.625	16.246	54.676	1.625	16.246	54.676
4	1.204	12.045	66.721	1.204	12.045	66.721
5	.944	9.436	76.157			
6	.721	7.209	83.366			
7	.614	6.143	89.508			
8	.442	4.416	93.924			
9	.318	3.179	97.104			
10	.290	2.896	100.000			

Extraction Method: Principal Component Analysis.

A scree plot of this principal component analysis (Figure 3.16) shows that an inflection occurs at the sixth eigenvector, where subsequent vectors begin to possess significantly lower eigenvalues. Factors with eigenvalues greater than one are considered to be valid, for this reason the first four components are considered.
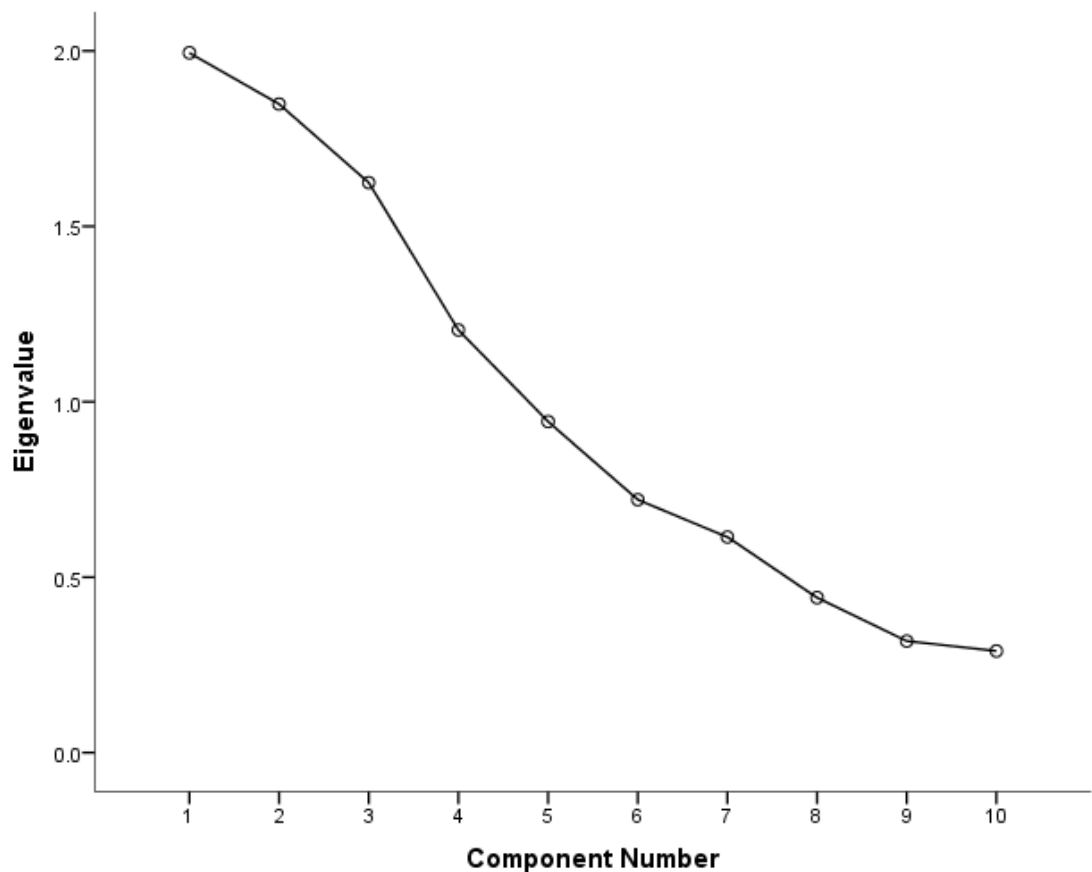
Figure 3.16 The Scree Plot associated with this principal components analysis lacks a clear inflection point within the first five components, indicating that each of those components is likely to be valid, and that they should be considered in relation to the percent of variance each contributes.

The first four principal components (PCs) were found to collectively account for 66.7 % of the variation in the lake sediment (Table x). The first PC represents 19% of variability and correlates strongly with particle sizes in each size class (Table x, Figure 3.17). This component is inversely correlated with the concentration of schist, and with biogenic silica, density and magnetic susceptibility (Figure 3.17).

The second component represents a further 18.5% of the variation in the dataset, and correlates most strongly with a* and b*, as well as biogenic silica (Figure 3.17). Strong inverse correlations occur with schist and magnetic susceptibility. Sections of the core which score highly on this axis are likely to have high biogenic silica concentrations and will exhibit a brighter colouration, with a yellow-red hue.

The third key component correlates inversely with MS, density and BSi, and positively with schistose sediment (Figure 3.17). This eigenvector represents 16.2% of component in the dataset.

Finally, the fourth PC represents 12% of variation and correlates inversely with density and positively with MS and L*.

Table 3.6. Component loading coefficient matrix, reflecting the four dominant components which account for a combined total of 66.7% of the variation within this dataset.

Variable	Component 1	Component 2	Component 3	Component 4
Density	-.216	.143	-.307	-.626
MS	-.353	-.241	-.229	.228
L*	-.157	.326	.233	.699
a*	.280	.419	.683	-.272
b*	.214	.742	.419	-.112
BSi	-.308	.675	-.388	.150
Schist	-.040	-.724	.473	-.024
Dx10	.641	.234	-.547	.007
Dx50	.828	-.272	-.174	-.014
Dx90	.718	-.035	.004	.289

Figure 3.17. Loading plots showing the distribution of each variable on each principal component within the lake sediment.

3.6.1 PCA using the complete core and using all normalised variables:

In the principal component analysis used to derive electrofacies for the complete core, the initial four components make up 77% of variation in the dataset, with 31% of variability explainable by the first component (Table 3.7). As in the previous analysis, the first component correlates strongly with density and colour, however this component has no relationship with biogenic silica concentration. The first component is associated with fine particle sizes (Table 3.7). The second component has a strong correlation with grainsize and a weak inverse relationship with biogenic silica. This component accounts for 17.3 % of dataset variance. The third principal component is dominated by variability in biogenic silica and schist (Table 3.7). The third component represents 16% of variance (Table 3.7).

The scree plot (Figure 3.18) indicates that the first four components have an eigenvalue exceeding one, whilst later components do not reach this threshold. An inflection point is present at component five, after which the change in eigenvalue % of variance decreases (Figure 3.18).

Table 3.7. Variance explained by each of the ten components identified through principal components analysis and subsequently included in cluster analysis. The majority of variation is explained by the first four components, whilst subsequent eigenvectors have a limited influence on variability in the dataset.

Total Variance Explained

Component	Initial Eigenvalues			Extraction Sums of Squared Loadings		
	Total	% of Variance	Cumulative %	Total	% of Variance	Cumulative %
1	3.147	31.468	31.468	3.147	31.468	31.468
2	1.733	17.332	48.800	1.733	17.332	48.800
3	1.596	15.958	64.758	1.596	15.958	64.758
4	1.230	12.299	77.057	1.230	12.299	77.057
5	.711	7.114	84.172			
6	.648	6.476	90.648			
7	.448	4.483	95.131			
8	.278	2.780	97.911			
9	.168	1.681	99.592			
10	.041	.408	100.000			

Extraction Method: Principal Component Analysis.

Table 3.8. Component Score Coefficient Matrix, reflecting the four dominant components which account for a combined total of 77.7% of the variation within this dataset.

	Component			
	1	2	3	4
Density	.811	.255	.110	-.337
MS	.345	.196	.107	-.662
L*	.864	.236	.092	-.136
a*	.565	-.026	-.084	.699
n*	.920	.179	.045	.275
Biogenic silica	.015	-.300	.827	.073
Schist	.057	-.034	-.864	-.128
DX10	-.581	.568	.337	-.018
DX50	-.341	.797	-.100	.078
DX90	-.028	.702	.036	.261

Extraction Method: Principal Component Analysis.

a. 4 components extracted.
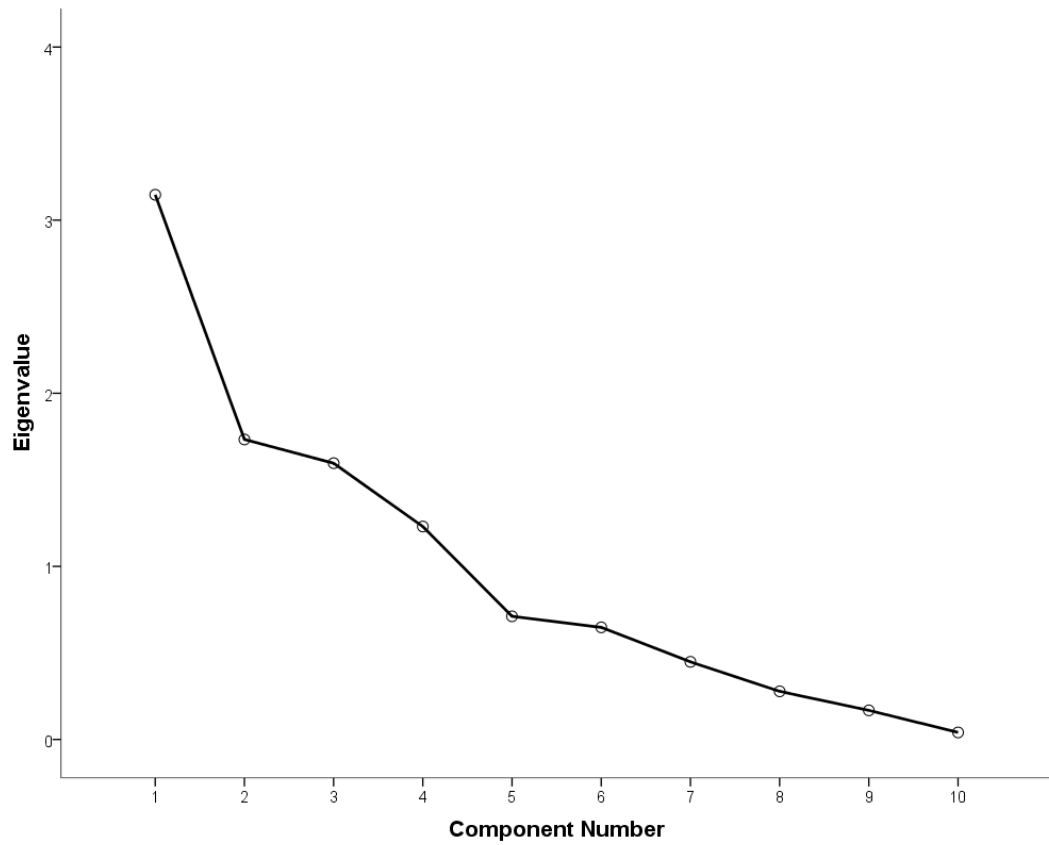
Figure 3.18 The scree plot associated with the complete core principal components analysis, indicating that each of the first four components is likely to be valid, and that they should be considered in relation to the percent of variance each contributes.

3.7. Electrofacies Analysis

3.7.1 Electrofacies analysis of lake sediment

On the basis of Schwarz's Bayesian Criterion values, principal component factor scores appears to identify six important clusters (Table 3.9). The smallest electrofacies identified in this analysis occupies 8.3% of the cases in the dataset, while electrofacies' five, two, three, and six make up 19.6%, 14.1%, 12.1% and 19.1% and of cases respectively. The majority of cases have been placed into electrofacies 3 (26.7%) (Figure 3.19). Each cluster has a different relationship with the four principal components, and these relationships are shown in Table 3.10 and Figure 3.20. The distribution of these clusters with respect to depth is shown if Figure 3.21.

Table 3.9. Schwarz's Bayesian Criterion values obtained using two-factor auto-clustering. BIC change becomes low at the seventh cluster, indicating that only the initial six clusters should be considered.

Auto-Clustering

Number of Clusters	Schwarz's Bayesian Criterion (BIC)	BIC Change[a]	Ratio of BIC Changes[b]	Ratio of Distance Measures[c]
1	2777.813			
2	2357.024	-420.788	1.000	1.347
3	2059.241	-297.783	.708	1.508
4	1880.827	-178.415	.424	1.100
5	1723.707	-157.120	.373	1.425
6	1630.200	-93.507	.222	1.519
7	1587.917	-42.282	.100	1.219
8	1563.375	-24.542	.058	1.131
9	1548.191	-15.184	.036	1.073
10	1537.854	-10.336	.025	1.343
11	1544.536	6.682	-.016	1.072
12	1554.562	10.026	-.024	1.032
13	1566.013	11.450	-.027	1.076
14	1580.643	14.630	-.035	1.074
15	1598.153	17.510	-.042	1.233

a. The changes are from the previous number of clusters in the table.

b. The ratios of changes are relative to the change for the two cluster solution.

c. The ratios of distance measures are based on the current number of clusters against the previous number of clusters.
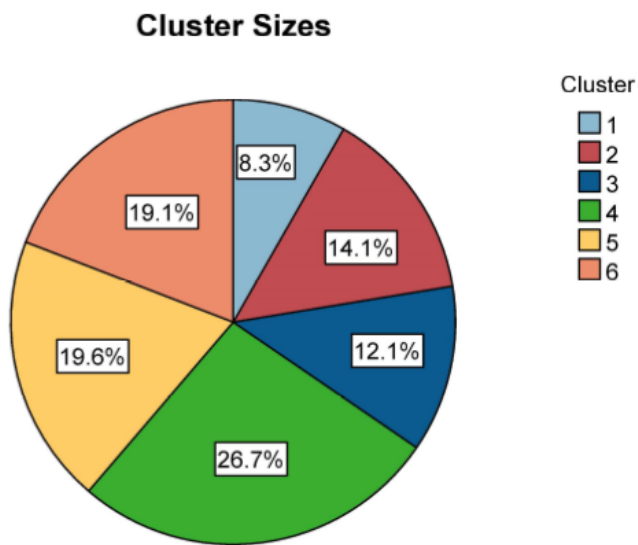
Cluster Sizes

Size of Smallest Cluster	129 (8.3%)
Size of Largest Cluster	416 (26.7%)
Ratio of Sizes: Largest Cluster to Smallest Cluster	3.22

Figure 3.19 Cluster analysis of factor scores produced five clusters of varying sizes. The majority of lake sediment within this core (55.1%) is classified as Electrofacies 3 (dark blue).
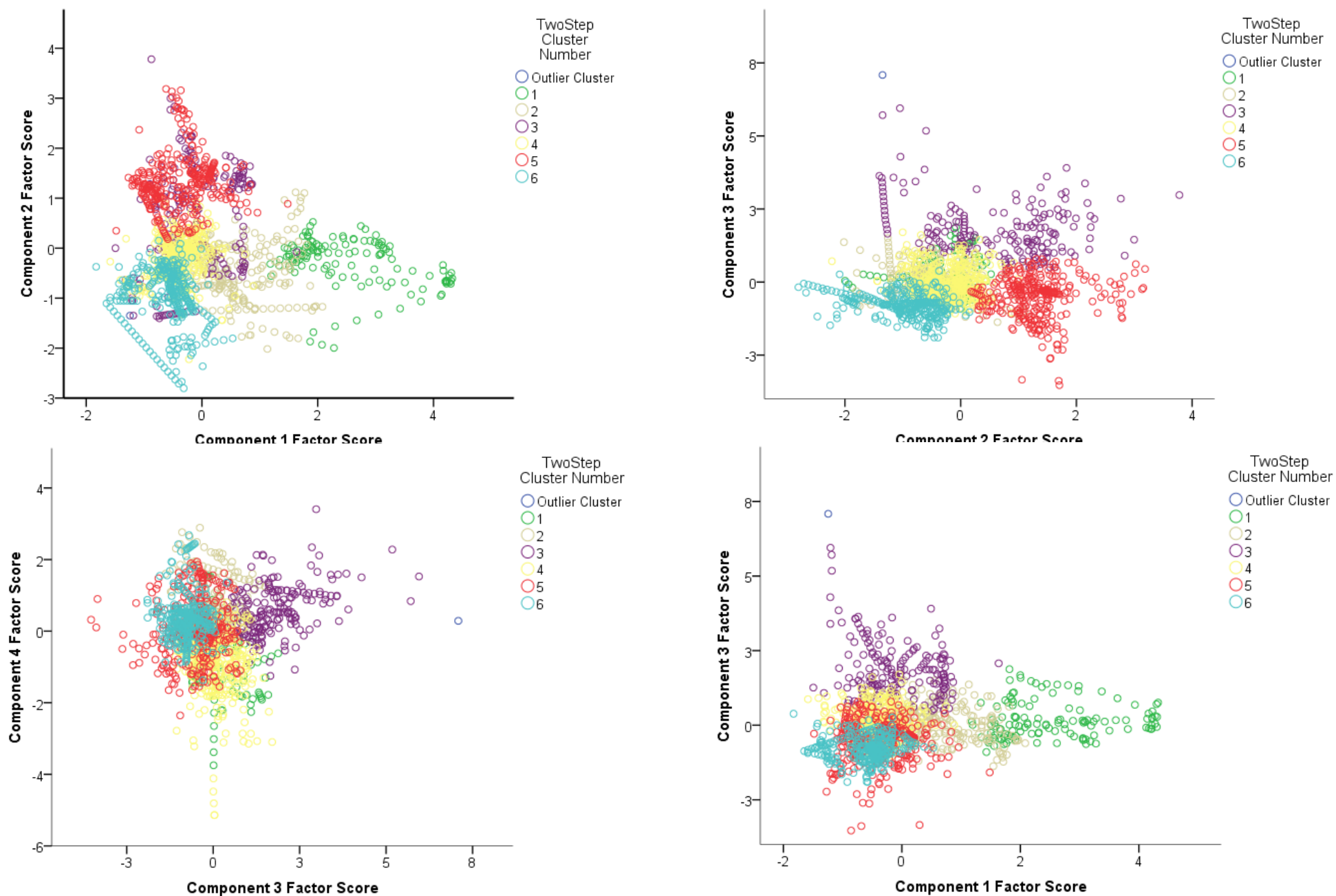
Figure 3.20 Position of case factor scores at each sampling location colour coded based on the Two-step electrofacies number.

Table 3.10. Mean and standard deviations in factor scores associated with sediment in each electrofacies, as determined using two step cluster analysis.

Centroids		Component 1 factor score		Component 2 factor score		Component 3 factor score		Component 4 factor score	
		Mean	Std. Deviation	Mean	Std. Deviation	Mean	Std. Deviation	Mean	Std. Deviation
Cluster	1	2.54	.89	-.3	.49	.18	.6	-.67	.96
	2	.66	.61	-.49	.58	.05	.57	.81	.7
	3	-.09	.59	.63	1.05	1.83	.94	.61	.69
	4	-.39	.33	-.21	.42	.03	.52	-.8	.85
	5	-.37	.48	1.32	.57	-.54	.71	.06	.88
	6	-.6	.40	-.97	.57	-.79	.4	.36	.65
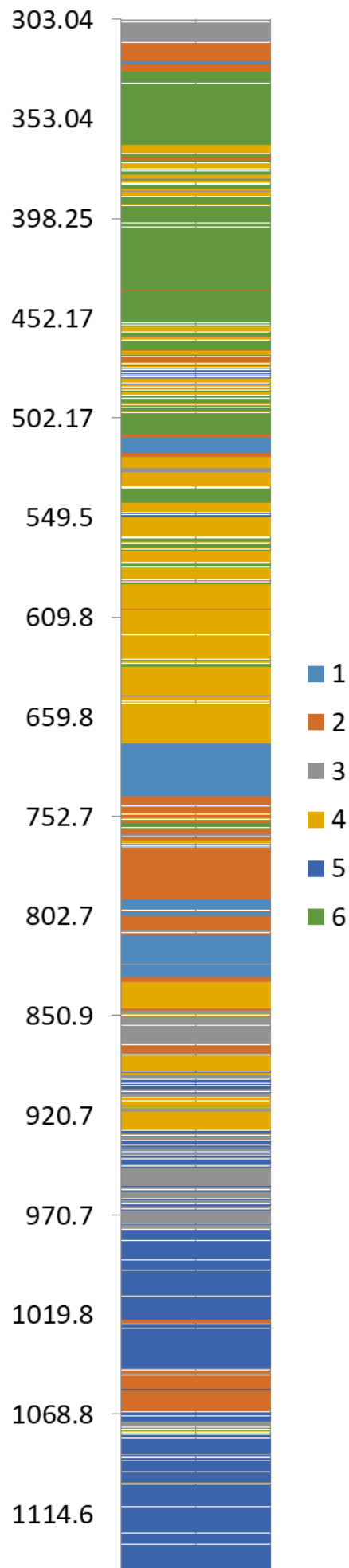
Figure 3.21 Summary of the occurrence of electrofacies identified using principal components analysis and cluster analysis within the lake sediment. six electrofacies occur within the laminated carbonaceous lake sediment. Electrofacies 4 represents the majority (26.7%) of material in the core.

104

3.7.2. Two-step cluster analysis of the complete core

Components produced for this purpose differ from those used in the previous principal components analysis which incorporated only the lake sediment (Tables x-x). This is because data in the previous analysis was excluded listwise where gaps occurred, and relied on a small sample of the available data, limited by the availability of grainsize and FTIR variables. This factor analysis is based on a much larger dataset where data is excluded pairwise. This analysis also includes non-lacustrine sediment sources. The Two-Step clustering algorithm determined, based on changes in the Schwarz Bayesian Criterion, that five clusters are suitable for this dataset (Table 3.11).

Table 3.11. Schwarz's Bayesian Criterion values obtained using two-factor auto-clustering. BIC change becomes low at the fifth cluster, indicating that only the initial four clusters should be considered.

Auto-Clustering

Number of Clusters	Schwarz's Bayesian Criterion (BIC)	BIC Change[a]	Ratio of BIC Changes[b]	Ratio of Distance Measures[c]
1	7549.973			
2	5446.956	-2103.017	1.000	2.025
3	4440.462	-1006.494	.479	1.257
4	3652.866	-787.596	.375	1.075
5	2924.393	-728.473	.346	2.004
6	2592.521	-331.872	.158	1.653
7	2416.721	-175.800	.084	1.300
8	2296.071	-120.649	.057	1.424
9	2230.148	-65.923	.031	1.036
10	2168.661	-61.487	.029	1.033
11	2111.207	-57.454	.027	1.388
12	2087.498	-23.708	.011	1.031
13	2066.369	-21.129	.010	1.200
14	2059.326	-7.043	.003	1.273
15	2067.353	8.027	-.004	1.240

a. The changes are from the previous number of clusters in the table.

b. The ratios of changes are relative to the change for the two cluster solution.

c. The ratios of distance measures are based on the current number of clusters against the previous number of clusters.

The smallest electrofacies identified in this analysis occupies 4.9% of the cases in the dataset, while Electrofacies' Five, Two and Four make up 7.6 %, 16.1% and 16.3% of cases. The majority of cases have been placed into Electrofacies 3 (55.1%) (Figure 3.22).
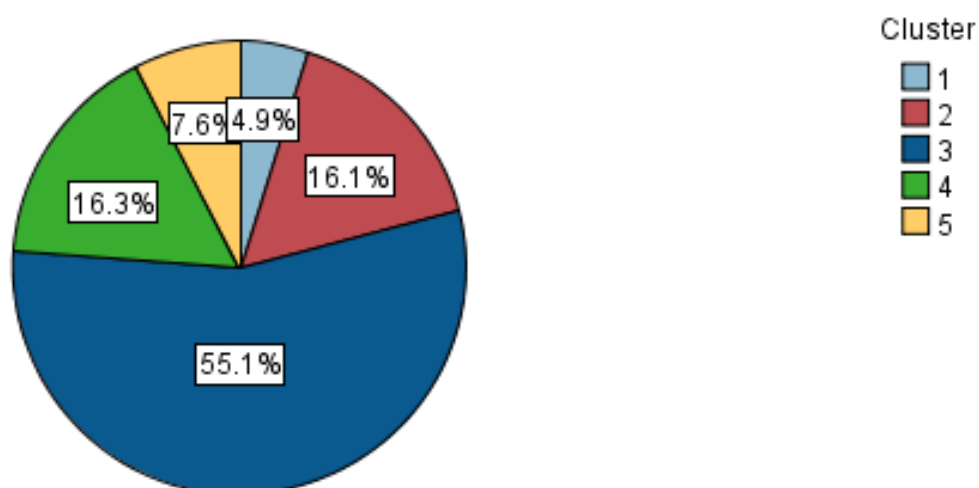
Size of Smallest Cluster	131 (4.9%)
Size of Largest Cluster	1489 (55.1%)
Ratio of Sizes: Largest Cluster to Smallest Cluster	11.37

Figure 3.22 Cluster analysis of factor scores produced five clusters of varying sizes. The majority of lake sediment within this core (55.1%) is classified as Electrofacies 3 (dark blue).

By overlaying case factor scores on principal component axes, and colour coding values based on the electrofacies to which they belong, it is possible to examine which properties are shared by each electrofacies (Figure 3.23, Figure 3.24). This information is also presented in Table 3.12. These figures show that Electrofacies 1 scores very highly on the first principal component (mean = 3.5) and moderately on the second principal component (mean = 0.46). The fourth principal component is also high within this electrofacies (mean = 1.85). Electrofacies 2 also has a relatively strong positive relationship with component 1 (mean = 0.7). Electrofacies 3 and 4 have a weak relationship with components 1 and 2, however Electrofacies 3 has a relatively low mean factor score on component 3 (-0.5) whilst Electrofacies 4 has a mean value of 1.54 on this eigenvector (Table 3.12). Electrofacies 5 is particularly strongly associated with component 2, and sediment that falls into this category has a mean factor score of 2.4. The depth of these electrofacies is presented in Figure 3.25.
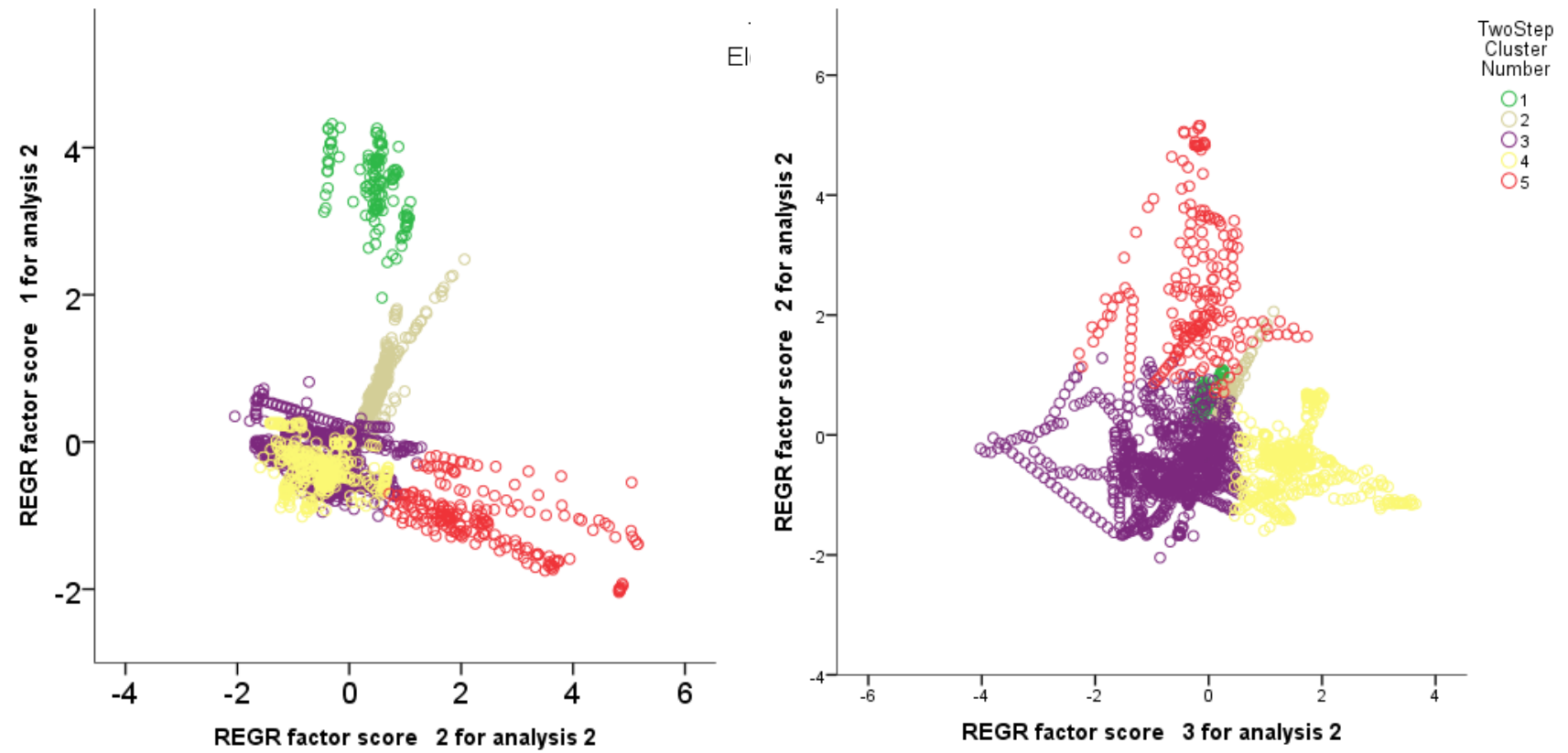
Figure 3.23 Position of case factor scores at each sampling location colour coded based on the Two-step electrofacies number.
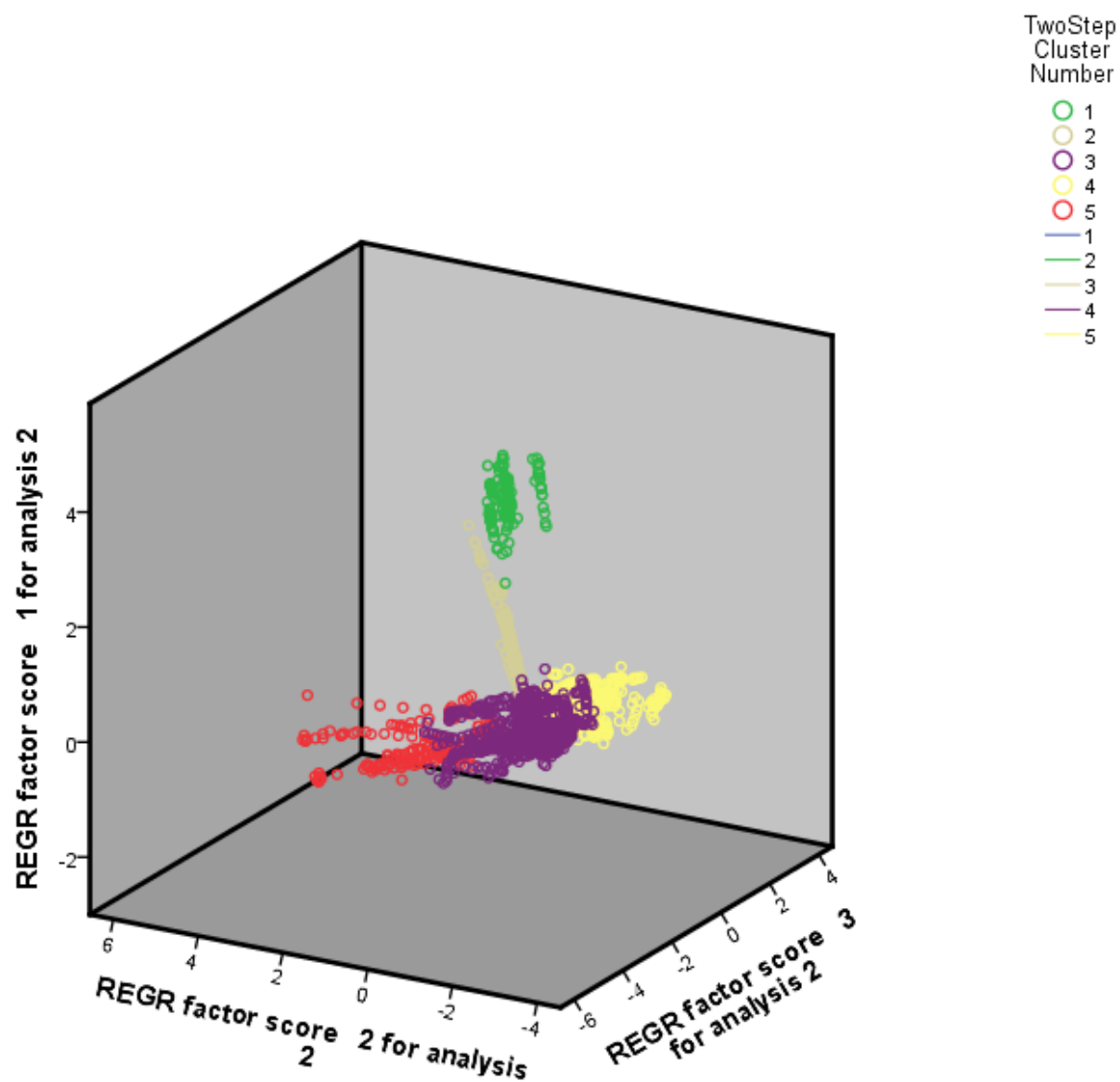
Figure 3.24 Position of case factor scores at each sampling location colour coded based on the Two-step electrofacies number.

Table 3.12. Mean and standard deviations in factor scores associated with sediment in each electrofacies, as determined using two step cluster analysis.

	REGR factor score 1		REGR factor score 2		REGR factor score 3		REGR factor score 4	
	Mean	Std. Deviation	Mean	Std. Deviation	Mean	Std. Deviation	Mean	Std. Deviation
Cluster 1	3.48	.45	.46	.40	-.04	.13	1.85	.84
2	.72	.38	.53	.24	.29	.12	-1.57	.98
3	-.26	.29	-.38	.51	-.50	.70	.07	.32
4	-.36	.26	-.49	.49	1.54	.65	.41	.39
5	-1.06	.41	2.42	1.15	-.24	.68	.74	.37
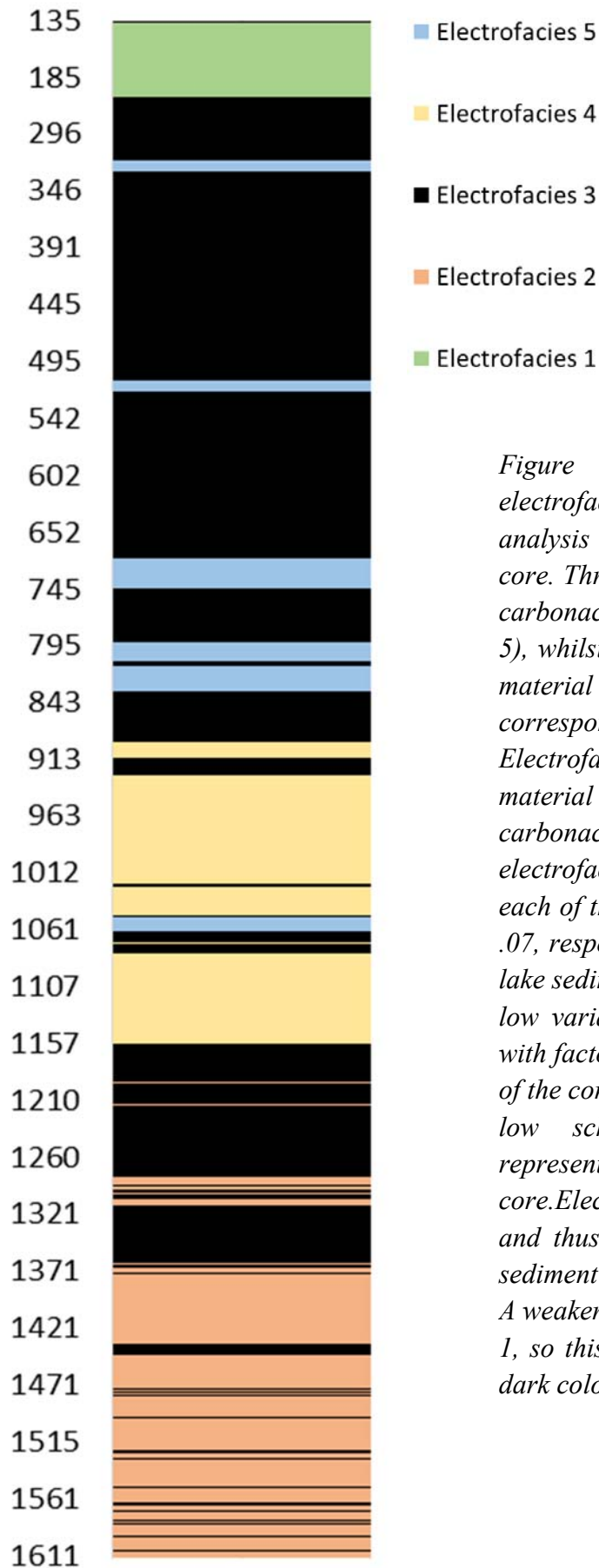
Figure 3.25 Summary of the occurrence of electrofacies identified using principal components analysis and cluster analysis within the complete core. Three electrofacies occur within the laminated carbonaceous lake sediment (electrofacies 3, 4 and 5), whilst electrofacies 2 represents brecciated rock material at the base of the core, and electrofacies 1 corresponds to the schist-rich overburden. Electrofacies 3 represents the majority (55%) of material in the core, and makes up most of the carbonaceous lake sediment present. This electrofacies has moderate mean factor scores for each of the first four components (-.26, -.38, -.5 and .07, respectively). This indicates that the majority of lake sediment has consistent physical properties with low variability. Electrofacies 4 correlates strongly with factor 3 (mean = 1.54), indicating that this part of the core is extremely diatomaceous and has a very low schist concentration. This electrofacies represents 16.3 % of sediment in the core. Electrofacies 5 correlates with component 2, and thus generally represents sections of the lake sediment core with a particularly large particle size. A weaker negative correlation exists with component 1, so this core section may have a low density and dark colouration.

3.8 Identification of cyclical signals

3.8.1 Sum of sinusoidal signals

Sum of sinusoidal signals was used to examine cyclicity in the dataset. Based on the assumption that some underlying orbital and solar cycles can be modelled by sinusoidal waves of varying amplitudes and wavelengths, several of the variables and principal components were analysed in this way (Figures 3.26, 3.27, 3.28). Several reoccurring cycles with the same period are present in many of the variables. Where common cycles are also present in a principal component, that component is taken to represent the process underlying those cycles. For instance, a cycle with a period of approximately 2000-2400 years is present in MS, L*, a*, BSi, PC1, PC2 and PC3. A cycle of this length in either or both of the processes represented by those principal components can may thus potentially explain much of the variability in those sediment properties. PC3 also has a 23000 year cycle and a 200 year cycle, both of which appear in BSi and MS. The 23000 year cycle appears in the schist variable.

In addition 4000 year cycles appear in MS, L*, b* and PC3, and ~2000 year cycles occur in MS, L*, a* PC1, PC2, PC4 and BSi. These cycles and others are shown in Table 3.13
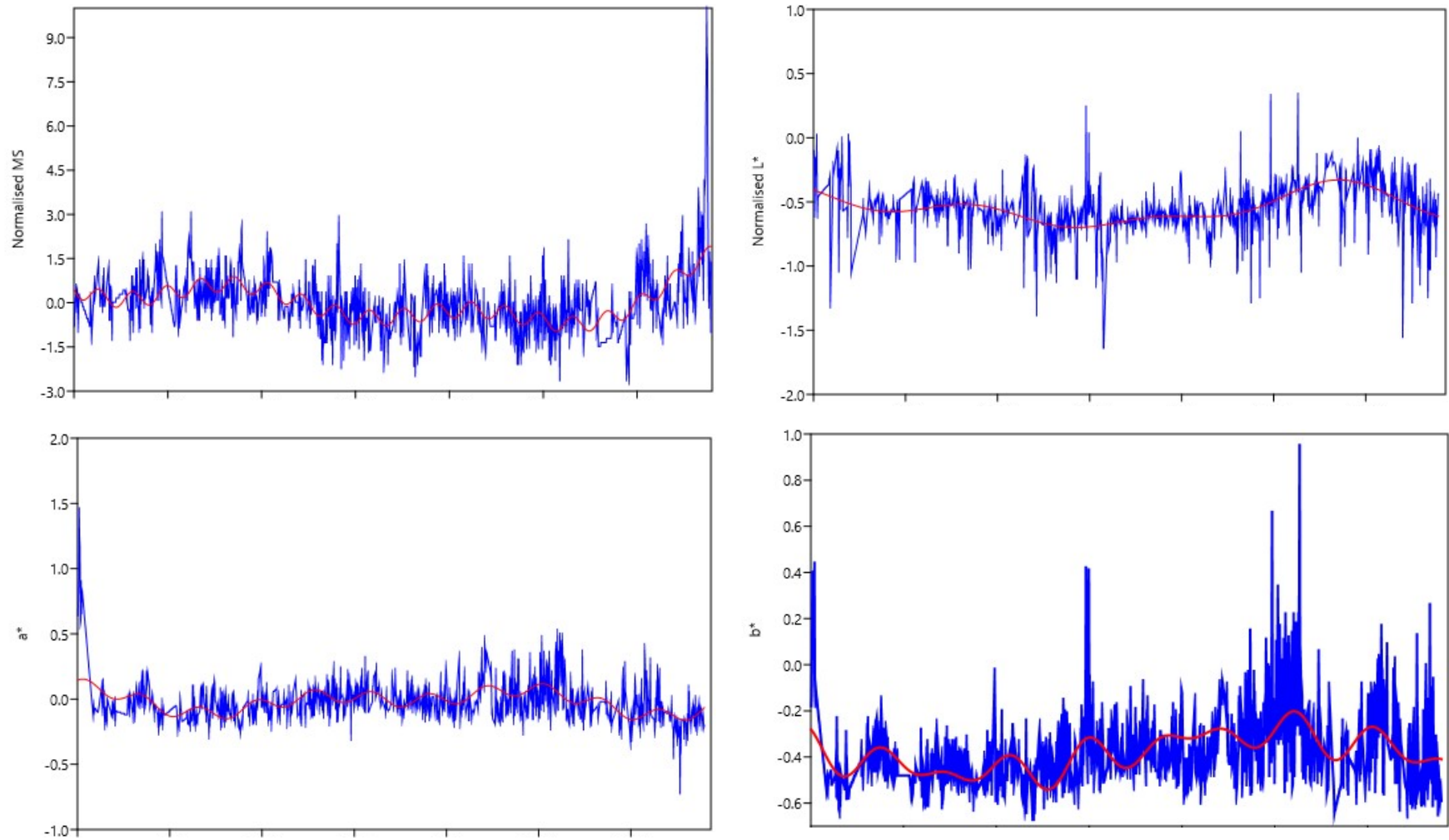
Figure 3.26 MS is modelled using four sinusoids, L* is modelled using three sinusoids ($R^2=0.266$), a* is modelled using three sinusoids ($R^2=0.24$), b* is modelled using three sinusoids ($R^2=0.27$), the period, amplitude and phase of these sinusoids is presented in table x.
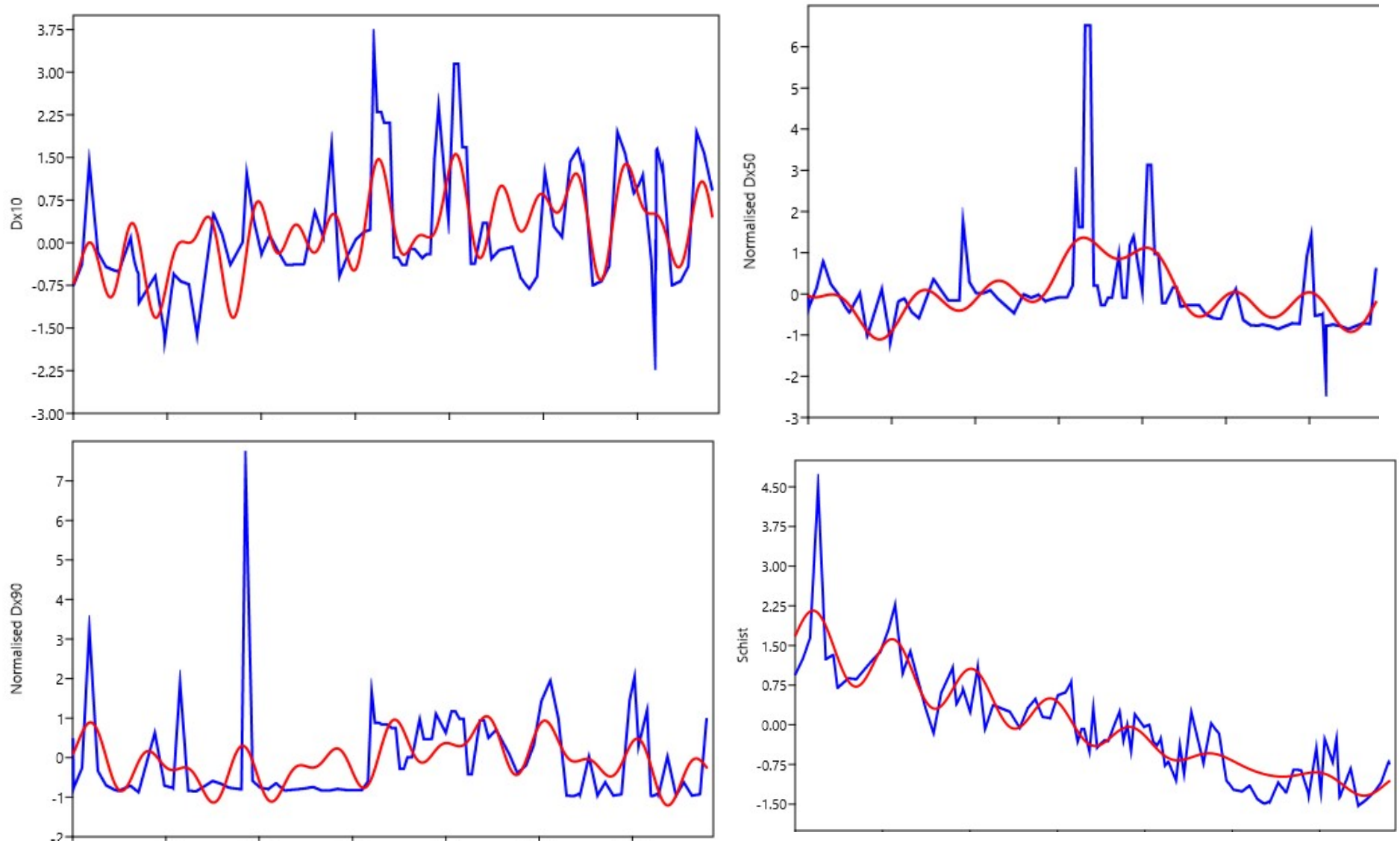
Figure 3.27 Dx10 is modelled using four sinusoids (R=0.48, Dx50 is modelled using three sinusoids (R^2=0.38), Dx90 is modelled using three sinusoids (R^2=0.29), Schist is modelled using three sinusoids (R^2=0.95), the period, amplitude and phase of these sinusoids is presented in table x.
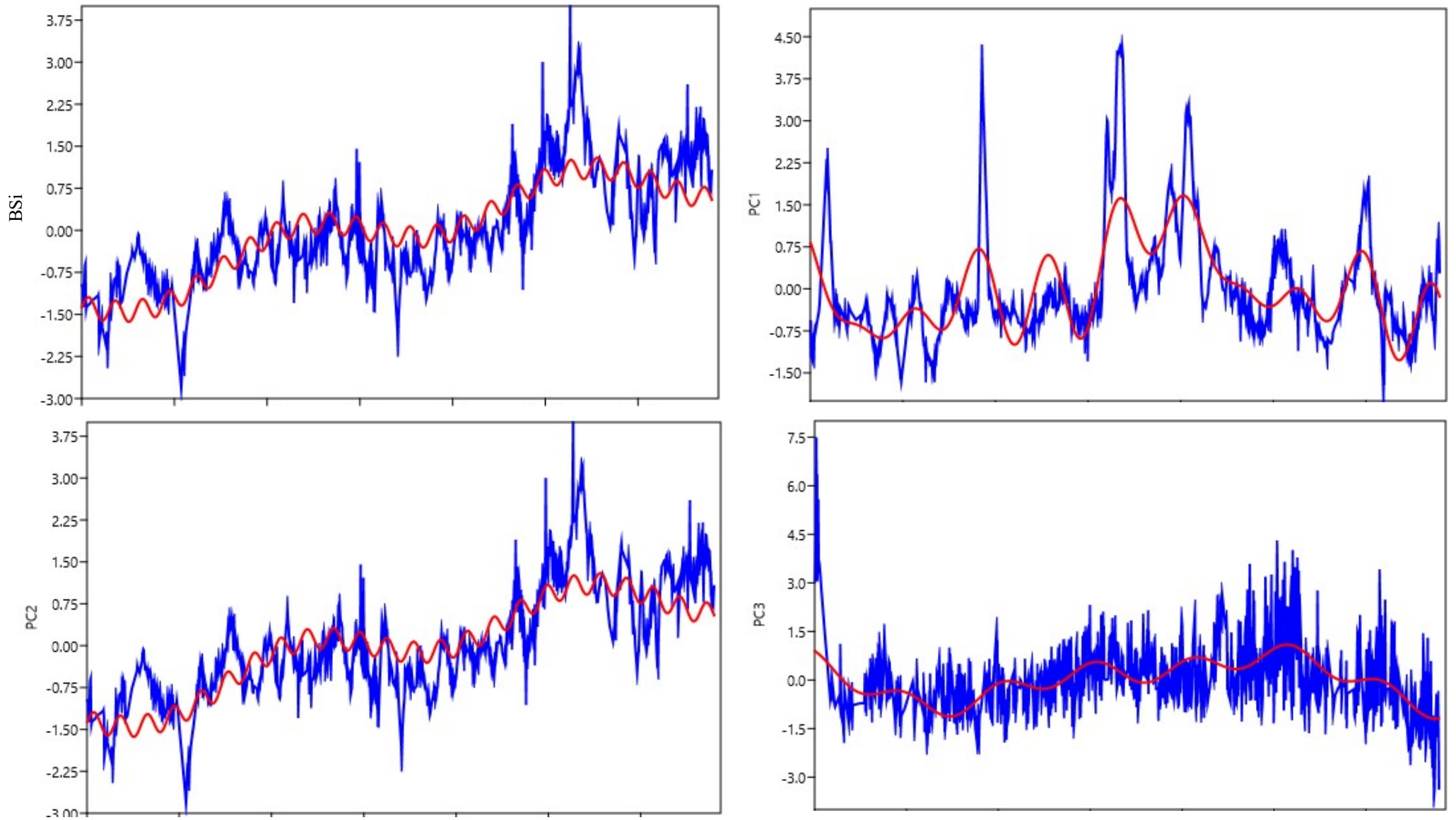
Figure 3.28 BSi is modelled using three sinusoids (R=0.63), PC1 is modelled using three sinusoids (R^2=0.51), PC2 is modelled using three sinusoids (R^2=0.88), PC3 is modelled using three sinusoids (R^2=0.32), the period, amplitude and phase of these sinusoids is presented in table x.

Table 3.13 Sinusoids used to model sediment variations in Figures 3.23 – 3.25. Common periods are highlighted by colour.

Variable	R^2	Sinusoid	Period (years)	Amplitude	Phase
Normalised MS	0.988	MS-1	6729	0.56	2.594
		MS-2	2265	0.38	-2.32
		MS-3	23196	7.96	-1.461
		MS-4	241	0.27	2.82
Normalised L*	0.266	L*-1	6332	0.12	0.13
		L*-2	2309	0.06	-1.48
		L*-3	3675	0.05	-1.58
Normalised a*	0.24	a*-1	2397	0.06	-0.09
		a*-2	5087	0.06	-0.54
		a*-3	710	0.05	-0.70
Normalised b*	0.27	b*-1	7076	0.09	-1.33
		b*-2	1201	0.05	-0.73
		b*-3	865	0.05	-0.6
Normalised Dx10	0.48	Dx10-1	12124	0.57	2.88
		Dx10-2	755	0.47	-0.06
		Dx10-3	493	0.45	2.85
		Dx10-4	1075	0.34	2.27
Normalised Dx50	0.38	Dx50-1	5270	0.73	-1.5
		Dx50-2	1069	0.38	2.7
		Dx50-3	2326	0.35	-1.3
Normalised Dx90	0.3	Dx90-1	952	0.45	1.1
		Dx90-2	5913	0.48	-1.02
		Dx90-3	608	0.37	2.6
Normalised BSi	0.63	BSi-1	23117	6.372	-1.42
		BSi-2	2312	0.77	-1.99
		BSi-3	225	0.07	2.72
Normalised Schist	0.94	Schist-1	23200	2.62	-1.43
		Schist-2	1066	0.35	1.71
		Schist-3	991	0.27	1.29
PC1	0.51	PC1-1	5546	0.7	-1.379
		PC1-2	2400	0.5	-1.2
		PC1-3	944	0.47	0.46
		PC1-4	786	0.45	-1.7
PC2	0.88	PC2-1	23200	2.337	-3
		PC2-2	2430	0.374	-1.2
		PC2-3	228	0.189	2.8
PC3	0.32	PC3-1	6127	0.65	-1.2
		PC3-2	3210	0.34	-0.6
		PC3-3	1192	0.32	-0.44
PC4	0.45	PC4-1	5822	0.71	0.46
		PC4-2	2219	0.47	-1.19
		PC4-3	1344	0.32	0.5

3.8.2 Tukey-Hamming Spectral analysis

Spectral analysis was another approach used to examine cyclicity in the dataset. Using this method, periodograms were produced for several high resolution variables (Figures 3.26 - 3.27). Logarithmic scales are used on the x-axis to fully show these results. The most common and generally most powerful cycles in occurred at 2300 year intervals. However cycles at 800 and 230 years were also observed in some variables. It is apparent but that identical cycles are not always found in the MSCL variables (Figures 3.26 - 3.27).
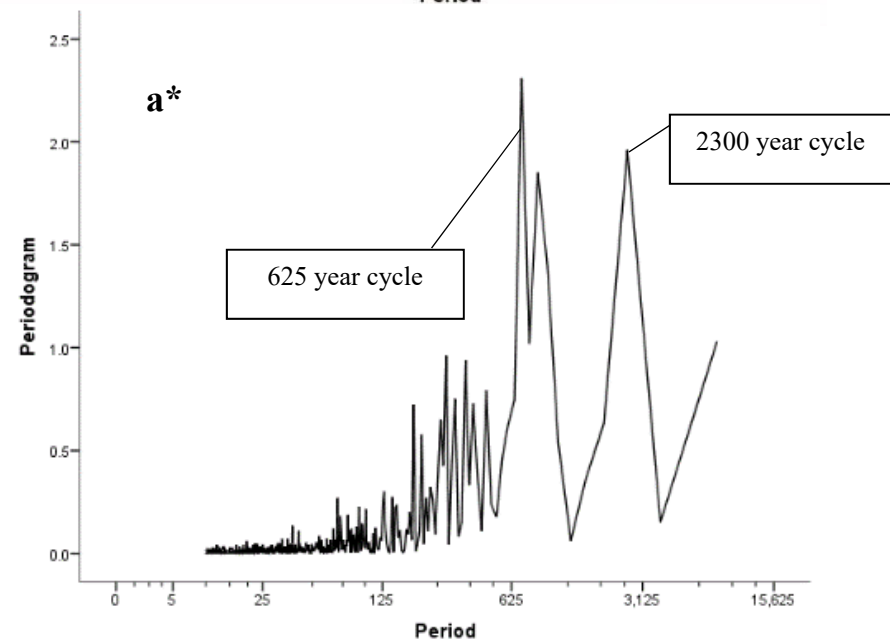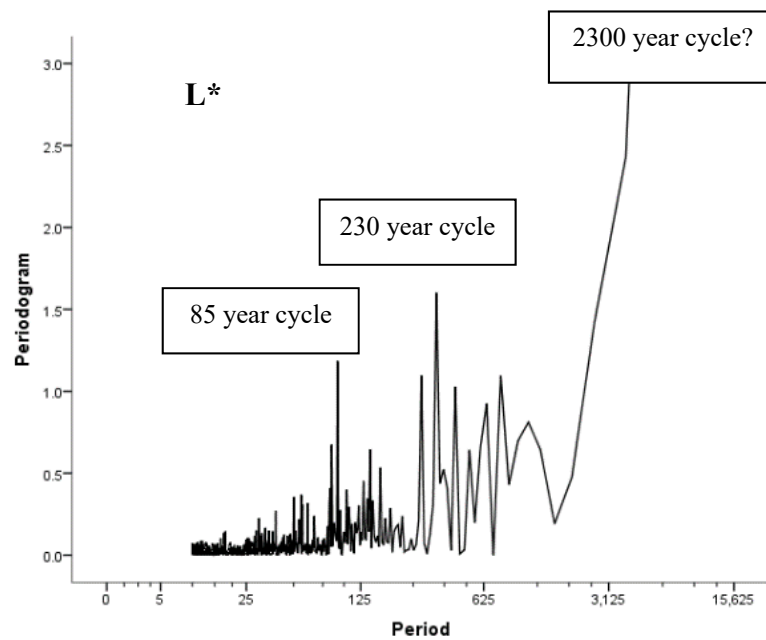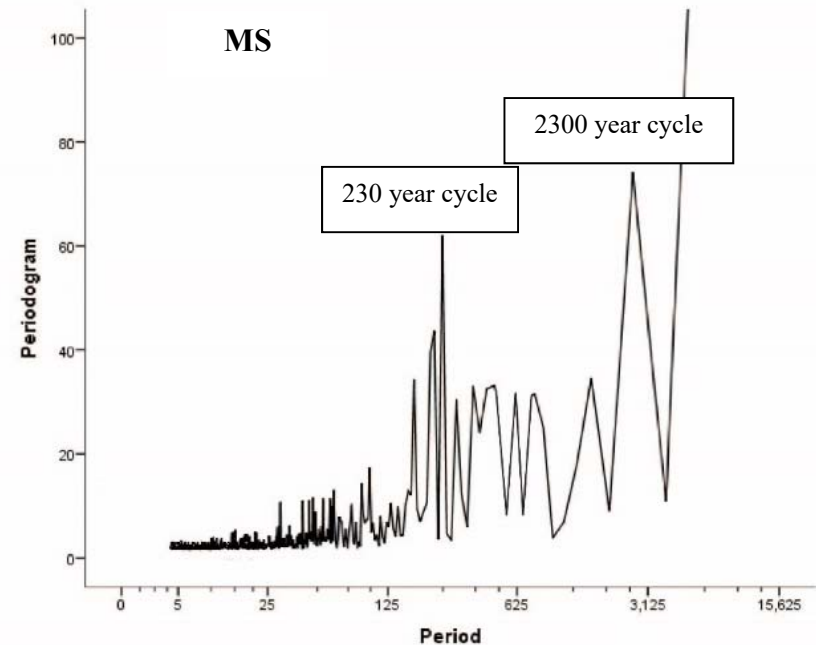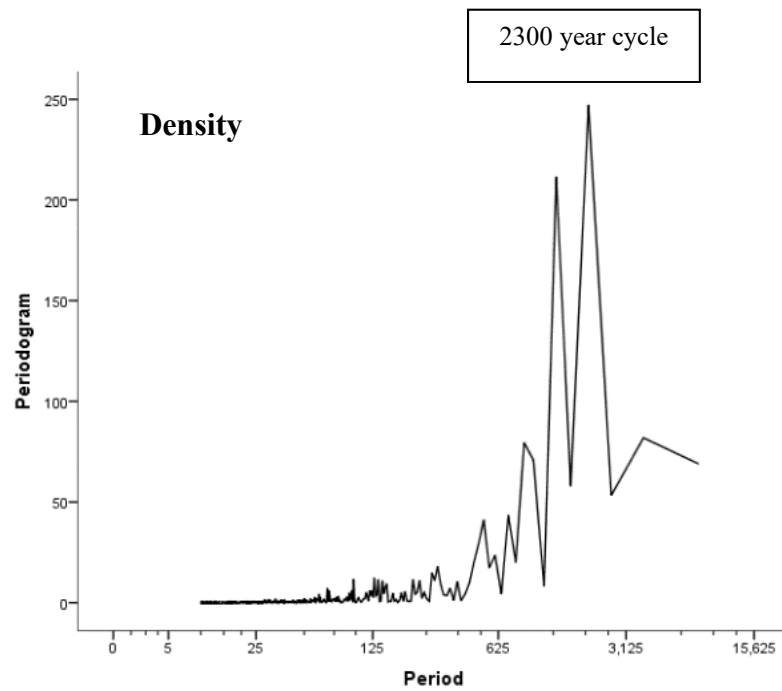
Figure 3.29 Tukey-Hamming periodogram produced using spectral analysis to identify cycles in the MS, density, L and a*.*
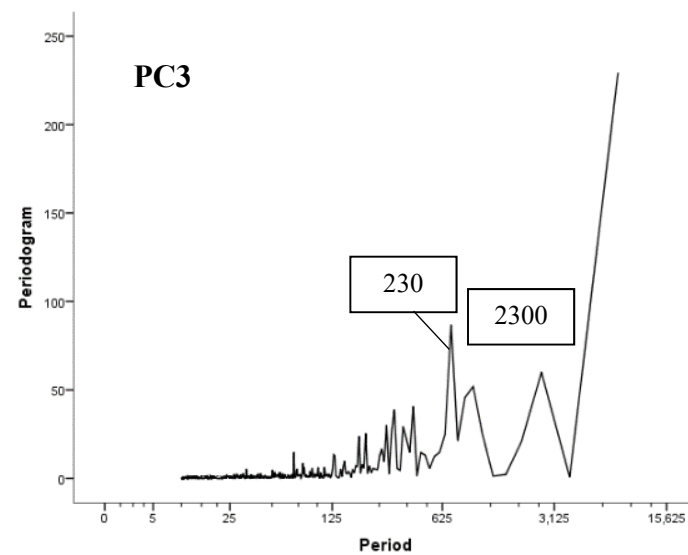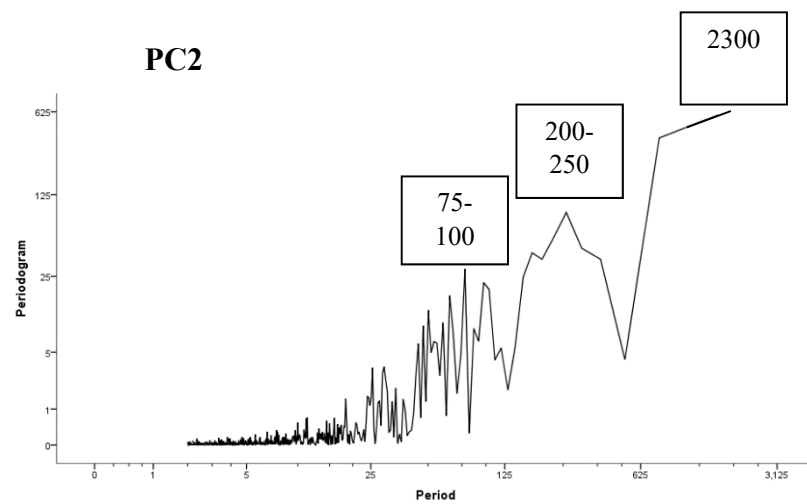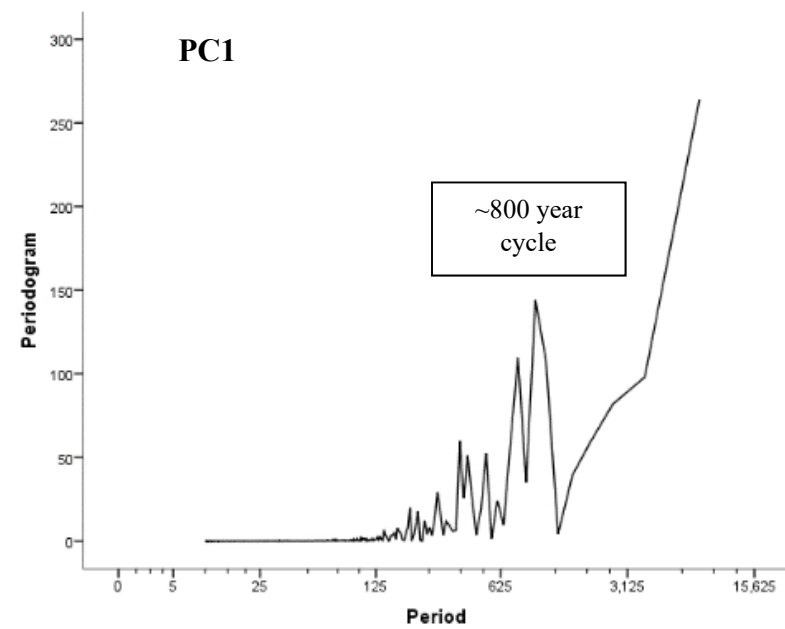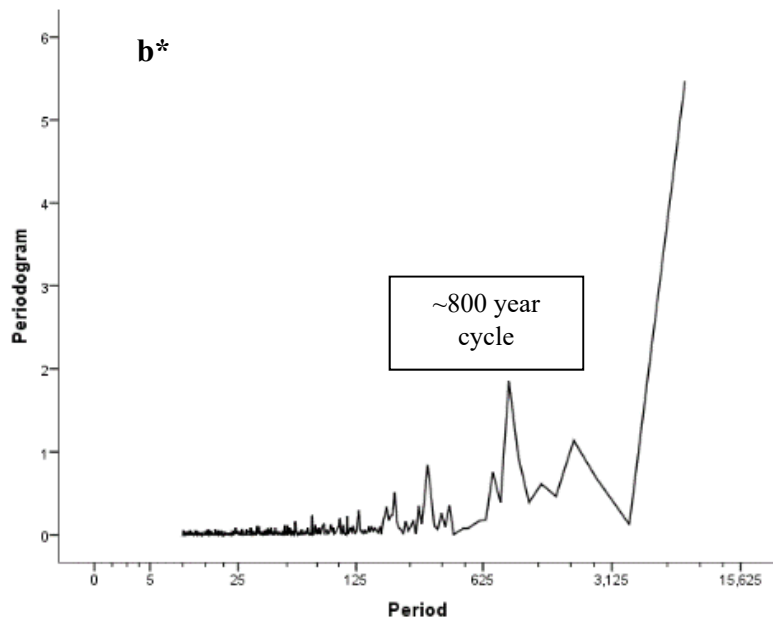
Figure 3.30 Tukey-Hamming periodogram produced using spectral analysis to identify cycles in the b*, PC1, PC2 and PC3.

3.8.3 Continuous wavelet transform

The same variables used to create periodograms (Figures 3.26 - 3.27) were analysed using continuous wavelet transformations (Figures 3.28 - 3.29). The most notable feature of these figures is a distinct cycle at around 2000-2300 years. This cycle is present in all of the variables displayed here except a* (Figures 3.28 - 3.29). Other cycles are somewhat less convincing, however a distinct cycle with a period of 1300-1500 years occurs in density, L* and b*, as well as in each of the plots of principal component factor scores (Figures 3.28 - 3.29).
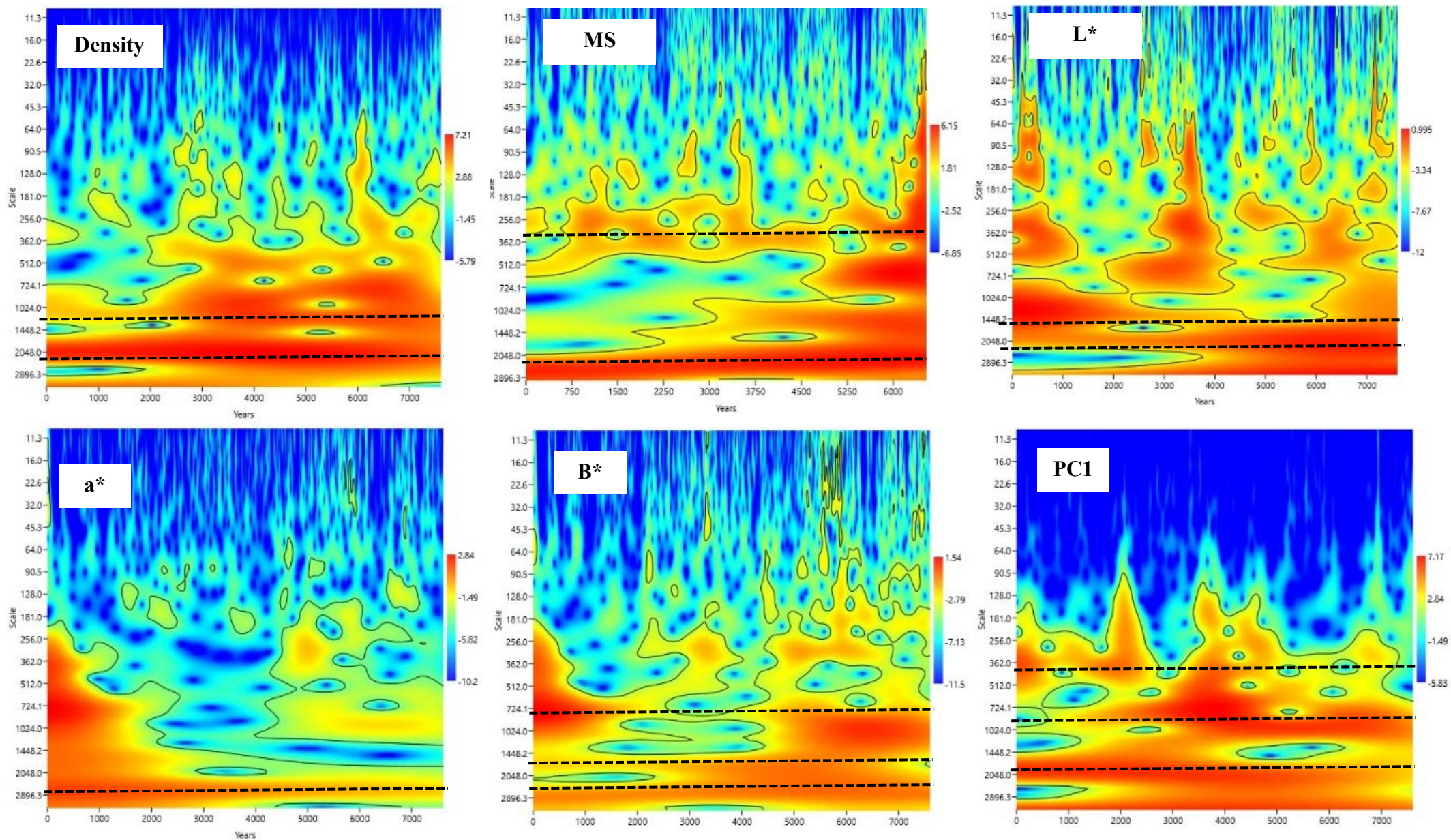
*Figure 3.31 Wavelet transformation produced to identify cycles in the MS, density, L*a*b* and PC1.*
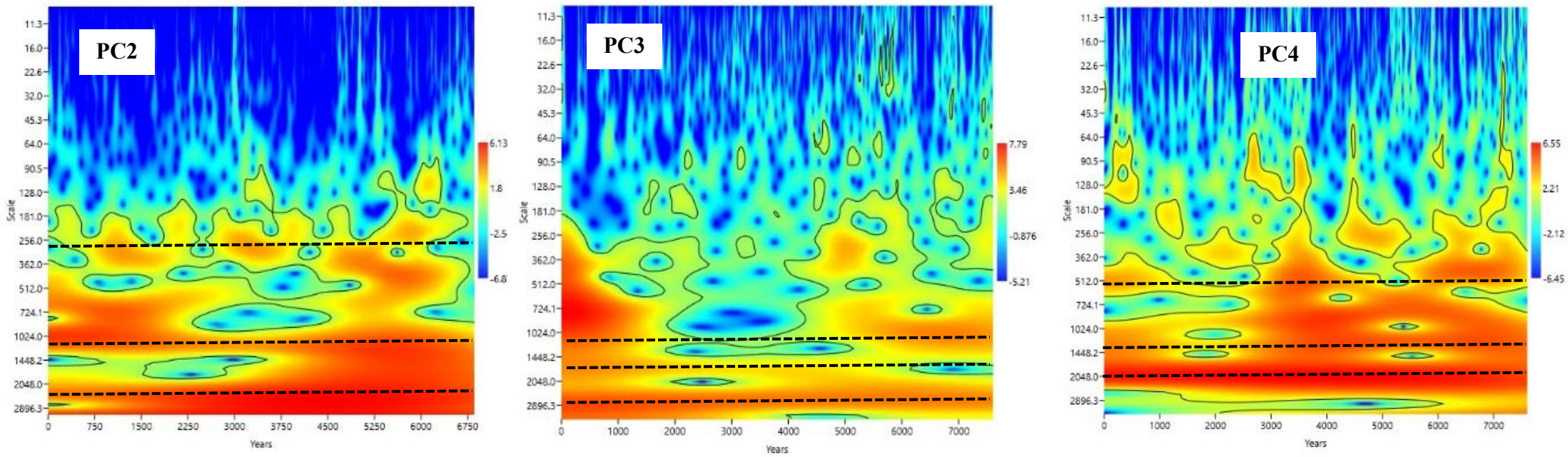
Figure 3.32 Wavelet transformation produced to identify cycles in the PC2, density, PC3 and PC4.

CHAPTER 4
Discussion

Interpretations of paleo-environmental conditions at Hindon Maar 3 throughout the duration of its deposition during the Mid-Miocene are based primarily on concentrations of organic carbon and biogenic silica. These proxies were considered suitable due to their high potential sensitivity to climate changes. However, these proxies are limited by a low sampling density, and the FTIR spectroscopy method used produces data with a relatively high degree of uncertainty. Geophysical properties and petrography offer further insight into sediment composition and the source of terrigenous material during this time, and also support inferences made using the organic carbon and biogenic silica proxies. Physical data were limited by the presence of numerous cracks present along the length of the core, the existence of which resulted in geophysical anomalies.

4.1 Formation of laminated sediments

Laminated lake sediment formation relies upon both the production and preservation of laminae. Heterogeneities in sediment composition and texture typically produce visually distinct laminae, and the preservation of these layers is enabled by a lack of physical and biological reworking (Chang, et al., 1998). A lake system likely to form biogenic laminated sediment must therefore consist of highly productive surficial waters, with a well-defined oxygen minimum zone present beneath the site of production (Chang, et al., 1998). While it is possible for

laminated sediments to also be preserved in oxygenated environments (e.g. Kemp and Baldauf, 1993; Boden and Backman, 1996), these environments generally result in the production of thick-mat laminae, where buoyant mats are comprised of entangled diatoms (Chang, et al., 1998).

Therefore, the presence of laminae and very high proportion of organic matter indicates that Hindon Maar three was a highly productive system with permanent stratification. The lake was therefore deep and narrow, although much of the crater depth has been eroded away.

4.2 Diatomite lamination styles

Diatomite lamination styles are highly variable, and those which occur within the Hindon Maar 3 core differ significantly from those identified within the Foulden Maar (despite the proximity of that lake). Chang et al. (1998) identified five lamina and couplet styles associated with diatomite on the basis of couplet bimodality, lamina thickness, compositional domination, lamina spacing and cyclicity (Table 4.1). These lamina types are relevant as they can be used to identify typical paleoenvironmental settings, biologically controlled sedimentation types, taphonomic processes and paleoecological associations (Chang, et al., 1998).

Whilst this model was based on marine sediment, the classification system is still generally relevant to lacustrine deposits, however some alterations must be made. For instance, where Chang *et al.* (1998) refers to detrital laminae, analogous features are more appropriately termed carbonaceous laminae in deposits such as Hindon Maar 3. Lamina classification is based on five parameters. The first of these, bimodality, is the relative difference in bulk density between adjacent laminae (Chang, et al., 1998). Colour contrasts are commonly used to examine the

bimodality of couplets, and couplets with a stark colour difference between the carbonaceous and diatomaceous laminae are referred to as high-bimodality couplets (Chang, et al., 1998). In contrast, low-bimodality couplets have only minor colour differences between detrital and diatomaceous couplets, in which case the diatomaceous layer generally possesses a relatively low diatom concentration (Chang, et al., 1998).

Throughout most of the Hindon Maar 3 lake sediment facies, the diatomite has an extremely low bimodality, such that differences between the carbonaceous and diatomaceous laminae are nearly indistinguishable, with the diatomaceous layer contributing little to the total thickness of the couplet. Some moderate-to-high bimodality sections are present, and generally occur in those portions of the core associated with very high productivity (e.g. 8.7 – 11.2 m). These sections of the diatomite possess a thicker diatomaceous layer relative to the detrital layer.

The second parameter used to describe and classify laminae is thickness (Chang, et al., 1998). Laminae with a thickness of less than 0.2 mm are have been described as razor-striped laminae, whilst pin-striped laminae are those between 0.2-1 mm. Finally, the term chalk-striped laminae is used to describe laminae between 1-1.5 mm. Razor-striped laminae may be discontinuous or continuous, and may be distinct or indistinct (Chang, et al., 1998). Thicker lamina classes, however, are usually distinct and discontinuous.

The majority of laminae within the Hindon Maar 3 core may be classified as relatively continuous, indistinct razor-striped laminae, whilst sediment within the more productive section of the core is occasionally pin-striped, distinct and discontinuous.

Domination is the term used to describe the concentration of diatoms within a laminated interval, relative to the proportion of non-diatomaceous material at that location (Chang, et al., 1998). Sections of the core with a ratio of >1.5:1 mud/detritus/organic carbon:biogenic silica are considered carbon-dominated, whilst diatom-dominated sections of the core have a ratio of >1.5:1 biogenic silica:mud/detritus/organic carbon. Where the two dominant components of the core are relatively equivalent, the couplet is classified as "subequal" (Chang, et al., 1998).

Although the overall concentration of biogenic silica is comparable to the concentration of organic carbon and schist within the core, individual laminae are generally classified as mud-dominated, due to the reduced thickness of the diatomaceous portion of the couplet.

The Hindon Maar 3 deposit has approximately 5-10 laminae/cm across the length of the core, and can be described as closely-moderately spaced on the basis of this, with wider spacing occurring in the more productive sections of the core.

The final criterion used in the classification of diatomaceous sediment is cyclicity. Cyclicity refers to the tendency of diatom laminations to form couplets, packets or bundles (Chang, et al., 1998). A couplet is a single individual pairing of a carbonaceous lamination and an associated diatomaceous lamination, whilst the term packet is used to identify a sequence of uninterrupted couplets which occurs over a scale of several centimetres, possibly representing decades of deposition (Chang, et al., 1998). Bundles are a suite of packets which alternate with periods extended periods of non-diatomaceous sedimentation. With the exception of occasional turbidite deposits during the early stages of the lake's formation, bundles

cannot be identified within this core. However, the Hindon Maar 3 deposit is comprised of multiple packets, each made up of a series of laminated couplets.

Table 4.1. Classification system used to describe diatomaceous deposits (from Chang et al. 1998).

Category	Descriptor	Specifications
Thickness	razor-striped	<0.2 mm
	pin-striped	0.2–1.0 mm
	chalk-striped	1.0–1.5 mm
Spacing	closely spaced	<10 laminae/cm
	moderately spaced	5–10 laminae/cm
	widely spaced	<5 laminae/cm
Bimodality	high bimodality	large contrast in grayscale and bulk density
	moderate bimodality	moderate contrast in grayscale and bulk density
	low bimodality	small contrast in grayscale and bulk density
Domination	mud-dominated	>1.5:1 mud or detritus
	diatom-dominated	>1.5:1 biosilica
	subequal	~1:1
Cyclicity	couplet	single pair of dark and light laminae
	packet	suite of couplets
	bundle	suite of packets alternating with muddy intervals

Carbonaceous laminae are those parts of the core thought to be associated with winter months and parts of the year during which diatoms are not blooming. In the Hindon core, these laminae have a higher concentration of organic carbon and are brown to olive in colour (5Y 2.5/2) to (2.5Y 6/2). Diatoms, amorphous organic carbon, silt-sand sized terrigenous particles and sponge spicules are observable under light microscopy (Figure 3.5). Carbonaceous laminae are usually razor-striped to pin-striped in thickness. In comparison, biosiliceous laminae are white to olive grey in colour (10YR 8/1 to 2.5Y 7/2), and generally possess a slightly greater thickness.

These observations of the nature and style of couplets may be used to identify changes in paleoenvironmental conditions. Lamina thickness, for instance, is a product of diatom flux variability, terrigenous influx (both as a source of detritus and organic carbon), and the occurrence of episodicity of allocyclic events such as

128

rainfall (Chang, et al., 1998). The sediment type which is dominant within this core (carbon-dominated, low thickness couplets with low bimodality) indicates a weak seasonality which limits heterogeneities in the sediment flux.

4.3 *Aulacoseira* and its paleoenvironmental significance

It was possible to identify the dominant diatom present in the Hindon Maar 3 sediment core to species level. It was found that the Hindon Maar 3 deposit was dominated by diatoms of the species *Aulacoseira ambigua*. SEM images of this species (from Tremain et al., 2012) are produced in Figure 4.1. The consistent dominance of *A. ambigua* has implications for paleoenvironmental conditions at this lake during the Mid-Miocene. For example, this species is widely regarded as a meso-eutrophic indicator (Liukkonen et al., 1993, Ollikainen et al. 1993) and has been reported to dominate at sites with local sources of eutrophication, and the species is associated with high phosphorous concentrations. Most *Aulacoseira* species (including *A. distans var. nivalis, A. distans var. nivaloides, and A. distans var. tenella*) have an optimal temperature range of between 10 and 12°C (Weckstrom et al. 1997). Several of these species are also typical of mildly acidic, oligotrophic waters (Leira 2005). Their presence is thus suggestive of relatively cold climatic conditions.

Furthermore, *Aulacoseira* are a heavily silicified genus, and require high levels of turbulence to prevent cells from sinking below the photic zone. Turbulence is also required to maintain the large nutrient supply necessary to support this taxa (Dean et al. 1984; Pilskaln and Johnson 1991; Ruhland et al. 2003). In a 1000 m wide lake with a maximal depth of six metres, wind speeds of 40 km/h are required to ensure unconsolidated sediments remain in suspension (Hakanson and Jansson 1983). It is

believed that, due to the volcanic nature of this landform, the Hindon Maar 3 lake would have been significantly smaller and much deeper than this estimate.

Studies on planktonic diatoms have found that in the Northern Hemisphere *Aulacoseira spp.* are positively inversely correlated with the length of the ice-free season, and positively correlated with the depth of the mixed epilimnion and the duration of the mixing period (Ruhland, 2008). The timing, duration and strength of thermal stratification may also be relevant as is the subsurface habitat development which may develop due to these factors (e.g. Chu et al., 2005, Fahnenstiel & Glime, 1983, Kilham et al., 1996, Lotter & Bigler, 2000, Pannard et al., 2008).

Unlike many diatomaceous taxa, some planktonic *Aulacoseira* species are able continue to blooming under ice cover (Kiss and Genkal, 1993), and this genus is also known to be associated with low levels of dissolved organic and inorganic carbon, as well as calcium. This genus is also generally able to dominate in deep lake sites with low SiO_2 and pH levels. A correlation has also been observed between water transparency and the occurrence of *Aulacoseira*, suggesting that the species is abundant in deep clearwater lakes such as those associated with arctic tundra (Pienitz & Smol, 1993). Finally, *A. ambigua* is has been linked with low salinity values. In a study of 100 diatom species across multiple genera, Cumming and Smol (1993) found that *A. ambigua* had the 93rd lowest optimal salinity (0.1g l^{-1}). However this species does have a relatively high tolerance for variation in lake salinity (Figure 4.2).

It is apparent that the consistent abundance of the *Aulacoseira* genus, and particularly the presence of the species *A. ambigua*, have important paleoenvironmental implications. This genus implies that throughout the deposition of this lake, conditions were likely to be relatively cold and the lake was likely to

be eutrophic and rich in phosphorous. It is also probable that the Hindon Maar 3

lake was comparatively transparent with a significant water depth. The pH within

this lake was likely to be low (4-6), and the lake was probably located in an exposed

position with high wind speeds. The blooming of this species does not indicate that

the lake was not covered by ice at times. In addition, the lake may have been

hyposaline during the accumulation of this material.
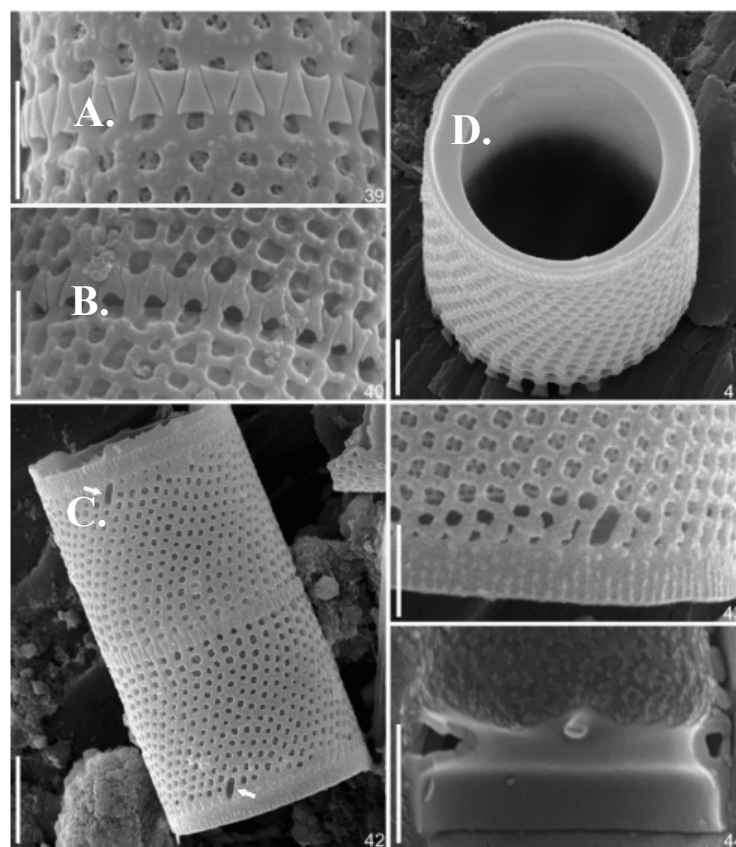
Figure 4.1. Scanning electromicroscope images of Aulacoseira ambigua from (Tremarin et al., 2012). A. Aspect of the ringleist. B. Mantle of the linking valves and location of external rimoportulae opening (arrows). C. Detail of the collum and external rimoportulae opening. D. Internal view of the rimoportulae opening and ringleist. Bars: Figs. 39-41, 43, 44 = 2 μm; Fig. 42 = 5 μm.

(1) *Nitzschia* cf. *perminuta* Lange-Bertalot
(2) *Navicula bulnheimii* Grunow
(3) *Nitzschia liebetruthii* Rabenhorst f.1 B.C.
(4) *Anomoeoneis sphaerophora* (Ehrenberg) Pfitzer f. 2 B.C.
(5) *Amphora* aff. *salina* W. Smith
(6) *Nitzschia frustulum* (Kützing) Grunow
(7) *Nitzschia* cf. *etoshensis* Cholnoky
(8) *Amphora acutiuscula* Kützing
(9) *Anomoeoneis sphaerophora* (Ehrenberg) Pfitzer
(10) *Amphora coffeaeformis* (Agardh) Kützing
(11) *Nitzschia liebetruthii* Rabenhorst f.2 B.C.
(12) *Surirella* cf. *brightwelli* W. Smith
(13) *Cymbella pusilla* Grunow
(14) *Fragilaria pulchella* (Ralfs) Lange-Bertalot
(15) *Anomoeoneis sphaerophora* (Ehrenberg) Pfitzer f. 1 B.C.
(16) *Mastogloia smithii* v. *lacustris* Grunow
(17) *Anomoeoneis sphaerophora* f. *costata* (Kützing) Hustedt
(18) *Navicula* sp. 2 B.C.
(19) *Nitzschia frustulum* (Kützing) Grunow f. 2 B.C.
(20) *Diatoma tenuis* v. *elongatum* (Lyngbye) Agardh
(21) *Amphora* sp. 1 B.C.
(22) *Cyclotella michiganiana* Skvortzow
(23) *Amphora subcapitata* (Kisselev) Hustedt
(24) *Navicula cuspidata* Kützing
(25) *Amphora veneta* Kützing
(26) *Navicula veneta* Kützing
(27) *Nitzschia commutata* Grunow
(28) *Fragilaria fasciculata* (Agardh) Lange-Bertalot
(29) *Navicula libonensis* Schoeman
(30) *Cymbella cymbiformis* Agardh
(31) *Navicula halophila* (Grunow) Cleve f. 1 B.C.
(32) *Cymbella angustata* (W. Smith) Cleve
(33) *Mastogloia smithii* Thwaites
(34) *Cymbella* cf. *aequalis* W. Smith
(35) *Fragilaria* cf. *tenera* (W. Smith) Lange-Bertalot
(36) *Achnanthes minutissima* Kützing
(37) *Nitzschia hungarica* Grunow
(38) *Navicula halophila* (Grunow) Cleve
(39) *Fragilaria nanana* Lange-Bertalot
(40) *Gomphonema parallelistriatum* Lange-Bertalot & Reichardt
(41) *Cymbella* cf. *cistula* (Ehrenberg) Kirchner
(42) *Rhopalodia gibba* (Ehrenberg) O. Müller
(43) *Navicula veneta/cryptocephala*
(44) *Nitzschia amphibia* Grunow
(45) *Nitzschia palea* (Kützing) W. Smith
(46) *Navicula cuspidata* var. *major* Meist.
(47) *Amphipleura pellucida* (Kützing) Kützing
(48) *Fragilaria delicatissima* (W. Smith) Lange-Bertalot
(49) *Cymbella minuta* Hilse
(50) *Nitzschia radicula* Hustedt
(51) *Epithemia adnata* (Kützing) Brébisson

(52) *Denticula kuetzingii* Grun.
(53) *Gomphonema clavatum* Ehrenb.
(54) *Anomoeoneis vitrea* (Grun.) Ross
(55) *Fragilaria ulna* (Nitzsch) Lange-Bertalot
(56) *Navicula oblonga* Kütz.
(57) *Cocconeis placentula* v. *euglypta* Ehrenb.
(58) *Stephanodiscus parvus* Stoermer & Håkansson
(59) *Epithemia turgida* (Ehrenberg) Kütz.
(60) *Cymbella microcephala* Grun.
(61) *Stephanodiscus hantzschii* Grun. f.1 PISCES
(62) *Amphora libyca* Ehrenb.
(63) *Fragilaria famelica* (Kütz.) Lange-Bertalot
(64) *Navicula pupula* Kütz.
(65) *Fragilaria capucina/distans*
(66) *Gomphonema pumilum* (Grun.) Reichardt & Lange-Bertalot
(67) *Cymbella* sp. 1 PISCES
(68) *Cyclotella bodanica* Grun.
(69) *Stephanodiscus hantzschii* Grun.
(70) *Cymbella proxima* Reimer
(71) *Pinnularia microstauron* (Ehrenb.) Cleve
(72) *Navicula cryptotenella* Lange-Bertalot
(73) *Cyclotella meneghiniana* Kütz.
(74) *Stephanodiscus hantzschii* v. *tenuis* (Hust.) Håkansson & Locker
(75) *Nitzschia acicularis* (Kütz.) W. Sm.
(76) *Gomphonema angustatum* Kütz.
(77) *Fragilaria brevistriata* Grun.
(78) *Cocconeis placentula* Ehrenb.
(79) *Gomphonema parvulum* Kütz.
(80) *Fragilaria capucina* v. *mesolepta* (Rabenh.) Rabenh.
(81) *Tabellaria flocculosa* str. IIIp sensu Koppen
(82) *Fragilaria construens* v. *venter* (Ehrenb.) Grun.
(83) *Navicula laevissima* Kütz.
(84) *Fragilaria crotonensis* Kitton
(85) *Navicula cryptocephala* Kütz.
(86) *Navicula diluviana* Krasske
(87) *Asterionella formosa* Hassall
(88) *Stauroneis anceps* f. *gracilis* Rabenh.
(89) *Fragilaria* sp. 1 PISCES
(90) *Stauroneis phoenicenteron* (Nitzsch) Ehrenb.
(91) *Amphora pediculus* (Kütz.) Grun.
(92) *Achnanthes clevei* Grun.
(93) *Aulacoseira ambigua* (Grun.) Simonsen
(94) *Achnanthes ziegleri* Lange-Bertalot
(95) *Fragilaria construens* (Ehrenb.) Grun.
(96) *Nitzschia bacillum* Hust.
(97) *Navicula utermoehlii* Hust.
(98) *Achnanthes conspicua* Mayer
(99) *Fragilaria pinnata* Ehrenb.
(100) *Navicula mutica* Kütz.

(38.5, 4, 1.7)
(29.8, 4, 2.2)
(27.6, 7, 2.3)
(11.0, 13, 7.5)
(10.5, 4, 3.1)
(9.8, 13, 5)
(9.6, 12, 4.7)
(8.9, 13, 6.1)
(8.7, 7, 1.8)
(8.1, 6, 3.4)
(5.6, 27, 7.6)
(5.1, 4, 1.2)
(4.4, 17, 4.8)
(4.1, 8, 4.7)
(3.3, 28, 12.9)

(3.0, 3, 2.5)
(2.4, 29, 12.2)
(2.3, 10, 2.3)
(2.2, 10, 2.2)
(2.1, 4, 2.7)
(2.1, 5, 2.3)
(1.9, 6, 3)
(1.8, 6, 2.7)
(1.7, 21, 5.9)
(1.4, 21, 3.1)
(1.4, 18, 7.4)
(1.3, 5, 4.1)
(1.2, 9, 3.1)
(1.2, 11, 5.1)
(1.1, 11, 7.3)
(1.0, 11, 5.6)
(1.0, 8, 5.9)
(1.0, 4, 1.8)
(1.0, 11, 6.4)
(1.0, 13, 4)
(0.9, 36, 20.2)
(0.9, 3, 2)
(0.9, 27, 9.3)
(0.8, 7, 1.4)
(0.8, 3, 2.2)
(0.8, 11, 8.3)
(0.7, 18, 2.9)
(0.7, 7, 2.5)
(0.7, 16, 2.4)
(0.7, 16, 7.5)
(0.6, 17, 4.4)
(0.6, 5, 3.5)
(0.6, 9, 5)
(0.6, 13, 7.7)
(0.6, 16, 10.5)
(0.5, 8, 5.7)

(0.5, 11, 3.9)
(0.5, 12, 3.7)
(0.4, 11, 6.9)
(0.4, 21, 7.7)
(0.4, 16, 6.3)
(0.4, 9, 3.6)
(0.4, 20, 7.5)
(0.4, 8, 6.3)
(0.3, 14, 7.2)
(0.3, 9, 2.7)
(0.3, 22, 5.9)
(0.3, 6, 3.3)
(0.3, 15, 9.4)
(0.3, 14, 4.4)
(0.3, 11, 6.9)
(0.3, 4, 1.7)
(0.3, 12, 2.5)
(0.3, 19, 5.4)
(0.3, 6, 4.7)
(0.3, 6, 2.4)
(0.3, 17, 6.2)
(0.2, 7, 4.9)
(0.2, 10, 1.7)
(0.2, 5, 1.7)
(0.2, 10, 3.8)
(0.2, 20, 3.5)
(0.2, 8, 5.5)
(0.2, 11, 6)
(0.2, 7, 4)
(0.2, 8, 3.4)
(0.2, 11, 1.4)
(0.2, 7, 3.1)
(0.2, 10, 5.3)
(0.1, 15, 4.6)
(0.1, 5, 3.6)
(0.1, 9, 4.8)
(0.1, 7, 1.3)
(0.1, 12, 4)
(0.1, 6, 4.3)
(0.1, 7, 4.5)
(0.1, 3, 2.6)
(0.1, 5, 1.2)
(0.1, 6, 3.2)
(0.1, 7, 2.4)
(0.1, 4, 3.5)
(0.1, 4, 2.9)
(0.1, 3, 2.3)
(0, 13, 4.3)
(0, 6, 2.1)

Salinity (g l^{-1})

0.1   1   10   100

Figure 4.2 Aulacoseira ambigua, the dominant diatom species in this lake, is associated with low salinity waters (from Cumming, 1993).

132

4.4 FTIR spectroscopy, silica maturation and silica dissolution

FTIR absorption spectra obtained using the Hindon Maar 3 lake sediment in combination with potassium bromide were highly analogous to peaks typically found in other FTIR studies of diatomaceous sediment (e.g. Stephens, 2011). Large peaks were identified at λ 1100 cm^{-1} and 450 cm^{-1}, each of which has been associated with SiO_4 present in the form of diatom frustules in other studies (e.g. Moschen et al, 2006, Figure 4.3).
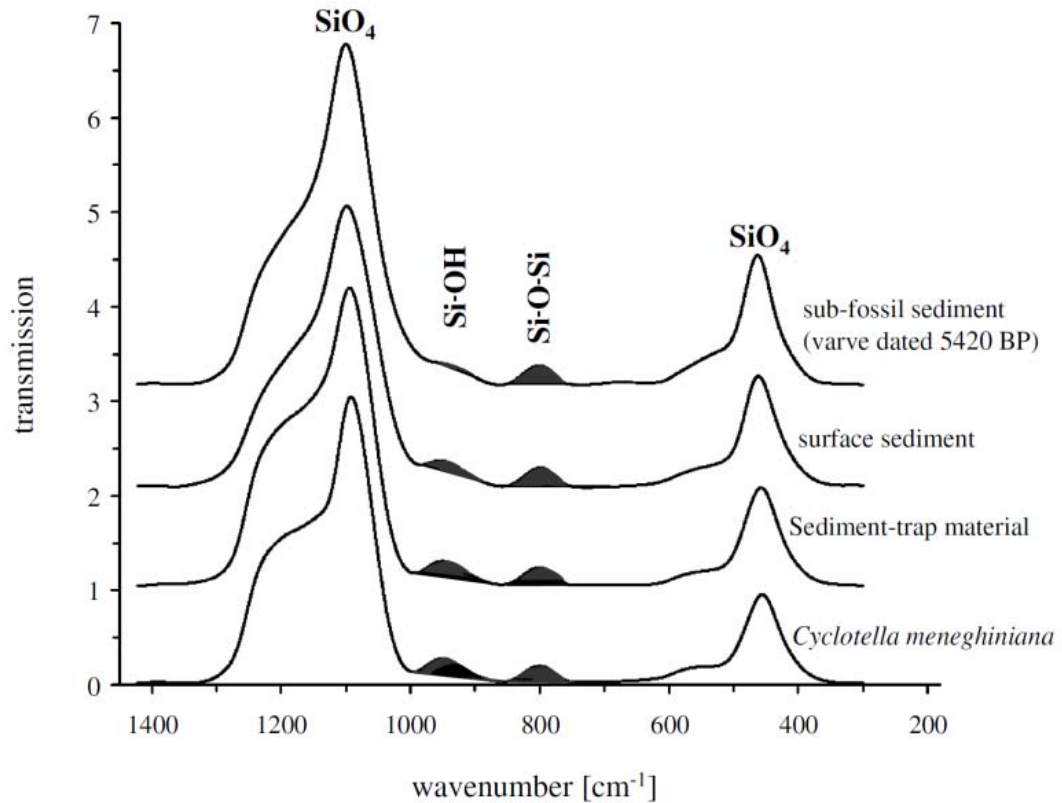
Figure 4.3. IR absorption spectra of 4 diatom samples from laboratory and field (Lake Holzmaar, Germany) cultures demonstrating markedly reduced Si-OH groups (945 cm^{-1}) in sub-fossil and surficial sediments vs. living and 7m (epilimnion) sediment trap material (Source: Moschen et al, 2006: 4376).

Using the method followed in order to collect FTIR data, it was possible to maintain a consistent approach in order to prevent the introduction of unnecessary laboratory error. For this reason, FTIR based estimates of organic carbon, schist and diatom concentrations are considered internally consistent. Despite this, the extremely small quantity of sample used in these measurements could have acted as a source of error.

Investigations into silica maturation have indicated that as diatomite matures, silica is lost despite the anaerobic nature of maar lake deposits. Studies comparing fresh diatoms with fossilized samples indicate that between 3 and 10% of silica may be lost during maturation. Furthermore, this change is not due to dissolution, as open-system cultivation experiments indicate that both living and senescent diatoms are isotopically homogenous (Schmidt et al, 2001). Schmidt et al. (2001) concluded that the loss of silica in fossilized diatoms is likely due to slow internal condensation reactions resulting in a loss of hydroxyl silica (Si-OH), following the reaction:

$$Si\text{-}^{18}OH + H^{16}O\text{-}Si \rightarrow Si\text{-}^{18}O\text{-}Si + H_2^{16}O$$
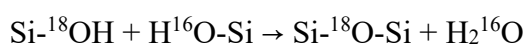
(Proposed condensation reaction in diatom silica [Source: Schmidt et al, 2001: 207])

Infra-Red spectroscopic analyses by Moschen et al (2006) indicated that the IR-absorption bands associated with Si-OH (945 cm^{-1}) were markedly reduced in fossilized diatoms in comparison to freshly harvested diatoms (*Cyclotella meneghiniana*), whilst the absorption and attributed to Si-O-Si (800 cm^{-1}) was unchanged in both samples. It has therefore been suggested that Si-OH is lost during early diagenesis (Figure 4.3). This effect is unlikely to have affected the accuracy of results obtained in this research, but has strong implications for any future studies

of the Hindon Maar diatomite, which may seek to investigate oxygen isotope ratios to obtain paleoclimate data.

4.4.1 Dissolution and reprecipitation

It must also be considered that biogenic silica may have been dissolved within the lake system. Many lacustrine systems are under-saturated with Si, leading to the dissolution of silicate compounds. This effect is particularly notable in high pH systems (Swann and Leng, 2009). BSi dissolution may occur at almost any depth within the lake, including within the sedimentary Si-asymptotic concentration zone (<30 cm beneath the sediment-water interface) (Swann and Leng, 2009). Dissolution may thus occur during the transport of diatom silica to the sediment, or within the deposited material itself. A large amount of dissolved diatom silica is recycled into the water column, and material which is not recycled then accumulates as the final lake deposit (Leng and Barker, 2007). Dissolution is an important mechanism in altering diatom assemblages, and apparent species richness. Conditions that encourage dissolution are likely to cause the preferential accumulation of densely silicified diatom species. The dissolution rate of sediment is controlled by several variables including temperature, sedimentation rate, trace metal presence, detritivory, alkalinity, silicification and detrital mineral abundance (Swann and Leng, 2009). It is necessary to be aware that these processes may have occurred, and to note their potential impact on findings based on biogenic silica.

4.5 Magnetic susceptibility variability during lacustrine sedimentation

Magnetic susceptibility variations towards the base of the core may be associated with mass flow events before or during the normal accumulation of lake sediment, with some primary volcanic products contributing to high magnetic susceptibility values at the greatest depths reached. These extreme values ($50\text{-}87$ SI x 10^{-5}) are due to an increase in the concentration of ferrimagnetic minerals and terrigenous sediment derived from the crater walls.

Within the lake sediment however, magnetic susceptibility remains somewhat variable, but the input of ferrimagnetic minerals is extremely low throughout. Despite this, a relationship is likely to exist between erosional processes and the concentration of magnetic minerals. Diamagnetic biogenic components (e.g. biogenic silica or organic matter) significantly dilute ferrimagnetic terrigenous components in the lake sediment, as evidenced by the weak negative correlation between biogenic silica and magnetic susceptibility (Table 3.1). Magnetic mineralogy may also have an impact on magnetic susceptibility (e.g. Snowball et al., 1999). For instance, magnetite in sediments is likely to correspond to relatively high magnetic susceptibility values, whilst intermediate MS lake sediment may contain high-coercivity hematite or goethite as well (Oldfield et al. 1983). The majority of variation in magnetic susceptibility is most likely to be related to changes in terrigenous input, possibly due to variation in wind speed and erosion rates.

In addition, the low-temperature oxidation of magnetite into Fe(III)-(oxyhydr)oxides can result in a decrease in magnetic susceptibility, and soil formation in an oxic depositional environment accompanied by the dissolution of Fe(III)-oxides could potentially explain some of the low magnetic susceptibility values (particularly within the first metre of the core) (Williamson et al., 1998).

Under particularly acidic (pH 4-6) and eutrophic conditions, iron reduction can occur in anoxic conditions (Williams, 1990). Such a reaction would remove most of the ferrimagnetic iron oxides such as goethite, hematite and magnetite from the sediment, producing low magnetic susceptibility values (Williamson et al., 1998). Because *Aulacoseira ambigua* is associated with acidic conditions, the observation of this species within the sediment suggests that potentially iron-reducing conditions were likely to have occurred in the lake. Acidic iron-reducing conditions could be responsible for sections where low-magnetic susceptibility values correlate with diatom-poor carbonaceous sediment (Williamson et al., 1998).

Based on these considerations, several environmental end-members may have occurred during the deposition of this sediment:

(1) During normal accumulation, detrital iron oxides were diluted by diamagnetic organic matter resulting in intermediate magnetic susceptibility values.

(2) In anoxic, acidic, eutrophic conditions, ferrimagentic iron oxides including goethite and hematite are likely to have been dissolved resulting in abnormally low MS values. Low magnetic susceptibility may thus be a proxy for low pH conditions.

(3) Remaining variation may be primarily due to changes in erosion rates, potentially associated with variation in wind speeds.

These hypothesized relationships are speculative without further magnetic data including anhysteretic and isothermal remanent magnetizations. Such information would allow the calculation of S-ratios, enabling high-coercivity hematite to be distinguished from low-coercivity magnetite. Further information is therefore required before assumptions about the origin of magnetic signatures can be verified.

4.6 Organic matter source

The limited data available regarding the source of organic matter within the core means that organic carbon concentrations are of limited value in interpreting paleo-environmental signals. It is currently unclear whether the source of organic matter varies through time, and the degree to which autochthonous and terrestrial plants contribute to total organic carbon is not known.

Future work could consider the source of organic material (whether derived from lacustrine algae or land plants) in greater depth, potentially through the use of downcore C/N ratios (Hopmans et al., 2004). It is likely that organic carbon was derived from a mixture of terrestrial and lacustrine sources, as evidenced by the rare occurrence of fossil leaves between laminae.

In order to consider whether observed changes in organic carbon concentrations are primarily the result of ongoing variation in diatom productivity, and to provide insight into the likely source of organic carbon, standard deviation centered organic carbon concentration values were plotted against normalised schist concentration estimates (Figure 4.4). At sections of the core where schist concentration and organic carbon decrease together, for example, the decrease in both of these products could be associated with an increase in the rate of diatom production, whilst both the rate of erosion and organic carbon accumulation remain relatively

constant. Sections where the two variables move together are common, and both generally follow similar trends. Parts of the core where schist and organic carbon concentrations increase or decrease together are denoted by black bars in Figure 4.4, whilst grey bars indicate sites where the two variables change independently.

Whilst schist concentration is considered to be a proxy for erosion, schist is likely to be a relatively minor component of the terrigenous material entering the lake due to erosion. It is likely that organic material could also be introduced to the lake in this manner. Thus correlations between organic carbon and schist (Figure 4.4) could indicate periods of increased erosion, when both terrestrial plant matter and terrigenous sediment were supplied to the core in greater quantities.

Whether the correlations between organic carbon and schist are caused by increases in diatom productivity or terrestrial overprinting can be examined by considering the relative concentrations of biogenic silica and schist at points represented by black bars in Figure 4.4. The most prominent and prolonged periods of correlation between organic carbon and schist (between 5.18 and 7.62 m, and between 8.14 and 10.82 m) occur during periods of reduced organic carbon and when concentrations of biogenic silica are extremely high. It is not possible to make inferences regarding the source and rates of organic carbon and schist accumulation during these times, except to say that these periods were dominated by diatom production leading to a lower proportion of organic carbon and schist overall.

In other, uncommon parts of the record, peak TOC values occur when schist is low, suggesting periods of low erosion and low diatom productivity or high organic carbon productivity. Organic carbon and schist are less likely to be correlated within the first five meters of the core, and between 7.7 and 8.15 meters depth. These two periods during which organic carbon and schist are independent occur for different

reasons. Between 7.7-8.15 meters, this observation reflects low diatom productivity and reduced erosion within the catchment. However in the first 5 meters, this occurs due to high diatom productivity, a reduced relative contribution from organic carbon, and high erosion rates in the catchment.

While the relationship between organic carbon and schist offers some insight into the development and paleoenvironmental conditions associated with Hindon Maar 3, these interpretations should be treated with caution because the organic carbon source cannot easily be verified without known C/N ratios. Due to the difficulty associated with determining the source of organic carbon, biogenic silica offers a much more reliable dataset for use in the consideration of paleoenvironmental conditions.
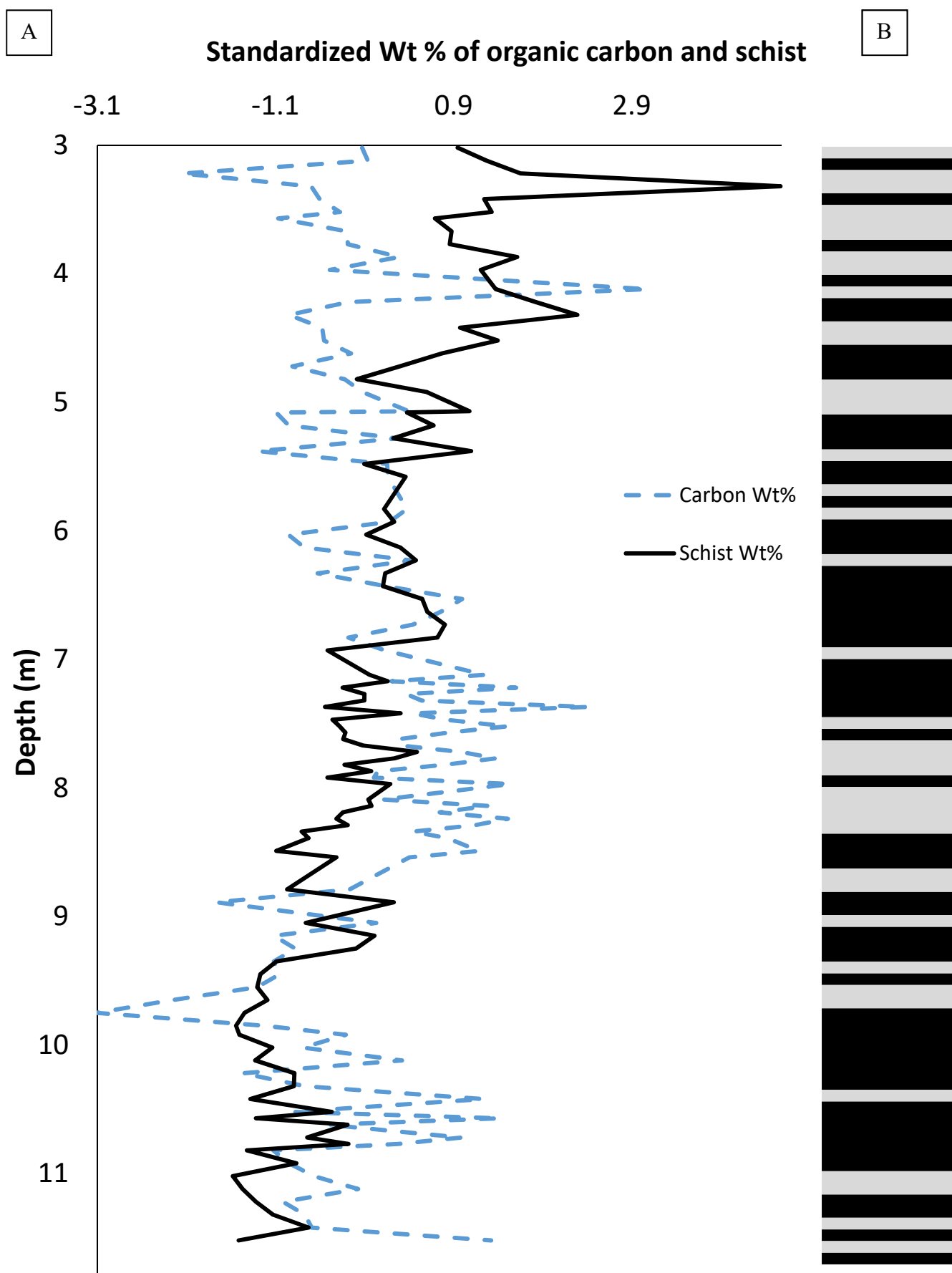
Figure 4.4. A. Normalised values of organic carbon and schist, as determined using FTIR spectroscopy and normalised using the standard deviation of each dataset. B. Figure indicates covariance between the two variables, where correlated sections of the core are denoted by black bars, and sections of the core where organic carbon and schist concentrations change independently are indicated by grey bars.

4.7 Biogenic Silica

Sedimentary BSi (diatom, chrysophyte and sponge spicule concentration) is controlled primarily by four factors: clastic sedimentation rate, aquatic production, post-depositional preservation of siliceous organisms and organic matter sedimentation (McKay et al., 2007). FTIR spectroscopy has been used to estimate the clastic sedimentation rate (0.5-5% of sediment deposited each year is inferred to be clastic in origin, Section 3.3), and post-depositional preservation of siliceous organisms within the Hindon Maar complex is considered to be exceptional due to the anaerobic conditions present within the lower portions of the lake.

As the clastic sedimentation rate and preservation potential within the lake thus have a limited influence on BSi concentrations, aquatic production may be the dominant factor recorded by the FTIR spectroscopy method. Aquatic production is a factor of water temperature, light and nutrient availability (Wetzel, 2001). Lacustrine diatom concentrations are likely to respond to high summer temperatures, as high temperatures will promote favourable growing conditions, and will reduce the amount any of seasonal ice cover (Wetzel, 2001). BSi may also be primarily controlled by wind speed, considering that the *Aulacoseira* genus favours cold water and turbulent waters (Wetzel, 2001). The combination of these effects will therefore result in a higher BSi concentration in the sediment.

BSi analysis is prone to several limitations, and it has been recognized that significant changes in lake chemistry can cause diatoms to become dissolved at the interface between sediment and water, thus lowering diatom concentrations (Swann et al., 2006). Furthermore, FTIR spectroscopy-based BSi studies are commonly inconsistent because they may not integrate the same spectral peak areas when

producing calibration models for specific lakes. As a result of this, the results from FTIR spectroscopy studies are internally consistent within the lake, but comparisons across separate lakes may be ineffective.

Finally, terrestrial dilution has an influence on the relative concentration of BSi and organic carbon. This has been accounted for by calibrating the model to calculate terrigenous sediment using a grey-schist sample as a likely analogue for non-biogenic silica (Figure 3.9). Whilst this approach has identified the influence of some terrigenous sediments on biogenic silica and organic carbon ratios, it does not reflect the concentration of minerals not associated with the schist country rock. While individual values of biogenic silica, terrigenous material and organic carbon are variable and prone to error, the analysis of broad-scale trends within each of these variables aids in reducing the uncertainty associated with laboratory error and terrigenous dilution. As the following discussion on Miocene climate variability during the infilling of the Hindon Maar lake deposit is based primarily on variation in biogenic silica concentrations, it is necessary to keep these considerations in mind.

4.8 Anomalous core features

In addition to detailing the potential origins of material and the general features of the core (as in the preceding sections), it is valuable to consider any anomalous physical or compositional core features. The following section seeks to identify and explain unusual values of biogenic silica, magnetic susceptibility, density and particle size in terms of paleoenvironmental variation.

4.8.1 Biogenic silica anomaly

Biogenic silica concentrations (as determined using FTIR spectroscopy) are relatively stable across the length of the core with the exception of a significant and prolonged increase in BSi concentration between 9.25 and 10.22 m (Figure 4.5). This increase in biogenic silica most likely reflects a period of increased productivity, though several environmental processes could potentially be linked to this variability in productivity. As mentioned in Section 4.7, light, nutrient availability and temperature have been known to control productivity (Wetzel, 2001). It is therefore important to consider which process is most likely to influence productivity in the Hindon Maar system.
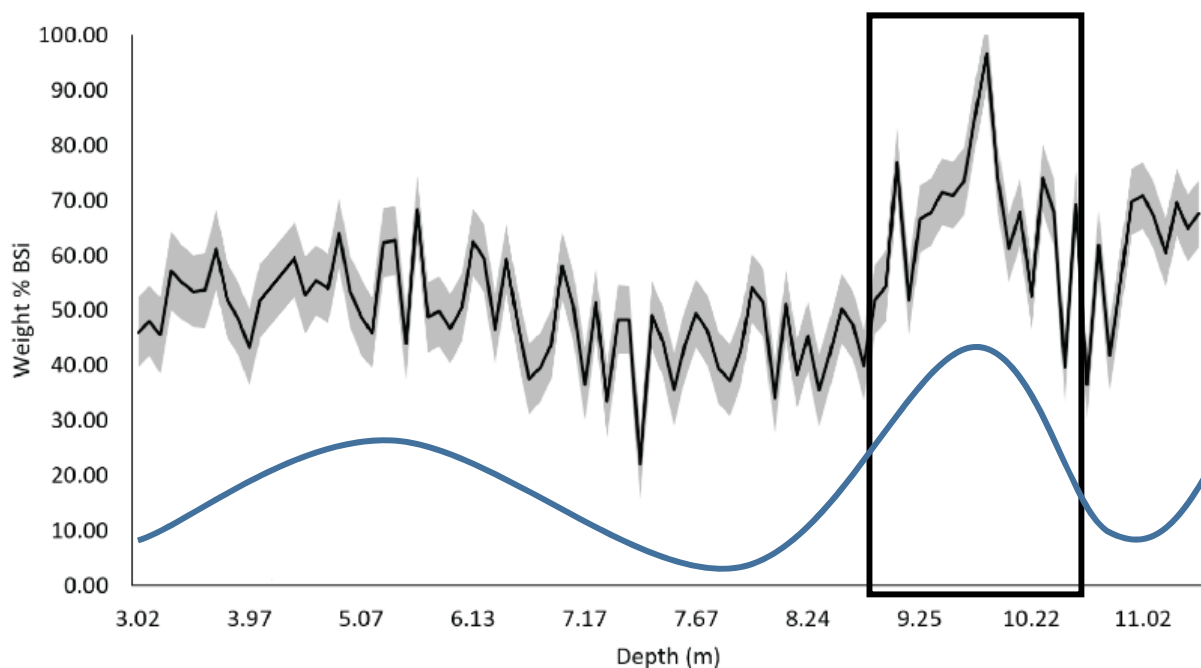
Figure 4.5. An unusually high concentration of biogenic silica is located at a depth between 9.25 and 10.4 metres. This variation may be due to changes in the wind speed or temperature.

Wind speed is one climatic variable likely to exert a strong influence over the paleoproductivity of this lake, and changes over sub-Milankovich time scales could have produced the BSi anomaly seen here, and a number of hypotheses have been suggested to explain that relationship. The influence of wind speed on diatom productivity is likely to be exacerbated in a small, deep lake such as Hindon Maar 3 where mixing depths and material suspension are easily altered. Wind speed changes can produce large increases in phytoplankton production, often due to pulses of nutrients being released into the overlying waters by resuspension (Carrick et al., 1993). Wind resuspension has been associated with higher levels of nutrients and turbidity (Maceina and Soballe, 1990). Two obvious benefits of high wind conditions for diatoms are that they cause destratification of the water column,

mixing diatoms from lower levels of the lake into the photic zone to seed new growth (Lewis 1978), and also that they enable dense, highly silicified diatoms (such as members of the *Aulacoseira* genus) to float within the water column due to turbidity. Diatoms, due to their need for turbulence to keep them entrained, grow during isothermal, mixed water periods and start to sink during warm, cold periods (Fuchs et al., 2016). Strong wind conditions cause the break-down of lake-thermal stratification, causing nutrient conditions to increase, whilst weak winds cause lakes to stratify, depleting P, N and Si in the epilimnion (Wang et al., 2008). Langmuir cells also begin to develop after a threshold of approximately 3 ms^{-1}, influencing the vertical distribuition of diatoms (Reynolds, 2006). However, the increased turbidity associated with windiness may also decrease light availability (Hellstrom, 1999).

The Southern Westerly Wind Belt (SWW) is the dominant wind belt affecting New Zealand (Romero et al., 2015), and it is very likely that changes in the latitude or intensity of this belt could change productivity on a centennial time scale. The SWW is known to shift equatorward and poleward in accordance with the extent of Antarctic ice and glacial-interglacial cyclicity (e.g. Flores et al., 1999; Rau et al., 2002; Peeters et al., 2004; Bard and Rickaby, 2009). Intense SWW caused by high ocean temperatures also cause precipitation to increase. Based on this, Reichgelt (2017) suggested that the SWW was at a higher latitude (47–48°S) for most of the mid/late Miocene than it is presently (~44–47°S), increasing drought potential and reducing moisture supply. Browne et al. (2017) showed that the strength and latitude of SWWs exhibited high variability on centennial and millennial-scales throughout the Late Holocene. Despite the generally warmer temperatures of the

Mid/Late Miocene, it is likely that similar changes on these timescales were ongoing during that epoch (Reichgelt, 2017).

Temperature may also have an influence on diatom productivity, and the sensitivity of biogenic silica to warming temperatures is widely recognized. However, several features of the core suggest that temperature may not be the primary factor controlling biogenic silica productivity. Irrespective of accumulation rates, this core is persistently dominated by *Aulacoseira ambigua*, which is limited to a relatively small temperature range. In the event that this temperature range was regularly exceeded, other diatomaceous taxa would be expected to replace this diatom (Wang et al., 2008). Furthermore, warmer temperatures are likely to increase thermal stratification, preventing the upwelling of nutrients into the photic zone (Michaud, 1991). Because of this, it is not clear that diatoms bloomed during warm months in mid-late Miocene New Zealand, and blooms may instead be associated with high nutrient, windy periods during winter, when the lake was isothermal, lacking a well-defined hypolimnion. While other proxies have been identified as representative of temperature (Section 4.10), it is less likely that biogenic silica is directly linked to warm conditions, and wind speed is probably the variable which has resulted in the formation of the centennial scale biogenic silica anomaly (Figure 4.6).

4.8.2 Particle size anomaly

One sample within the grain-size dataset was found to have an exceptionally high median particle size, suggesting the majority of particles at this point are much larger than those noted elsewhere in the lake sediment, which are otherwise relatively consistent (Figure 4.6). This anomaly is not associated with a substantive increase in sand sized particles, as the quantity of sand sized particles had already increased to ~10 to ~30 % of the core several decimetres above this point (Figure 4.8). The particle size anomaly is associated with a drop in silt-sized particles however (Figure 4.7), suggesting that diatoms former a significantly smaller portion of the material at this point. Thus, this point may not reflect a turbidite or other event, and instead is more likely to relate to a decline in biogenic silica which occurs at the same depth (Figure 4.6). Several decades of extremely low productivity could therefore account for this anomaly.

Median particle size (um)

Diatom concentration %
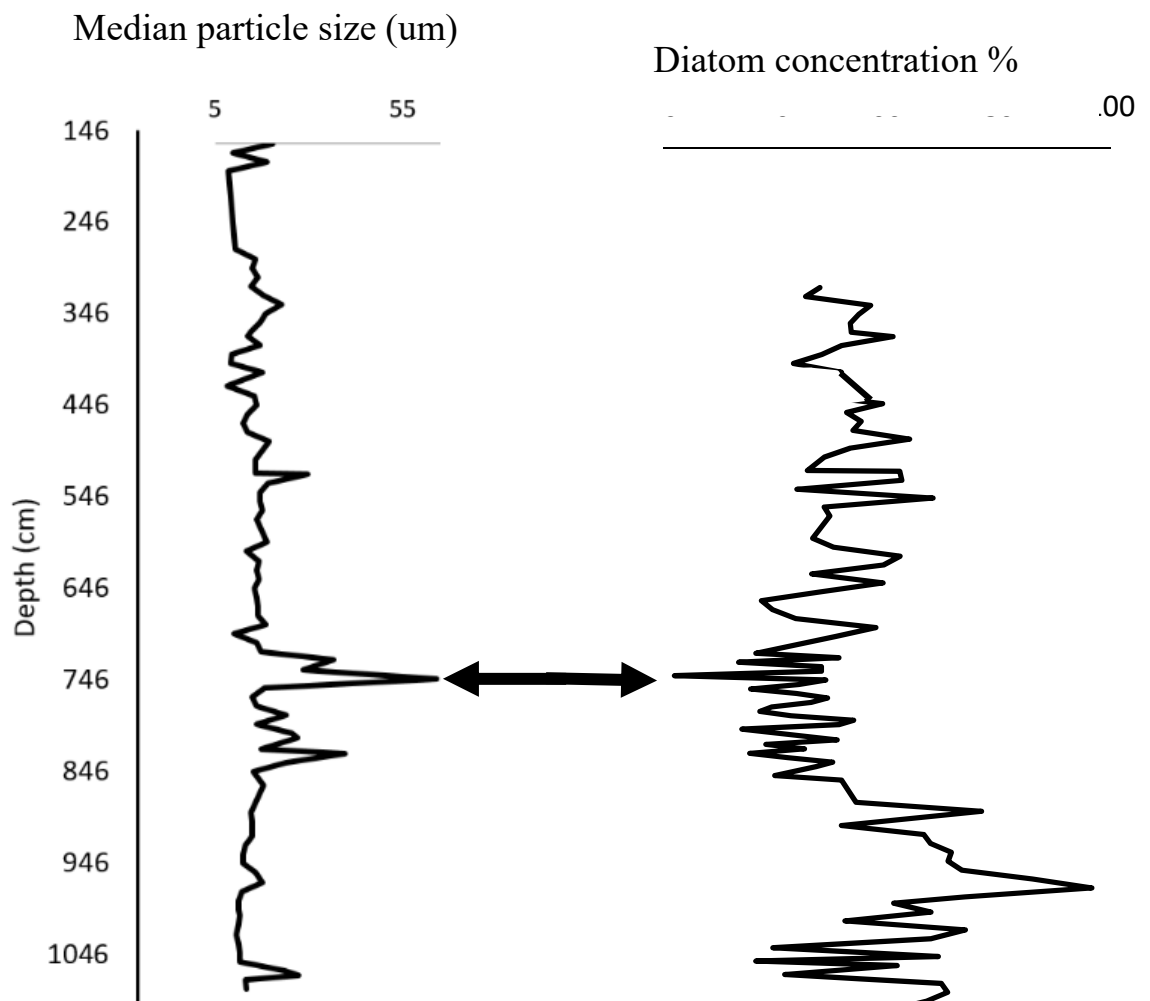
Figure 4.6. The median particle size anomaly is located at a depth of 7.46 m and is indicated by an arrow in this figure. This increase is correlated with a substantial decline in biogenic silica
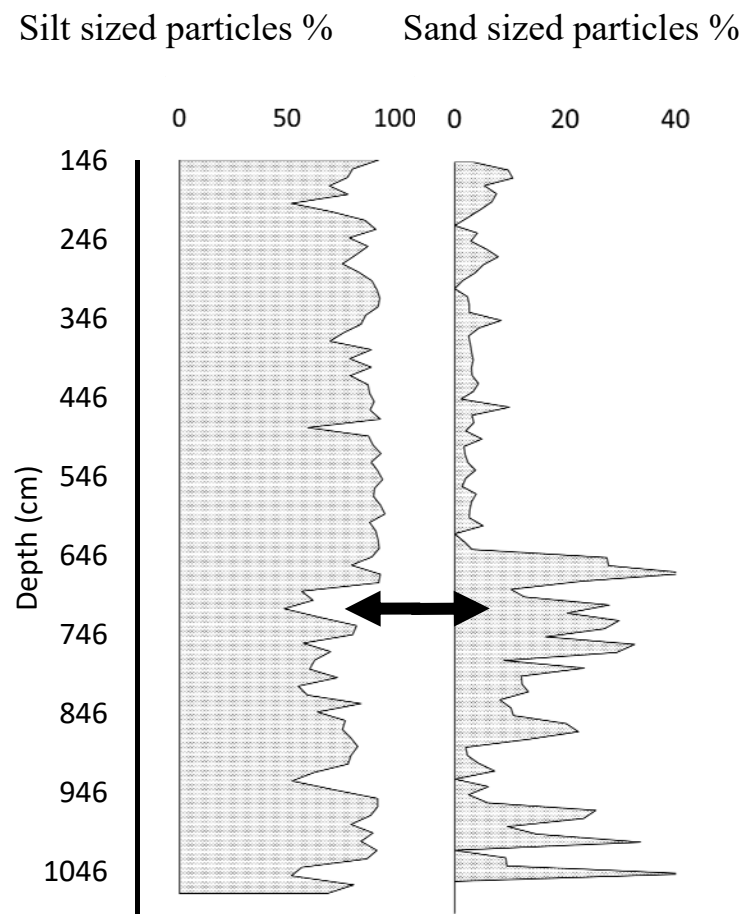
Figure 4.7. The particle size anomaly coincides with a decrease in the proportion of silt sized particles, but not with an abnormal increase in sand sized particles.

4.8.3 Magnetic susceptibility anomaly

An anomaly is present in the lower section (11.5-14 m) of the lake sediment facies, above the onset of brecciated volcaniclastic material (Figure 4.8). A high concentration of ferromagnetic and ferrimagnetic minerals is expected to be present within the brecciated section of the core, however the occurrence of unusually high MS minerals within lake sediment which is otherwise unremarkable is of interest.
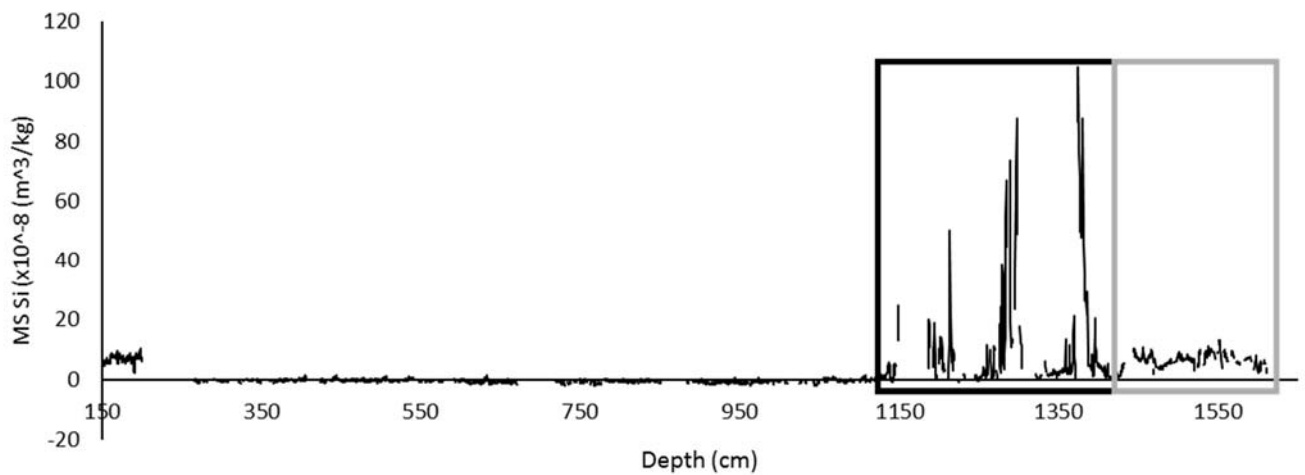
Figure 4.8. Sediment magnetic susceptibility increases significantly towards the base of the lake sediment facies. This material is comprised predominantly of biogenic silica and organic carbon, with a minor contribution from schistose and basaltic terrigenous sediment. The black box represents a sequence of at least three turbidite deposits, whilst the grey box reflects the moderate magnetic susceptibility values associated with the brecciated volcaniclastic and schistose facies.

Layers with high magnetic susceptibility values are occasionally linked with turbidites and other mass movement events (Wet, 2013). Such events can be identified by considering three primary criteria. First, mass movement events are associated with high magnetic susceptibility values. Furthermore, these sections are likely to exhibit high Ti counts. Finally, core sections associated with turbidites are

likely to show a visually identifiable fining upwards sequence which is non-laminated. Photographs and visual observation of the core (Figure 4.9) do not demonstrate an obvious decrease in particle size upwards, however organic carbon and biogenic silica are clearly well mixed when observed in thin section, lacking the clearly laminated style noted in other petrographic images. In thin section, the base of the turbidite does appear to have an increased concentration of dense, large terrigenous particles in comparison to the upper section of the turbidite.

Possible poorly-defined normal sorting across this interval.

Well mixed biogenic silica and organic carbon, no evidence of planar

Opaque grains likely to be iron-bearing minerals.

Sand-sized schistose minerals concentrated towards the base of the section.
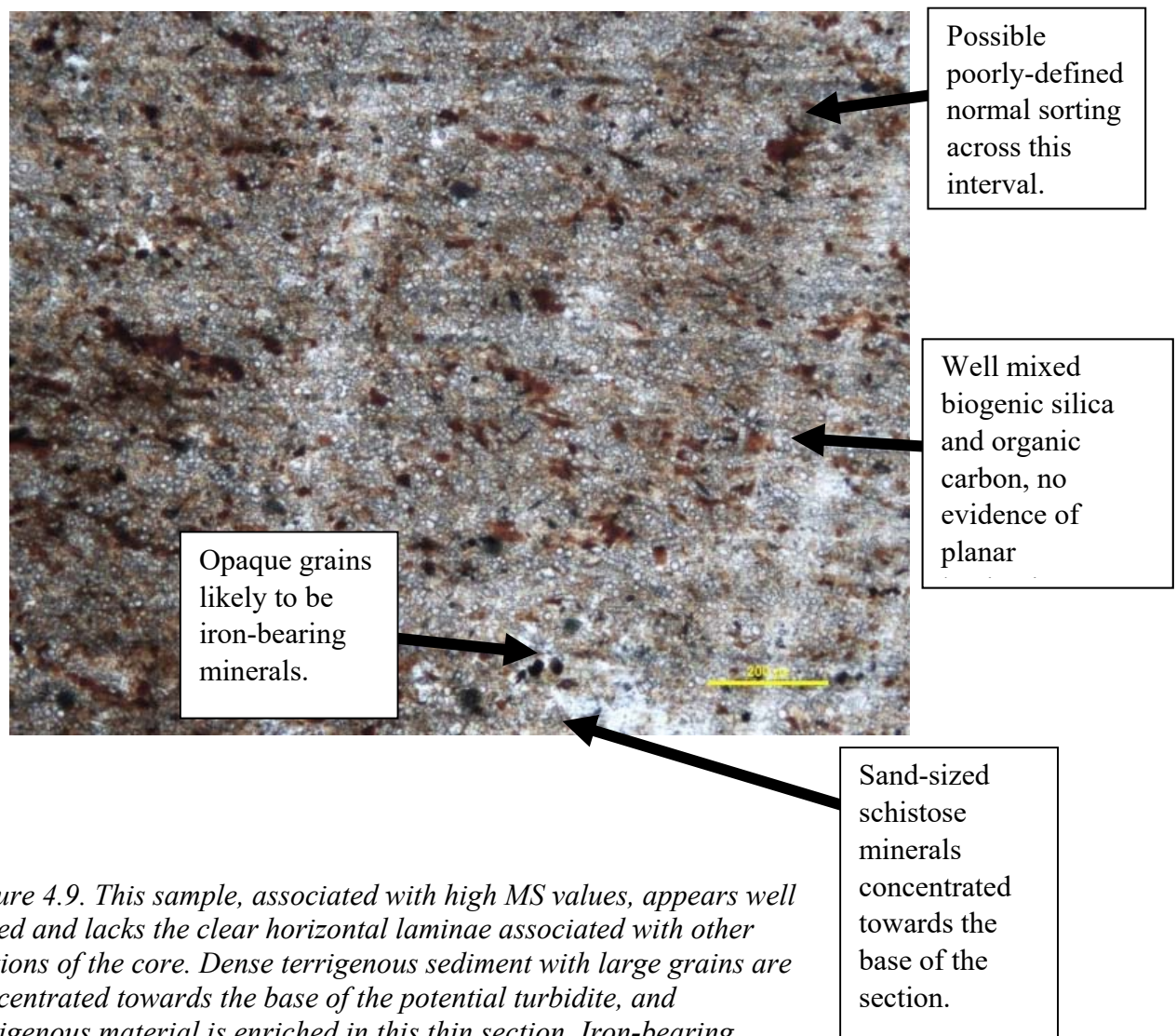
Figure 4.9. This sample, associated with high MS values, appears well mixed and lacks the clear horizontal laminae associated with other sections of the core. Dense terrigenous sediment with large grains are concentrated towards the base of the potential turbidite, and terrigenous material is enriched in this thin section. Iron-bearing minerals are also identified which may be the source of high MS values in this sediment.

The length of this anomalous section (<1m) is consistent with that of turbidites and other instantaneous slump events from similar maar-lake settings (DeWet, 2013). This section possesses a similar composition to sections of the core which are considered characteristic of normal lacustrine sedimentation, but also contains a more significant detrital component, with sand-sized particles considered to be schistose in nature (Figure 4.10). The source of this detrital component is considered to be the surrounding schist country rock, and this section may also be enriched in the products of the eruption which originally formed the maar. An increased quantity of iron-rich minerals is believed to be the source of heightened magnetic susceptibility values at this point in the core, and these minerals may have been deposited due to a mass-flow of basalt-rich material from the side of the crater shortly after the eruption (Figure 4.10).
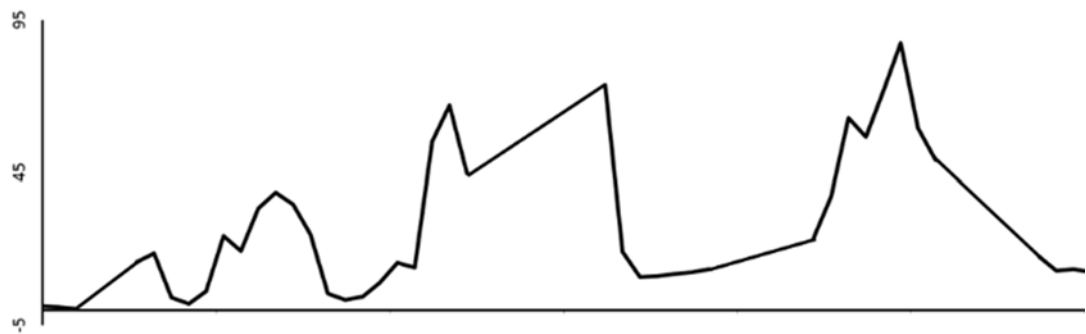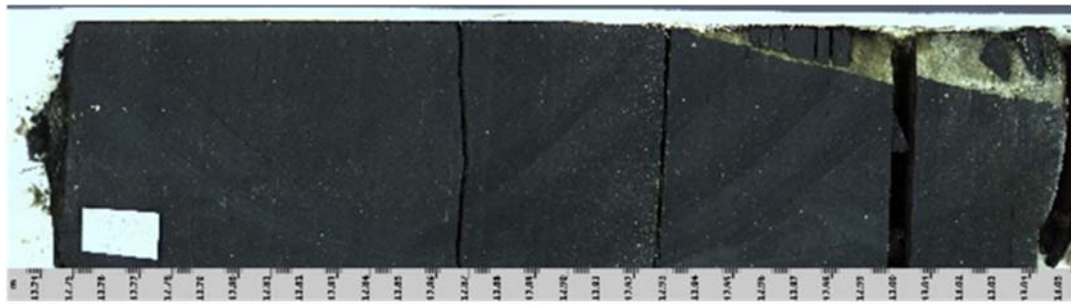
Figure 4.10. Colour photograph and magnetic susceptibility values from Hindon Maar 3 turbidite 1 (12.71-13.05m. This section of the core is visually and compositionally similar to characteristic lake sediment material. However the high magnetic susceptibility and normally-graded particles indicate that this section may be a turbidite.

A second high magnetic susceptibility section is observed shortly below the first likely turbidite (approximately 13.6 m to 13.88 m). This section is visually dissimilar to the previous turbidite and to the remainder of the lake sediment facies. This section appears to represent several small mass flows interbedded with laminated lake sediment. Compositionally, this interval generally appears to be dominated by diatomaceous material and organic carbon. However, portions of the turbidite with the greatest magnetic susceptibility values are represented by a light-grey medium sand, which may be derived primarily from schist. Since turbidites are generally normally graded, it is likely that this sand deposit marks the base of a mass flow. Several decimeters of material beneath this sand deposit also have a

high magnetic susceptibility, and are therefore likely to represent another mass flow. The interval beneath this sand deposit is rich in diatomite and organic carbon, but also contains ash and schist-derived particles (Figure 4.11). Deformation of the diatomite is clear within the lower part of this interval (Figure 4.11).
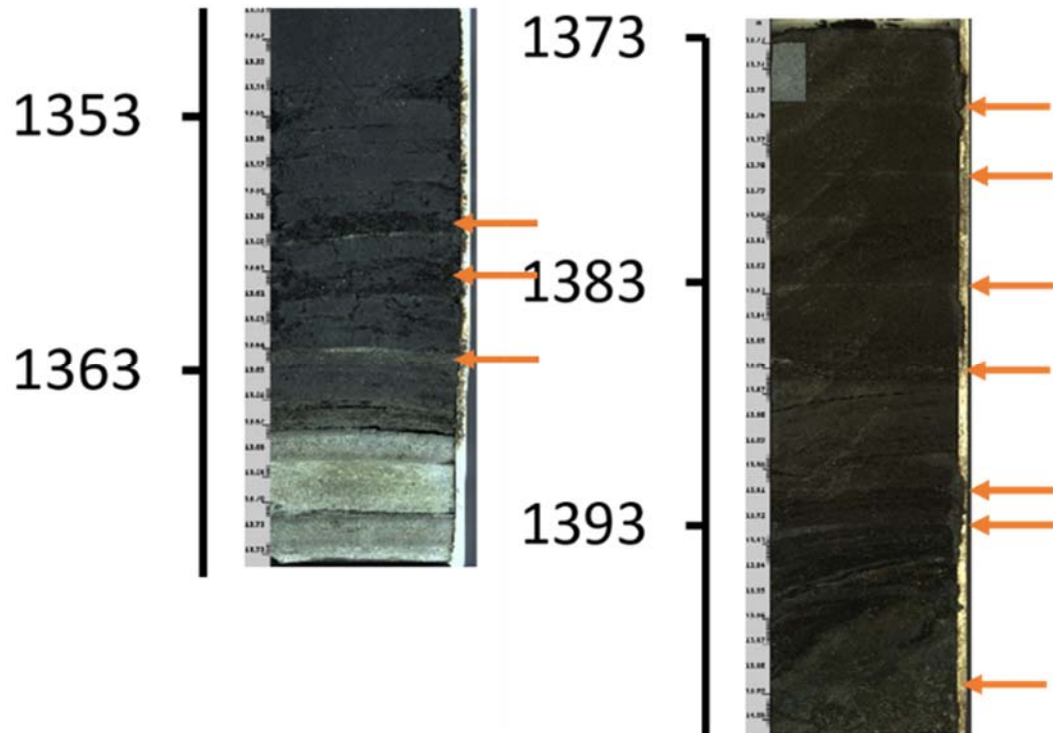
Figure 4.11. Colour photograph of Hindon maar 3 turbidites (positions indicated by arrows). Although predominantly diatomaceous, these sections of the core exhibit high magnetic susceptibility values and normally-graded particles which may indicate that these sections are turbidites.

The likely turbidites observed at the base of the core have a number of relevant paleoenvironmental implications. It suggested that the material from 11.49 m to 14.2 m represents a succession of at least multiple mass flow deposits, between which several periods of normal lacustrine sedimentation took place. The increased occurrence of mass flow and turbidite events during this period may be related in part to high erosion rates assumed at the tephra ring (which is likely to have had steep, unstable walls), encouraging the rapid movement of material from the tephra ring to the lake floor (e.g. Fox et al., 2015). This implies that for several hundred years after the initial phreatomagmatic eruption which formed the eventual lake system, the sides of the maar were gradually stabilized by mass flow deposits. The frequency of these mass flows decreased over time due to a decrease in the maar ring slope angle, and due to the gradual recolonisation by vegetation across the maar sides (e.g. Fox et al., 2015). Turbidites eventually failed to generate enough energy to reach the sampling location for the entire duration of the deposition of the remainder of the core, suggesting that maar sides became significantly more stable.

It is noteworthy that the sediment associated with the lithologically diverse breccia of juvenile pyroclasts and wallrock fragments (Figure 3.13., grey box) exhibits generally lower magnetic susceptibility values than do the turbidite sequence. This low-MS brecciated section appears to be dominated by schist country rock, and the observation of low MS values at this point is of interest.

4.9 Correlation Matrices

The Pearson correlation matrix produced using all the quantified physical properties of the core revealed several noteworthy relationships which should be considered (Table 3.1). Many of the correlations between raw GEOTEK MSCL variables were statistically significant (Table 3.1), but the strength of these correlations is also an important consideration.

It was noted using correlation analysis that biogenic silica shows a moderate inverse relationship with the normalised percentage of schist at a given point in the core (-0.503, Table 3.1). However, the organic carbon concentration is not negatively correlated with the concentration of terrigenous sediment and do not have a strong relationship with this schist concentration. This suggests that both the terrigenous sediment and organic carbon input may potentially be relatively constant through time and are both negatively correlated with lake productivity, and that the schist and organic carbon may vary randomly with respect to each other. In warmer, highly productive years when biogenic silica accumulation rates are highest, the relatively minor but likely consistent terrigenous sediment contribution is outpaced by diatom production. In low-productivity years, however, terrigenous sediment and organic carbon both appear to make a larger proportion of the total deposit composition, due to lower lake sediment accumulation rates overall. In other words, the significant changes in BSi accumulation rates may override the generally minor changes in schist and organic carbon.

The relationship between BSi and particle size classes is of interest. The correlation matrix indicates that BSi has a weak positive correlation with Dx10 (.181), as well as a weak inverse relationship with Dx50 and Dx90 (-.186 and -.13, respectively).

This suggests that productive periods in the lake's history yield more homogenous, well-sorted particle assemblages with consistent size profiles and little variance. During highly productive periods, particles are slightly finer on average than those which accumulate during less productive periods. As the samples used in particle size analysis are comprised solely of biogenic silica and terrigenous sediment, these differences likely represent the almost complete absence of terrigenous sediment during productive years. Samples used in particle size analysis from productive years therefore consisted almost entirely of diatoms (predominantly *Aulacoseira ambigua*), as well as a small number of sponge spicules, whilst fragments of schist are less common. All of these effects are small however, and should be treated with caution.

Organic carbon, biogenic silica and terrigenous sediment do not bear a statistically significant relationship with the gamma density measurements obtained using the GEOTEK MSCL system. This observation is of interest as it indicates that the sediment's density is relatively unrelated to the composition of material within the core. Although not significant (potentially due to the low sampling resolution used in composition estimates), the presence of organic carbon has an inverse relationship with density (-0.81). It can be concluded that within the lake sediment facies, sediment composition is likely to have a minor impact on gamma density, and that high density sections of the core are somewhat enriched in biogenic silica.

The weakness of this relationship suggests that organic carbon and biogenic silica may have a somewhat similar density, and high density terrigenous material is present in quantities which are too low to significantly influence overall core density. However, density does have a weak but significant inverse relationship with particle size (particularly Dx10, where Z = 0.34). Because gamma bulk density

measurements are given by the ratio of mass to volume and are thus dependent on the particle volume, inter-particle void volume and pore volume, it is probable that within the lake sediment facies density is primarily controlled by the degree of compaction and the presence of pores. Sections within the core which feature fine particles may have less pore space and thus a higher apparent density, and these low porosity core sections may occur due to the well-sorted, fine particles present.

Within the lake sediment facies, magnetic susceptibility is not correlated with density, showing that the low proportion of ferromagnetic minerals present is not sufficient to alter overall core density. This in turn suggests that concentrations of detrital materials as a whole may be too low to affect density. In contrast the volcaniclastic breccia exhibits a very strong positive correlation between density and magnetic susceptibility (0.88, $p<0.05$). It is interpreted that the high density at the base of the core is caused by the presence of high-MS breccia.

L* and b* are positively correlated with biogenic silica and negatively correlated with organic carbon concentrations, such that diatom-rich sections are brighter and possess a yellow tinge, while carbonaceous sections are darker. This observation is in good agreement with visual observations from the core, and photographs presented in the appendices confirm that diatomaceous sections are lighter in colour. Another observation was that biogenic silica was independent from magnetic susceptibility measurements. Together, L* and b* correlate with BSi at a higher resolution than could be obtained using FTIR spectroscopy, and these variables are thus highly informative. Furthermore, this observation provides some validation to the FTIR spectroscopy approach.

4.10 Principal Components Analysis and paleoenvironmental interpretation of components

Principal component analysis was performed a total of three times in order to consider different aspects of the core. In general, variables were included in accordance with their collinearity with other related variables as determined using a Pearson correlation matrix (Table 3.1). As such, the RGB variables and organic carbon variables were excluded from each statistical test. The first PCA incorporated all available variables including density, magnetic susceptibility, L*A*B* colour data, biogenic silica concentration and schist concentration. This initial PCA was limited to the diatomaceous lake sediment facies only, and is thus considered to provide a greater potential for paleoenvironmental interpretation than is afforded by the remaining factor reductions, one of which considered only GEOTEK MSCL variables due to their high resolution, and one which included the entire length of the core, including overburden soil material and the basal volcanic breccia.

In order to best explain paleoenvironmental changes in the core over time, it is necessary to consider the likely conditions which may have produced each of the important components. The first principal component has a weak inverse correlation with density, biogenic silica, schist-concentration and luminescence (Figure 4.12). In addition particle sizes within each of the grain size classes are very strongly correlated with this component. It was found that this principal component is defined foremost by variation in grain size, and grain size is most likely a

predictor of the terrigenous material-to-biogenic silica/organic carbon ratio in the sediment (section 2).

The low density, biogenic silica and luminescence values all suggest that this component represents a process through which organic carbon is caused to accumulate more rapidly than biogenic silica. This could indicate either that vegetation from the surrounding catchment is being transported into the lake at a higher rate, and/or lacustrine plants are growing at a high rate due to this process. In light of this, material which possesses high factor scores along this component is likely to be subject to high rates of erosion, introducing terrigenous sediment and organic carbon from vegetation into the core. The underlying process most likely to be associated with this component is therefore rainfall which could effectively drive erosion in this setting.

The exceptional features of PC2 include its low magnetic susceptibility and its relatively strong yellow-red colouration, as well as an exceptionally high concentration of biogenic silica. The schist-concentration is also low at this point. Particle sizes in this section are not abnormal, but the relatively low median particle size can be linked to the small quantity of schist in sediment with a strong factor score on this axis. The high density associated with this component is most a result of the high concentration of biogenic silica and accordingly low proportion of organic carbon. Considering all of these variables, component two unambiguously represents the greatest rate of biogenic silica accumulation. It is unclear which underlying process this high biogenic silica accumulation rate represents, as increased production could be linked to either high wind speeds, or to changes in temperature (Section 4.8.1). Despite this, observations of the core and literature lead me to suggest that the increased production rate is primarily a result of wind

speed variability, rather than temperature. The low concentration of schist does not suggest an abnormally low rate of erosion, and is instead a direct result of rapid diatom productivity. This material exposes a key limitation of the varimax transformation previously applied to this data. Biogenic silica is not associated with Component Two in the varimax rotated iteration of this analysis, suggesting that although varimax rotation effectively minimizes correlation of variables with more than one component, it also removes loadings which have a theoretical basis. To further explore this, an Oblimin rotation was applied. Oblimin rotation is beneficial as this approach does not force the results to be orthogonal.

PC3 is correlated with material which is rich in schist and extremely low in biogenic silica, with a red colouration and low luminosity. This component also suggests a relatively low density. PC3's relationships with BSi, density, schist and luminosity suggests that relative organic carbon accumulation rates are high in this sediment, and low grain sizes and MS values may be indicative of low erosion rates. If biogenic silica is not correlated with warm temperatures in this environment (and is instead related to wind speed, see section 4.8.1), PC3 may represent an underlying process of increased temperatures and light availability, leading to an increase in organic matter production and a decrease in erosion).

Component four presents a dimension in which density possesses an inverse relationship with luminescence, whilst other values are relatively unchanged. In the core, density and luminescence are generally well correlated, as the quantity of biogenic silica is the primary factor controlling both the density of the sediment, as well as its brightness. Material which scores highly on this axis could occur at the top of the core, where sediment is likely to possess a relatively low density due to the partial oxidation of organic carbon, whilst also being enriched in magnetic

162

material and possessing a relatively high luminescence. The component may reflect edaphic processes and oxidation for that reason.

The unusual relationship between density and luminosity on this axis suggests that despite high organic carbon concentrations, luminosity remains high. This could indicate the presence of highly reflective sand-sized muscovite grains or other terrigenous materials derived from the erosion of schist. This is supported by high Dx90 and magnetic susceptibility values. This assumption would contend that turbidites are not more dense than lake sediment in this core, possibly due an increase in interstitial space and reduced concentration of biogenic silica relative to organic carbon, an observation reinforced by geophysical data (Figure 3.4). It was intended that data representing turbidite deposits be removed from the core, however these deposits appear extremely difficult to distinguish from laminated material in the core. This principal component may also reflect changes in terrestrial plant productivity independent of temperature and wind speed. To conclude, no obvious theoretical basis or process can be identified for this principal component. As it only accounts for 12% of variation in the core, it is possible that PC4 does not reflect a process, and that no explanation can thus be provided.

Figure 4.12 summarizes the paleoenvironmental interpretations of each of the first four components. It must be remembered that each of the measurements has a factor score for each component. Whilst each of the first three components are inferred to be partially underlain by climatic factors, material must behave theoretically consistently on each of these components in order for valid paleoenvironmental interpretations to be made. Cluster analysis can be used on the factor scores to determine whether material behaves consistently, and to further elucidate paleoenvironmental interpretations.

Component 1 paleoenvironmental interpretation:

High precipitation leading to increased erosion and larger particle sizes.

Component 4 paleoenvironmental interpretation:

Cold temperatures during which diatoms are unable to accumulate rapidly due to low wind strength. Slow plant accumulation leads to high luminescence.

Component	1	2	3	4
Density	-0.088	0.121	-0.092	-0.664
MS	-0.041	-0.264	-0.444	0.289
L	-0.137	0.22	-0.213	0.739
A	-0.009	0.55	0.687	0.043
B	0.028	0.775	0.411	0.105
BSi	-0.13	0.632	-0.563	-0.081
S	-0.22	-0.575	0.589	0.089
DX10	0.821	0.18	-0.212	-0.133
DX50	0.849	-0.225	0.114	-0.045
DX90	0.711	-0.017	0.102	0.294

Component 2 paleoenvironmental interpretation:

High wind strengths and high seasonality enabling the rapid production of biogenic silica and a high accumulation rate of lake sediment.

Component 3 paleoenvironmental interpretation:

Very cold temperature conditions and low seasonality precluding production of biogenic silica. Low pH, eutrophic conditions may lead to peat accumulation and the dissolution of hematite.

Figure 4.12., Paleoenvironmental interpretations of each of the first four components used in the dataset.

4.11 Paleoenvironmental interpretation of electrofacies zonation

PCA analysis is benficial as it enables the identification of underlying processes (e.g. Fox et al., 2017). This information is best combined with electrofacies analysis, as this statistical approach allows that understanding of processes to be used to identify paleoenvironmental states within the core (Frank *et al.,* 2013).

Cluster analysis combined with principal component analysis yielded electrofacies models based on the physical and compositional properties of the core, including the magnetic susceptibility, density, grain size, LAB colour and biogenic silica/organic carbon/schist concentrations present. K cluster analysis enabled the models to automatically select the ideal number of clusters and electrofacies numbers to be included. This approach also presents advantages over typical sedimentological facies analysis, as electrofacies analysis is not based primarily on visually identifiable features of the core, but instead relies also on geophysical properties and colour properties which may be too subtle to be consistently recognized through more conventional methods. This is particularly relevant when examining lake sediment which is largely visually homogenous (e.g. Frank *et al.,* 2013).

4.11.1 Paleoenvironmental interpretation of complete core electrofacies zonation

The first electrofacies analysis conducted using this method examined all parts of the core, including the soil overburden and the brecciated volcaniclastic material and turbidites present at the base of the core (Figure 4.13). This statistical test confirmed other observations regarding the general nature of major facies present in the core. In particular, the basal volcanic breccia was recognized as distinct from the remainder of the core due to its bright colouration, high density and high

magnetic susceptibility. This analysis divided the lake sediment into three electrofacies, the first of which represents slow diatom accumulation in a relatively cold or nutrient-poor environment (Elecrofacies 3). The second electrofacies which occurred as part of the lake sediment (Electrofacies 4) represents relatively bright coloured sediment which is rich in diatoms and has a relatively high density due to the great concentration of biogenic silica present and low concentration of organic carbon. It is inferred that conditions during the deposition of the Electrofacies 4 material favoured the rapid accumulation of *Aulacoseira Spp.* diatoms, likely including relatively warmer temperatures, whilst maintaining the high wind run and low salinity conducive to the success of this species.

Electrofacies 5 is likely to represent cold periods of abnormally slow diatom reproduction and lake productivity. Throughout this facies, diatoms make up a minor proportion of the total composition of the lake sediment, with organic carbon and terrigenous material making up a larger fraction of the sediment. Following the digestion of organic matter using hydrogen peroxide, Electrofacies 5 also has a larger average particle size than Electrofacies 3 and 4. This is likely due to the higher proportion of schist and other terrigenous material accumulating in these samples due to the slow rate of diatom production.

The soil and schist based overburden, as well as the basal volcaniclastic material each also registered as individual electrofacies on the initial cluster analysis. In both cases, material was characterised by a high density and magnetic suscepbility and relatively bright luminescence values. However, the recognition of these units as separate electrofacies is of limited use in interpreting the paleoenvironmental and lithological evolution of this lake.
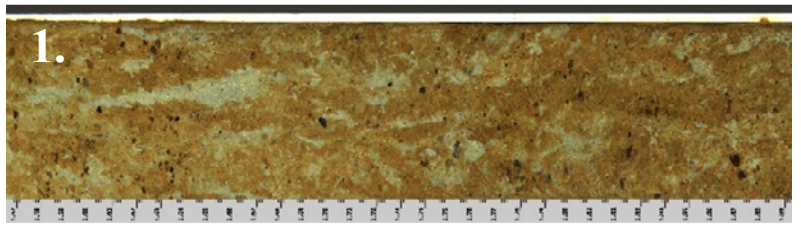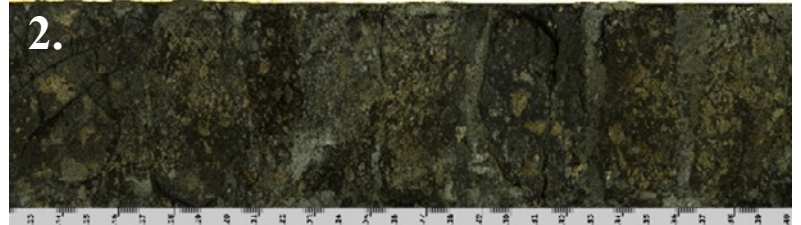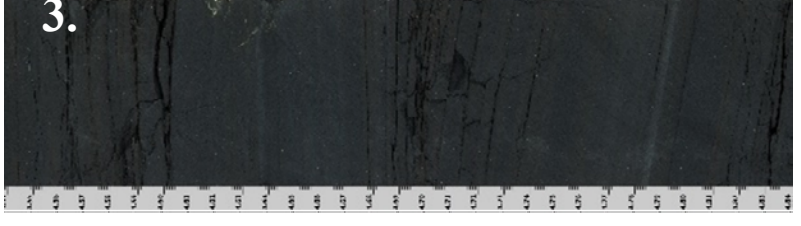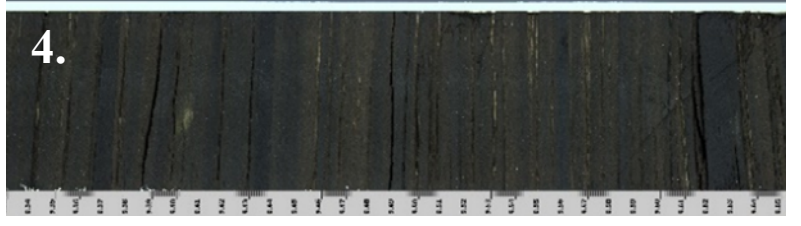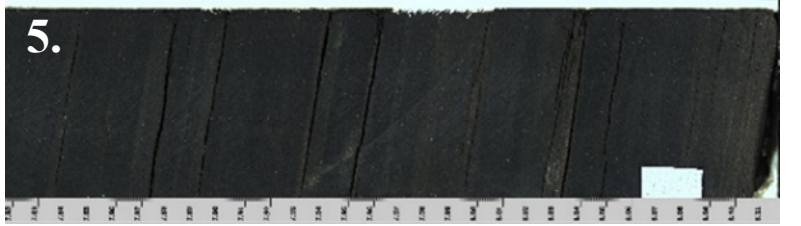
Electrofacies classification with examples from Hindon Maar 3	Geophysical/compositional properties	Interpretation
1.	High density schist-rich overburden with a very bright colouration. This section contains a high magnetic susceptibility, grain size and density in comparison to other parts of the core.	Schist-rich sandy overburden and soil component deposited following cessation of lacustrine accumulation.
2.	High density gravel dominated basal volcanicastic or mass flow dominated material with a bright colouration. This section contains a high magnetic susceptibility, grain size and density in comparison to other parts of the core.	Brecciated volcanic material and schist country rock deposited following the Hindon Maar eruption events.
3.	Low density lake sediment with a relatively dark colouration. This electrofacies contains an average grain size in comparison to the remaining sections of the core.	*Aulacoseira Spp.* dominated razor-striped detrital diatomaceous lake sediment deposited slowly in relatively cold conditions. Organic material is derived from lacustrine and terrestrial sources.
4.	Bright coloured, high density lake sediment with a high concentration of diatoms in comparison to other sections of lake sediment in the core. This section of the core possesses an average particle size in comparison to other lake sediment sections.	*Aulacoseira Spp.* dominated pin-striped diatomaceous lake sediment deposited quickly in relatively windy conditions. Organic material is derived from lacustrine and terrestrial sources.
5.	Low density lake sediment with a relatively dark colouration. This electrofacies contains larger particles on average in comparison to other sections of the core, and exhibits a low BSi to organic carbon ratio.	*Aulacoseira Spp.* dominated razor-striped organic-rich diatomaceous lake sediment deposited very slowly in dry, windless conditions. Organic material is derived from lacustrine and terrestrial sources.

Figure 4.13. Electrofacies descriptions based on PC analysis of the whole core.

4.12.2 Paleoevironmental interpretation of lake sediment Electrofacies Zonation

The second electrofacies analysis conducted using this method examined only sections of the core within the black diatomaceous lake sediment facies, excluding the soil overburden, the brecciated volcaniclastic material and the turbidites present at the base of the core. The paleoenvironmental interpretations of each of the clusters identified is based on the lake sediment principal components analysis which was used to derive factor scores upon which each of the facies was defined (Table 4.2). The paleoenvironmental interpretation of each component is discussed in Section 4.4. Using this information, the six clusters defined using two-step cluster analysis can be considered on the basis of their mean correlations with each of the four components (Table 4.3). Figure 4.14 shows the position of electrofacies and several variables, whilst Figure 4.15 presents a summary of electrofacies interpretations.

Table 4.2. Component matrix used to derive factor scores upon which cluster analysis is based. These components are used to interpret the characteristics and paleoenvironmental meaning of each cluster.

Variable	Component 1	Component 2	Component 3	Component 4
Density	-.216	.143	-.307	-.626
MS	-.353	-.241	-.229	.228
L*	-.157	.326	.233	.699
A*	.280	.419	.683	-.272
B*	.214	.742	.419	-.112
BSi	-.308	.675	-.388	.150
Schist	-.040	-.724	.473	-.024
Dx10	.641	.234	-.547	.007
Dx50	.828	-.272	-.174	-.014
Dx90	.718	-.035	.004	.289

Table 4.3. Mean factor scores for each electrofacies in relation to each of the principal components.

Electrofacies	Component 1	Component 2	Component 3	Component 4
	Mean	Mean	Mean	Mean
1	2.54	-0.30	0.18	-0.67
2	0.66	-0.49	0.05	0.81
3	-0.09	0.63	1.83	0.61
4	-0.39	-0.21	0.03	-0.80
5	-0.37	1.32	-0.54	0.07
6	-0.60	-0.97	-0.79	0.36

Electrofacies One possesses an extremely strong mean factor score on the first component, 2.54 standard deviations greater than average. This indicates that Electrofacies One primarily represents material with large particle sizes at the tenth, 50th and 90th percentiles. This also suggests that the electrofacies has a low concentration of biogenic silica and a high concentration of organic carbon (Figure 4.14). Furthermore, this cluster has a low density and magnetic susceptibility, and is relatively dark (Table 4.3). The second strongest correlation associated with this factor is a negative relationship with Component 4 (-0.67). The relationship with Component 4 partially counteracts the low density of this facies, but further reinforces the observation that Electrofacies One has a low magnetic susceptibility and luminosity (Figure 4.14). The relationships with other components are relatively weak, and are unlikely to have a strong influence on the properties of these sections. Electrofacies One occurs primarily between 700 and 850 cm depth, alternating with a section of Electrofacies Two. Across the length of the core, conditions represented by Electrofacies One are expected to have persisted for a duration of approximately 400 years (Figure 4.14). Electrofacies One represents lake sediment material which is rich in organic carbon and terrigenous material. This was due to enhanced erosion in the catchment, increasing the quantity of organic carbon and terrigenous material transported into the lake.

Electrofacies Two has a relatively strong positive relationship with both Component Four (0.81) and Component One (0.66). This suggests a lower than average density and an average concentration of biogenic silica. The negative correlation with Component Two (-0.49) further suggests that biogenic silica values are not remarkably high at this point. Electrofacies Two is thus distinguished from

Electrofacies One by possessing a higher magnetic susceptibility and luminescence, as well as slightly more biogenic silica. Particle sizes may also be somewhat lower in Electrofacies Two than in Electrofacies One. Across the length of the core, conditions represented by Electrofacies One are expected to have persisted for a duration of approximately 775 years, and Electrofacies Two is primarily located between a depth of 750 and 810 cm depth, where it alternates with Electrofacies One (Figure 4.14). Rainfall and erosion rates were thus enhanced during the deposition of this material, but lake productivity was also somewhat higher in this sediment than in electrofacies one, probably due to a slight increase in wind speed. This increase in wind speed and mixing may have also raised the pH of the lake, preventing any dissolution of magnetic minerals and explaining the higher magnetic susceptibility in this sediment.

The third electrofacies has a very strong relationship with Component 3 (1.83), indicating that the cluster is principally defined by its relative brightness, red-yellow colouration and a low particle size, density, magnetic susceptibility and biogenic silica concentration as well as a large concentration of schist. These observations regarding the concentration of schist and biogenic silica are largely offset by the correlation of this cluster with components Two and Four (0.63 and 0.61, respectively) (Table 4.3). Overall, this cluster thus has an approximately average composition, but features a low density and magnetic susceptibility and a relatively bright colouration. Electrofacies Three was deposited over a combined duration of approximately 665 years (primarily in two separate intervals, one with a length of ~400 years, and another with a possible length of ~200 years) (Figure 4.14). At the top of the core, this electrofacies is taken to indicate the removal of material due to oxidizing, soil forming conditions during the erosion of lake

171

sediment above this deposit. Towards the lower end of the core, however, where this Electrofacies occurs adjacent to Electrofacies 4 and 5, it is more likely to represent warm conditions which did not favour the rapid production of diatoms but allowed organic carbon to accumulate rapidly in the form of plant matter. This electrofacies may also therefore represent moderate wind-speed periods during which the SSWs were migrating towards the equator or poles. Electrofacies three thus may represent warm conditions with moderate wind speeds.

Electrofacies Four was the largest cluster identified during this analysis and possesses relatively moderate relationships with each of the compositional and geophysical variables. A strong inverse relationship exists with Component 4 (-0.8), indicating a considerable density and dark colour. This component also suggests that the sediment may have a low magnetic susceptibility and BSi concentration (Figure 4.14). The cluster's negative relationship with Component One (-0.39) suggests that this material may have a small particle size (Table 4.3). This component also offsets the low magnetic susceptibility and BSi concentration suggested by the previous component, indicating that these values are relatively unremarkable. Overall, this electrofacies possesses a low density, low BSi concentration and dark colour, indicating that it is somewhat enriched in organic carbon, but is less extreme in this regard than Electrofacies One. This deposit occurs frequently throughout the core (primarily in the middle of the deposit), with a total thickness of 208 cm. Assuming this material accumulated at the average rate, this material was deposited over 1465 years (Figure 4.14). Based on these component scores, this material represents conditions which had warm temperatures but experienced relatively little rainfall and mild wind speeds. The extensive section of

this electrofacies in the middle of the deposit could thus represent a movement in the SSW to higher latitude over a period of multiple centuries.

Electrofacies Five occurs predominantly towards the base of the core and correlates very strongly with Component Two (1.32). This relationship with Component Two primarily suggests extremely high biogenic silica concentrations, as well as a high density, bright yellow-red colouration, and a low schist concentration indicating high wind speeds. The negative correlation of this cluster with component 3 (-0.54) reinforces the high biogenic silica concentration, but somewhat moderates the sediment's colour, density and magnetic susceptibility, possible suggesting low temperatures (Figure 4.14). The cluster's negative relationship with Component One (-0.37) gives a high BSi estimate, as well as an increased density, luminosity and magnetic susceptibility. This component suggests a relatively low grainsize, likely to indicate a reduced erosion rate due to low rainfall. Electrofacies Five can be taken to indicate high productivity due to maximal wind speeds during the accumulation of the core. Climate during this time was highly seasonal relative to the rest of the core, and favoured the rapid accumulation of diatoms. A combined thickness of 152 cm is categorised as Electrofacies Five (Figure 4.14). Considering the enhanced deposition rate during the accumulation of this material indicated by wide laminae (Section 3.1.1), it is possible that Electrofacies 5 was deposited over a period of between 800-1000 years. This change may be partially explained by the movement of SSW to low latitudes.

Electrofacies 6 has a very strong negative relationship with components One, Two and Three (-0.6, -0.97 and -0.79, respectively). The negative relationship with Component Two suggests a low BSi, though this is offset by components One, Three and Four. This material has an average-to-slightly low density after

considering the interactions of the four components, and three of the components indicate a high magnetic susceptibility value. This material generally has a high luminescence but lacks green-red and blue-yellow components, yielding a relatively monochromatic core. Electrofacies 6 can therefore be interpreted as representing relatively typical lacustrine sedimentation under moderate-to-low temperatures. Seasonality was low at this time, but erosion rates contributing schist and a high magnetic susceptibility were almost at their highest. Some of this may represent sections at the top of the core where oxidization has removed organic carbon and caused an enrichment in terrigenous sediment (Figure 4.14). It is likely that part of this electrofacies also represents material which accumulated while erosion rates were relatively high and mass flows occurred frequently. High schist concentrations and magnetic susceptibility values are therefore not an artefact caused by high or low biogenic silica accumulation rates, in this instance. 149 cm of this material is present, and it may have accumulated over a period of approximately 1024 years.
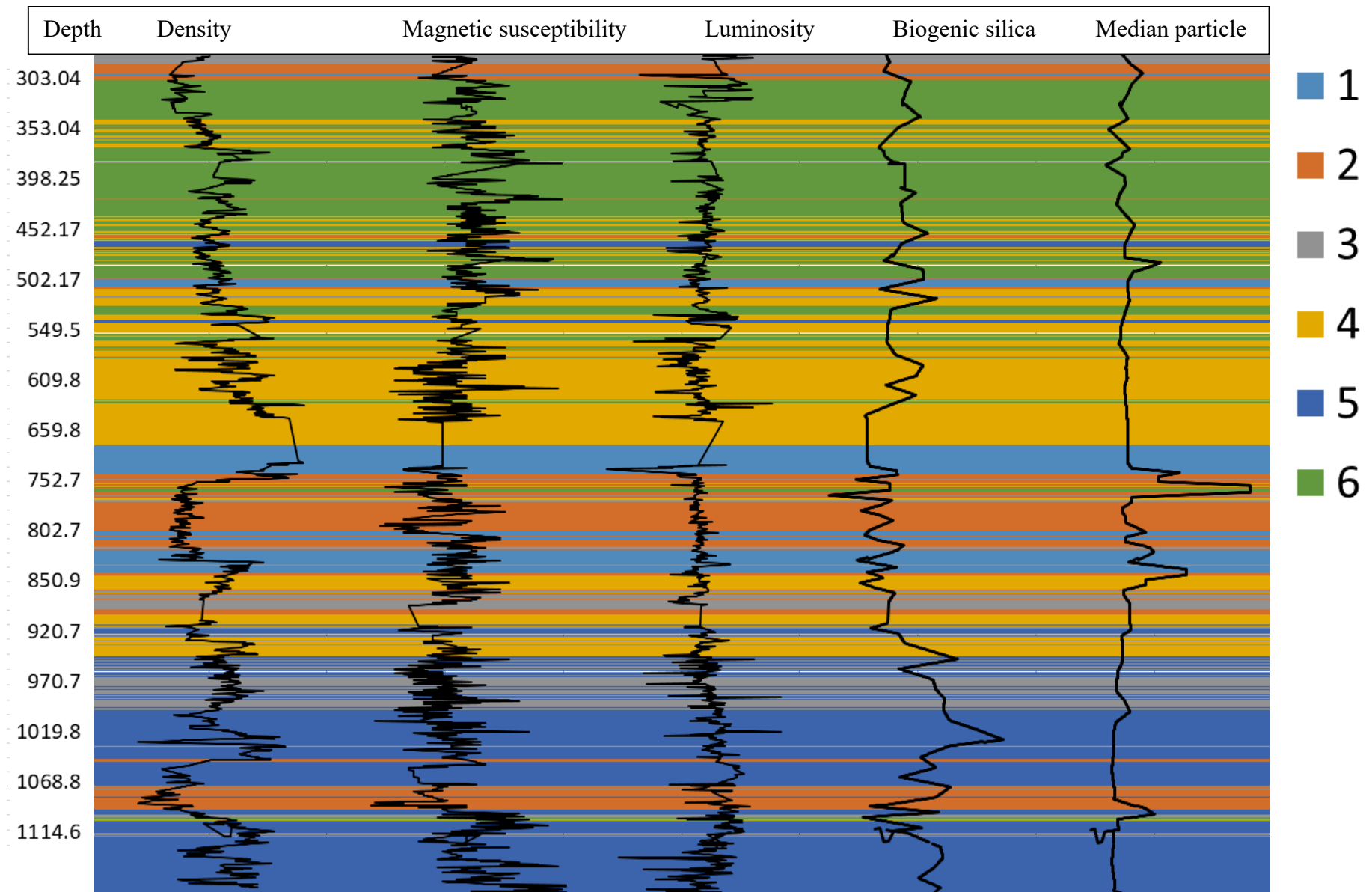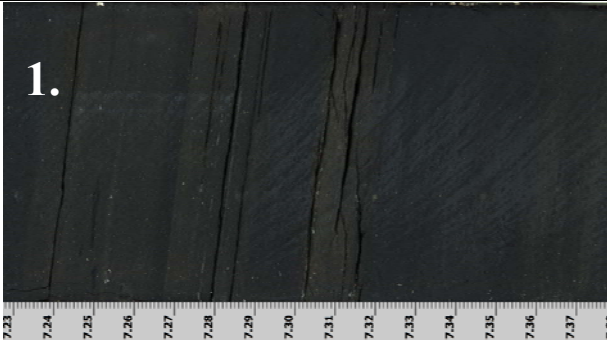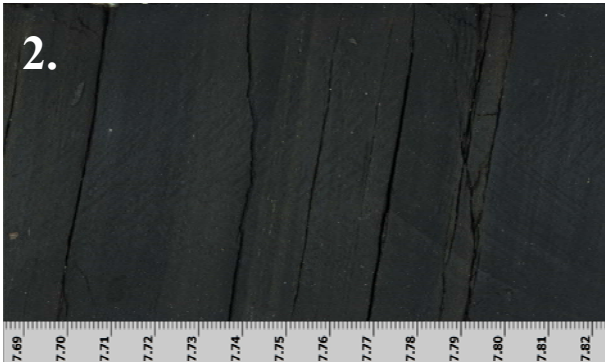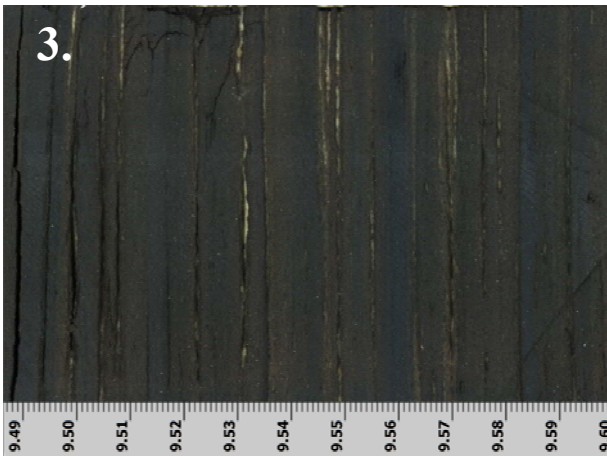
Figure 4.14 Normalised density, magnetic susceptibility, luminosity, biogenic silica and median particle size against electrofacies.

175

Electrofacies classification with examples from Hindon Maar 3	Key	Geophysical/compositional properties	Interpretation
1.		Low magnetic susceptibility, luminescence and biogenic silica. High Dx10, Dx50, Dx 90, A* and B*. Moderate density and schist concentration.	High erosion rates bringing increased terrigenous material and organic carbon into the lake. Most likely generated by increased rainfall. Relatively low wind speeds.
2.		Low density, biogenic silica, A* and B*. High schist concentration and grain size. Moderate magnetic susceptibility and luminescence.	Relatively low wind speeds and productivity with high precipitation.
3.		Low density, magnetic susceptibility, Dx10 and Dx50. High L*A*B* and schist. Moderate BSi and Dx90.	Relatively low precipitation and windspeed but high temperatures and light availability.
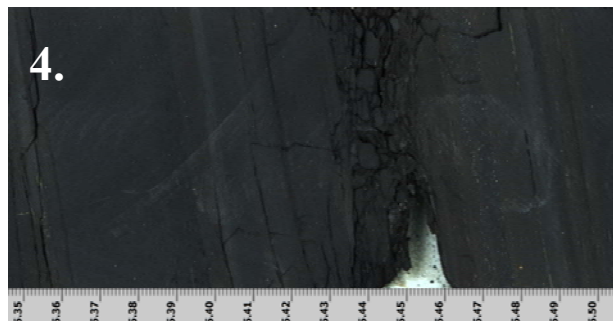
	Low Dx10, Dx50, Dx90 and L*. High Density. Moderate magnetic susceptibility, A*,B*, BSi and schist concentration.	Relatively low precipitation, windspeed, temperatures and light availability.
	Low schist concentration, Dx50 and Dx 90. High Density, L*, B*, BSi. Moderate Dx10, L*, magnetic susceptibility.	*Aulacoseira Spp.* dominated razor-striped detrital diatomaceous lake sediment deposited very rapidly in warm conditions. Organic material is derived from lacustrine and terrestrial sources.
	Low A*, B*, Dx90. High magnetic susceptibility and schist concentration. Moderate L*, Dx10, Dx50, BSi.	Predominantly low production of organic carbon, which has led to an increased concentration of schist and a higher MS at this point. Electrofacies may also be associated with minor oxidation at the top of the core.
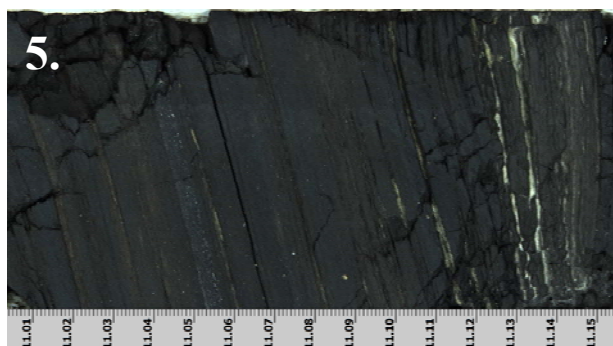
Figure 4.15. Electrofacies descriptions and paleoenvironmental interpretation based on PC analysis of the whole core.

4.13 Orbital and sub-Milankovich scale variation

It must be emphasised that any links drawn between inferred paleoenvironmental conditions, core characteristics and solar/orbital cycles should be treated with extreme caution and are highly speculative. This is partially because the floating age model used in this project does not allow the construction of cycles for the period of deposition. Furthermore, cycles are not necessarily consistent across all of the variables. Finally, analysis of this nature relies on the assumption that laminations were deposited at an equal rate across the length of the core and that no major unconformities are present (Yiou et al., 1996). This discussion provides a possible explanation for some of the cycles seen in the core, but significantly more study and data is needed to verify any of the hypotheses provided in this section.

A periodogram of PC2 produced using Tukey-Hamming suggests that this variable is subject to significant cyclicity (Figure 4.16), and this observation is also supported by wavelet analysis (Figure 4.17). Similar cycles are identified in magnetic susceptibility (Figure 4.18, 4.19). These cycles and others in the dataset may suggest the influence of oribital or solar forcing, and potentially important cycles are therefore discussed.
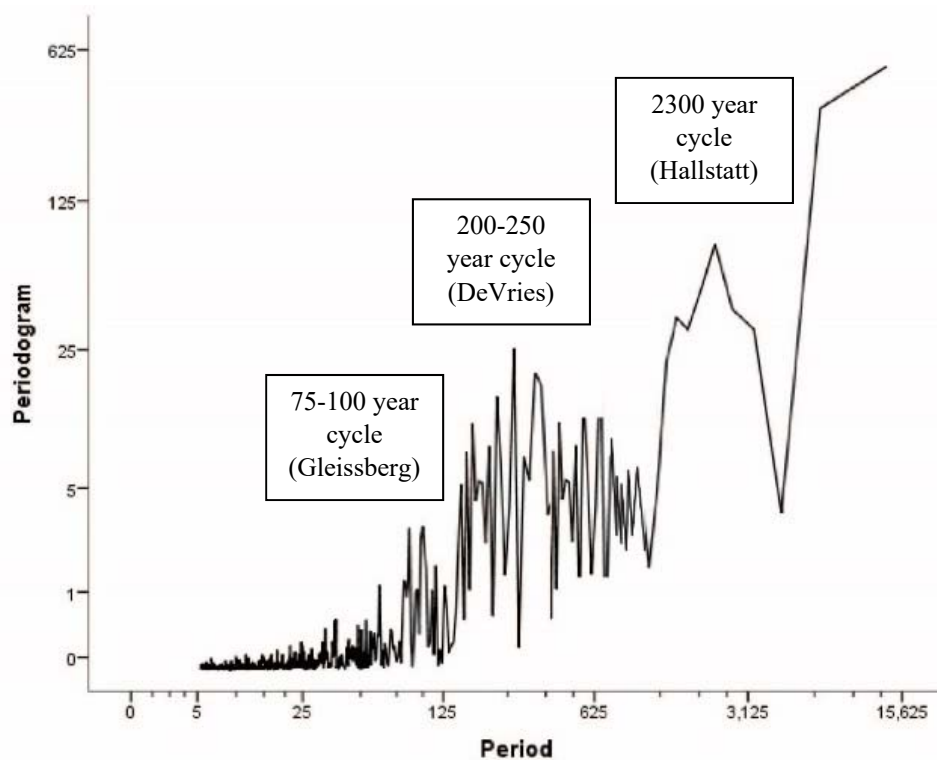
Figure 4.16 Tukey-Hamming periodogram produced using spectral analysis was used to identify cycles in the PC2 dataset. These cycles are similar to some observed in other deposits.
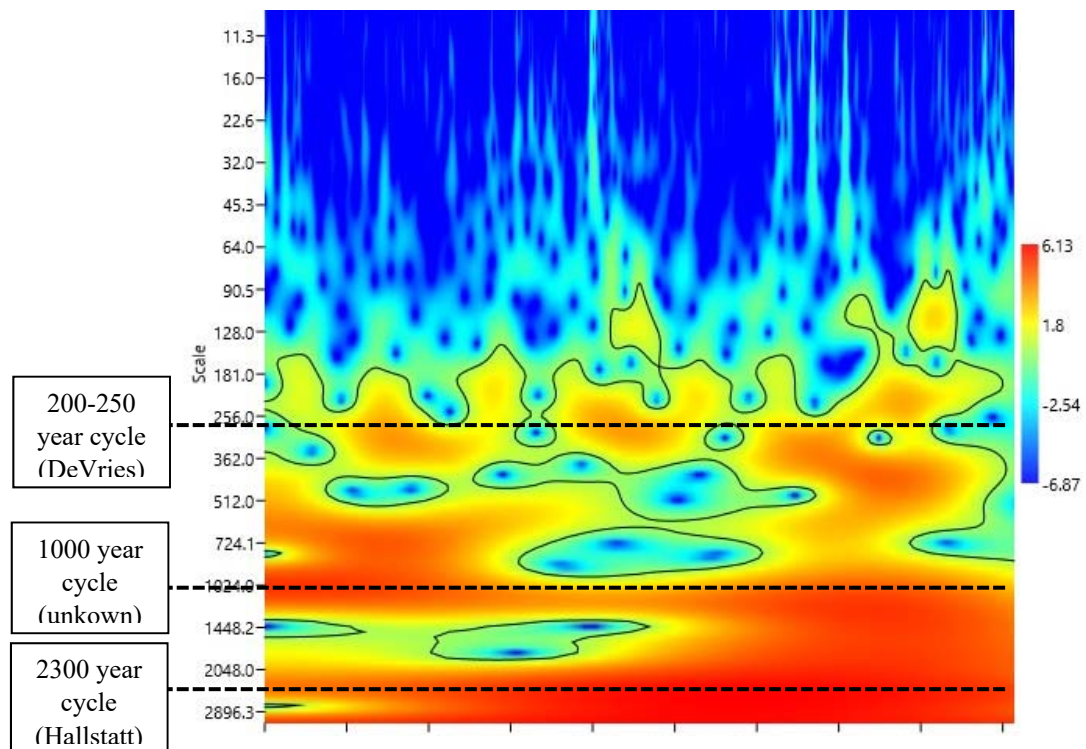
Figure 4.17 Wavelet analysis cycles of the PC2 dataset suggests the presence of several cycles in the dataset. A logarithmic scale is used to properly show the extent of both axes.

179
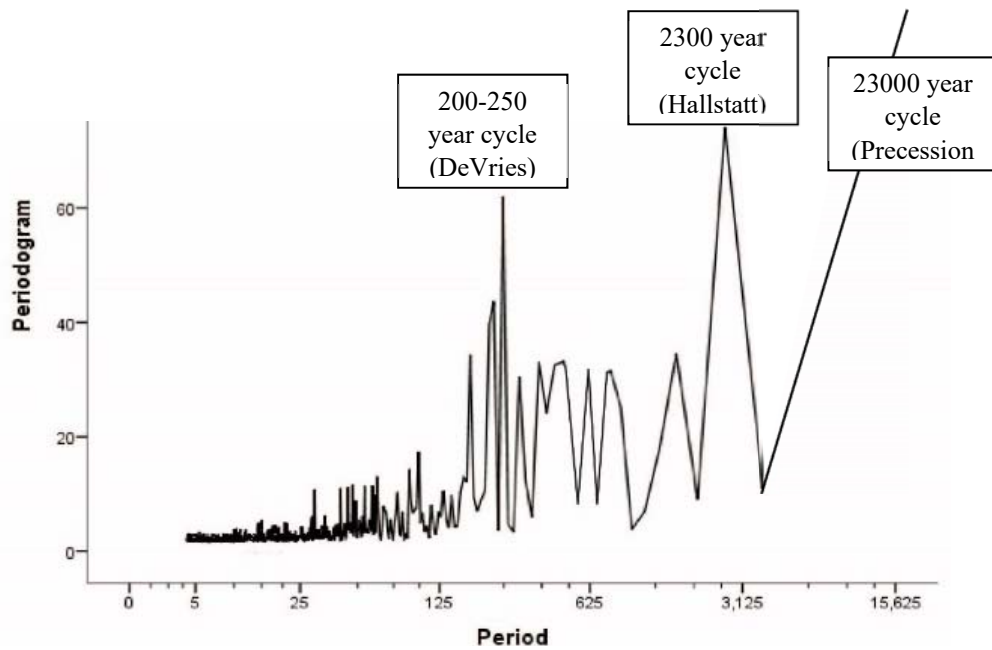
Figure 4.18 Tukey-Hamming periodogram produced using spectral analysis was used to identify cycles in the MS dataset. A logarithmic scale is used to properly show the extent of both axes.
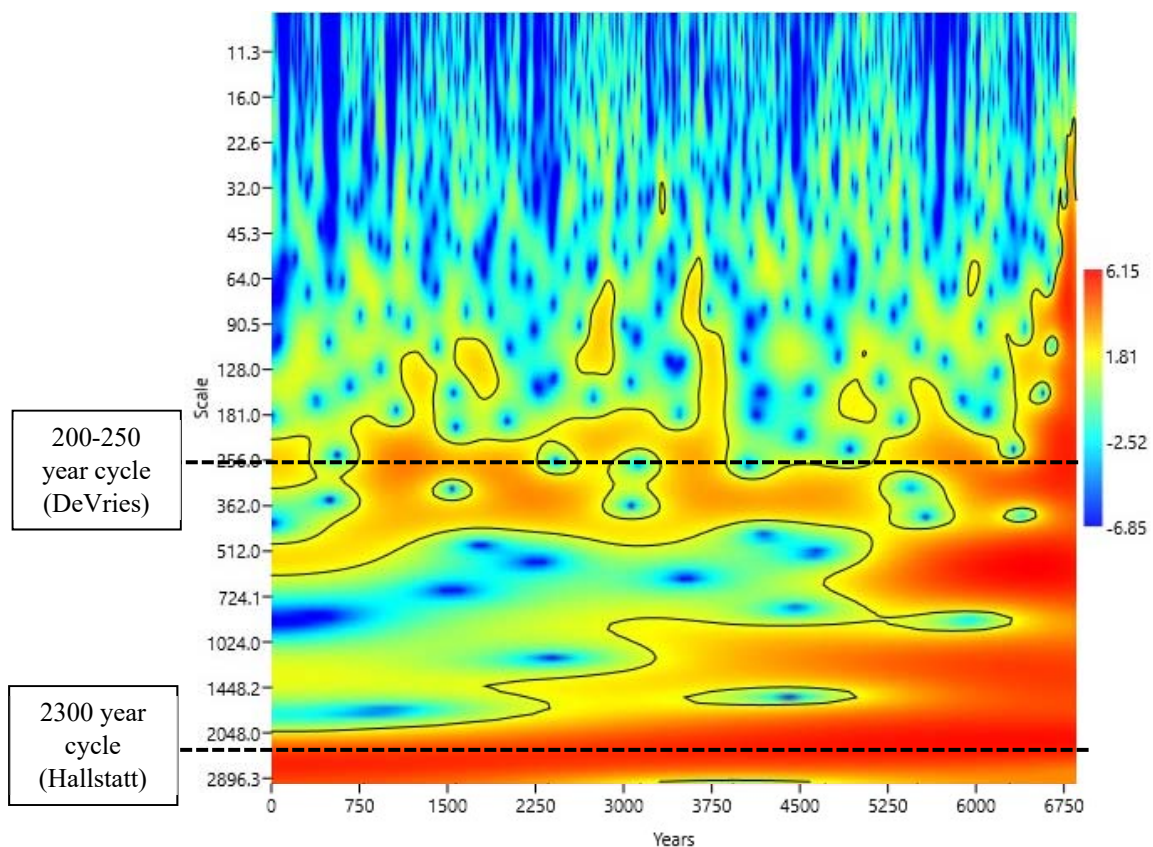
Figure
4.19 Wavelet analysis cycles of the MS dataset suggests the presence of several cycles in the dataset. A logarithmic scale is used to properly show the extent of both axes.

4.13.1 Obliquity

Obliquity has a significant effect on the seasonality of climate at both high latitudes and mid-latitudes. High obliquity is linked to strong seasonality, where the temperature difference between winter and summer is extreme. Evidence of high annual productivity (including thick siliceous laminae) would be expected if temperatures began to warm earlier in the year and cooled later in the year, and also if insolation increased. As obliquity possesses a period 41000 years, this core does not contain an entire obliquity cycle, and instead the tilt of the earth's axis is likely to have changed by 0.5 degrees during the accumulation of this core.

This small change could potentially be linked to the change from high varve bimodality observed during the early stages of the lake's development to the low bimodality in more recent sections of the core.

4.13.2 Precession

Obliquity has little direct influence on the quantity of sunlight reached at this latitude, and precession is more likely to influence this variable. As precession has ~20 ka cycle, this sediment core has preserved approximately one third of a single cycle. Light levels and temperature would have varied significantly during the deposition of this lake as a direct result of this, and the resultant changes in productivity may be recorded in the sediment core. Precession also has a significant influence on seasonality, and variations over this timescale could greatly strengthen the contrast between summer and winter temperatures (Mallinson et al., 2003). The large-scale compositional change between 8 and 11 metres depth characterised by increased laminae bimodality and biogenic silica could be part of a precession cycle.

At high latitudes in the southern hemisphere, precession is the primary orbital factor influencing wind speed and precipitation (Mallinson et al., 2003; Botsford et al, 2003; Bradtmiller et al, 2006). Southern hemisphere precession maxima lead to warmer summers, cooler winters and increased seasonality. This causes the intensification of sub-tropical highs resulting in great wind velocities (Mallinson et al., 2003). Warm summers would also lead to a reduction in precipitation rates and vegetation cover, and so may also increase erosion rates (Mallinson et al., 2003). Strengthened pressure gradients would also lead to an increase in meridional pressure gradients, causing upwelling along the polar front and increasing wind speeds and siliceous productivity (Mallinson et al., 2003).

Southern hemisphere precession minima result in cool summers and warm winters with reduced seasonality. The weakening of the Australian low pressure cell leads to reduced wind temperatures, and this also causes a reduction in chemical weathering (Mallinson et al., 2003). Due to low wind speeds and high precipitation, aeolian weathering is decreased and fluvial transport is enhanced (Mallinson et al., 2003).

Increased insolation caused by precession cycles have been shown to drive monsoon winds at mid-high latitudes in the northern hemisphere (Clemens and Prell, 1991). Furthermore, deMenocal (1993) showed that the concentration of *Aulacoseira spp.* diatoms in African lake beds had an extremely close correlation with precession during the Pleistocene (Figure 4.20). Based on this, deMenocal (1993) concluded that African monsoon intensity was controlled by orbital precession. *Aulacoseira* productivity in Hindon Maar 3 indicates that precession may have also controlled wind speeds during the Miocene at high latitudes.

Figures 4.20 explores the possibility that precession could have a dominant impact on biogenic silica accumulation and wind speed. When placed on the same time scales, it is apparent that precession may have some influence on these two variables. It must be noted that these figures represent an inferred position of the precession cycle, and the true stage of cycle at the time of deposition is unknown. This figure instead places the observed paleoenvironmental fluctuation on the same time scale as precession cycles, suggesting a possible position which would explain most of the observed variation. Although precession has elsewhere been reported as a key factor influencing *Aulacoseira* productivity (Mallinson et al., 2003), the limited available data does not allow predictions to be made at this timescale.
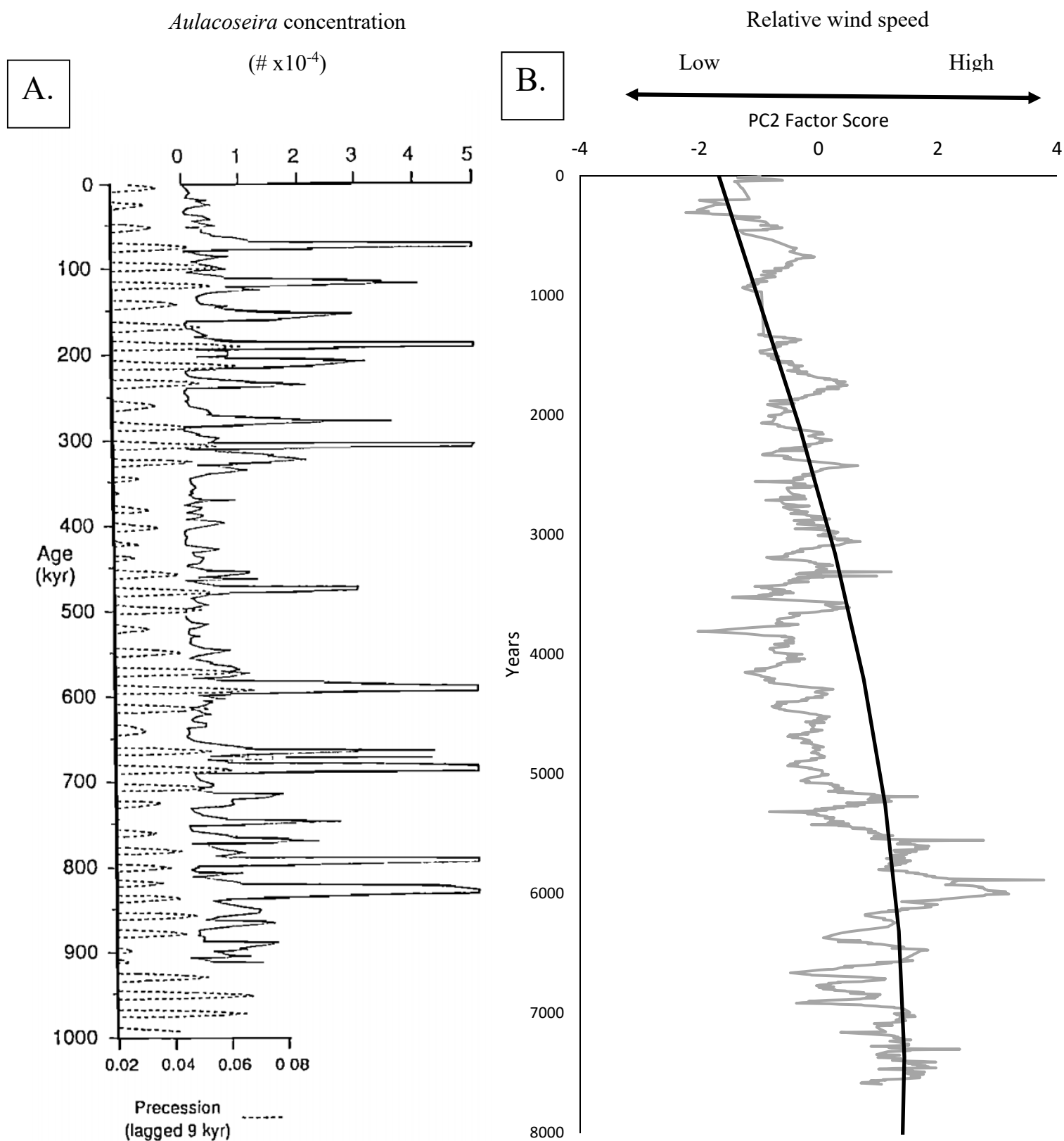
Figure 4.20. (A.) deMenocal (1993) reported that *Aulacoseira* concentration varies in accordance to wind speed controlled primarily by precession cycles. (B.) One third of a precession cycle was completed during the deposition of the Hindon Maar 3 deposit, which could explain changes in the wind speed proxy and BSi.

The limited quantity of core available means that only partial orbital cycles are available. While these cycles are likely to have a dominant effect on variation in the core, it is not possible to easily identify their influence with the available data. This is particularly true in the case of obliquity, in which the minor change which would have occurred during the deposition of this sediment is not captured here Marzocchi et al. (2015). Based on the close agreement between the length of precession cycles and the change in wind speeds and BSi at Hindon Maar 3, the correlation between *Aulacoseira Spp* concentration and precession reported by deMenocal (1993), and the evidence that precession has exerted a control over wind speeds in New Zealand (Mallinson et al., 2003), precession cycles could conceivably be linked to wind speed and paleoproductivity observed in Hindon Maar 3 during the Mid-Miocene climatic optimum. Smaller scale, sub-Milankovich cycles may also influence wind speeds and productivity.

4.13.3 Solar cycles

In addition to the overall trend of increasing wind speeds with depth in the core, smaller scale cycles can also be observed in the component thought to represent productivity. The idea that these cycles may have influenced conditions at the Hindon Maar is suggested due to wavelet and spectral analysis (Figures 4.16, 4.17, 4.18 and 4.19). These cycles are likely to represent the influence of solar forcing on wind speeds, temperatures and overall climate. High latitude climate is especially sensitive to solar forcing (Braun et al., 2005). The first notable cycle is a quasi-200 year oscillation (Figure 4.21, blue line). This cycle may be related to the DeVries/Suess cycle, which also exhibits a periodicity of 200 years. The DeVries cycle has a significant effect on modern climatic variability. For instance, it is

believed to have been the dominant factor controlling climate in northeast Brazil over the last 3000 years (Novello et al., 2012), and numerous other papers have recognized this cycle. In addition to the DeVries cycle, another solar cycle with a wavelength of 2300 years also explains some of the variability in productivity (4.21, orange line). The wavelength of this longer cycle indicates that it most likely represents the influence of the Hallstatt cycle, and it is thus most likely also linked to solar variability (Scafetta et al., 2016). The sum of sinusoidal signals model for PC2 has the same wavelengths as are identified in the periodogram and wavelet analysis and hence may reflect the influence of solar cycles (Figure 4.22).

This analysis indicates that changes in productivity may potentially be related to a combination of precession and solar cycles, perhaps through the mechanisms of wind speed change and an effect on vegetation cover.
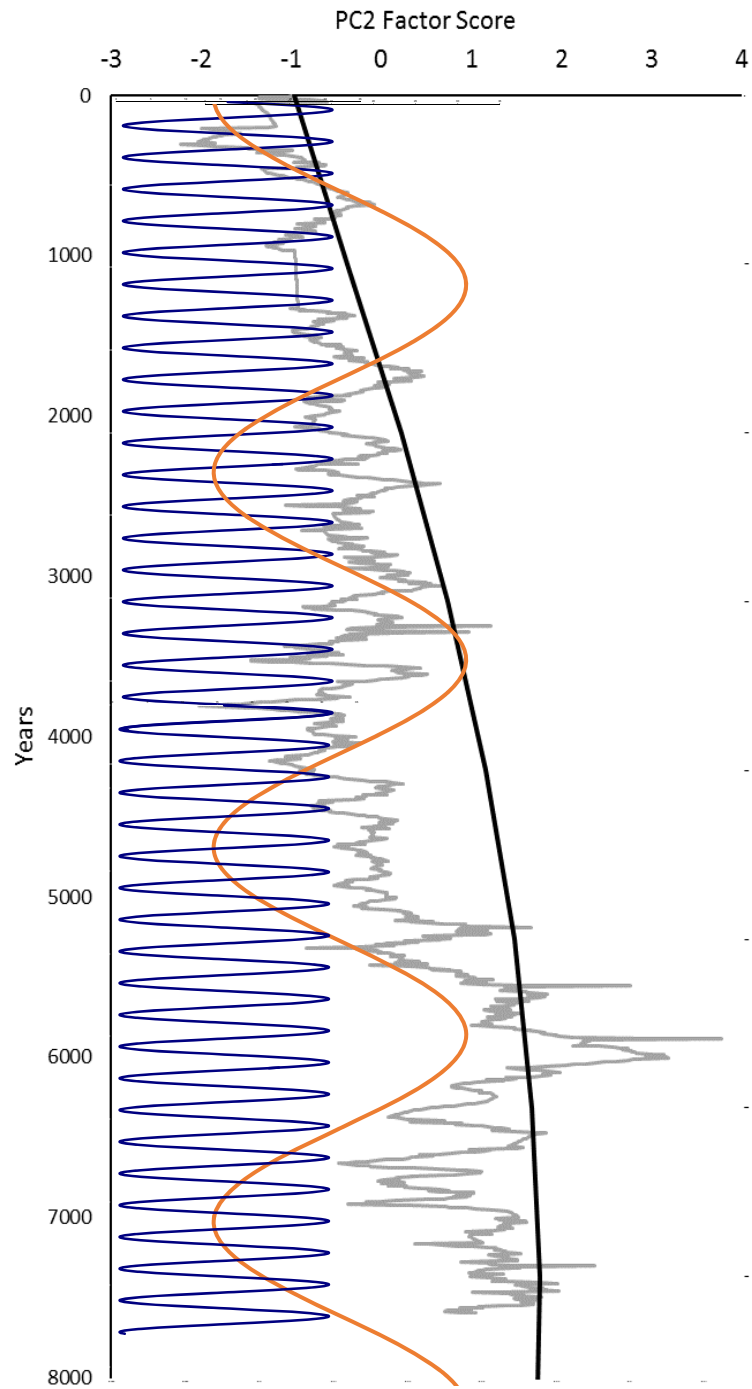
Figure 4.21. The observed trends in biogenic silica productivity and the wind speed proxy may be the result of at least three interacting cycles: Precession (black), the DeVries component (blue), and the Hallstatt cycle (orange).
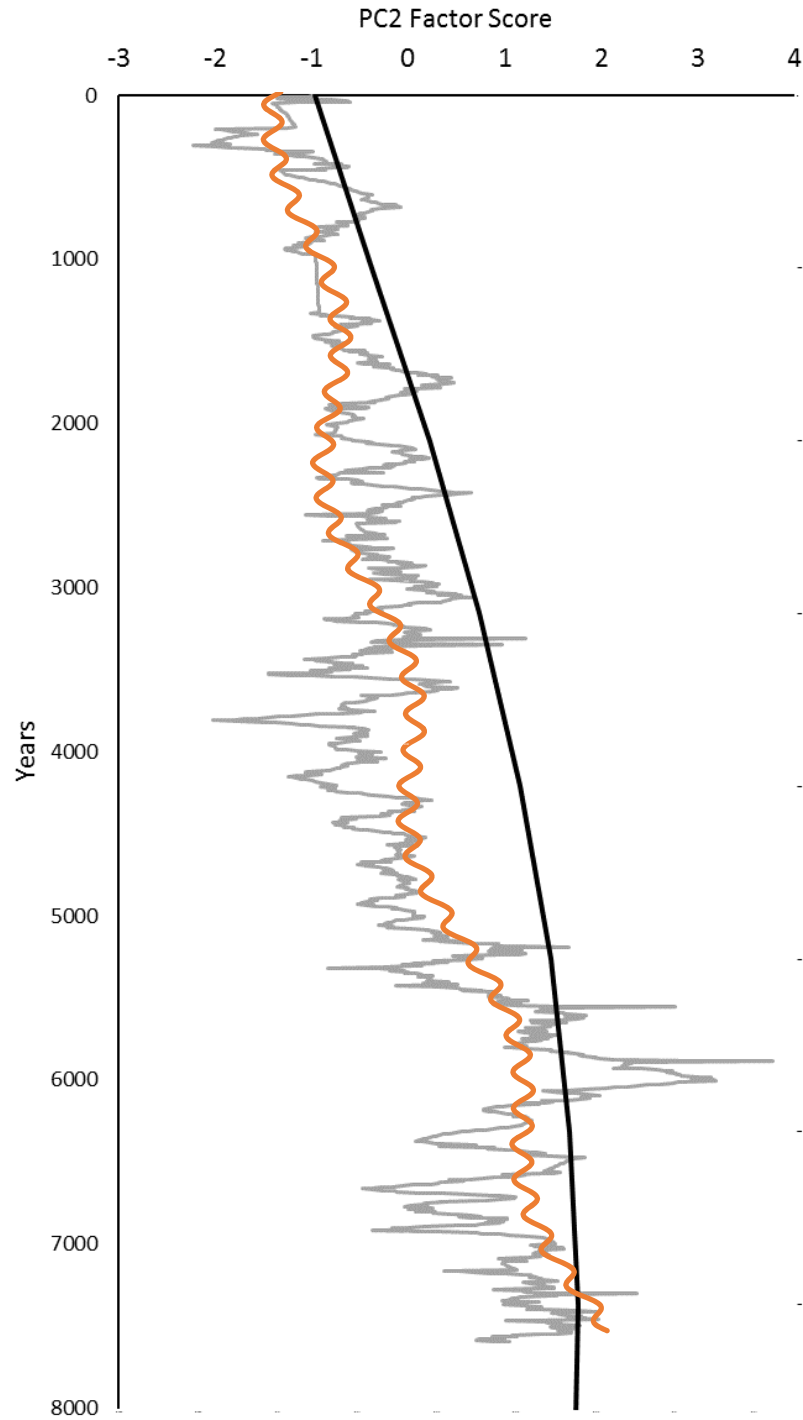
Figure 4.22. A model combining the signature of the DeVries cycle, the Hallstatt cycle and orbital precession is presented. This model bears a vague resemblance to the time-series of the component taken to represent lake productivity. Amplitudes used in this model are taken from the sum of sinusoidal signals analysis (Table 3.13).

4.13.4 Dansgaard-Oeschger events

Cycles approximating 1500 years have been observed in several of the wavelet analyses (density, L*, b*, PC1, PC2, PC3). These cycles could conceivably represent Dansgaard–Oeschger events which have been recorded on a 1470 year cycle in Greenland ice cores (Braun et al., 2005). It has been suggested that these events occur due to the combined effects of DeVries and Gleissberg cycles (Braun et al., 2005), though the influence of this potential factor cannot be effectively verified.

4.14 Lithological history and paleoclimate record from Hindon Maar 3

The deposition of diatomaceous sediment is likely to have commenced shortly following the phreatomagmatic eruption which generated this maar-diatreme in the Mid-Miocene. The lowest sections of this core are occupied by mass flows containing fragmented Otago schist rock grading into a dense sand deposit. Overlying this is a two metre section of fractured, wall rock debris including schist, and a significant quantity of mud clasts. This lithologically diverse section is made up mainly of post-eruptive rock fall products, as well as some subaqueous flow deposits. This sediment may have taken several months or years to finally amass.

A period of lake sedimentation occurred at this point. Resedimentation was common due to weak vegetation cover and soil erosion of the crater slopes. As such, this material is laminated but contains gravel sized rock units and turbidite deposits. As these deposits are primarily made up of high magnetic susceptibility turbidites, it is likely that they were deposited over several decades or potentially hundreds of years. This material is succeeded by a one metre section of biogenic lake sediment in which turbidites still frequently occur.

Ar-Ar dating suggests that the eruption which formed this lake occurred in the Mid-Miocene (15.2 Ma, personal communication Daphne Lee). As such, the Hindon Maar complex presents a high resolution archive of southern hemisphere paleoenvironmental variability during the Miocene climatic optimum. The paleoenvironmental history of this region during the accumulation of Hindon Maar 3 is thus divided into the following sequence of events (Figure 4.23):

PC and cluster analysis suggest that the first ~1150 years of lake sedimentation following the decline in mass flows represents accumulation when temperatures were average (relative to the rest of the core), precipitation was up to one standard deviation lower than average, and wind speeds were 1.5-2 standard deviations above average. For 200 years following this warm period, temperatures decline and wind strength is reduced. This period of particularly high rain fall and cool temperatures is indicated by the transition to Electrofacies Two (Figure 4.23).

The core then transitions back into Electrofacies Five, where high wind speeds and warm temperatures are thought to have occurred. Precipitation decreases due to greater temperatures, possibly induced by the combination of both solar forcing components and the precession cycle.

The component linked with temperature reaches its maximum over the next 500 years, represented by a transition into Electrofacies 3. Wind speed and BSi productivity decreases over this period, and low density, carbon rich sediment with some terrigenous sediment suggests that plant productivity and precipitation were relatively high. A peak in the 200 year DeVries cycle may have enhanced temperature, and the inferred location of the precession cycle and Hallstatt cycle potentially caused relatively high temperatures are maintained. The specific combination of high precipitation, somewhat low wind speeds and high

temperatures were ideal for plant growth and poorly suited to the specific requirements of *Aulacoseira Spp.* diatoms. As a result, organic carbon accumulation outpaced BSi productivity during this sub-tropical period.

The next 1150 years may be influenced by their supposed position on the descending arm of the Hallstatt cycle. For 100 years the lake transitions through Electrofacies 5 and briefly into Electrofacies 4 (Figure 4.23). Over a further 100 years, this pattern is reversed and Electrofacies 5 briefly reoccurs, before being again replaced by Electrofacies 4. Period 4 represents approximately 400 years of sedimentation. This alternation between electrofacies occurs on a similar scale to the DeVries cycle, but it remains unclear that this had any influence on lake productivity. The aforementioned change in electrofacies is mostly due to wind speed changes (Figure 4.23., PC2), and precipitation appears to steadily increase throughout period 4.

The next period represents about 400 years of sedimentation. At this point wind speeds continue to decline, possibly explained by assumed position of the Hallstatt and precession cycles. Electrofacies 4 occurs at 200 year intervals indicating intermittently low precipitation, wind speed, temperature and productivity (Figure 4.23). The transition to and from the peak of this cycle shows a transition to Electrofacies 3 via Electrofacies 2. This suggests that temperatures rose and over 100 years, and plant productivity increased with temperature. Prior to the extensive establishment of plant life in the catchment, organic carbon inputs were somewhat lower and erosion rates were higher (Electrofacies 2). The lake transitions back through electrofacies 2 into conditions associated with Electrofacies 4 over in the second half of this period (100 years), representing a decline in precipitation,

temperature, catchment plant productivity and wind speeds. This may represent DeVries scale variation, or may be unrelated.

Period six represents a period of about 1000 years of deposition. Conditions are thought to be relatively constant conditions for at least 800 years, and this expected relationship is observed in the PC2 (relative wind strength). Precipitation is highly variable during this period however, and peaks at the beginning and end of this period. A notable parabola can also be seen in PC4, with factor scores coinciding with reduced rainfall. During high rainfall the lake thus produces high density, dark coloured sediment at this time. At the centre of this period, however, relatively high luminescence, low density material is produced during dry conditions. It may be assumed that, because BSi production was somewhat constant over this period (due to consistent wind conditions), any changes in density and luminescence during this 1000 year period are linked with changing plant productivity and the erosion rate, as well as the compaction of the sediment. During rainy conditions, plant productivity in the catchment increased and this material was transported at a high rate into the lake leading to low luminescence and relatively high density. As rainfall decreased, BSi and the erosion rate remained relatively unchanged (or experienced a slight decrease), but plant production declined significantly. Plant material from the catchment built up at a lower rate, leading to an overall decrease in density and an increase in luminescence. High rainfall events are represented by electrofacies 1, whilst the drier conditions primarily correspond to electrofacies 2 (Figure 4.23).

The next 1150 years are defined as period 7, and productivity and wind speed decrease weakly over this time. By this point however, the long term trend of decreasing productivity has exerted a dominant control on paleoenvironment, and

from this point onwards it is possible that the strong influence of orbital cycles (or similar scale long term events) on wind strength, temperature, seasonality and productivity means possible solar cycles are of a reduced importance. This period is represented by Electrofacies 4 (Figure 4.23). Organic carbon production by plants in the catchment appears less sensitive to paleoenvironmental changes than biogenic silica, this variable does not change until further decreases in temperature and rainfall occur during the ensuing periods.

Wind speeds, seasonality and lake productivity remain relatively constant throughout this 1000 year period. However, about half-way through this period, plant productivity in the catchment begins to respond negatively to low temperatures and precipitation. This is shown by a transition into Electrofacies 6 (Figure 4.23).

The most recent 1500 year see an overall reduction in temperatures. In addition wind speeds and precipitation are at their lowest point. BSi and organic carbon (both in the catchment and lake) respond to these changes, and productivity is considered to have been very low, as indicated by a prolonged transition to Electrofacies 6.

Some post-depositional erosion and oxidation of the first 100 cm of core has occurred. This variation has no paleoenvironmental significance and can be ignored.
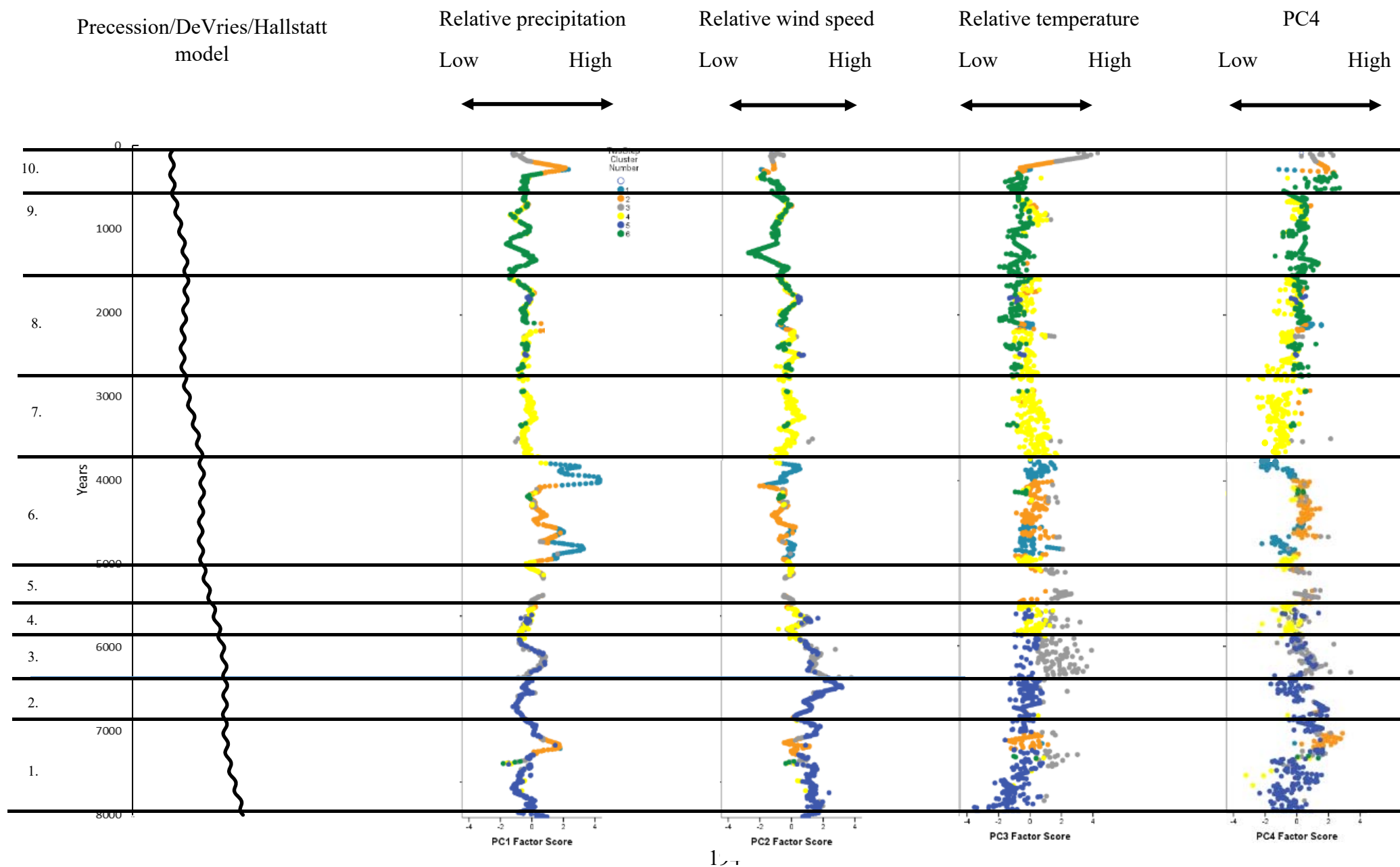
Figure 4.23. Summary of paleoenvironmental conditions and periods, showing variation in PCA factor scores, electrofacies and a suggesting a potential orbital/solar explanation.

CHAPTER 5
Conclusions

Hindon Maar provides a unique high-resolution record of the Miocene Climatic Optimum, and offers the chance to reconstruct the effect of Milankovitch and Sub-Milankovitch scale cyclicity on the Southern Hemisphere for the first time during this event.

The analysed sediment core from Hindon Maar 3 records a complex paleoenvironmental signal influenced by numerous factors, some of which appear to be climate related and may potentially be caused by instability in the catchment. Underlying cooling and corresponding reductions in wind speed over the 7600 years represented in this core are cautiously linked to the precession cycle, and obvious wind speed fluctuations on shorter timescales (200 and 2300 years) may potentially be associated with solar forcing due to the DeVries and Hallstatt cycles.

The observation that the heavily silicified freshwater diatom, *Aulacosiera ambigua*, was dominant in this lake provided key evidence that biogenic silica productivity was linked with wind speeds, and the principal component thought to most closely represent *Aulacosiera* productivity was thus taken as a proxy for relative wind strength. This proxy closely correlates with the three primary cycles which may be acting on this time scale.

When combined with the identification of underlying processes using principal components analysis, electrofacies analysis (via two-step cluster analysis) provides an effective means of identifying shifts between common paleoenvironmental

states. This was the basis of a proposed high resolution paleoenvironmental reconstruction.

Biogenic silica, organic carbon and schist analysis using FTIR spectroscopy provided an inexpensive technique to measure concentrations downcore at a high resolution, and particle size distributions were also obtained at the same resolution. The remaining variables were obtained using a GEOTEK MSCL system, and together these provided an important insight into the role of orbital and solar cycles on the latitude of dominant westerly wind bands during the Middle Miocene. Overall, this research expands our understanding of climatic variability during the Middle Miocene Climatic Optimum.

References

Adams, C. J., & Graham, I. J. (1997). Age of metamorphism of Otago Schist in eastern Otago and determination of protoliths from initial strontium isotope characteristics. *New Zealand Journal of Geology and Geophysics*, *40*(3), 275–286.

Barth, N. G. (1984). *Modern methods of particle size analysis*. John Wiley & Sons, Inc.

Beierle, B. D., Lamoureux, S. F., Cockburn, J. M. H., & Spooner, I. (2002). A new method for visualizing sediment particle size distributions. *Journal of Paleolimnology*, *27*(2), 279–283.

Bertaux, J., Ledru, M.-P., Soubiès, F., & Sondag, F. (1996). The use of quantitative mineralogy linked to palynological studies in palaeoenvironmental reconstruction : the case study of the "Lagoa Campestre" lake, Salitre, Minas Gerais, Brazil. *Comptes Rendus de l'Académie Des Sciences de Paris.Série 2a : Sciences de La Terre et Des Planètes*, *323*, 65–71.

Billups, K., & Schrag, D. P. (2002). Paleotemperatures and ice volume of the past 27 Myr revisited with paired Mg/Ca and 18O/16O measurements on benthic foraminifera. *Paleoceanography*, *17*(1), 3–1.

Blass, A., Bigler, C., Grosjean, M., & Sturm, M. (2007). Decadal-scale autumn temperature reconstruction back to AD 1580 inferred from the varved sediments of Lake Silvaplana (Southeastern Swiss Alps). *Quaternary Research*, *68*(2), 184–195.

Bodén, P., & Backman, J. (1996). A laminated sediment sequence from the northern North Atlantic Ocean and its climatic record. *Geology*, *24*, 507.

Böhme, M. (2003). The Miocene Climatic Optimum: evidence from ectothermic vertebrates of Central Europe. *Palaeogeography, Palaeoclimatology, Palaeoecology*, *195*(3), 389–401.

Botsford, L. W., Lawrence, C. A., Dever, E. P., Hastings, A., & Largier, J. (2003). Wind strength and biological productivity in upwelling systems: an idealized study. *Fisheries Oceanography*, *12*(4–5), 245–259.

Bowie, E. (2015). Geophysical Characterisation of the Hindon Maar Complex · Otago Geology Thesis.

Bradtmiller, L. I., Anderson, R. F., Fleisher, M. Q., & Burckle, L. H. (2006). Diatom productivity in the equatorial Pacific Ocean from the last glacial period to the present: A test of the silicic acid leakage hypothesis. *Paleoceanography*, *21*(4), PA4201.

Brauer, A., Endres, C., Günter, C., Litt, T., Stebich, M., & Negendank, J. F. W. (1999). High resolution sediment and vegetation responses to Younger Dryas climate change in varved lake sediments from Meerfelder Maar, Germany. *Quaternary Science Reviews*, *18*(3), 321–329.

Braun, H., Christl, M., Rahmstorf, S., Ganopolski, A., Mangini, A., Kubatzki, C., … Kromer, B. (2005). Possible solar origin of the 1,470-year glacial climate cycle demonstrated in a coupled model. *Nature*, *438*(7065), nature04121.

Browne, I. M., Moy, C. M., Riesselman, C. R., Neil, H. L., Curtin, L. G., Gorman, A. R., & Wilson, G. S. (2017). Late Holocene intensification of the westerly winds at the subantarctic Auckland Islands (51° S), New Zealand. *Clim. Past*, *13*(10), 1301–1322.

Buczkó, K., Ognjanova-Rumenova, N., & Magyari, E. (2010). Taxonomy, morphology and distribution of some aulacoseira taxa in glacial lakes in the South Carpathian Region. *Polish Botanical Journal*, *55*(1), 149–163.

C Hopmans, E., W.H Weijers, J., Schefuß, E., Herfort, L., Sinninghe-Damste, J., & Schouten, S. (2004). A novel proxy for terrestrial organic matter in sediments based on branched and isoprenoid tetraether lipids. *Earth and Planetary Science Letters*, *224*, 107–116.

Carrick, H. J., Aldridge, F. J., & Schelske, C. L. (1993). Wind Influences phytoplankton biomass and composition in a shallow, productive lake. *Limnology and Oceanography*, *38*(6), 1179–1192.

Cavanaugh, T. (2017). Applications of Spectrophotometry for Paleoclimate Interpretations from Lacustrine Sediment Records.

Cerling, T. E., Harris, J. M., MacFadden, B. J., Leakey, M. G., Quade, J., Eisenmann, V., & Ehleringer, J. R. (1997). Global vegetation change through the Miocene/Pliocene boundary. *Nature*, *389*(6647), 153–158.

Chang, A. S. (1997). *Sedimentary processes and paleoenvironmental significance of laminated diatomaceous sediments from the miocene monterey formation, California, USA*. University of British Columbia.

Chang, A. S., Grimm, K. A., & White, L. D. (1998). Diatomaceous sediments from the Miocene Monterey Formation, California; a lamina-scale investigation of biological, ecological, and sedimentary processes. *PALAIOS*, *13*(5), 439–458.

Chen, C.-W. (1977). Chapter 2 - ferromagnetism and ferrimagnetism. In *Magnetism and Metallurgy of Soft Magnetic Materials* (pp. 15–60). Elsevier.

Chu, G., Liu, J., Sun, Q., Lu, H., Gu, Z., Wang, W., & Liu, T. (2002). The 'Mediaeval Warm Period' drought recorded in Lake Huguangyan, tropical South China. *The Holocene*, *12*(5), 511–516.

Clemens, S. C., & Prell, W. L. (1991). Late Quaternary forcing of Indian Ocean summer-monsoon winds: A comparison of Fourier model and general circulation model results. *Journal of Geophysical Research: Atmospheres*, *96*(D12), 22683–22700.

Coates, J. (2006). Interpretation of Infrared Spectra, A Practical Approach. In *Encyclopedia of Analytical Chemistry*. John Wiley & Sons, Ltd.

Colman, S. M., Peck, J. A., Hatton, J., Karabanov, E. B., & King, J. W. (1999). Biogenic silica from the BDP93 drill site and adjacent areas of the Selenga Delta, Lake Baikal, Siberia. *Journal of Paleolimnology*, *21*(1), 9–17.

Conley, D., & Schelske, C. (2006). Biogenic Silica (pp. 281–293).

Coombs, D. S., Adams, C. J., Roser, B. P., & Reay, A. (2008). Geochronology and geochemistry of the Dunedin Volcanic Group, eastern Otago, New Zealand. *New Zealand Journal of Geology and Geophysics*, *51*(3), 195–218.

Cumming, B. F., & Smol, J. P. (1993). Development of diatom-based salinity models for paleoclimatic research from lakes in British Columbia (Canada). *Hydrobiologia*, *269–270*(1), 179–196.

Cunningham, L., Vogel, H., Nowaczyk, N., Wennrich, V., Juschus, O., Persson, P., & Rosén, P. (2013). Climatic variability during the last interglacial inferred from geochemical proxies in the Lake El'gygytgyn sediment record. *Palaeogeography Palaeoclimatology Palaeoecology*.

Dam, H. van. (2013). *Proceedings of the Twelfth International Diatom Symposium, Renesse, The Netherlands, 30 August – 5 September 1992*. Springer Science & Business Media.

De Wet, G. (2013). Holocene Paleo-environmental Variability Reconstructed from a Lake Sediment Record from Southeast Greenland. *Masters Theses 1911 - February 2014*.

Dean, W. E., Bradbury, J. P., Anderson, R. Y., & Barnosky, C. W. (1984). The Variability of Holocene Climate Change: Evidence from Varved Lake Sediments. *Science*, *226*(4679), 1191–1194.

Debret, M., Desmet, M., Balsam, W., Copard, Y., Francus, P., & Laj, C. (2006). Spectrophotometer analysis of Holocene sediments from an anoxic fjord: Saanich Inlet, British Columbia, Canada. *Marine Geology*, *229*(1), 15–28.

deMenocal, P. B., Ruddiman, W. F., & Pokras, E. M. (1993). Influences of High- and Low-Latitude Processes on African Terrestrial Climate: Pleistocene Eolian Records from Equatorial Atlantic Ocean Drilling Program Site 663. *Paleoceanography*, *8*(2), 209–242.

Demers, S., Therriault, J.-C., Bourget, E., & Bah, A. (1987). Resuspension in the shallow sublittoral zone of a macrotidal estuarine environment: Wind influence1. *Limnology and Oceanography*, *32*(2), 327–339.

Dietrich, S., & Seelos, K. (2010). The reconstruction of easterly wind directions for the Eifel region (Central Europe) during the period 40.3–12.9 ka BP. *Clim. Past*, *6*(2),

Duhau, S., & Jager, C. de. (2016). On the Origin of the Dansgaard–Oeschger Events and Its Time Variability. In *Marine Isotope Stage 3 in Southern South America, 60 KA B.P.-30 KA B.P.* (pp. 23–47). Springer, Cham. Retrieved from

Eshel, G., Levy, G., Mingelgrin, U., & Singer, M. (736). *Critical Evaluation of the Use of Laser Diffraction for Particle-Size Distribution Analysis* (Vol. 68).

F. Williams, D., Peck, J. A., B. Karabanov, E., A. Prokopenko, A., Kravchinsky, V., King, J., & I. Kuzmin, M. (1997). *Lake Baikal Record of Continental Climate Response to Orbital Insolation During the Past 5 Million Years* (Vol. 278).

Fahnenstiel, G., & Glime, J. (1983). Subsurface Chlorophyll Maximum and Associated Cyclotella Pulse in Lake-Superior. *Internationale Revue Der Gesamten Hydrobiologie*, *68*(5), 605–616.

Farrar, J. (1999). *Standard Penetration Test Driller's / Operator's Guide* (No. DSO-98-17) (pp. 1–30). U.S. Department of Interior Bureau of Reclamation Dam Safety Office.

Field, B. D., Crundwell, M. P., Lyon, G. L., Mildenhall, D. C., Morgans, H. E. G., Ohneiser, C., … Chanier, F. (2009). Middle Miocene paleoclimate change at Bryce Burn, southern New Zealand. *New Zealand Journal of Geology and Geophysics*, *52*(4), 321–333.

Flower, B. P., & Kennett, J. P. (1994). The middle Miocene climatic transition: East Antarctic ice sheet development, deep ocean circulation and global carbon cycling. *Palaeogeography, Palaeoclimatology, Palaeoecology*, *108*(3), 537–555.

Fox, B. R. S., Wartho, J., Wilson, G. S., Lee, D. E., Nelson, F. E., & Kaulfuss, U. (2015). Long-term evolution of an Oligocene/Miocene maar lake from Otago, New Zealand. *Geochemistry, Geophysics, Geosystems*, *16*(1), 59–76.

Fox, B., Wilson, G., & Lee, D. E. (2016). A unique annually laminated maar lake sediment record shows orbital control of Southern Hemisphere midlatitude climate across the Oligocene-Miocene boundary. *Geological Society of America Bulletin*, *128*, 609–626.

Frank, U., Nowaczyk, N. R., Minyuk, P., Vogel, H., Rosén, P., & Melles, M. (2013). A 350 ka record of climate change from Lake El'gygytgyn, Far East Russian Arctic: refining the pattern of climate modes by means of cluster analysis. *Climate of the Past*, *9*, 1559–1569.

Fuchs, A., Selmeczy, G. B., Kasprzak, P., Padisák, J., & Casper, P. (2016). Coincidence of sedimentation peaks with diatom blooms, wind, and calcite precipitation measured in high resolution by a multi-trap. *Hydrobiologia*, *763*(1), 329–344.

Gasson, E., DeConto, R. M., Pollard, D., & Levy, R. H. (2016). Dynamic Antarctic ice sheet during the early to mid-Miocene. *Proceedings of the National Academy of Sciences*, *113*(13), 3459–3464.

Geotek Ltd. (2016). *GEOTEK Multi-Sensor Core Logger*. Sopwith Way Drayton Fields Daventry Northamptonshire.

Gerland, S., & Villinger, H. (1995). Nondestructive density determination on marine sediment cores from gamma-ray attenuation measurements. *Geo-Marine Letters*, *15*(2), 111–118.

Giosan, L., Flood, R. D., & Aller, R. C. (2002). Paleoceanographic significance of sediment color on western North Atlantic drifts: I. Origin of color. *Marine Geology*, *189*(1–2), 25–41.

Goebel, N. L., Wing, S. R., & Boyd, P. W. (2005). A mechanism for onset of diatom blooms in a fjord with persistent salinity stratification. *Estuarine, Coastal and Shelf Science*, *64*(2), 546–560.

Hahn, A., Kliem, P., Ohlendorf, C., Zolitschka, B., & Rosén, P. (2013). Climate induced changes as registered in inorganic and organic sediment components from

Laguna Potrok Aike (Argentina) during the past 51 ka. *Quaternary Science Reviews*, *71*, 154–166.

Håkanson, L. (1981). Determination of characteristic values for physical and chemical lake sediment parameters. *Water Resources Research*, *17*(6), 1625–1640.

Håkanson, L., & Jansson, M. (1983). *Principles of Lake Sedimentology*. Berlin, Heidelberg: Springer Berlin Heidelberg. Retrieved from

Hand, S. J., Lee, D. E., Worthy, T. H., Archer, M., Worthy, J. P., Tennyson, A. J. D., … Lindqvist, J. K. (2015). Miocene Fossils Reveal Ancient Roots for New Zealand's Endemic Mystacina (Chiroptera) and Its Rainforest Habitat. *PLOS ONE*, *10*(6), e0128871.

Helmke, J. P., Schulz, M., & Bauch, H. A. (2002). Sediment-Color Record from the Northeast Atlantic Reveals Patterns of Millennial-Scale Climate Variability during the Past 500,000 Years. *Quaternary Research*, *57*(1), 49–57.

Herbert, T. D., Lawrence, K. T., Tzanova, A., Peterson, L. C., Caballero-Gill, R., & Kelly, C. S. (2016). Late Miocene global cooling and the rise of modern ecosystems. *Nature Geoscience*, *9*(11), ngeo2813.

Hirabara, M., Ishizaki, H., & Ishikawa, I. (2007). Effects of the Westerly Wind Stress over the Southern Ocean on the Meridional Overturning. *Journal of Physical Oceanography*, *37*, 2114.

Holbourn, A., Kuhnt, W., Kawamura, H., Jian, Z., Grootes, P., Erlenkeuser, H., & Xu, J. (2005). Orbitally paced paleoproductivity variations in the Timor Sea and Indonesian Throughflow variability during the last 460 kyr. *Paleoceanography*, *20*(3), PA3002.

Holbourn, A., Kuhnt, W., Schulz, M., Flores, J.-A., & Andersen, N. (2007). Orbitally-paced climate evolution during the middle Miocene "Monterey" carbon-isotope excursion. *Earth and Planetary Science Letters*, *261*(3–4), 534–550.

Hu, F. S., Kaufman, D., Yoneji, S., Nelson, D., Shemesh, A., Huang, Y., … Brown, T. (2003). Cyclic Variation and Solar Forcing of Holocene Climate in the Alaskan Subarctic. *Science*, *301*(5641), 1890–1893.

Iluz, D., Dishon, G., Capuzzo, E., Meeder, E., Astoreca, R., Montecino, V., … Marra, J. (2009). Short-term variability in primary productivity during a wind-driven diatom bloom in the Gulf of Eilat (Aqaba). *Aquatic Microbial Ecology - AQUAT MICROB ECOL*, *56*, 205–215.

Ivanov, D. (2005). Late Eocene to early Miocene climate and vegetation of Bulgaria. *Review of Palaeobotany and Palynology*.

Ivanov, D., Utescher, T., Mosbrugger, V., Syabryaj, S., Djordjević-Milutinović, D., & Molchanoff, S. (2011). Miocene vegetation and climate dynamics in Eastern and Central Paratethys (Southeastern Europe). *Palaeogeography, Palaeoclimatology, Palaeoecology*, *304*(3), 262–275.

Jackson, M. L. (1956). Soil chemical analysis: advanced course: Published by the author. *Madison, Wis.*, 895.

Johnson, S. E. (1990). Lack of porphyroblast rotation in the Otago schists, New Zealand: implications for crenulation cleavage development, folding and deformation partitioning. *Journal of Metamorphic Geology*, *8*(1), 13–30.

Johnson, T. C., Chan, Y., Beuning, K., Kelts, K., Ngobi, G., & Verschuren, D. (1998). Biogenic Silica Profiles in Holocene Cores from Lake Victoria: Implications for Lake Level History and Initiation of the Victoria Nile. In *Environmental Change and Response in East African Lakes* (pp. 75–88). Springer, Dordrecht.

Justino, F., Marengo, J., Kucharski, F., Stordal, F., Machado, J., & Rodrigues, M. (2013). *Influence of Antarctic ice sheet lowering on the Southern Hemisphere climate: Modeling experiments mimicking the mid-Miocene* (Vol. 42).

Kaiser, H. F. (1974). An index of factorial simplicity. *Psychometrika*, *39*(1), 31–36.

Kaulfuss, U., & Moulds, M. (2015). A new genus and species of tettigarctid cicada from the early Miocene of New Zealand: Paratettigarcta zealandica (Hemiptera, Auchenorrhyncha, Tettigarctidae). *ZooKeys*, (484), 83–94.

Kelly, M., Juggins, S., Guthrie, R., Pritchard, S., Jamieson, J., Rippey, B., … Yallop, M. (2008). Assessment of ecological status in U.K. rivers using diatoms. *Freshwater Biology*, *53*(2), 403–422.

Kemp, A. E. S., & Baldauf, J. G. (1993). Vast Neogene laminated diatom mat deposits from the eastern equatorial Pacific Ocean. *Nature*, *362*(6416), 362141a0.

Kern, A. K., Harzhauser, M., Piller, W. E., Mandic, O., & Soliman, A. (2012). Strong evidence for the influence of solar cycles on a Late Miocene lake system revealed by biotic and abiotic proxies. *Palaeogeography, Palaeoclimatology, Palaeoecology*, *329–330*(Supplement C), 124–136.

Keys, W. S. (1996). *A Practical Guide to Borehole Geophysics in Environmental Investigations*. CRC Press.

Kilham, S. S., Theriot, E. C., & Fritz, S. C. (1996). Linking planktonic diatoms and climate change in the large lakes of the Yellowstone ecosystem using resource theory. *Limnology and Oceanography*, *41*(5), 1052–1062.

Kiss, K. T., & Genkal, S. I. (1993). Winter blooms of centric diatoms in the River Danube and in its side-arms near Budapest (Hungary). *Hydrobiologia*, *269–270*(1), 317–325.

Kissoon, L. T. T., Jacob, D. L., Hanson, M. A., Herwig, B. R., Bowe, S. E., & Otte, M. L. (2015). Multi-Elements in Waters and Sediments of Shallow Lakes: Relationships with Water, Sediment, and Watershed Characteristics. *Wetlands (Wilmington, N.C.)*, *35*(3), 443–457.

Klee, R., & Houk, V. (2007). Valve Ultrastructure Studies of Discosᵀᴱᴸla Glomerata (bachmann) Houk & Klee. *Diatom Research*, *22*(1), 89–103.

Knorr, G., & Lohmann, G. (2014). *Climate Warming during Antarctic ice sheet expansion at the Middle Miocene transition* (Vol. 7).

Knowles, J. W. (1968). IV - crystal diffraction spectroscopy of nuclear γ-rays. In K. Siegbahn (Ed.), *Alpha-, Beta- and Gamma-Ray Spectroscopy* (pp. 203–243). Amsterdam: Elsevier.

Köster, D., & Pienitz, R. (2006). Seasonal Diatom Variability and Paleolimnological Inferences – A Case Study. *Journal of Paleolimnology*, *35*(2), 395–416.

Kürschner, W. M., Kvaček, Z., & Dilcher, D. L. (2008). The impact of Miocene atmospheric carbon dioxide fluctuations on climate and the evolution of terrestrial ecosystems. *Proceedings of the National Academy of Sciences*, *105*(2), 449–453.

Landis, C. A., Campbell, H. J., Begg, J. G., Mildenhall, D. C., Paterson, A. M., & Trewick, S. A. (2008). The Waipounamu Erosion Surface: questioning the antiquity of the New Zealand land surface and terrestrial fauna and flora.

Last, W. M. (2002). Textural Analysis of Lake Sediments. In *Tracking Environmental Change Using Lake Sediments* (pp. 41–81). Springer, Dordrecht.

Last, W. (2017) Tracking Environmental Change Using Lake Sediments - Volume |4 Penguin.

Le Cohu, R. (1996). Further Observations and Some Comments on the Fine Structure of the Centric Diatom Aulacoseira Islandica (bacillariophyceae)1. *Journal of Phycology*, *32*(2), 333–338.

Li, Y.-M., Ferguson, D., Wang, Y.-F., & Li, C.-S. (2010). Paleoenvironmental inferences from diatom assemblages of the middle Miocene Shanwang Formation, Shandong, China. *Journal of Paleolimnology*, *43*, 799–814.

Liebrand, D., Bakker, A. T. M. de, Beddow, H. M., Wilson, P. A., Bohaty, S. M., Ruessink, G., … Lourens, L. J. (2017). Evolution of the early Antarctic ice ages. *Proceedings of the National Academy of Sciences*, *114*(15), 3867–3872.

Lindqvist, J., & Lee, D. (2009). High-frequency paleoclimate signals from Foulden Maar, Waipiata Volcanic Field, southern New Zealand: An Early Miocene varved lacustrine diatomite deposit. *Sedimentary Geology*, *222*, 98–110.

Liu, Z., Yoshimura, K., Bowen, G. J., Buenning, N. H., Risi, C., Welker, J. M., & Yuan, F. (2014). Paired oxygen isotope records reveal modern North American atmospheric dynamics during the Holocene. *Nature Communications*, *5*.

Liukkonen, M., Kairesalo, T., & Keto, J. (1993). Eutrophication and recovery of Lake Vesijärvi (south Finland): Diatom frustules in varved sediments over a 30-year period. In *Twelfth International Diatom Symposium* (pp. 415–426). Springer, Dordrecht.

Lomas, M. W., & Bates, N. R. (2004). Potential controls on interannual partitioning of organic carbon during the winter/spring phytoplankton bloom at the Bermuda Atlantic time-series study (BATS) site. *Deep Sea Research Part I: Oceanographic Research Papers*, *51*(11), 1619–1636.

Lotter, A. F., & Bigler, C. (2000). Do diatoms in the Swiss Alps reflect the length of ice-cover? *Aquatic Sciences*, *62*(2), 125–141.

LST1G+ Geotechnical Drill Rig. (2017, November 13). Retrieved November 13, 2017, from http://www.lonestardrills.com/lst1g/

Lüdecke, H.-J., Weiss, C. O., & Hempelmann, A. (2015). Paleoclimate forcing by the solar De Vries/Suess cycle. *Clim. Past Discuss.*, *2015*, 279–305.

Mallinson, D. J., Flower, B., Hine, A., Brooks, G., & Garza, R. M. (2003). Paleoclimate implications of high latitude precession-scale mineralogic fluctuations during early Oligocene Antarctic glaciation: the Great Australian Bight record. *Global and Planetary Change*, *39*(3), 257–269.

Malvern Ltd. (2011). *Mastersizer 3000 User Manual*. MAN0474 Issue 1.0 October 2011.

Markle, B. R., Steig, E. J., Buizert, C., Schoenemann, S. W., Bitz, C. M., Fudge, T. J., … Sowers, T. (2016). Global atmospheric teleconnections during Dansgaard–Oeschger events. *Nature Geoscience*, *10*(1), ngeo2848.

McCave, I. N., Bryant, R. J., Cook, H. F., & Coughanowr, C. A. (1986). Evaluation of a Laser-Diffraction-Size Analyzer for Use with Natural Sediments: RESEARCH METHOD PAPER. *Journal of Sedimentary Research*, *56*(4).

McKay, N. P., Kaufman, D. S., & Michelutti, N. (2008). Biogenic silica concentration as a high-resolution, quantitative temperature proxy at Hallet Lake, south-central Alaska. *Geophysical Research Letters*, *35*(5), L05709.

Meyer-Jacob, C., Vogel, H., Boxberg, F., Rosén, P., Weber, M. E., & Bindler, R. (2014). Independent measurement of biogenic silica in sediments by FTIR spectroscopy and PLS regression. *Journal of Paleolimnology*, *52*(3), 245–255.

Meyer-Jacob, C., Vogel, H., Gebhardt, A. C., Wennrich, V., Melles, M., & Rosén, P. (2014). Biogeochemical variability during the past 3.6 million years recorded by

FTIR spectroscopy in the sediment record of Lake El'gygytgyn, Far East Russian Arctic. *Clim. Past*, *10*(1), 209–220.

Micheels, A., Bruch, A. A., Eronen, J., Fortelius, M., Harzhauser, M., Utescher, T., & Mosbrugger, V. (2011). Analysis of heat transport mechanisms from a Late Miocene model experiment with a fully-coupled atmosphere–ocean general circulation model. *Palaeogeography, Palaeoclimatology, Palaeoecology*, *304*(3), 337–350.

Mikhailik, V. B., Kapustyanyk, V., Tsybulskyi, V., Rudyk, V., & Kraus, H. (2015). Luminescence and scintillation properties of CsI -- a potential cryogenic scintillator. *Physica Status Solidi (B)*, *252*(4), 804–810.

Mikolajewicz, U., & Crowley, T. J. (1997). Response of a coupled ocean/energy balance model to restricted flow through the Central American Isthmus. *Paleoceanography*, *12*(3), 429–441.

Möller, A. L., Kaulfuss, U., Lee, D. E., & Wappler, T. (2017). High richness of insect herbivory from the early Miocene Hindon Maar crater, Otago, New Zealand. *PeerJ*, *5*.

Morales, E. A., Rivera, S. F., Rubin, S. D., Vis, M. L., & Houk, V. (2015). Aulacoseira kruegeriana (Diatomeae, Coscinodiscophyceae): a new centric diatom from high-elevation Andean rivers and streams of Bolivia. *Diatom Research*, *30*(3), 269–277.

Morrish, A. H. (2001a). Diamagnetic and Paramagnetic Susceptibilities. In *The Physical Principles of Magnetism* (pp. 31–77). John Wiley & Sons, Inc. Retrieved

Morrish, A. H. (2001b). Ferrimagnetism. In *The Physical Principles of Magnetism* (pp. 486–538). John Wiley & Sons, Inc.

Morrish, A. H. (2001c). Ferromagnetism. In *The Physical Principles of Magnetism* (pp. 259–331). John Wiley & Sons, Inc.

Morrish, A. H. (2001d). The Magnetic Field. In *The Physical Principles of Magnetism* (pp. 1–30). John Wiley & Sons, Inc.

Morrish, A. H. (2001e). The Magnetization of Ferromagnetic Materials. In *The Physical Principles of Magnetism* (pp. 332–431). John Wiley & Sons, Inc.

Mortimer, N. (1993). Jurassic tectonic history of the Otago Schist, New Zealand. *Tectonics*, *12*(1), 237–244.

Neiler, J. H., & Bell, P. R. (1968). V - The scintillation method. In K. Siegbahn (Ed.), *Alpha-, Beta- and Gamma-Ray Spectroscopy* (pp. 245–302). Amsterdam: Elsevier.

Nemeth, K. (2017). Geochemical evolution, vent structures, and erosion history of small-volume volcanoes in the Miocene intracontinental Waipiata Volcanic Field, New Zealand.

Nemeth, K., & White, J. (2003). Reconstructing eruption processes of a Miocene monogenetic volcanic field from vent remnants: Waipiata Volcanic Field, South Island, New Zealand. *Journal of Volcanology and Geothermal Research*, *124*, 1–21.

Nowaczyk, N. R., Frederichs, T. W., Kassens, H., Nørgaard-Pedersen, N., Spielhagen, R. F., Stein, R., & Weiel, D. (2001). Sedimentation rates in the Makarov Basin, central Arctic Ocean: A paleomagnetic and rock magnetic approach. *Paleoceanography*, *16*(4), 368–389.

Nowaczyk, N. R., Melles, M., & Minyuk, P. (2007). A revised age model for core PG1351 from Lake El'gygytgyn, Chukotka, based on magnetic susceptibility

variations tuned to northern hemisphere insolation variations. *Journal of Paleolimnology*, *37*(1), 65–76.

Oldfield, F., Barnosky, C., Leopold, E. B., & Smith, J. P. (1983). Mineral magnetic studies of lake sediments. In *Paleolimnology* (pp. 37–44). Springer, Dordrecht.

Ollikainen, M., Simola, H., & Niinioja, R. (1993). Changes in diatom assemblages in the profundal sediments of two large oligohumic lakes in eastern Finland. *Hydrobiologia*, *269–270*(1), 405–413.

Pagani, M., Zachos, J. C., Freeman, K. H., Tipple, B., & Bohaty, S. (2005). Marked decline in atmospheric carbon dioxide concentrations during the Paleogene. *Science (New York, N.Y.)*, *309*(5734), 600–603.

Pannard, A., Bormans, M., & Lagadeuc, Y. (2008). Phytoplankton species turnover controlled by physical forcing at different time scales. *Canadian Journal of Fisheries and Aquatic Sciences*, *65*(1), 47–60.

Pearson, P. N., & Palmer, M. R. (2000). Atmospheric carbon dioxide concentrations over the past 60 million years. *Nature*, *406*(6797), 695–699.

Pienitz, R., & Smol, J. P. (1993). Diatom assemblages and their relationship to environmental variables in lakes from the boreal forest-tundra ecotone near Yellowknife, Northwest Territories, Canada. *Hydrobiologia*, *269–270*(1), 391–404.

Pilskaln, C. H., & Johnson, T. C. (1991). Seasonal signals in Lake Malawi sediments. *Limnology and Oceanography*, *36*(3), 544–557.

Pole, M. (2003). New Zealand climate in the Neogene and implications for global atmospheric circulation. *Palaeogeography, Palaeoclimatology, Palaeoecology*, *193*, 269–284.

Pole, M. (2014). The Miocene climate in New Zealand: Estimates from paleobotanical data. *Palaeontologia Electronica*, *17*(2), 1–79.

Poppe, E., Fredericks, J., Rendigs, R., Blackwood, D., & Polloni, C. (2008). *Chapter 1: grain-size analysis of marine sediments: methodology and data processing* (USGS open-file report). USGS, Woods Hole: Coastal and Marine Geology Program, USGS.

Poth, D., & Negendank, J. F. W. (1993). Paleoclimate reconstruction at the Pleistocene/Holocene transition—A varve dated microstratigraphic record from Lake Meerfelder Maar (Westeifel, Germany). In *Paleolimnology of European Maar Lakes* (pp. 209–222). Springer, Berlin, Heidelberg. Retrieved from

Pratt, D. M. (1965). The Winter-Spring Diatom Flowering in Narragansett Bay1. *Limnology and Oceanography*, *10*(2), 173–184.

Raspopov, O. M., Dergachev, V. A., Esper, J., Kozyreva, O. V., Frank, D., Ogurtsov, M., … Shao, X. (2008). The influence of the de Vries (~200-year) solar cycle on climate variations: Results from the Central Asian Mountains and their global link. *Palaeogeography, Palaeoclimatology, Palaeoecology*, *259*(1), 6–16.

Raymo, M. E., & Ruddiman, W. F. (1992). Tectonic forcing of late Cenozoic climate. *Nature*, *359*(6391), 359117a0.

Recasens, C., Ariztegui, D., Maidana, N. I., & Zolitschka, B. (2015). Diatoms as indicators of hydrological and climatic changes in Laguna Potrok Aike (Patagonia) since the Late Pleistocene. *Palaeogeography, Palaeoclimatology, Palaeoecology*, *417*(Supplement C), 309–319.

Reichgelt, T. (2015). *Reconstructing southern New Zealand Miocene terrestrial climate and ecosystems from plant fossils* (PhD Thesis). University of Otago.

Reichgelt, T., Kennedy, E., C. Mildenhall, D., Conran, J., Greenwood, D., & Lee, D. (2013). Quantitative palaeoclimate estimates for Early Miocene southern New Zealand: Evidence from Foulden Maar. *Palaeogeography, Palaeoclimatology, Palaeoecology*, *378*, 36–44.

Research, I. S. for D., & Researchers, A. A. of D. (2002). *Proceedings of the 15th International Diatom Symposium: Perth, Australia 28 September -2 October 1998*. A.R.G. Gantner Verlag.

Romero, O. E., Kim, J.-H., Bárcena, M. A., Hall, I. R., Zahn, R., & Schneider, R. (2015). High-latitude forcing of diatom productivity in the southern Agulhas Plateau during the past 350 kyr. *Paleoceanography*, *30*(2), 2014PA002636.

Rosén, P., & Persson, P. (2006). Fourier-transform Infrared Spectroscopy (FTIRS), a New Method to Infer Past Changes in Tree-line Position and TOC using Lake Sediment. *Journal of Paleolimnology*, *35*(4), 913–923.

Rosén, P., Vogel, H., Cunningham, L., Reuss, N., Conley, D. J., & Persson, P. (2010). Fourier transform infrared spectroscopy, a new method for rapid determination of total organic and inorganic carbon and biogenic silica concentration in lake sediments. *Journal of Paleolimnology*, *43*(2), 247–259.

Rühland, K. M., Smol, J. P., & Pienitz, R. (2003). Ecology and spatial distributions of surface-sediment diatoms from 77 lakes in the subarctic Canadian treeline region. *Canadian Journal of Botany*, *81*(1), 57–73.

Sandgren, P., & Snowball, I. (2001). The Late Weichselian sea level history of the Kullen Peninsula in northwest Skåne, southern Sweden. *Boreas*, *30*(2), 115–130.

Sandgren, P., & Snowball, I. (2002). Application of Mineral Magnetic Techniques to Paleolimnology. In *Tracking Environmental Change Using Lake Sediments* (pp. 217–237). Springer, Dordrecht.

Savin, S. M., & Douglas, R. G. (1985). Sea Level, Climate, and the Central American Land Bridge. In *The Great American Biotic Interchange* (pp. 303–324). Springer, Boston, MA.

Scafetta, N., Milani, F., Bianchini, A., & Ortolani, S. (2016). On the astronomical origin of the Hallstatt oscillation found in radiocarbon and climate records throughout the Holocene. *Earth-Science Reviews*, *162*(Supplement C), 24–43.

Schulz, M., & Stattegger, K. (1997). Spectrum: spectral analysis of unevenly spaced paleoclimatic time series. *Computers & Geosciences*, *23*(9), 929–945.

Severijns, C. A., & Hazeleger, W. (2010). The efficient global primitive equation climate model SPEEDO V2.0. *Geosci. Model Dev.*, *3*(1), 105–122.

Shackleton, N. J. (1975). Paleotemperature History of the Cenozoic and the Initiation of Antarctic Glaciation: Oxygen and Carbon Isotope Analyses in DSDP Sites 277, 279 and 281. *Initial Reports of the Deep Sea Drilling Project*, *29*.

Shevenell, A. E., Kennett, J. P., & Lea, D. W. (2004). Middle Miocene Southern Ocean Cooling and Antarctic Cryosphere Expansion. *Science*, *305*(5691), 1766–1770.

Shuter, E., & Teasdale, W. (1989). Application of drilling, coring, and sampling techniques to test holes and wells. In *collection of environmental data*. washington: united states government printing office.

Siegbahn, K. (Ed.). (1968). A - Attenuation coefficients of various elements. In *Alpha-, Beta- and Gamma-Ray Spectroscopy* (pp. 827–839). Amsterdam: Elsevier.

Sime, L. C., Kohfeld, K. E., Le Quéré, C., Wolff, E. W., de Boer, A. M., Graham, R. M., & Bopp, L. (2013). Southern Hemisphere westerly wind changes during the Last Glacial Maximum: model-data comparison. *Quaternary Science Reviews*, *64*(Supplement C), 104–120.

Singh, H. K. A., Bitz, C. M., & Frierson, D. M. W. (2016). The Global Climate Response to Lowering Surface Orography of Antarctica and the Importance of Atmosphere–Ocean Coupling. *Journal of Climate*, *29*(11), 4137–4153.

Sirocko, F., Dietrich, S., Veres, D., Grootes, P. M., Schaber-Mohr, K., Seelos, K., … Grim, S. (2013). Multi-proxy dating of Holocene maar lakes and Pleistocene dry maar sediments in the Eifel, Germany. *Quaternary Science Reviews*, *62*, 56–76.

Snowball, I., Sandgren, P., & Petterson, G. (1999). The mineral magnetic properties of an annually laminated Holocene lake-sediment sequence in northern Sweden. *Holocene*, *9*, 353–362.

Snowball, I., & Sandgrena, P. (2002). Geomagnetic field variations in northern Sweden during the Holocene quantified from varved lake sediments and their implications for cosmogenic nuclide production rates. *The Holocene*, *12*(5), 517–530.

Stephens, T. (2011). *A Diatom Stable Isotope Paleolimnology of Lake Pupuke, Auckland, New Zealand* (Thesis).

Striewski, B., Mayr, C., Flenley, J., Naumann, R., Turner, G., & Lücke, A. (2009). Multi-proxy evidence of Late Holocene human-induced environmental changes at Lake Pupuke, Auckland (New Zealand). *Quaternary International*, *202*, 69–93.

Stuart, B. (2000). Infrared Spectroscopy. In *Kirk-Othmer Encyclopedia of Chemical Technology*. John Wiley & Sons, Inc.

Stuart, B. H. (2004). *Infrared Spectroscopy: Fundamentals and Applications*. John Wiley & Sons.

Swann, G. E. A., & Leng, M. J. (2009). A review of diatom δ18O in palaeoceanography. *Quaternary Science Reviews*, *28*(5), 384–398.

Swann, W., DP, T., HJ, M., HW, H., MD, M., & DJ, M. (1996). Analysis of phytoplankton of the Australian sector of the Southern Ocean: comparisons of

microscopy and size frequency data with interpretations of pigment HPLC data using the "CHEMTAX" matrix factorisation program. *Marine Ecology Progress Series*, *144*, 285–298.

Szczuciński, W., Kokociński, M., Rzeszewski, M., Chagué-Goff, C., Cachão, M., Goto, K., & Sugawara, D. (2012). Sediment sources and sedimentation processes of 2011 Tohoku-oki tsunami deposits on the Sendai Plain, Japan — Insights from diatoms, nannoliths and grain size distribution. *Sedimentary Geology*, *282*(Supplement C), 40–56.

Takano, H. (Tokai R. F. R. L. (1981). Notes on twisting of diatom colonies. *Bulletin of Tokai Regional Fisheries Research Laboratory (Japan)*.

Trapero, J. R., Sira-Ramírez, H., & Batlle, V. F. (2008). On the algebraic identification of the frequencies, amplitudes and phases of two sinusoidal signals from their noisy sum. *International Journal of Control*, *81*(3), 507–518.

Tremarin, P., Ludwig, T., & Torgan, L. (2012). Ultrastructure of *Aulacoseira brasiliensis sp*. nov. (Coscinodiscophyceae) and comparison with related species. *Journal of the Czech Phycological Society*, *12*, 171–188.

Tremblay, J.-E., Gratton, Y., Fauchot, J., & Price, N. M. (2002). Climatic and oceanic forcing of new, net, and diatom production in the North Water. *Deep Sea Research Part II: Topical Studies in Oceanography*, *49*(22), 4927–4946.

Trivedi, S., Dey, S., & Kumar, A. (2017). *Handbook of Research on Advanced Data Mining Techniques and Applications for Business Intelligence*.

Turney, C., Wilmshurst, J., Jones, R., Wood, J., Palmer, J., Hogg, A. G., … Thomas, Z. (2017). Reconstructing atmospheric circulation over southern New Zealand: Establishment of modern westerly airflow 5500 years ago and implications for

Southern Hemisphere Holocene climate change. *Quaternary Science Reviews*, *159*, 77–87.

Usoskin, I. G., Gallet, Y., Lopes, F., Kovaltsov, G. A., & Hulot, G. (2017). Solar activity during the Holocene: the Hallstatt cycle and its consequence for grand minima and maxima. *Astronomy & Astrophysics*, *587*, A150.

Utescher, T., Ivanov, D., Harzhauser, M., Bozukov, V., Ashraf, A. R., Rolf, C., … Mosbrugger, V. (2009). Cyclic climate and vegetation change in the late Miocene of Western Bulgaria. *Palaeogeography, Palaeoclimatology, Palaeoecology*, *272*(1), 99–114.

V. Demicco, R., Lowenstein, T., & A. Hardie, L. (2003). Atmospheric pCO2 since 60 Ma from records of seawater pH, calcium, and primary carbonate mineralogy. *Geology*, *31*.

Verducci, M., Foresi, L. M., Scott, G. H., Sprovieri, M., Lirer, F., & Pelosi, N. (2009). The Middle Miocene climatic transition in the Southern Ocean: Evidence of paleoclimatic and hydrographic changes at Kerguelen plateau from planktonic foraminifers and stable isotopes. *Palaeogeography, Palaeoclimatology, Palaeoecology*, *280*(3–4), 371–386.

Vincent, E., & Berger, W. H. (1985). Carbon Dioxide and Polar Cooling in the Miocene: The Monterey Hypothesis. In E. T. Sundquist & W. S. Broecker (Eds.), *The Carbon Cycle and Atmospheric CO2: Natural Variations Archean to Present* (pp. 455–468). American Geophysical Union.

Vogel, H., Meyer-Jacob, C., Melles, M., Brigham-Grette, J., Andreev, A. A., Wennrich, V., … Rosén, P. (2013). Detailed insight into Arctic climatic variability during MIS 11c at Lake El'gygytgyn, NE Russia. *Clim. Past*, *9*(4), 1467–1479.

von der Heydt, A., & Dijkstra, H. A. (2006). Effect of ocean gateways on the global

    ocean circulation in the late Oligocene and early Miocene. *Paleoceanography*,

    21(1), PA1011.

W. E. Lemasurier, & landis, c. A. (1996). Mantle-plume activity recorded by low-relief

    erosion surface in West Antarctica and New Zealand. *Geological Society of*

    America Bulletin, *108*, 1450–66.

Wang, L., Lu, H., Liu, J., Gu, Z., Mingram, J., Chu, G., … Liu, T. (2008). Diatom-

    based inference of variations in the strength of Asian winter monsoon winds

    between 17,500 and 6000 calendar years B.P. *Journal of Geophysical Research:*

    Atmospheres, *113*(D21), D21101.

Weckström, J., Korhola, A., & Blom, T. (1997). Diatoms as quantitative indicators of

    pH and water temperature in subarctic Fennoscandian lakes. *Hydrobiologia*,

    347(1–3), 171–184.

Wei, J. H., Finkelstein, D. B., Brigham-Grette, J., Castañeda, I. S., & Nowaczyk, N.

    (2014). Sediment colour reflectance spectroscopy as a proxy for wet/dry cycles at

    Lake El'gygytgyn, Far East Russia, during Marine Isotope Stages 8 to 12.

    Sedimentology, *61*(6), 1793–1811.

Wetzel, R. G. (2001). 8 - Structure and productivity of aquatic ecosystems. In

    Limnology (Third Edition) (pp. 129–150). San Diego: Academic Press.

Williams, M. (1992). Evidence for the dissolution of magnetite in recent Scottish peats.

    Quaternary Research, *37*(2), 171–182.

Williamson, D., Jelinowska, A., Kissel, C., Tucholka, P., Gibert, E., Gasse, F., …

    Wieckowski, K. (1998). Mineral-magnetic proxies of erosion/oxidation cycles in

    tropical maar-lake sediments (Lake Tritrivakely, Madagascar):

paleoenvironmental implications. *Earth and Planetary Science Letters*, *155*(3), 205–219.

Woodruff, F., & Savin, S. (1991). Mid-Miocene isotope stratigraphy in the deep sea: High-resolution correlations, paleoclimatic cycles, and sediment preservation. *Paleoceanography*, *6*(6), 755–806.

Yiou, P., Baert, E., & Loutre, M. F. (1996). Spectral analysis of climate data. *Surveys in Geophysics*, *17*(6), 619–663.

You, Y., Huber, M., Muller, R. D., Poulsen, C. J., & Ribbe, J. (2009). Simulation of the middle miocene climate optimum. *Geophysical Research Letters*, *36*(4), L04702.

Youngson, J. (1993). Mineralized vein systems and Miocene maar crater sediments at Hindon, East Otago, New Zealand · Otago Geology Theses. Retrieved November 3, 2017

Zachos, J., Pagani, M., Sloan, L., Thomas, E., & Billups, K. (2001). Trends, rhythms, and aberrations in global climate 65 Ma to present. *Science (New York, N.Y.)*, *292*(5517), 686–693.

APPENDICES

6.1. Principal components

6.1.1 PCA limited to lake sediment and using only normalised, GEOTEK MSCL variables:

These tables were produced using high resolution variables only, but are considered less informative than analyses incorporating all variables.

Table 6.1 Correlation matrix reporting the relationships between normalised Z-scores for the variables included in the principal components analysis within the complete core.

		Density	MS	L	A	B
Correlation	Density	1.000	.020	-.136	-.009	.065
	MS	.020	1.000	.138	-.237	-.176
	L	-.136	.138	1.000	-.015	.119
	A	-.009	-.237	-.015	1.000	.611
	B	.065	-.176	.119	.611	1.000

Table 6.2. Kaiser-Meyer-Olkin measure of sampling adequacy and Bartlett's Test of Sphericity

Kaiser-Meyer-Olkin Measure of Sampling Adequacy.		.508
Bartlett's Test of Sphericity	Approx. Chi-Square	832.433
	df	10
	Sig.	.000

Table 6.3. Table of communalities before and after extraction.

221

	Initial	Extraction
Density	1.000	.309
MS	1.000	.369
L	1.000	.703
A	1.000	.763
B	1.000	.759
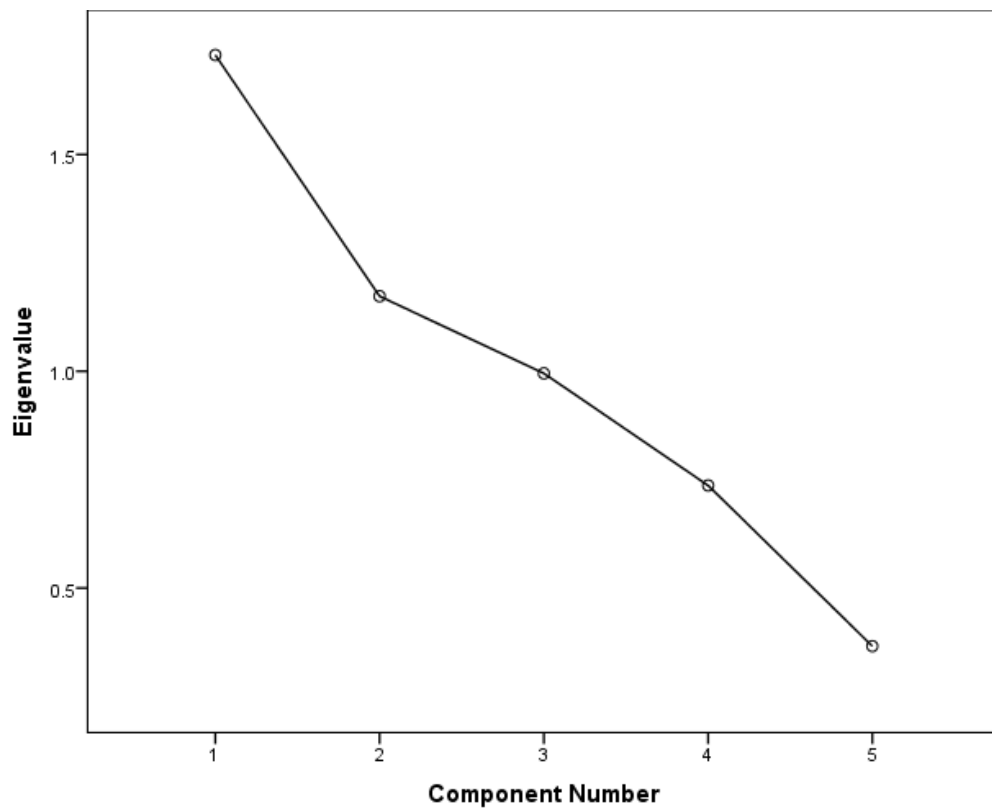
Figure 6.1 Scree plot from PCA 3. Only two factors were acceptable

Table 6.4. Variance explained by each of the two components identified through principal components analysis and subsequently included in cluster analysis. The majority of variation is explained by these components, whilst subsequent eigenvectors have a limited influence on variability in the dataset.

	Component	
	1	2
Density	.048	-.553
MS	-.485	.366
L	.022	.838
A	.872	.048
B	.855	.168

Extraction Method: Principal Component Analysis.

a. 2 components extracted.
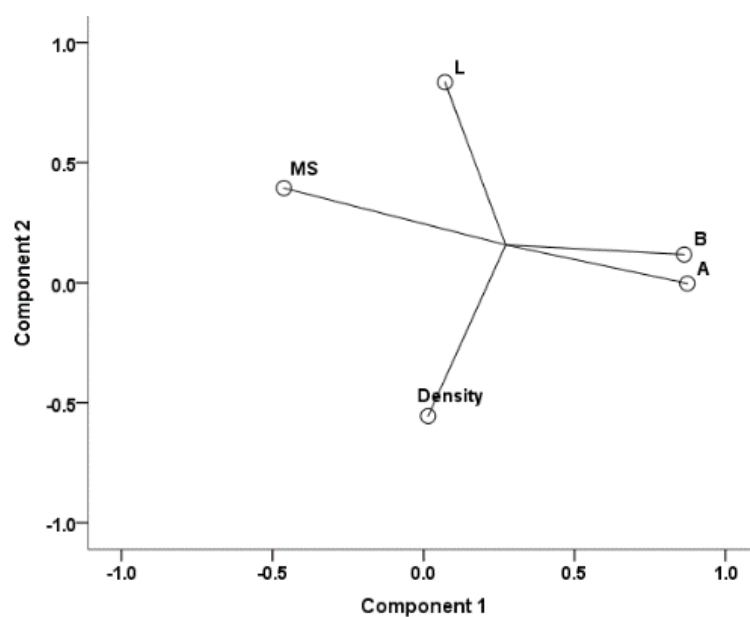
Figure 6.2 Loading plot showing effects of component 1 and 2 on PCA 3

6.1.2 PCA including lake sediment, schist overburden and volcanic breccia using all moderately correlated, normalised variables:

Table 6.5. is a second correlation matrix featuring only the normalised variables included in the PCA analysis.

Table 6.5. Correlation matrix reporting the relationships between normalised Z-scores for the variables included in the Principal components analysis, using data available for the entire length of the core.

		Schist	DX10	DX50	DX90	Density	Magnetic Susceptibility	L*	A*	B*
Correlation	BSI	-.503	.164	-.162	-.104	.009	.070	.154	.041	.166
	Schist		-.369	-.018	-.135	-.018	.021	-.252	-.103	-.311
	DX10			.623	.340	.058	-.016	.025	.082	.136
	DX50				.468	.005	.062	-.139	-.036	-.017
	DX90					-.179	.055	.048	.071	.145
	Density						-.042	-.159	-.014	-.020
	Magnetic Susceptibility							.111	-.278	-.161
	L*								-.017	.082
	A*									.755

The KMO value reported through this analysis (0.597, Table 6.5) is at the borderline of acceptability, and indicates that the variables are partially noncollinear and that factor analysis may not be appropriate in this instance

As the Bartlett's test is highly significant ($p < 0.001$), factor analysis is considered appropriate.

Table 6.6. Kaiser-Meyer-Olkin measure of sampling adequacy and Bartlett's Test of Sphericity

Kaiser-Meyer-Olkin Measure of Sampling Adequacy.		.597
Bartlett's Test of Sphericity	Approx. Chi-Square	353.478
	df	45
	Sig.	.000

Table 6.6 reports the table of communalities before and after extraction. The greatest communalities are present in the density and DX50 variables (where 83.2 % and 86.1 % of their variance is explained by underlying factors). Magnetic susceptibility is largely unrelated to other variables, and only 39.7% of variance within this variable is explained by an underlying factor.

Table 6.7. Variable communalities before and after extraction.

Communalities

	Initial	Extraction
BSI	1.000	.793
Schist	1.000	.759
DX10	1.000	.823
DX50	1.000	.861
DX90	1.000	.655
DENSITY	1.000	.832
MS	1.000	.397
L*	1.000	.828
A*	1.000	.800
B*	1.000	.788

Ten linear components were identified using Principal Components Analysis, with the first four components representing 75.37 % of variation within the dataset. Components 5 and beyond each account for less than 9 % of variability and are unlikely to be statistically important (Table 6.6).

Table 6.8. Variance explained by each of the ten components identified through principal components analysis using a subset of the available geophysical data. The majority of variation is explained by the first four components, whilst subsequent eigenvectors have a limited influence on variability in the dataset.

| Component | Initial Eigenvalues | | | Extraction Sums of Squared Loadings | | |
	Total	% of Variance	Cumulative %	Total	% of Variance	Cumulative %
1	2.950	29.498	29.498	2.950	29.498	29.498
2	2.258	22.579	52.077	2.258	22.579	52.077
3	1.313	13.130	65.207	1.313	13.130	65.207
4	1.016	10.159	75.366	1.016	10.159	75.366
5	.869	8.685	84.051			
6	.604	6.035	90.086			
7	.465	4.647	94.733			
8	.211	2.114	96.847			
9	.171	1.708	98.555			
10	.145	1.445	100.000			

Extraction Method: Principal Component Analysis.

A scree plot of this principal component analysis (Figure 6.3) shows that an inflection occurs at the fifth eigenvector, where subsequent vectors begin to possess significantly lower eigenvalues. Factors with eigenvalues greater than one are considered to be valid, for this reason the first four components are considered.
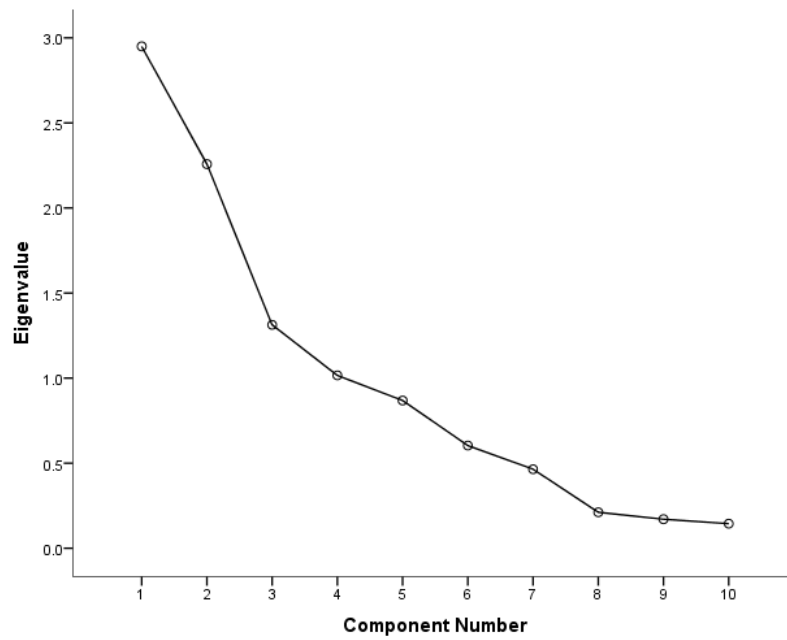
Figure 6.3 The Scree Plot associated with this Principal Components Analysis lacks a clear inflection point within the first four components, indicating that each of those components is likely to be valid, and that they should be considered in relation to the percent of variance each contributes.
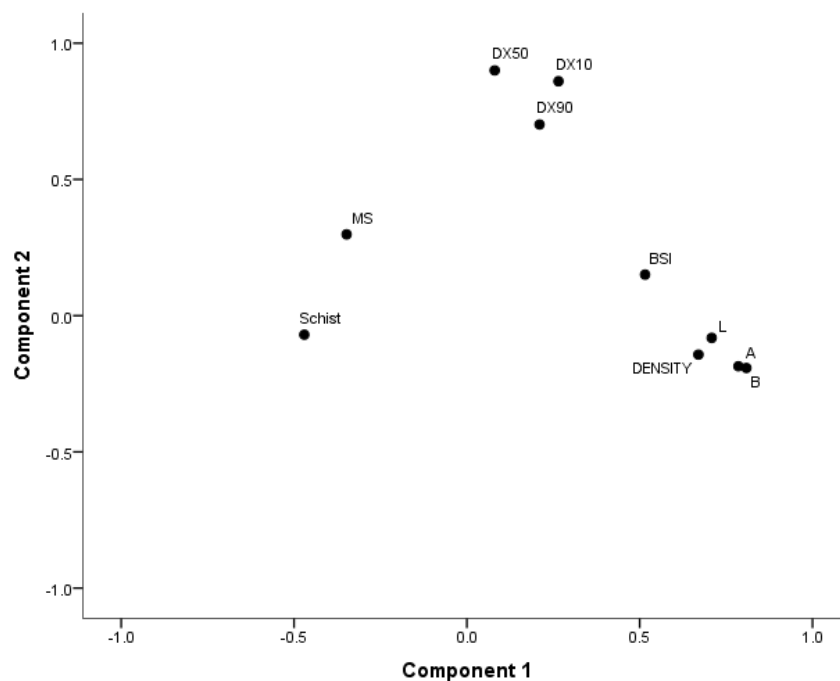
Figure 6.4 Loading plot of components 1 and 2 for PCA 4

227

Following an eigenvalue decomposition, four components were found to collectively account for 75.37 % of the variation in this dataset. The first eigenvector represents 29.5% of variability and correlates strongly with biogenic silica concentration ($Z = 0.516$). A positive correlation was also found in this component with luminosity (0.708) and A and B colour components (0.785 and 0.808, respectively) (Table 6.8). Density is also positively correlated with this component (0.67). A weak inverse correlation was identified between this component and the concentration of terrigenous material within the core. Material which possesses a high factor score on this component is thus dense, rich in biogenic silica and low in terrigenous material. In addition, high factor scores on this axis indicate bright material with a relatively reddish-yellow colouration. This is consistent with the expected colouration of diatom-rich sediment (Table 6.9).

The second component identified through this analysis represents a further 22.6% of the variation in the dataset, and correlates most strongly with grain-size measurements and magnetic susceptibility (Table 6.9). Sections of the core which score highly on this axis are likely to have moderate biogenic silica concentrations and will exhibit a darker colouration, with a green-blue hue.

The third key eigenvector observed correlates with material which is extremely low in biogenic silica ($Z = -0.396$) and rich in terrigenous sediment ($Z=0.719$). Material which correlates strongly with this axis has a relatively high magnetic susceptibility and above average density (Table 6.9). This eigenvector represents 13.13 % of variation in the dataset. Finally, the fourth component represents 10.2% of variation and represents material which is both rich in biogenic silica ($z=0.607$), and possesses a moderately high magnetic susceptibility ($z=0.364$). This material has a relatively fine particle size and high luminescence with a green-blue hue.

Table 6.9. Component Score Coefficient Matrix, reflecting the four dominant components which account for a combined total of 74.7% of the variation within this dataset.

| | Component | | | |
	1	2	3	4
BSI	.516	.151	-.369	.607
Schist	-.470	-.070	.719	-.128
DX10	.265	.860	-.091	.066
DX50	.080	.900	.175	-.117
DX90	.210	.702	.074	-.336
DENSITY	.670	-.143	.581	.160
MS	-.348	.298	.233	.364
L	.708	-.082	.453	.338
A	.785	-.186	.006	-.386
B	.808	-.192	-.138	-.281

Extraction Method: Principal Component Analysis.

a. 4 components extracted.

Figure 6.5 is a factor score plot showing the distribution of individual measurements along the first two component axes (accounting for 49% of the variability in the dataset). High values on the y-axis in this figure indicate dense portions of the lake sediment core considered to possess a moderately large grain size and a tendency towards a reddish-yellow colour. Samples at the top of this axis are also rich in BSi, and low in terrigenous sediment. In contrast, high values on the x-axis (component 2) have moderate biogenic silica values and exhibit low schist concentrations. These variables have a high magnetic susceptibility and a very large grainsize. This axis also correlates with dark colours in the core and those that trend towards greenish blue. Schist is present in values that correlate strongly with the second component, and this is also associated with an increase in magnetic susceptibility values. The second component is thus likely to reflect dark sections of the core which are somewhat rich in organic carbon.
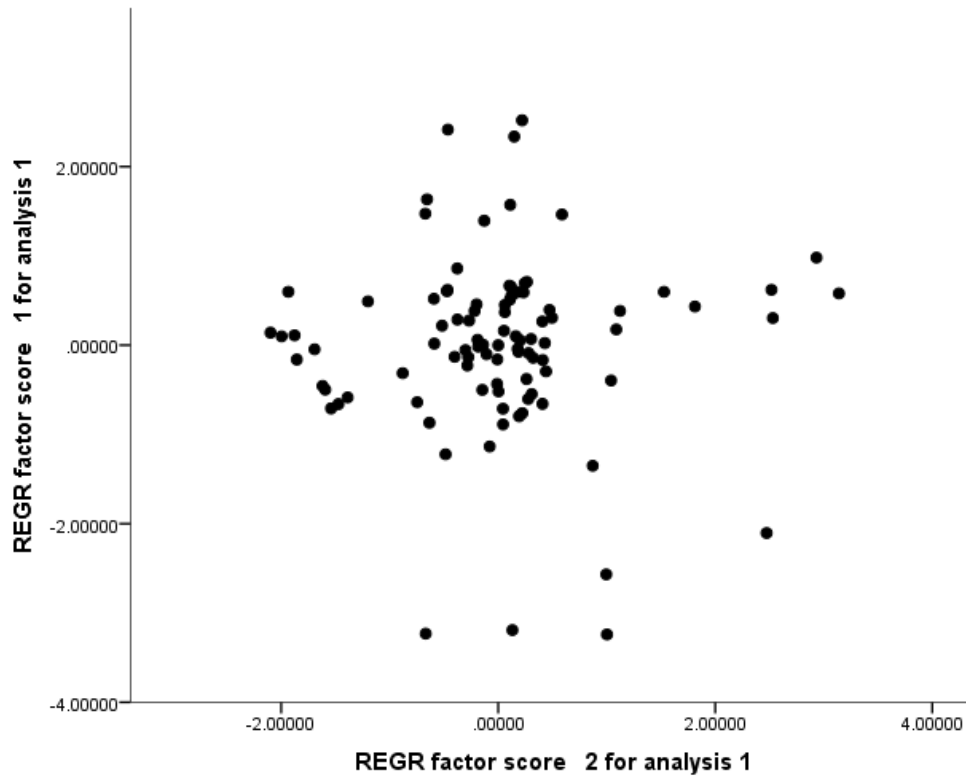
Figure 6.5., Distribution of factor scores along primary components.

6.2. GEOTEK MSCL data summary

The following section presents several columns of processed data derived from MSCL measurements. Each section includes measurements of magnetic susceptibility, density, reflectance and L*A*B* colour intensity. Different scales are used in each figure.

Depth (cm)	Density (g cm^{-3})	Average Reflectance (%)	Magnetic Susceptibility (x10^{-8} m^3 kg^{-1})	L*A*B*

Depth (cm)		Density (g cm^{-3})	Average Reflectance (%)	Magnetic Susceptibility (x10^{-8} m^3 kg^{-1})	L*A*B*

Depth (cm)		Density (g cm^{-3})	Average Reflectance (%)	Magnetic Susceptibility (x10^{-8} m^3 kg^{-1})	L*A*B*
		1 1.5 2	0 5	-1.5 0.5	0 10 20

| Depth (cm) | Density (g cm^{-3}) | Average Reflectance (%) | Magnetic Susceptibility (x10^{-8} m^3 kg^{-1}) | L*A*B* |

Depth (cm)		Density (g cm^{-3})		Average Reflectance (%)		Magnetic Susceptibility (x10^{-8} m^3 kg^{-1})		L*A*B*		
		1	1.5	1	2	-2.5	-0.5	0	10	20

Depth (cm)	Density (g cm⁻³)	Average Reflectance (%)	Magnetic Susceptibility (x10⁻⁸ m³ kg⁻¹)	L*A*B*

Depth (cm)		Density (g cm^{-3})	Average Reflectance (%)	Magnetic Susceptibility (x10^{-8} m^3 kg^{-1})	L*A*B*

Depth (cm)		Density (g cm^{-3})	Average Reflectance (%)	Magnetic Susceptibility (x10^{-8} m^3 kg^{-1})	L*A*B*

Depth (cm)		Density (g cm^{-3})	Average Reflectance (%)	Magnetic Susceptibility (x10^{-8} m^3 kg^{-1})	L*A*B*

Depth (cm)	Density (g cm^{-3})	Average Reflectance (%)	Magnetic Susceptibility (x10^{-8} m^3 kg^{-1})	L*A*B*

Depth (cm)	Density (g cm^{-3})	Average Reflectance (%)	Magnetic Susceptibility (x10^{-8} m^3 kg^{-1})	L*A*B*

Density (g cm^{-3}): 1 2 3

Average Reflectance (%): 0 10

Magnetic Susceptibility (x10^{-8} m^3 kg^{-1}): -5 5 15

L*A*B*: 0 50

Depth (cm):
1473
1483
1493
1503
1513
1523
1533
1543
1553
1563
1573

Depth (cm)	Density (g cm^{-3})	Average Reflectance (%)	Magnetic Susceptibility (x10^{-8} m^3 kg^{-1})	L*A*B*
	1 3	0 5 10	-5 5 15	0